DISS. ETH NO. 18225

Sea Surface Topography and Marine Geoid by Airborne Laser Altimetry and Shipborne Ultrasound Altimetry in the Aegean Sea

A dissertation submitted to
ETH ZURICH
for the degree of
Doctor of Sciences

presented by
PHILIPPE LIMPACH
Ing. Génie Rural EPFL
born September 7, 1977
citizen of Luxembourg

accepted on the recommendation of
Prof. Dr. H.-G. Kahle, examiner
Prof. Dr. M. Becker, co-examiner
Prof. Dr. A. Geiger, co-examiner

2009

Abstract

The aim of this thesis was to contribute to the improvement of sea level monitoring and to provide local-scale information on the short-wavelength structure of the marine gravity field, by developing enhanced methods for offshore sea surface height observations. The methods investigated included airborne laser altimetry, shipborne ultrasound altimetry and GPS-equipped buoys.

In a first step, instrumental aspects of sea surface height observations by airborne and shipborne altimetry are analyzed and discussed. Knowledge of high-precise position and attitude of the range sensor is crucial for an accurate sea surface height computation. For this purpose, the aircraft and boat were equipped with a multi-antenna GPS array and inertial systems. Instantaneous sea surface heights were computed from the range data by direct georeferencing. Important aspects are the influences of errors in the differential kinematic GPS positioning and in the attitude determination, as well as the calibration of boresight misalignments. In a second step, the instantaneous sea surface heights were reduced to mean sea surface by applying corrections for geophysical effects, including waves, tides and atmospheric pressure and wind forcing.

In the framework of this work, several regional campaigns for sea surface height surveys based on airborne and shipborne altimetry were carried out in the Eastern Mediterranean Sea. Dedicated offshore sea surface height surveys, including deployments of GPS buoys, were performed along Jason-1 radar altimetry ground-tracks, providing in situ sea surface height information. Airborne laser altimetry data was acquired along densely-spaced flight-tracks covering an area of 200 km by 200 km around the western part of the island of Crete, Greece, in the vicinity of the Hellenic Trench. The objective was the determination of a detailed regional geoid and sea surface topography model in the framework of the GAVDOS project, funded by the European Union. Furthermore, several campaigns for shipborne sea surface height observations were carried out in the North Aegean Sea, in the vicinity of the North Aegean Trough.

Based on the airborne and shipborne altimetry data, a high-resolution sea surface topography of the survey areas was computed, with a vertical accuracy below 10 cm. Geoid heights were derived from the sea surface heights by subtracting the mean dynamic ocean topography, induced by ocean currents. Around western Crete, the geoid obtained from airborne laser altimetry is characterized by very pronounced gradients, with an average slope of 20 m along a distance of only 200 km and maximum local gradients of 22 cm/km. These gradients are a clear indication for strong gravity effects caused by the bathymetry and the geodynamic system of the Hellenic Trench. In the North Aegean Sea, the geoid obtained from shipborne altimetry shows a distinct depression of more than 1.5 m, indicating a connection with the bathymetry and the geodynamic features of the North Aegean Trough.

The high resolution and accuracy of the geoid heights obtained in both survey areas was shown by comparisons with mean sea surface models from multi-mission spaceborne radar altimetry and with global and regional geoid models. The reduction of the geoid heights for modeled mass effects of topography, bathymetry, marine sedimentary deposits and crust/mantle boundary revealed strong gravity anomalies related to the geodynamic processes in the survey areas.

Zusammenfassung

Ziel der Dissertation ist die präzise Bestimmung der Meeresoberfläche als Beitrag zur Verbesserung der Beobachtung des Meeresspiegels und zur lokalen Bestimmung der kurzwelligen Strukturen des Schwerefeldes. Zu diesem Zweck wurden mehrere Methoden zur präzisen und flächendeckenden Vermessung der Meeresoberfläche untersucht, weiterentwickelt und eingesetzt. Es handelt sich hierbei um flugzeuggestützte Laser-Altimetrie, schiffsgestützte Ultraschall-Altimetrie und GPS Bojen-Messungen.

In einem ersten Schritt werden die instrumentellen Aspekte von Meereshöhenbeobachtungen mittels flugzeug- und schiffsgestützter Altimetrie analysiert und diskutiert. Für die genaue Berechnung der Meereshöhen ist die präzise Kenntnis von Position und Lage der Messplattform von entscheidender Bedeutung. Zu diesem Zweck wurden Flugzeug und Schiff mit mehreren GPS-Antennen und einem Inertialsystem ausgerüstet. Die momentanen Meereshöhen wurden mittels direkter Georeferenzierung aus den Altimeterdaten berechnet. Die wichtigsten Aspekte sind hierbei die Einflüsse von Fehlern in der differentiellen kinematischen GPS-Positionierung, Fehlern in der Lagebestimmung, sowie Orientierungsfehler der Sensoren. In einem zweiten Schritt wurden zeitabhängige Variationen der Meereshöhe, verursacht durch Einflüsse von Wellen, Gezeiten, Luftdruck und Wind, korrigiert.

Im Rahmen dieser Arbeit wurden mehrere regionale Messkampagnen im östlichen Mittelmeer durchgeführt. Die Messgebiete beinhalten Ground-Tracks des Radar-Altimeter Satelliten Jason-1. Entlang dieser Tracks wurden Messungen während Überflügen von Jason-1 durchgeführt. In einem Gebiet von 200 auf 200 km rund um die Insel Kreta wurde die Meeresoberfläche mittels flugzeuggestützte Laser-Altimetrie vermessen. Das Gebiet umfasst einen Teil des Hellenischen Grabens. Ziel dieser Messkampagne war die Bestimmung eines detaillierten Geoid- und Meeresoberflächenmodells im Rahmen des GAVDOS-Projektes, unterstützt von der Europäischen Union. Des Weiteren wurden mehrere Messkampagnen mittels schiffsgestützter Ultraschall-Altimetrie in der Nord-Ägäis durchgeführt. Ein besonderes geodynamisches Merkmal dieser Region ist der Nordägäische Graben.

Mit Hilfe der Flugzeug- und Schiffsdaten konnte eine hochauflösende Meerestopographie mit einer vertikalen Genauigkeit unter 10 cm bestimmt werden. Durch Abzug der dynamischen Meerestopographie, welche durch Meeresströmungen verursacht wird, wurden aus den beobachteten Meereshöhen Geoidhöhen abgeleitet. Das resultierende Geoid rund um Kreta zeigt sehr starke Gradienten, mit einem durchschnittlichen Gefälle von 20 m auf 200 km und maximalen Gradienten von 22 cm/km. Diese Gradienten sind ein klarer Hinweis auf signifikante Schwerefeldeffekte, verursacht durch die Bathymetrie und das geodynamische System des Hellenischen Grabens. Das Geoid in der Nord-Ägäis zeigt eine ausgeprägte Depression von etwa 1.5 m, welche mit der Bathymetrie und den geodynamischen Eigenschaften des Nordägäischen Grabens in Verbindung gebracht werden kann.

Die hohe Auflösung und Genauigkeit der berechneten Geoidhöhen konnten durch Vergleiche mit Modellen der mittleren Meereshöhe aus Satelliten-Radar-Altimetrie, sowie mit globalen und regionalen Geoidmodellen, aufgezeigt werden. Des Weiteren wurden durch die Reduktion von modellierten Masseneffekten, verursacht durch Topographie, Bathymetrie, marinen Sedimenten und Krusten/Mantel-Grenze, starke Anomalien im Schwerefeld detektiert, welche mit den geodynamischen Prozessen in den Messgebieten in Verbindung stehen.

Acknowledgements

I am deeply grateful to Prof. Dr. Hans-Gert Kahle for giving me the opportunity to work in this very interesting field of geodesy. In addition, I would like to thank all the people who contributed to the successful completion of this research project. These are in alphabetical order:

Dr. Franz Barthelmes, GFZ Potsdam, Germany

Prof. Dr. Matthias Becker, Institut für Physikalische Geodäsie, TU Darmstadt, Germany

Dr. Beat Bürki, Geodesy and Geodynamics Lab, ETH Zurich, Switzerland

Dr. Etienne Favey, μBlox AG, Switzerland

Jules Fenner, Institute of Geodesy and Photogrammetry, ETH Zurich, Switzerland

Dr. Rene Forsberg, Geodynamics Department, National Survey and Cadastre of Denmark (KMS), Denmark

Prof. Dr. Alain Geiger, Geodesy and Geodynamics Lab, ETH Zurich, Switzerland

Vassilios N. Grigoriadis, Dept. of Geodesy and Surveying, Aristotle University of Thessaloniki, Greece

Joel C. Hagen, Acumen Instruments Corporation, Ames, IA, USA

Marcel van Hak, Xsens Technologies B.V., The Netherlands

Katrin Höland, University Children's Hospital, Zurich, Switzerland

Dr. Christine Hollenstein, Geodesy and Geodynamics Lab, ETH Zurich, Switzerland

Dr. Philippe Kehl, Geodesy and Geodynamics Lab, ETH Zurich, Switzerland

Jürg Lieberherr, Pepperl+Fuchs AG, Studen, Switzerland

Dr. Simon Lutz, Astronomisches Institut, Universität Bern, Switzerland

Prof. Dr. Stelios P. Mertikas, Geodesy and Geomatics Engineering Lab, Technical University of Crete, Greece

Michael Müller, Geodesy and Geodynamics Lab, ETH Zurich, Switzerland

Jrène Müller-Gantenbein, Geodesy and Geodynamics Lab, ETH Zürich

Hanspeter Oesch, Institute of Geodesy and Photogrammetry, ETH Zurich, Switzerland

Dr. Erricos C. Pavlis, Joint Center for Earth Systems Technology (JCET), UMBC, USA

Dr. Alex Somieski, Geodesy and Geodynamics Lab, ETH Zurich, Switzerland

Dr. Anna Somieski, Geodesy and Geodynamics Lab, ETH Zurich, Switzerland

Paul Sorber, Institute of Geodesy and Photogrammetry, ETH Zurich, Switzerland

Dr. Marc Troller, Geodesy and Geodynamics Lab, ETH Zurich, Switzerland

Prof. Dr. Ilias N. Tziavos, Dept. of Geodesy and Surveying, Aristotle University of Thessaloniki, Greece

Contents

Abbreviations

A/D	Analog-to-Digital
AHRS	Attitude and Heading Reference System
ADT	Absolute Dynamic ocean Topography
AIUB	Astronomical Institute of the University of Bern
AUTH	Aristotle University of Thessaloniki
AVISO	Archiving, Validation and Interpretation of Satellite Oceanographic data
CLS	Collecte Localisation Satellites
CLS01	Mean sea surface model 2001 by CLS Space Oceanography Division
CNES	Centre National d'Etudes Spatiales
CNRS	Centre National de la Recherche Scientifique
DAC	Dynamic Atmospheric Correction
DNSC	Danish National Space Center
DORIS	Détermination d'Ornite et de Radiopositionnement Intégrés par Satellite
DOT	Dynamic Ocean Topography
DOV	Deflections of the Vertical
DTM	Digital Terrain Model
DT	Delayed-Time
DUACS	Data Unification andd Altimeter Combination System
ECMWF	European Centre for Medium-Range Weather Forecasts
EDM	Electronic Distance Measurement
EGM96	Earth Geopotential Model 1996
EGM2008	Earth Geopotential Model 2008
EOSDIS	Earth Observing System Data and Information System
ESA	European Space Agency
ESC	European Seismological Commission
ETH(Z)	Eidgenössische Technische Hochschule (Zürich)
EU	European Union
EUMETSAT	European Organization for the Exploitation of Meteorological Satellites
FFT	Fast Fourier Transformation
FIR	Flight Information Region
GDR	Geophysical Data Records
GFZ	Geo Forschungs Zentrum (Postdam)
GGL	Geodesy and Geodynamics Laboratory
GLOSS	Global Sea Level Observing System
GNSS	Global Navigation Satellite System
GPS	Global Positioning System
GOCE	Gravity Field and Steady-State Ocean Circulation Explorer
GRGS	Groupe de Recherche de Geodésie Spatiale
GRS80	Geodetic Reference System 1980
GSFC	Goddard Space Flight Center (NASA)
HNHS	Hellenic Navy Hydrographic Service
IAG	International Association of Geodesy
IB	Inverse Barometer
IBC	Inverse Barometer Correction
IERS	International Earth Rotation and Reference Systems Service

IGS	International GNSS Service
INS	Inertial Navigation System
IMU	Inertial Measurement Unit
IOC	Intergovernmental Oceanographic Commission
ITS	International Temperature Scale
ITRF	International Terrestrial Reference Frame
IUGG	International Union of Geodesy and Geophysics
KMS	National Survey and Cadastre of Denmark (Kort & Matrikelstyrelsen)
LAGEOS	Laser Geodynamics Satellite
LEGOS	Laboratoire d'Études en Géophysique et Océanographie Spatiale
LSQ	Least-Squares
MDT	Mean Dynamic ocean Topography
MEMS	Micro-Electro-Mechanical Systems
MOG2D	2D Gravity Wave Model
MSS	Mean Sea Surface
NASA	National Aeronautics and Space Administration
NAT	North Aegean Trough
NED	North, East, Down coordinate system
NGA	National Geospatial-Intelligence Agency
NIMA	National Imagery and Mapping Agency
NOAA	National Oceanic and Atmospheric Administration
NRT	Near Real Time
OSTM	Ocean Surface Topography Mission
PODAAC	Physical Oceanography Distributed Active Archive Center
POL	Proudman Oceanographic Laboratory
RMS	Root-Mean-Square
SELF	Sea Level Fluctuation Project
SLA	Sea Level Anomaly
SLR	Satellite Laser Ranging
SMDT	Synthetic Mean Dynamic ocean Topography
SSALTO	CNES multimission ground-segment
SSH	Sea Surface Height
SST	Sea Surface Topography
UT	Universal Time
UTC	Universal Time Coordinated
WGS84	World Geodetic System 1984
WMO	World Meteorological Organization
ZPD	Zenith Path Delay

1 Introduction

1.1 Motivation and Goals

Concerns of the future are associated with the fact that non-natural processes have begun to influence life on our planet at a global scale. Global change has become of major interest, raising the need to describe the Earth as a changing system. One of the internationally widely accepted scientific focuses is pointed upon the sea level and its variability. Since the sea surface reflects the integral of both the amount of water and the heat content of the oceans, it is a key quantity that responds to climate change and short-term variability. With an increasing understanding of the processes involved in sea surface variability, precise sea surface height observations will provide long-term benefits in environment management, safety and protection, and contribute to the assessment of global change. Interdisciplinary studies of climatic interactions in the Mediterranean area are important for the surrounding countries. Sea-level fluctuations in the region have long history and can result in tremendous economic losses, regarding the present distribution of coastal cities. The aim of this thesis was to contribute to the research fields of geoprocesses and geomonitoring by investigating methods providing reliable observations of the sea surface.

On a global scale, satellite radar altimetry missions are the basic means for sea surface height monitoring over the deep sea, with dense and homogeneous coverage in space and time. For the past decades, Europe has invested in several radar altimetry space missions (ERS-1, ERS-2, and ENVISAT, operated by ESA), as well as in the joint participation of the French Space Agency CNES and the United States NASA in the missions TOPEX/Poseidon (AVISO, 1996) and its follow-on mission Jason-1 (Picot et al., 2003). In June 2008, Jason-2, also called Ocean Surface Topography Mission (OSTM), was launched as another follow-on mission (OSTM, 2008). Important outputs of satellite radar altimetry missions are information on the short- and long-term variability of the sea surface. A result of major concern is the evidence of global sea level rise of 3.3 mm/yr detected by continuous radar altimetry observations since 1992 (Fig. 1.1). Half of this rise is most likely due to the dilatation of the water associated with global ocean temperature increase. The global image of sea level variations provided by radar altimetry shows the large geographical variability of sea level trends (Fig. 1.2). Furthermore, radar altimetry missions allowed to captured the evolution of El Niño/La Niña events and broadened our understanding of these phenomena like no other source of information has done before. In addition, they provide a major source for improvement in the knowledge of the short- and mid-wave structure of the marine geoid.

Due to the increasing requirements in accuracy and long-term integrity of spatio-temporal monitoring, it has become mandatory to validate and calibrate satellite radar altimetry system. Hence, the availability of ground-truth data have become a major target for current and future altimeter missions, leading to an international effort to establish calibration sites (Bonnefond et al., 2003; Haines et al., 2003; Pavlis et al., 2004). Common methods applied are tide gauge observations and deployments of GPS-equipped buoys underneath satellite tracks. With such calibration facilities, the accuracy of the oceanographic products is being improved. What is often missing, however, is offshore calibration data in the open sea.

The major aim of this project was to contribute to the improvement of sea level monitoring by developing enhanced methods for offshore regional sea surface height observations. The methods investigated included airborne laser altimetry, shipborne ultrasound altimetry and GPS-equipped buoys. By deploying these methods adjacent to radar altimetry sub-satellite tracks, they can

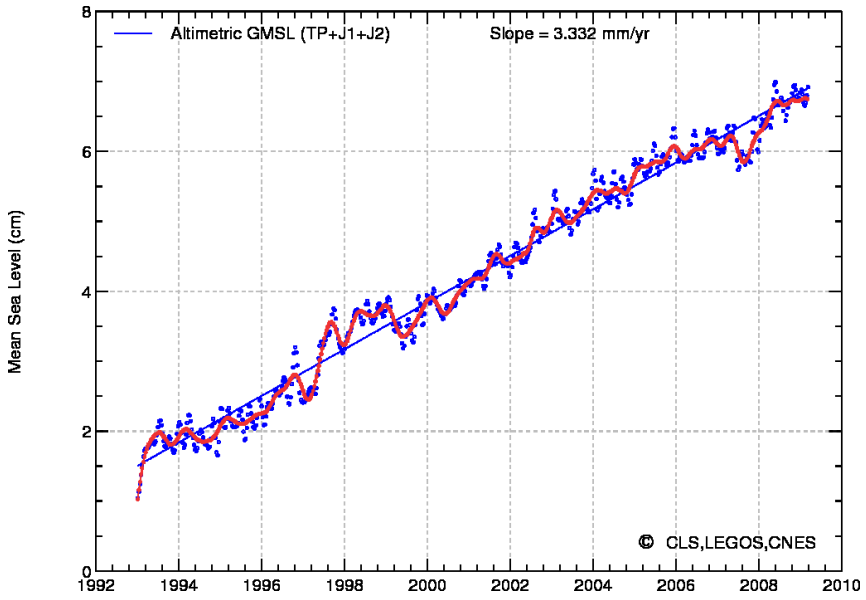

Figure 1.1: Global mean sea level (1992 to 2009) from the combination of data from TOPEX/Poseidon, Jason-1 and Jason-2. Seasonal variations have been removed. (Credits: CNES, CLS, LEGOS).

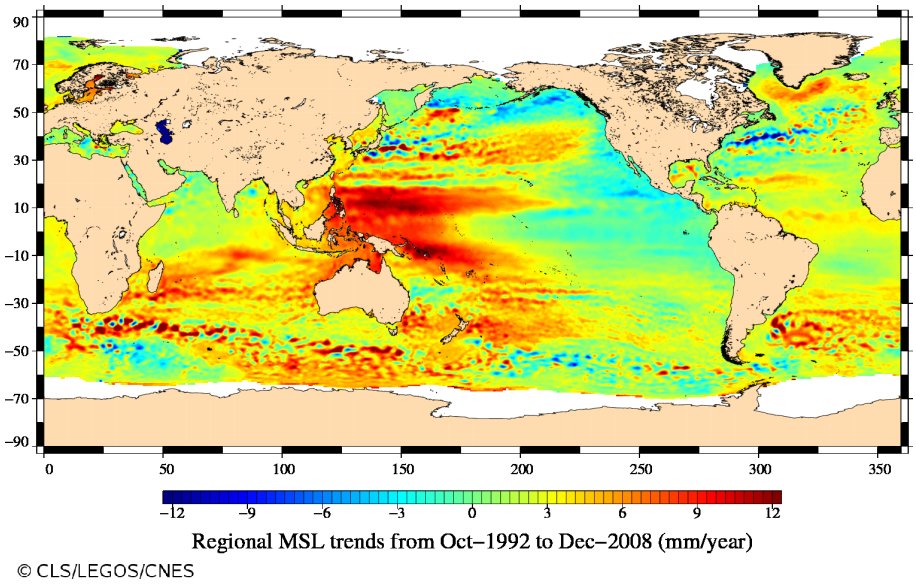

Figure 1.2: Sea level variation trends since 1992. (Credits: CNES, CLS, LEGOS).

contribute to the validation and calibration of spaceborne radar altimetry missions. In addition, these methods can be used to provide a link between offshore radar altimetry data and onshore tide-gauge stations. The final goal of this project was the analysis of the obtained regional sea surface topography and derived geoid heights in connection with geodynamic processes. The mean sea surface corresponds in a very good approximation to an equipotential surface of the Earth's gravity field. Thus, the gathered sea surface height data provides local-scale information on the short-wave structure of the marine geoid and related gravity field and can be used to improve local geoid solutions. Since the geoid is an equipotential surface of the Earth's gravity field, it depends on the mass distribution of the Earth's interior. The knowledge of mass distribution is of great

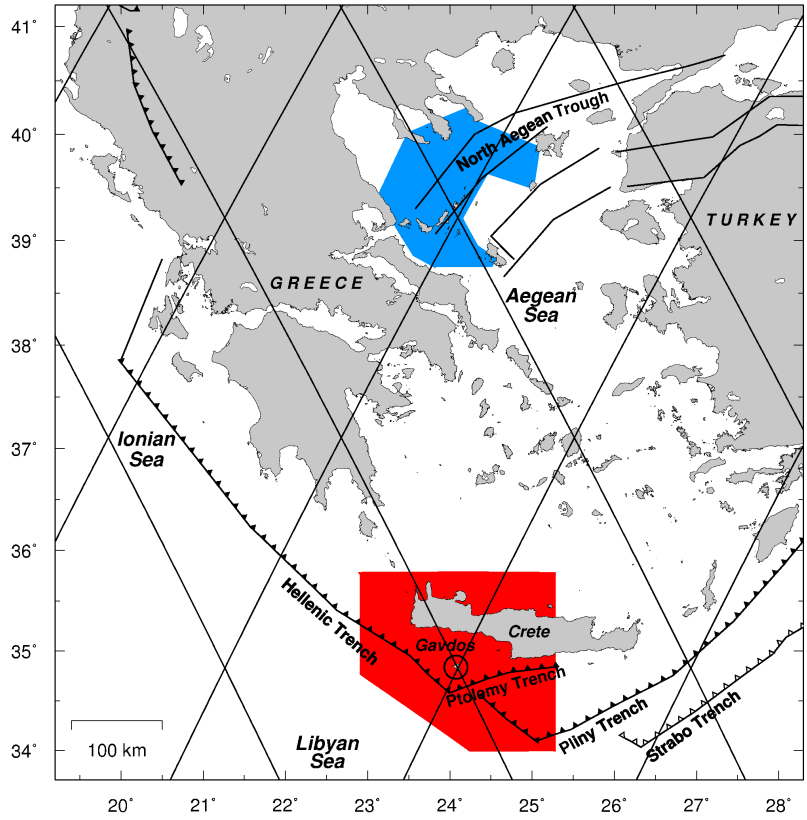

Figure 1.3: Survey areas in the Eastern Mediterranean Sea. Red surface: survey area for airborne laser altimetry around western Crete. Blue: survey area for shipborne ultrasound altimetry in the North Aegean Sea. Diagonal gridlines: Jason-1 ground-tracks.

importance for geophysical and geodynamical research. With the inversion of mean sea surface and geoid data, models of mass distribution can be constrained.

The area of investigation is the Eastern Mediterranean Sea, where two regional survey areas were chosen adjacent to Jason-1 radar altimetry ground-tracks (Fig. 1.3). A detailed airborne laser altimetry campaign was carried out around the western part of the island of Crete, in the vicinity of the Hellenic Trench and the Hellenic subduction zone. Several campaigns for shipborne sea surface height surveys were carried out in the North Aegean Sea, in the vicinity of the North Aegean Trough. The sea surface height observations were concentrated on these areas in order to contribute to the improvement of the knowledge of the local gravity field, which could improve the understanding of the complex geodynamic processes related to the Hellenic subduction zone and the North Aegean Trough.

1.2 Geophysical Characteristics of the Eastern Mediterranean

The Mediterranean Sea is located between Africa and Europe and has a surface of $2.5{\cdot}10^6$ km^2, with a limited access to the Atlantic Ocean at the Strait of Gibraltar. Due to its semi-closed nature, the sea surface height of the Mediterranean Sea is strongly influenced by the seasonal atmospheric variations over Europe and North Africa, like wind tension, surface heat flow, rainfall and evaporation. A second forcing is formed by the mass flow through the Strait of Gibraltar.

The Eastern Mediterranean region is located in the slope region between the geoid high in the

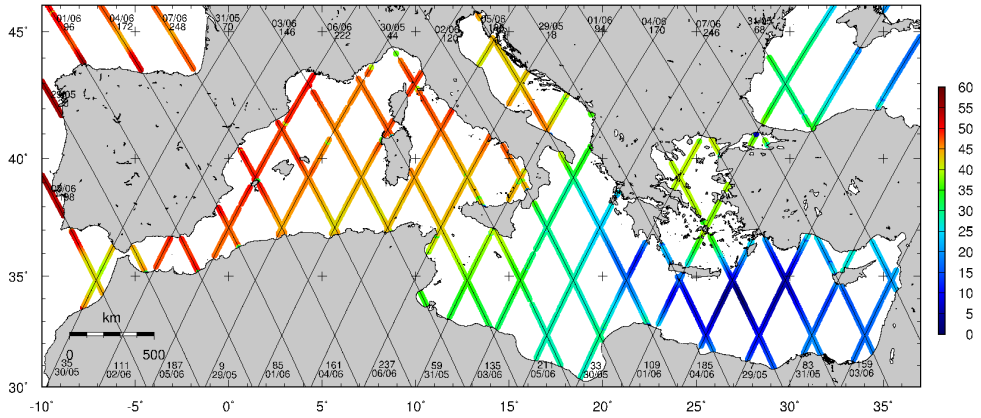

Figure 1.4: Jason-1 ground-tracks in the Mediterranean Sea, with color-coded sea surface heights above the reference ellipsoid from radar altimetry. A pronounced regional slope of the sea surface is seen, ranging from 50 m in the Balearic Sea down to 5 m in the Southern Aegean Sea.

North Atlantic and the low in the Indian Ocean, associated with values of 40 m in the North Aegean down to 1 m in the Libyan Sea, south of Crete (Fig. 1.4). The Eastern Mediterranean is a region of high geodynamic activity, exposed to considerable earthquake and tsunami risks related to different types of active plate-tectonic boundaries. The region is mainly characterized by the collision between the Eurasian and African lithospheric plates (Fig. 1.5) (Kahle and Mueller, 1998). This collision is closely related to continental subduction and formation of the Hellenic Arc and Hellenic Trench system (Fig. 1.3). Superimposed on the relatively slow motion of the African plate, complex dynamic processes affect the lithospheric blocks between the two major plates (Kahle et al., 2000). The most prominent kinematic feature is the rapid motion of the Anatolia and Aegean regions to the west and south-west, reaching velocities of up to 4 cm/yr, relative to Eurasia (McClusky et al., 2000; Hollenstein, 2006). The Hellenic Trench zone south of Crete is characterized by strong normal compression strain (Fig. 1.6). It is commonly accepted that the subduction and large-scale motion of the lithospheric blocks are associated with crustal and upper mantle mass anomalies causing pronounced geoid undulations which are also reflected in the sea surface topography.

Besides the Hellenic Trench, a second important geodynamic feature in the Eastern Mediterranean is the North Aegean Trough (NAT), situated in the North Aegean Sea (Fig. 1.5). The NAT is a tectonic graben-like feature characterized by a zone of deep water reaching 1500 m and trending from north-east to south-west. It is considered to form the western continuation of the seismically active North Anatolian Fault Zone (NAFZ) (Fig. 1.5). The area of the NAFZ and NAT is identified as a major strike-slip boundary, characterized by high seismicity, separating the Anatolia-Aegean plate from Eurasia (McNeill et al., 2004). It is accompanied with dextral shear strain rates of up to 170 nstrain/yr, combined with normal extension and isolated normal compression (Fig. 1.6) (Hollenstein, 2006). Compared to other strike slip boundaries between major tectonic plates, the GPS derived strain rates found along the NAFZ-NAT are of similar magnitude as those of the San Andreas fault zone (Kahle et al., 1999).

1.3 Former Work by the GGL in related Fields of Research

The Geodesy and Geodynamics Lab (GGL) collaborated in various international projects covering the Mediterranean and Black Sea regions in the 1990's, such as the sea level fluctuation projects SELF–I and SELF–II (Zerbini et al., 1996; Becker et al., 2002), and a WEGENER study (Plag et al., 1998). The GGL has been active in the field of airborne laser altimetry since 1994. The

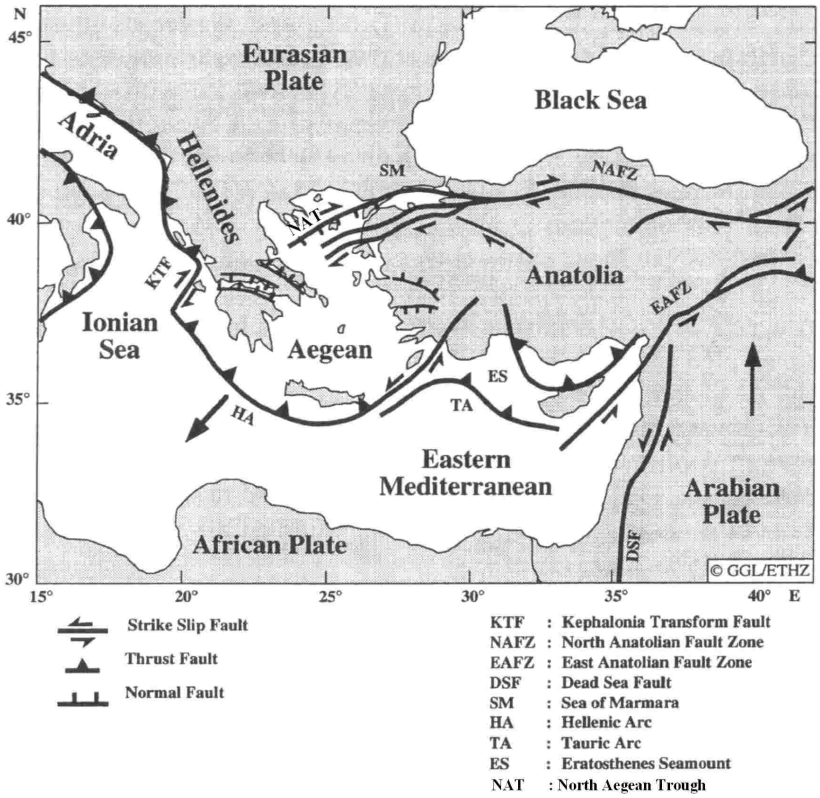

Figure 1.5: Simplified tectonic setting of the Eastern Mediterranean. From (Kahle and Mueller, 1998).

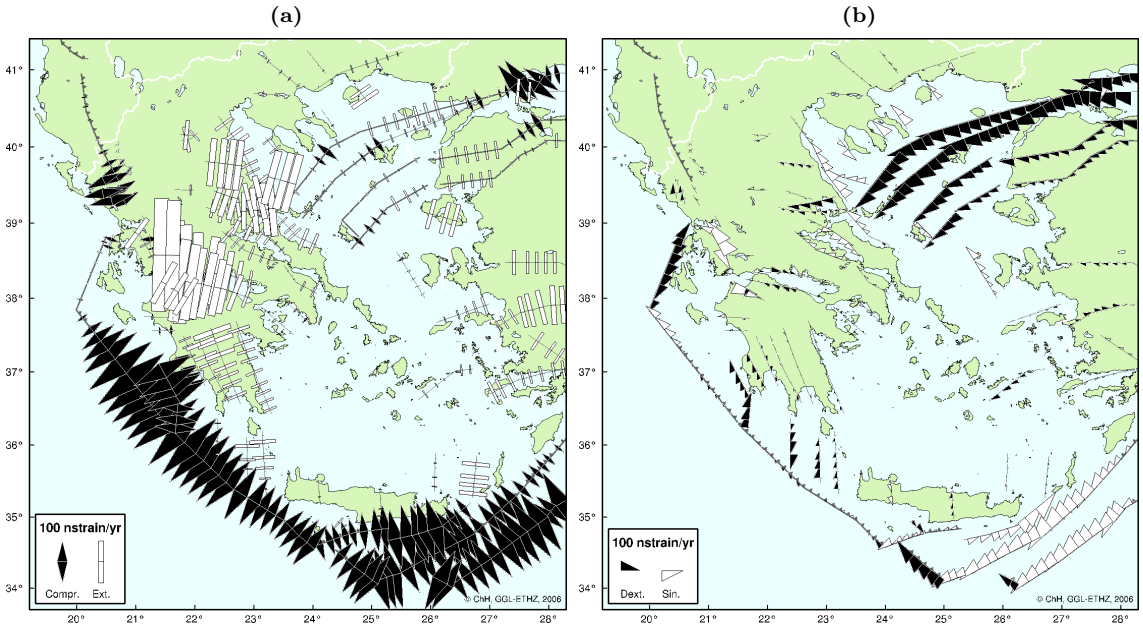

Figure 1.6: Normal **(a)** and shear **(b)** strain rate field in the Eastern Mediterranean, derived from GPS (Hollenstein, 2006).

technique was used for geoid determination in the Ionian and Aegean Seas, Greece (Cocard et al., 2002), as well as at the Lakes of Geneva (Favey and Schlatter, 1998) and Constance, Switzerland. Airborne laser altimetry surveys were conducted over the Unteraar glacier, Bernese Alps, Switzerland, with the goal to generate repeated surface models of the glacier used for mass balance determination and glacier monitoring (Favey, 2001; Favey et al., 2002). Besides airborne laser altimetry, airborne gravimetry was another main research area of the GGL (Verdun et al., 2003; Baumann, 2003). Satellite geodesy and GPS technology are other important research fields. Apart from high-precision static applications, kinematic aspects and dynamic positioning were intensively investigated. Different tests and feasibility studies have been carried out, leading to the development of software for highly precise kinematic GPS positioning (Cocard, 1995).

1.4 Research Tasks and Thesis Outline

The project is structured in four main research tasks (Fig. 1.7):

1. Determination of instantaneous sea surface heights (SSH)

   This task focuses on the precise determination of instantaneous SSH profiles by airborne laser altimetry and shipborne ultrasound altimetry. For accurate SSH determination, the datasets have to be corrected for instrumental errors, like ranging errors due to atmospheric refraction and boresight misalignment. GPS-equipped buoys are used to provide ground-truth SSH data, for the calibration of the airborne and shipborne altimetry systems.

2. Transformation from instantaneous SSH to time-independent sea surface topography (SST)

   Based on the instantaneous SSH from research task 1, a time-independent SST is generated, by applying corrections for time-dependent geophysical effects, including ocean waves, tides, atmospheric pressure (inverse barometer effect) and wind forcing.

3. Validation of satellite radar altimetry missions

   This research task concentrates on the comparison of the detailed SST from airborne laser altimetry and shipborne ultrasound altimetry with the ones obtained from spaceborne radar altimetry missions, especially Jason-1.

4. Geoscientific exploitation

   This research task includes the modeling of local mass density distribution and the interpretation of sea surface height anomalies over the Hellenic Trench and the North Aegean Trough.

Based on the research tasks presented above, the thesis is organized in the following chapters:

Chapter 2: Geoid, Sea Surface and Dynamic Ocean Topography gives an overview of the theoretical background concerning these three geophysical quantities, as well as their interrelationship. The basic definitions and equations of gravitational potential, geoid, gravity anomalies, modeling of mass effects, mean sea surface, sea level anomalies, absolute and mean dynamic ocean topography and permanent tides are presented.

Chapter 3: Geophysical Effects on Sea Surface Heights gives an overview of the theoretical background of geophysical effects influencing the height of the sea surface on a time-dependent basis. The effects covered in this chapter are ocean waves, tides, atmospheric pressure and wind forcing.

Chapter 4: Airborne Laser Altimetry Technique describes the instrumental setup used during the airborne altimetry surveys, as well as the theoretical background of laser ranging and refraction of light in the atmosphere.

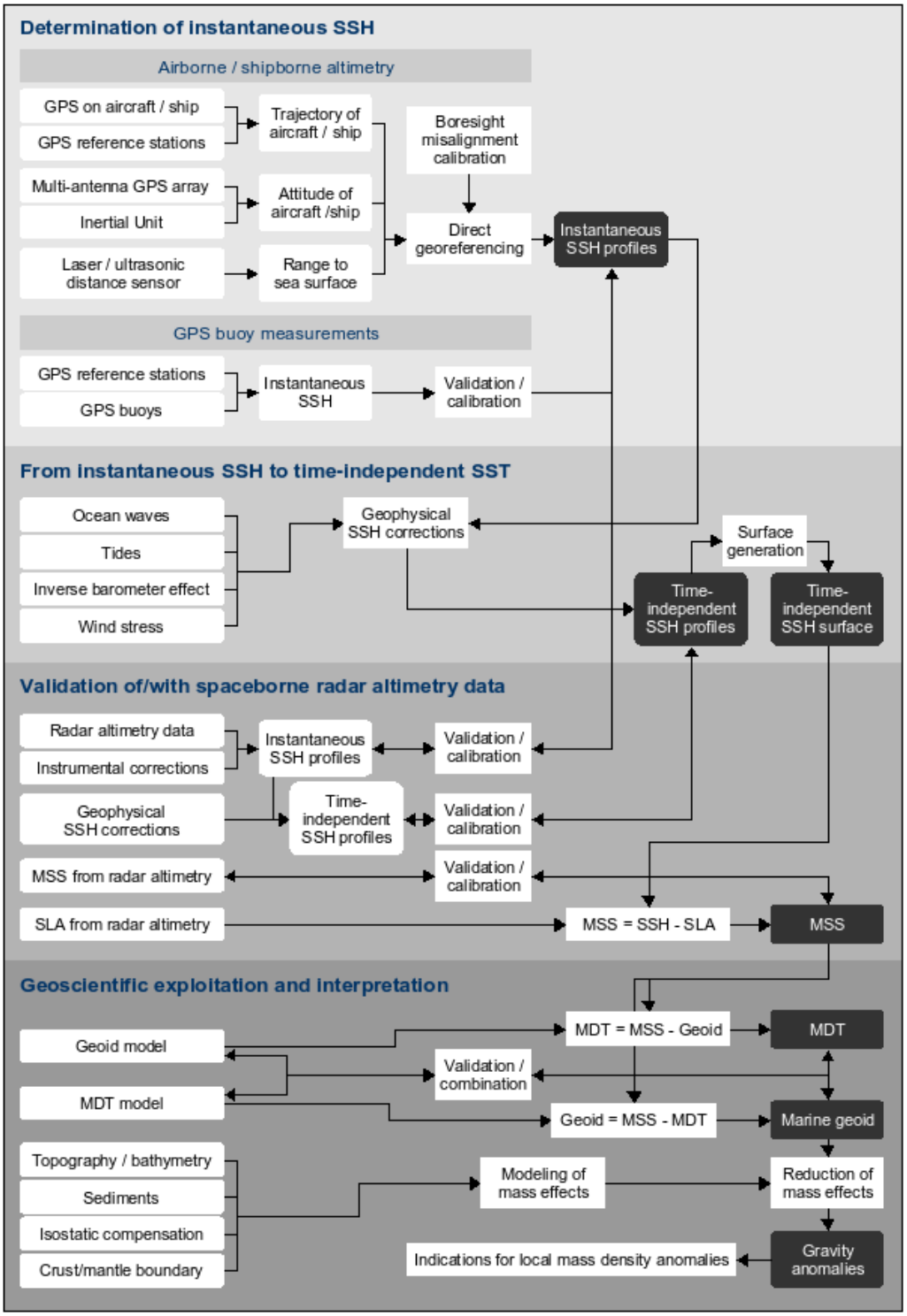

Figure 1.7: Flow diagram showing the four research tasks and the main results and outcomes (in black).

Chapter 5: Shipborne Ultrasound Altimetry Technique describes the instrumental setup used during the shipborne altimetry surveys, as well as the theoretical background of ultrasound ranging and sensor synchronization.

Chapter 6: GPS-equipped Buoys, describes the GPS-equipped buoys used for sea surface height observations.

Chapter 7: Direct Georeferencing presents an approach for direct georeferencing, valid for both airborne laser and shipborne ultrasound altimetry. The GPS based trajectory and attitude recovery is discussed, and comparisons with attitude solutions from inertial units are made. In addition, a calibration method for boresight misalignment in airborne laser altimetry is presented.

Chapter 8: Sea Surface Heights by Airborne Laser Altimetry around western Crete gives a description of the airborne laser altimetry surveys. Instantaneous sea surface height results are presented. The obtained sea surface heights are corrected for geophysical effects, including ocean tides, atmospheric pressure and wind forcing. A repeatability analysis and least-squares adjustment based on crosspoints is carried out, and the finally obtained time-independent sea surface topography is presented.

Chapter 9: Sea Surface Heights by Shipborne Ultrasound Altimetry in the North Aegean Sea is equivalent to Chapter 8 for shipborne ultrasound altimetry in the North Aegean Sea.

Chapter 10: Validation of Spaceborne Radar Altimetry Data presents a comparison between sea surface heights from airborne laser altimetry and Jason-1. Furthermore, a validation of mean sea surface from CLS01 and DNSC08 from multi-mission radar altimetry with airborne and shipborne results is carried out.

Chapter 11: Geoscientific Exploitation of Airborne Altimetry Data around western Crete presents marine geoid heights, gravity anomalies, geoid gradients and deflections of the vertical derived from airborne laser altimetry around western Crete. A comparison of the obtained local altimetric geoid heights with existing models is carried, namely with the global models EGM96, EGM2008, EIGEN-5S, EIGEN-5C, and with a regional model for the area of Greece computed by the Aristotle University of Thessaloniki. Attempts to determine the mean dynamic topography from the difference with existing geoid models are presented. Finally, mass effects have been modeled for the survey area and used to reduce to obtained geoid heights, for the purpose of mass anomaly detection.

Chapter 12: Geoscientific Exploitation and Interpretation in the North Aegean is equivalent to Chapter 11 for shipborne ultrasound altimetry in the North Aegean Sea.

Chapter 13: Summary and Conclusions draws a summary and the major conclusions of this research work.

2 Geoid, Sea Surface and Dynamic Ocean Topography

2.1 Introduction

Techniques like spaceborne radar altimetry, airborne laser altimetry and shipborne ultrasound altimetry provide observations of the instantaneous sea surface height SSH_i above the reference ellipsoid (Fig. 2.1). After correcting SSH_i for geophysical effects like tides and atmospheric pressure, contributing to the relief of the sea surface on a time-dependent basis, time-independent sea surface heights SSH_c are obtained (Chapter 3).

The geoid forms the main permanent part of the sea surface topography, while ocean currents form both a permanent and a variable part. The permanent part is usually called mean dynamic topography MDT, whereas the sum of the permanent and the variable part is called absolute dynamic topography ADT. The SSH_c above the reference ellipsoid, provided by altimetry, is the sum the geoid height N above the same ellipsoid and the ADT:

$$SSH_c \;=\; N \;+\; ADT \tag{2.1}$$

The mean sea surface MSS above the reference ellipsoid, the geoid undulations N above the same ellipsoid and the mean dynamic topography MDT are related by the following equation:

$$MSS \;=\; N \;+\; MDT \tag{2.2}$$

In the following sections, the constituents of the above equations will be described in more detail.

2.2 Geoid

2.2.1 Gravitational Potential, Geoid and Gravity Anomalies

The gravity potential W of the Earth, at a point $P(x, y, z)$ on or outside the Earth's surface, is the sum of the gravitational potential V and the potential V_c of the centrifugal force:

$$W(P) \;=\; V(P) \;+\; V_c(P) \tag{2.3}$$

The gravitational potential V is given by Newton's integral:

$$V(P) \;=\; G \iiint_v \frac{dm}{l} \;=\; G \iiint_v \frac{\rho}{l}\, dv \tag{2.4}$$

where $G = 6.6742 \cdot 10^{-11}$ [$\mathrm{m^3 \cdot kg^{-1} \cdot s^{-2}}$] is Newton's gravitational constant, dm is an element of mass, dv is an element of volume, ρ is the mass density of the element and l is the distance between the mass element dm and the attracted point P.

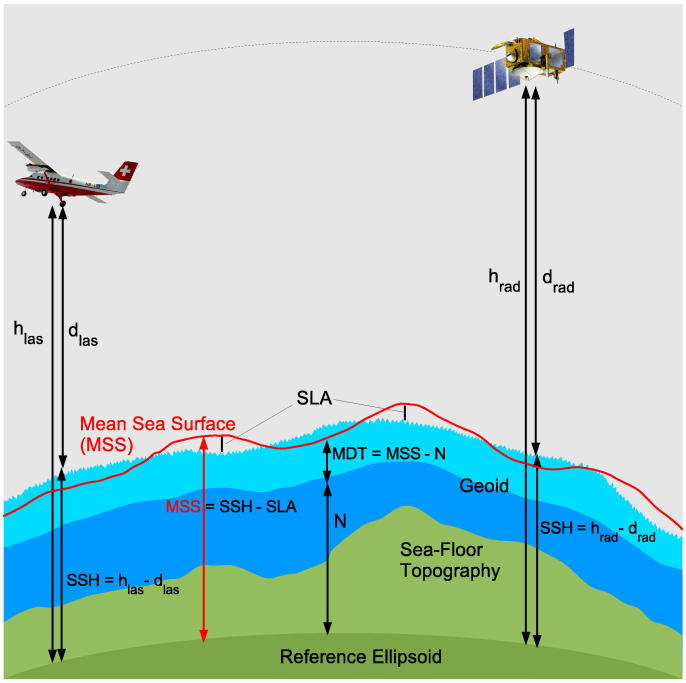

Figure 2.1: Schematic diagram of altimetric sea surface height observations and relations between sea surface heights, geoid, and dynamic topography.

The geoid is an equipotential surface of the Earth's gravity field that is closely associated with the location of the mean sea surface (Picot et al., 2003). The constant gravity potential on the geoid is defined by:

$$W(P) \;=\; W_0 \;=\; \text{constant} \tag{2.5}$$

The normal gravity potential U is given by:

$$U(Q) \;=\; V_e(Q) \;+\; V_c(Q) \tag{2.6}$$

where Q is a point on the ellipsoid, $V_e(Q)$ is the gravitational potential of the reference ellipsoid representing the best approximation of the geoid and $V_c(Q)$ is the potential of the centrifugal force. The reference ellipsoid is defined in a way that its gravity potential on its surface is equal to the potential of the geoid:

$$U(Q) \;=\; W_0 \;=\; \text{constant} \tag{2.7}$$

The vector gravitational acceleration, or gravity vector, $\overrightarrow{g}$ is the gradient of W:

$$\overrightarrow{g} \;=\; grad\; W \;=\; \left(\frac{\partial W}{\partial x}, \frac{\partial W}{\partial y}, \frac{\partial W}{\partial z}\right) \tag{2.8}$$

$\overrightarrow{g}$ is always perpendicular to the equipotential surface, meaning that there are no lateral gravitational forces along the geoid. Analogous, The normal gravity vector $\overrightarrow{\gamma}$ is the gradient of U:

$$\overrightarrow{\gamma} \;=\; grad\; U \;=\; \left(\frac{\partial U}{\partial x}, \frac{\partial U}{\partial y}, \frac{\partial U}{\partial z}\right) \tag{2.9}$$

The magnitude of the normal gravity vector $\overrightarrow{\gamma}$ on the surface of the ellipsoid can be obtained by the closed formula:

$$\gamma \;=\; \gamma_e \;\frac{1 + k\sin^2\phi}{\sqrt{1 - e^2\sin^2\phi}} \tag{2.10}$$

where $k = \frac{b\cdot\gamma_p}{a\cdot\gamma_e} - 1$, a and b are the semi-major and semi-minor axes of the ellipsoid, γ_e and γ_p are the theoretical gravity at the equator and poles, e is the first ellipsoid eccentricity and ϕ is the geodetic latitude. The definition and values of the ellipsoidal parameters of the reference ellipsoid WGS84, used throughout this project, can be found in (NIMA, 2000).

The anomalous or disturbing gravity potential T is given by the difference between the real gravity potential $W(P)$ and the normal gravity potential $U(P)$:

$$T(P) \;=\; W(P) \;-\; U(P) \tag{2.11}$$

The surface of the geoid is generally described in terms of geoidal undulations N, which are the heights of the geoid with respect to the reference ellipsoid. The geoid height N is related to the anomalous gravity potential T by Brun's formula:

$$N \;=\; \frac{T}{\gamma} \tag{2.12}$$

where γ is the normal gravity related to the reference ellipsoid (2.10). The most negative geoidal undulations of (-106 m) are found in the Indian Ocean, whereas the most positive geoidal heights are encountered over Indonesia (85 m) and in the Northern Atlantic Ocean (61 m).

The gravity anomaly vector $\Delta\overrightarrow{g}$ is given by the difference between the gravity vector $\overrightarrow{g}$ (2.8) and the normal gravity vector $\overrightarrow{\gamma}$ (2.9):

$$\Delta\overrightarrow{g} \;=\; \overrightarrow{g}(P) \;-\; \overrightarrow{\gamma}(Q) \tag{2.13}$$

where P is a point on the geoid and Q is the projection of P onto the ellipsoid along the ellipsoidal normal. Analogous, the difference in magnitude is the gravity anomaly Δg:

$$\Delta g \;=\; g(P) \;-\; \gamma(Q) \tag{2.14}$$

Other equivalent formulas of the gravity anomaly are given by (Hofmann-Wellenhof and Moritz, 2006):

$$\Delta g \;=\; -\frac{\partial T}{\partial z} + \frac{1}{\gamma}\,\frac{\partial \gamma}{\partial z}\,T \tag{2.15}$$

$$\Delta g \;=\; -\frac{\partial T}{\partial z} + \quad\frac{\partial \gamma}{\partial z}\,N \tag{2.16}$$

where z denotes the vertical direction, normal to the ellipsoid. In (2.15) and (2.16), the first term on the right-hand side is the gravity disturbance δg at the point P on the geoid:

$$\delta g(P) \;=\; g(P) \;-\; \gamma(P) \;=\; -\frac{\partial T}{\partial z} \tag{2.17}$$

The second term of (2.15) and (2.16) accounts for the gravity change between point P on the geoid and point Q on the ellipsoid. In practice, e.g. in free-air gravity reduction, the vertical gradient of

normal gravity is usually approximated by:

$$\frac{\partial \gamma}{\partial z} \;=\; -0.3086 \;\; [\text{mGal/m}] \tag{2.18}$$

The deflection of the vertical is the angle between the normal to the geoid and the normal to the ellipsoid. It is defined by an east component η and an north component ξ. They correspond to the slope of the geoid in east and north direction, and are given by (Heiskanen and Moritz, 1967):

$$\eta \;=\; -\frac{\partial N}{\partial x}\,, \quad \xi \;=\; -\frac{\partial N}{\partial y} \tag{2.19}$$

and with the spherical approximation:

$$\eta \;=\; -\frac{1}{a\cos\phi}\frac{\partial N}{\partial \lambda}\,, \quad \xi \;=\; -\frac{1}{a}\frac{\partial N}{\partial \phi} \tag{2.20}$$

where ϕ is the geodetic latitude, λ is the longitude and a is the mean radius of the Earth.

Anomalies of the marine gravity field can be derived from the marine geoid using Laplace's equation (Sandwell and Smith, 1997):

$$\frac{\partial^2 T}{\partial x^2} \;+\; \frac{\partial^2 T}{\partial y^2} \;+\; \frac{\partial^2 T}{\partial z^2} \;=\; 0 \tag{2.21}$$

Substitution of (2.12), (2.15) and (2.19) in Laplace's equation (2.21), and considering that $\frac{\partial^2 \gamma}{\partial z^2} = 0$, yields the following relation between the vertical gravity gradient and the curvature of the geoid (Sandwell and Smith, 1997):

$$\frac{\partial \Delta g}{\partial z} \;=\; \gamma\left(\frac{\partial^2 N}{\partial x^2} + \frac{\partial^2 N}{\partial y^2}\right) \;=\; -\gamma\left(\frac{\partial \eta}{\partial x} + \frac{\partial \xi}{\partial y}\right) \tag{2.22}$$

The differential equation (2.22) can be solved in the frequency domain by Fourier transformation of gridded geoid heights (Sandwell and Smith, 1997). In this project, the gravity anomalies were computed from marine geoid heights using the GMT (Generic Mapping Tools) software (Wessel and Smith, 1998, 2005). The use of Laplace's equation (2.21) intrinsically implies that there are no masses outside the geoid. For the marine geoid, this condition is always verified. However, in coastal areas, the marine gravity field and geoid are influenced by topographic masses outside the geoid.

More details on the theory of gravitational potential, geoid and gravity anomalies can be found in many textbooks on physical geodesy, e.g. (Heiskanen and Moritz, 1967; Moritz, 1980; Hofmann-Wellenhof and Moritz, 2006).

2.2.2 Marine Geoid and Sea Surface

As stated in the previous subsection, the geoid is an equipotential surface of the Earth's gravity field that is closely associated with the location of the mean sea surface (Picot et al., 2003). In the absence of other forcing (e.g. pressure gradients, wind forcing, or tides), the sea surface would be a surface of constant gravitational potential, the marine geoid (Chelton, 1988). Although the geoid undulations are primarily long-wavelength phenomena, short-wavelength changes in the geoid undulation are seen over seamounts, trenches and ridges in the oceans (Picot et al., 2003).

Variations in gravitational acceleration over the Earth's surface result in an uneven distribution of water mass in the oceans (Chelton, 1988). Variations in the gravitational acceleration result

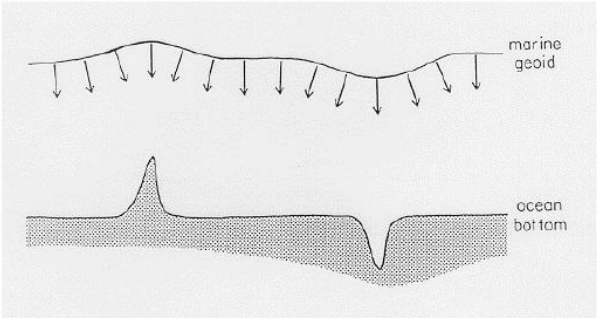

Figure 2.2: Schematic diagram of a bump and a depression on the ocean bottom and the corresponding marine geoid. The vectors indicate the gravitational acceleration along the geoid. The gravitational acceleration is locally deflected towards the bump and away from the depression and is tangentially perpendicular to the geoid. From (Chelton, 1988).

in deformations of the sea surface. The gravitational acceleration at the sea surface is slightly stronger over bumps on the ocean bottom and slightly weaker over depressions in the bathymetry (Chelton, 1988). The vector gravitational acceleration at the sea surface in the vicinity of a bump is deflected towards the bump (Fig. 2.2). The amount of deflection depends on the composition of the bathymetric feature and decreases with the inverse square of the distance from the bump. Thus, a bump in the far field has essentially no effect on the local gravitational acceleration. The marine geoid over a bump is also a bump, but smoothed due to the inverse-square dependence on the distance from the bump. Similarly, the marine geoid over a depression in the bathymetry (e.g. a trench) is also depressed (Chelton, 1988). In a first approximation, the marine geoid can be considered as a low-pass filtered image of the bathymetry (Fig. 2.2).

2.2.3 Geoid Models analysed in this Project

On a global scale, the geoid is usually defined using spherical harmonic expansions of the Earth's gravitational potential. A brief description of the gravity models, used in Section 11.2 and Section 12.2 for comparison with the geoid heights obtained from airborne and shipborne altimetry, is given below:

- The Earth Gravitational Model **EGM96** was developed by the NASA GSFC and NIMA (Lemoine et al., 1998). The data used to derive the EGM96 include orbital perturbations from over 20 satellites, surface and airborne gravimetric surveys from different regions and sea surface heights from radar altimetry missions GEOSAT, ERS-1 and TOPEX/Poseidon. The EGM96 is complete to spherical harmonics degree and order 360, corresponding to a spatial resolution of approximately 55 km.
- The Earth Gravitational Model **EGM2008** has been publicly released by the U.S. NGA EGM Development Team in April 2008 (Pavlis et al., 2008). It combines gravitational information from the GRACE mission with a global gravity anomaly database of 5'×5' resolution from surface gravity data and altimetry data. The EGM2008 does not incorporate any GPS/leveling data or astronomic deflections of the vertical. It is complete to spherical harmonics degree and order 2159, and contains additional coefficients extending to degree 2190 and order 2159, corresponding to a spatial resolution of approximately 10 km. Geoid heights computed from EGM2008 over the Mediterranean Sea are shown in Fig. 2.3.
- The **EIGEN-5C** is a combined gravity field model computed by the GFZ-GRGS cooperation (Foerste et al., 2008). It is a combination of GRACE data from Feb. 2003 to Jan. 2007 and LAGEOS data from Jan. 2002 to Dec. 2006, as well as 0.5°×0.5° surface gravimetric and

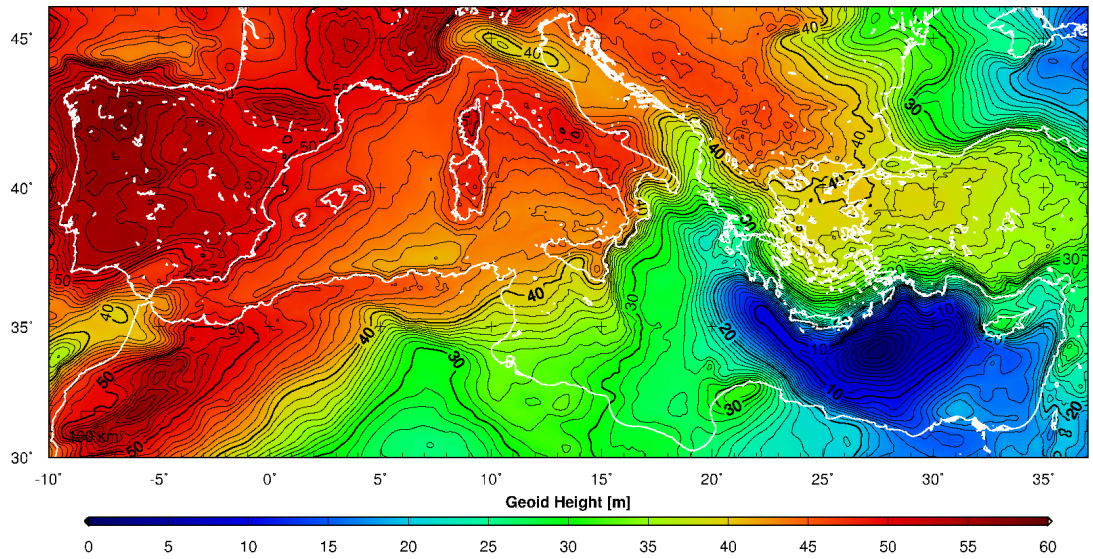

Figure 2.3: EGM2008 geoid heights above the WGS84 reference ellipsoid in the Mediterranean Sea. The pronounced regional slope of the marine geoid ranges from 50 m in the Balearic Sea in the Western Mediterranean down to 0 m in the Eastern Mediterranean. Contour interval: 1 m.

altimetric data. The EIGEN-5C is complete to spherical harmonics degree and order 360, corresponding to a spatial resolution of approximately 55 km.

- The **EIGEN-5S** is a satellite-only model associated with the EIGEN-5C. It includes only GRACE and LAGEOS data, and is therefore independent of surface data (including radar altimetry data). Since missions like GRACE and LAGEOS do not resolve short-wavelength signals, the EIGEN-5S is only complete to spherical harmonics degree and order 150, corresponding to a spatial resolution of approximately 130 km.
- The **AUTH2008** is a gravimetric geoid model based on free-air gravity anomaly data, covering the area of Greece. It was computed by the Aristotle University of Thessaloniki (AUTH), Greece (Tziavos and Andritsanos, 1999; Vergos et al., 2004; Grigoriadis, 2009). For the area of Crete, the model is partly based on airborne gravimetric data collected during the combined airborne gravimetry/altimetry campaign in the framework of the GAVDOS project (Tziavos et al., 2004) (Section 8.1).

2.2.4 Modeling of Mass Effects and Mass Reduction

Anomalies of the gravity potential are caused by mass anomalies from topography, bathymetry, sedimentary deposits, crust/mantle boundary, and lithosphere structures like subducting slabs. Mass effects can be modeled and used to reduce observed geoid heights or gravity. The effect of mass elements on the gravitational potential V is given by Newton's integral (2.4). Denoting the coordinates of the attracted point P by (x_p, y_p, z_p), and the coordinates of the mass element dm by (x, y, z), the disturbing potential T caused by mass anomalies can be written as:

$$T(x_p, y_p, z_p) \;=\; G \iiint_v \frac{\rho\,(x, y, z)}{l}\; dx\; dy\; dz \tag{2.23}$$

with $l = \sqrt{(x - x_p)^2 + (y - y_p)^2 + (z - z_p)^2}$ the distance between the mass element and the attracted point P. The effect of the mass elements on the geoid height N at the computation point

$P(x_p, y_p, z_p)$ is obtained from (2.23) using Brun's formula (2.12):

$$N(x_p, y_p, z_p) \;=\; \frac{T}{\gamma} = \frac{G}{\gamma} \iiint\limits_v \frac{\rho(x,y,z)}{l}\; dx\; dy\; dz \tag{2.24}$$

Based on (2.16), the effect of the mass elements on the gravity anomaly Δg at the computation point $P(x_p, y_p, z_p)$ is obtained from (2.23), by first order derivation along the vertical z direction:

$$\Delta g(x_p, y_p, z_p) \;=\; \frac{\partial T}{\partial z} \;=\; G \iiint\limits_v \frac{\rho(x,y,z)\;(z - z_p)}{l^3}\; dx\; dy\; dz \tag{2.25}$$

Note that in (2.25), the term $\frac{\partial \gamma}{\partial z} N$ of (2.16) was neglected. Hence the gravity anomaly Δg in (2.25) is more precisely a gravity disturbance δg as defined in (2.17).

Due to the $1/l^3$ dependency of the gravity anomaly Δg on the distance l between the mass element and the attracted point P in (2.25), the influence of a mass element on gravity decreases much more rapidly than its influence on the geoid height N (2.24). Hence, as compared to geoid heights, gravity anomalies have the advantage that they are not affected by the long-wavelength part of the gravitational potential and are therefore better suited for the analysis of local gravity anomalies. On the other hand, geoid heights N are comparable to low-pass filtered gravity anomalies, mainly affected by large-scale mass anomalies.

A method to compute mass effects on geoid heights or on gravity based on (2.24) or (2.25) consists in dividing the present masses into mass cuboids. The derivation of the complete formulas for the potential of a finite cuboid and the derivations of the potential to the third degree can be found in (Mader, 1951). The following formula gives the potential of a finite cuboid, obtained by solving the integral in (2.23) for a finite cuboid (Mader, 1951):

$$\begin{aligned} \frac{1}{G\;\rho}\; T \;=\; \frac{\gamma}{G\;\rho}\; N \;=\; & \{x_2 y_2 z_2\} - \{x_1 y_2 z_2\} - \{x_2 y_2 z_1\} + \{x_1 y_2 z_1\} \\ & - \{x_2 y_1 z_2\} + \{x_1 y_1 z_2\} + \{x_2 y_1 z_1\} - \{x_1 y_1 z_1\} \end{aligned} \tag{2.26}$$

with e.g.

$$\begin{aligned} \{x_2 y_2 z_2\} \;=\; & y_2\; z_2\; \log(x_2 + r_{222}) \;+\; x_2\; y_2\; \log(z_2 + r_{222}) \;+\; x_2\; z_2\; \log(y_2 + r_{222}) \\ & -\; \frac{x_2^2}{2}\; \arctan\left(\frac{y_2\; z_2}{x_2\; r_{222}}\right) \;-\; \frac{y_2^2}{2}\; \arctan\left(\frac{x_2\; z_2}{y_2\; r_{222}}\right) \;-\; \frac{z_2^2}{2}\; \arctan\left(\frac{x_2\; y_2}{z_2\; r_{222}}\right) \end{aligned}$$

where x_1, x_2, y_1, y_2, z_1, z_2 are the coordinates of the edges of the cuboid and $r_{222} = \sqrt{x_2^2 + y_2^2 + z_2^2}$. Geoid heights are obtained from (2.26) using Brun's formula (2.12).

Similar to (2.26), gravity anomalies are obtained by solving the integral in (2.25) for a finite cuboid (Mader, 1951):

$$\begin{aligned} \frac{1}{G\;\rho}\; T_z \;=\; \frac{1}{G\;\rho}\; \Delta g \;=\; & \{x_2 y_2 z_2\} - \{x_1 y_2 z_2\} - \{x_2 y_2 z_1\} + \{x_1 y_2 z_1\} \\ & - \{x_2 y_1 z_2\} + \{x_1 y_1 z_2\} + \{x_2 y_1 z_1\} - \{x_1 y_1 z_1\} \end{aligned} \tag{2.27}$$

Table 2.1: Density values used in the modeling of mass effects and isostatic compensation.

Layer	Density [10^3 kg/m^3]
Sea water	1.03
Light sediments	2.30
Upper crust (topography)	2.67
Lower crust (above crust/mantle boundary)	2.90
Upper mantle	3.30

with e.g.

$$\{x_2 y_2 z_2\} \;=\; y_2 \;\log(x_2 + r_{222}) \;+\; x_2 \;\log(y_2 + r_{222}) \;-\; z_2 \;\arctan\left(\frac{x_2 \; y_2}{z_2 \; r_{222}}\right)$$

where $T_z = \frac{\partial T}{\partial z}$ is the first order derivative of the potential along the vertical z direction, corresponding to the gravity anomaly Δg.

Since the computation of the effects of cuboid masses using (2.26) and (2.27) can be very CPU-intensive, a simplified method to compute approximate mass effects on geoid heights and on gravity based on (2.24) and (2.25) consists in concentrating the mass of each cuboid at its center of mass (point mass). In order to assess the impact of this approximation, the effects on geoid heights computed based on cuboid masses and on point masses were compared in Section 11.4.7 ans Section 12.4.7.

In Section 11.4 and Section 12.4, mass effects of topography, bathymetry, sediments and crust/mantle boundary (Moho) on geoid heights and on gravity anomlies were computed using (2.24) and (2.25), respectively (2.26) and (2.27). The survey areas are the North Aegean Sea and western Crete. The mass densities ρ in Tab. 2.1 were used in the computation. The topography and bathymetry were taken from the SRTM30 (Shuttle Radar Topography Mission) digital terrain model, published by the United States Geological Survey (USGS). It has a resolution of 30'×30', corresponding to approx. 900 m. A maximum radius of influence l_{max} of 275 km was chosen. The distances l were computed using geocentric coordinates of the computation points $P(x_p, y_p, z_p)$ and mass coordinates (x, y, z), in order to avoid effects of Earth's curvature on the distance.

For the computation of the effect of crust/mantle boundary (Moho) anomalies, the digital Moho depth map published by the ESC (European Seismological Commission) Working Group was used (Grad et al., 2009). The Moho map covers the whole European plate, from 40°W to 70°E and from 28°N to 86°N, with a resolution of 0.1°× 0.1°(Fig. 2.4). It was compiled from more than 250 datasets of individual seismic profiles, 3D models obtained by body and surface waves, receiver function results and maps of seismic and/or gravity data compilations. As an alternative to the ESC Moho model, Moho depth were computed based on the isostatic compensation theory using the Airy-Heiskanen isostasy model. A reference Moho depth of 30 km was used. The obtained Moho depths were smoothed to obtain a more realistic regional compensation instead of the local compensation of the Airy-Heiskanen model. This is a simplified method to obtain regional compensation. A more rigorous method would rely on flexure theory of a thin-elastic plate floating on a fluid mantle.

More details on the theory of mass effects and isostatic compensation can be found in textbooks on physical geodesy, e.g. (Heiskanen and Moritz, 1967; Moritz, 1980; Hofmann-Wellenhof and Moritz, 2006).

With the mass reduction, the mass effects computed with (2.24) or (2.25) are removed from the geoid heights or the gravity anomlies, respectively. The residual geoid heights after mass reduction, called cogeoid, represent the geoid heights caused by un- or mismodeled mass effects. Hence, the mass reduction allows to detect anomalous gravitational potentials caused by mass anomalies with respect to the modeled masses. Positive residuals indicate an existing mass excess with respect to

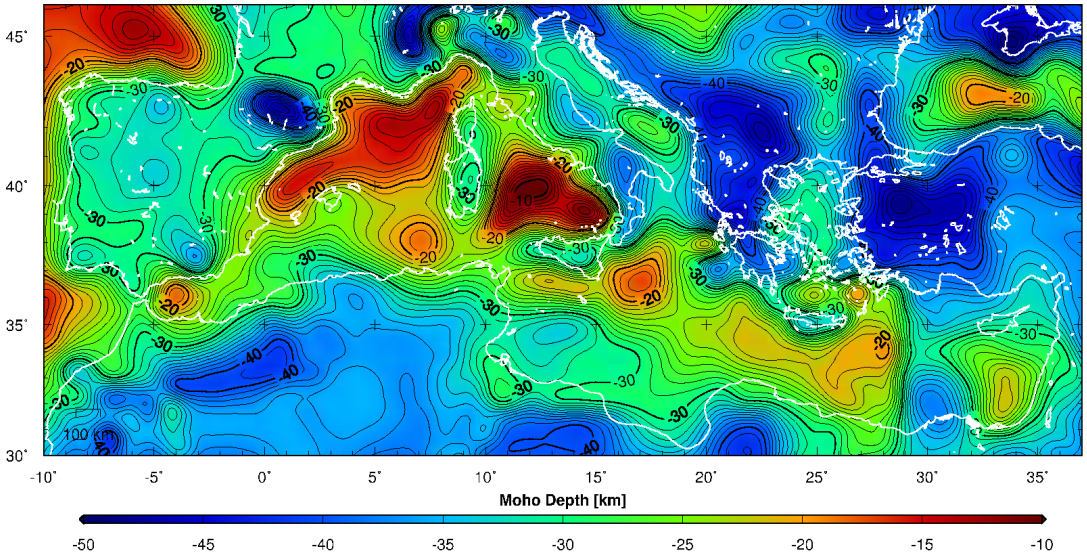

Figure 2.4: Extract of the digital Moho depth map published by the ESC (European Seismological Commission) Working Group (Grad et al., 2009). Contour interval: 1 km.

the modeled masses or an underestimation of the mass effect in the model. On the other hand, negative residuals indicate an existing mass deficiency with respect to the modeled masses or an overestimation of the mass effect in the model. In Section 11.5 and Section 12.5, the modeled mass effects were used to reduce the geoid heights and gravity anomalies derived from the sea surface heights obtained from airborne and shipborne altimetry, in the area of Crete and in the North Aegean Sea, respectively.

2.3 Mean Sea Surface

The mean sea surface MSS represents the position of the ocean surface averaged over an appropriate time period to remove annual, semi-annual, seasonal, and spurious sea surface height signals (Picot et al., 2003). The MSS is a height above a reference ellipsoid. It corresponds to the sum of the geoid undulation N and the mean dynamic topography MDT averaged over a selected period (Hernandez and Schaeffer, 2001), according to (2.2).

MSS models are essentially based on spaceborne radar altimetry data. They are used for various purposes, such as for the computation of along-track and cross-track geoid gradients, needed as corrections in the repeat orbit method, for the computation of gridded gravity anomalies, for the operational computation of sea level anomalies SLA (Section 2.4) and to provide a common reference for distinct satellite missions. The MSS models used in this project to validate the sea surface heights obtained by airborne and shipborne altimetry are the CLS01 and DNSC08 (Section 10.3 and Section 10.4):

- The **CLS01** was produced by CLS Space Oceanography Division and distributed by AVISO, with support from CNES (Hernandez and Schaeffer, 2000). The reference time period of the CLS01 is from 1993 to 1999 (7 years). It was computed using TOPEX/Poseidon mean profiles over 7 years, ERS-1/2 mean profiles over 5 years, GEOSAT mean profiles over 2 years and ERS-1 data. The CLS01 is determined oceanwide between 80°S and 82°N. Over continents, it is given by the EGM96 geoid, with a smooth transition in coastal areas. The CLS01 is provided on a regular grid with a spatial resolution of 2'×2' ($\simeq$ 4 km). However, the inherent resolution of along-track radar altimetry data is limited to about 10 km by their

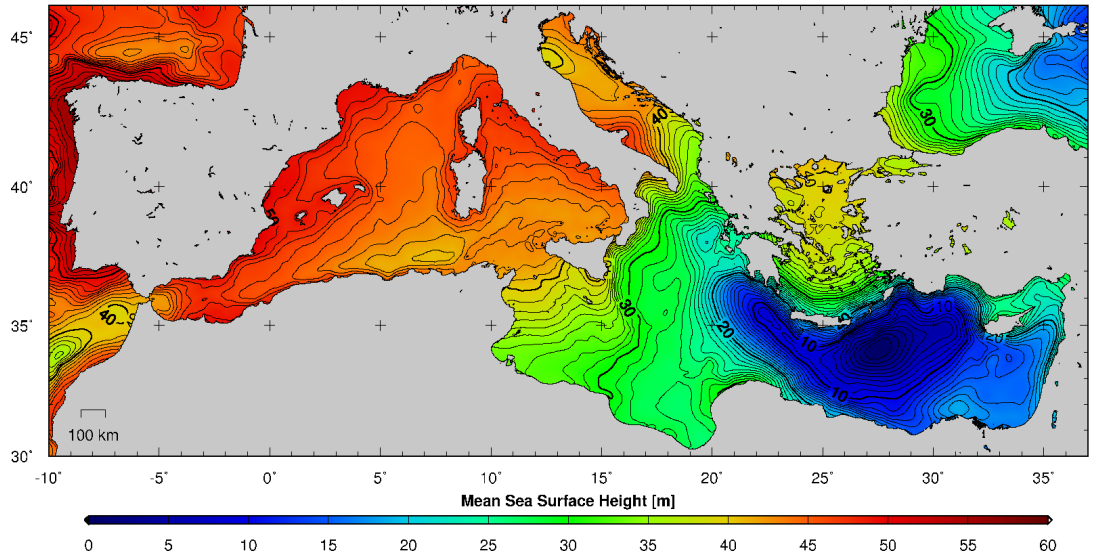

Figure 2.5: DNSC08 mean sea surface above the WGS84 reference ellipsoid in the Mediterranean Sea. The pronounced regional slope of the sea surface ranges from 50 m in the Balearic Sea in the Western Mediterranean down to 0 m in the Eastern Mediterranean. Contour interval: 1 m.

footprint diameter. In addition, ground-track spacing between multi-mission data can reach even higher values. Furthermore, the CLS01 is based on a local least square collocation, using altimetric data in a radius of 200 km (Hernandez and Schaeffer, 2001). Hence, the CLS01 can resolve wavelengths down to 10-20 km.

- The **DNSC08** is the most recent MSS released by the Danish National Space Center (DNSC) (Andersen et al., 2007; Andersen and Knudsen, 2008). An extract of the DNSC08 in the Mediterranean Sea is shown in Fig. 2.5. It is based on multi-mission radar altimetry data from TOPEX/Poseidon, Jason-1, ERS-1/2, ENVISAT, GFO and GEOSAT, as well as ICESAT data. The DNSC08 is provided on a regular grid with a spatial resolution of 1'×1' ($\simeq$ 2 km). The coverage is global (90°S to 90°N). The MSS of the DNSC08 is identical to the DNSC07. Similar to the remarks concerning the CSL01 above, the DNSC08 can resolve wavelengths down to 10-20 km.

The MSS heights from CLS01 and DNSC08 are both referenced to the TOPEX/Poseidon Earth ellipsoid (a=6378136.3 m, 1/f=298.257, GM=398600.4415 km^3/s^2). For comparison purposes with the sea surface heights from airborne and shipborne altimetry determined in this project, the MSS heights were transformed to the WGS84 reference ellipsoid. This transformation corresponds to a mean vertical shift of -0.705 m at the latitudes of the Mediterranean Sea.

2.4 Sea Level Anomaly

The sea level anomaly SLA is the difference between the time-independent sea surface height SSH_c from (3.1) and the mean sea surface MSS from (2.2):

$$SLA \;=\; SSH_c \;-\; MSS \tag{2.28}$$

The only means to observe SLA on a global and regional scale is satellite radar altimetry, since repeated observations of the sea surface at the same location over time periods of several years

are needed. In (2.28), the MSS can either be a multi-mission mean sea surface (Section 2.3) or a mono-mission mean sea surface profile computed along repeated tracks of the same mission. The SLA always refers to the reference height MSS used to compute it.

The SLA products used in this project are delayed-time SSALTO/DUACS SLA (AVISO, 2008). They are produced by SSALTO/DUACS and distributed by AVISO, with support from CNES. DUACS (Data Unification and Altimeter Combination System) is part of the CNES multi-mission ground segment SSALTO. The SSALTO/DUACS are multi-mission products from TOPEX/-Poseidon, Jason-1, ENVISAT, GFO, ERS-1/2 and GEOSAT. Delayed-time SLA products from SSALTO/DUACS are provided as along-track data for each altimetry mission, as well as gridded products merging data from all missions. Altimetry observations are resampled along a theoretical ground-track (or mean track) associated to each mission. Then, a mean profile is subtracted from the resampled data to obtain along-track SLA, using (2.28). The mean profile is a time average of similarly resampled data over a long period. For example, the mean profiles used for TOPEX/Poseidon and Jason-1 were computed with TOPEX/Poseidon data from January 1993 to December 1999, using the new 2008 GDR standards. The gridded products are provided on a global 1/3° Mercator grid and on regional grids, e.g. a 1/8° regular grid for the Mediterranean Sea, based on one week of altimeter data.

An example of gridded weekly SLA from multi-mission SSALTO/DUACS over the Mediterranean Sea is shown in Fig. 2.6, corresponding to the time period of the GAVDOS airborne campaign (Section 8.1). A high spatial variability was observed, with SLA values ranging from -15m to 25 cm. The average sea surface of the Mediterranean Sea was higher than the reference height, with positive mean SLA values of 8.6 cm and 2.8 cm for 2003/01/08 and 2003/01/15, respectively. The rapid decrease of the mean SLA by 5.8 cm during only one week, as well as local SLA variations of up to 15 cm, underline the highly dynamic characteristics of sea level variations in time (Fig. 2.6, bottom).

The SLA products from SSALTO/DUACS are sea level anomalies with respect to the mean profiles used to compute them. Since the mean profiles used in the SSALTO/DUACS products are computed using the newest processing standards for altimetry data (e.g. 2008 GDR standards for TOPEX/Poseidon), they are not compatible with former mean sea surface models like CLS01. Even if the same raw altimetry data, covering the same time period, were used to compute SSALTO/DUACS mean profile and CLS01, they do not represent the same reference, since for CLS01, the processing standards of 2001 were used. This important aspect is illustrated by computing the differences along Jason-1 ground-tracks between mono-mission Jason-1 DT-SLA, referring to CLS01, and mono-mission Jason-1 SSALTO/DUACS SLA, referring to SSALTO/DUACS mean profiles (Fig. 2.7). A significant mean offset of 10.3 cm, with a standard deviation of 3.6 cm, is observed, indicating that the SSALTO/DUACS mean profiles are about 10 cm higher than the CLS01. This offset was confirmed by personal communication from the SSALTO/DUACS team to be a constant bias of 10 cm. Besides this bias, non-constant discrepancies are observed along the satellite ground-tracks (Fig. 2.7), due to the introduction of orbit error mitigation and corrections from long wavelength errors in the recent multimission SSALTO/DUACS products.

2.5 Dynamic Ocean Topography

2.5.1 Absolute and Mean Dynamic Topography

Due to the close relation between the oceanic circulation systems, the dynamic ocean topography is an important indicator in the study of ocean-dynamics (Dobslaw, 2007). From an oceanographic perspective, the primary purpose of sea surface height observations is the determination of the sea surface elevation induced by ocean currents. This sea surface elevation is called absolute dynamic topography ADT of the ocean. Based on (2.1), the ADT is given by the difference between the

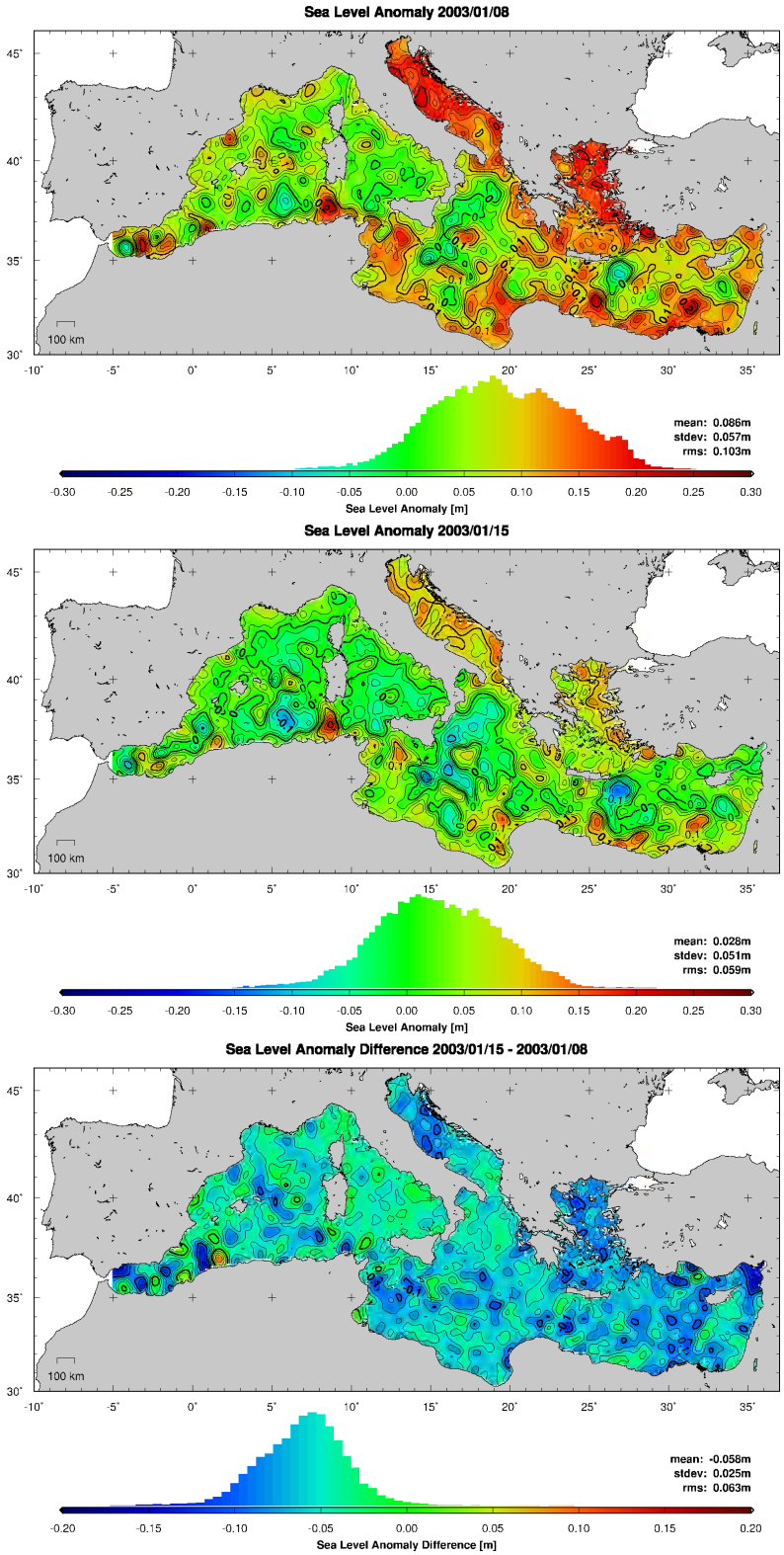

Figure 2.6: Weekly sea level anomaly SLA from SSALTO/DUACS merged multi-mission altimetric data in the Mediterranean Sea, on 2003/01/08 (top) and 2003/01/15 (center). (bottom) Sea level anomaly SLA difference between the two consecutive weekly datasets in this Figure. Contour intervals: 2.5 cm

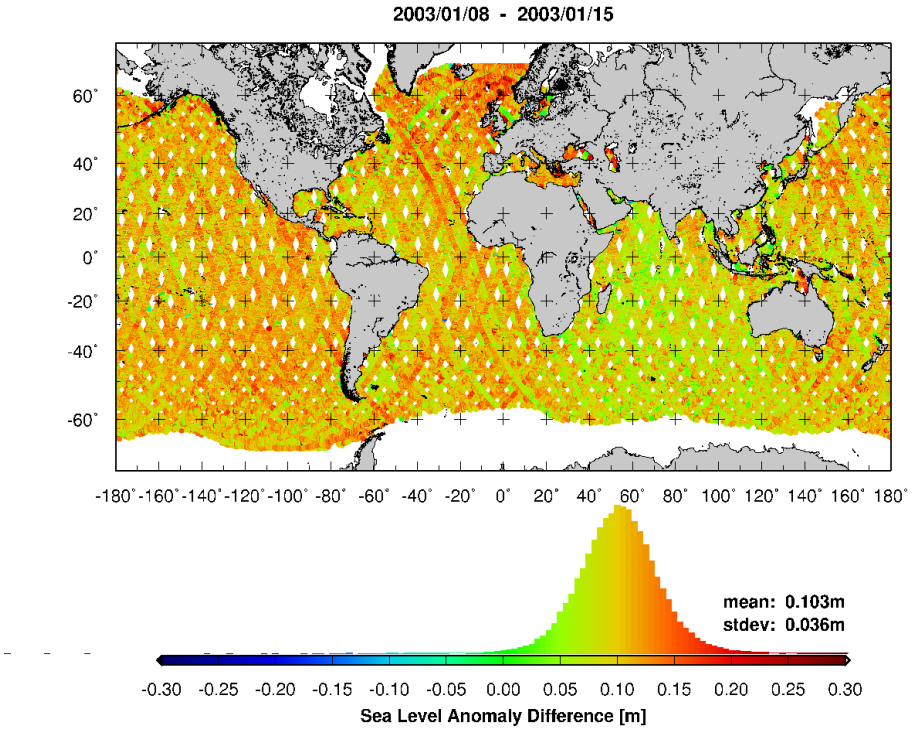

Figure 2.7: Sea level anomaly SLA differences along Jason-1 ground-tracks, between mono-mission Jason-1 DT-SLA (referring to CLS01) and mono-mission Jason-1 SSALTO/DUACS SLA (referring to SSALTO/DUACS mean profiles), from 2003/01/08 to 2003/01/15.

sea surface height SSH_c, corrected mainly for tidal and atmospheric effects (3.1), and the geoid undulation N:

$$ADT \;=\; SSH_c \;-\; N \tag{2.29}$$

The major application of retrieving absolute dynamic signals from altimetry is the assimilation of absolute altimetric data into general circulation models, which is crucial for the development of operational forecasting systems (Rio et al., 2007). Analogous to (2.29), the mean dynamic topography MDT of the ocean is obtained from (2.2) as the residual surface between the mean sea surface MSS and the geoid undulations N:

$$MDT \;=\; MSS \;-\; N \tag{2.30}$$

The MDT is the part of the MSS produced by permanent ocean currents. In (2.30), MSS can either be a gridded multi-mission MSS or a mono-mission MSS profile along repeated tracks of the same mission. Both the ADT and MDT are orthometric sea surface heights above the geoid. Equations (2.29) and (2.30) are called *direct method* for the computation of the absolute and mean dynamic topography. The *direct method* requires that the accuracies of the geoid and sea surface heights are compatible with the amplitudes and wavelength of oceanic effects. Important aspects of the oceanic circulation typically contain wavelengths as short as 100-200 km (Rio and Hernandez, 2004). The altimetric MSS resolves spatial scales as short as 10-20 km (Section 2.3), while geoid models are usually only available at a lower resolutions (Section 2.2.3). In this case, the MSS has to be low-pass filtered to make it compatible with the resolution of the geoid model. Hence, the geoid model is generally the limiting factor for the resolution of the dynamic ocean topography determined with the *direct method*.

As demonstrated in (Rio et al., 2006), combined geoid solutions, enhancing the satellite-only solutions by introducing in-situ gravimetric and altimetric data to better estimate the shortest scales of the geoid, produce better MDT results. However, the combined solutions intrinsically include information on the mean ocean circulation, and the obtained MDT is therefore not independent of this a priori information. It was shown in (Rio et al., 2006) that using the most recent satellite-only geoid models from GRACE (at that time the EIGEN-GL04S), the MDT could only be estimated with sufficient accuracy at spatial scales of 300-400 km. However, the real MDT contains scales shorter than 130 km (Rio et al., 2006). Hence, geoid model resolving such small wavelengths, independently of altimetric data, are needed. Such a geoid model is expected from the GOCE mission, who's launch is scheduled for March 2009. GOCE aims to provide geoid heights with cm-level accuracy at a resolution better than 100 km. In order to bypass large geoid uncertainties, altimetric missions were designed with repeated orbits, allowing to compute very accurate along-track MSS profiles and to deduce SLA at cm-level accuracy. By inserting (2.29) and (2.30) in (2.28), the SLA can be defined as:

$$SLA \;=\; ADT \;-\; MDT \tag{2.31}$$

In theory, the SLA represents the change of the sea surface height related to effects that are not considered during the correction for geophysical effects like tides and atmospheric pressure (3.1). The major part of these residual effects are changing ocean currents. Thus, by neglecting all other residual effects, the SLA corresponds to the variable part of the dynamic ocean topography, or the deviation of the absolute dynamic topography ADT from the mean dynamic topography MDT, according to (2.31). This method is the so-called repeat-track method, providing the variable part of the dynamic topography with 3 to 4 cm accuracy (Rio and Hernandez, 2004). The analysis of the SLA has led to numerous progresses in our knowledge of ocean dynamics, but the inference of the ADT and MDT from altimetric measurements remains a challenge (Rio et al., 2006). A method used to estimate the MDT independently of the geoid and its uncertainties is the so-called *synthetic method*. Based on (2.31), it allows to locally estimate the MDT by subtracting the SLA, as observed by altimetry (2.28), from in situ ADT observations, obtained from satellite-tracked drifting buoys (Rio and Hernandez, 2004; Rio et al., 2007).

In the real world, however, the SLA is not only produced by changing ocean currents, but also by sea surface height variations related to other unconsidered or mismodeled effects in (3.1), as well as residual measurement errors. The SLA can e.g. be affected by errors in the tidal model and errors in the model of the response to atmospheric pressure and wind. Residual measurement errors can be produced by altimeter ranging errors, orbit errors, errors in the sea state bias correction, tropospheric correction, ionospheric correction and skewness of the sea surface. One of the major challenges in spaceborne radar altimetry is therefore to reduce the model errors on the instrumental and sea surface height correction levels, in order that their impact on the SLA becomes negligible as compared to the effect of changing ocean currents, so that (2.31) holds.

2.5.2 Geostrophic Flow Fields from Dynamic Ocean Topography

Dynamic ocean currents can be derived geostrophically from the ADT and MDT, on an instantaneous and permanent basis, respectively. These flow fields are of great importance for hydrological and oceanographic research. Under the assumption of the geostrophic equilibrium, the ocean circulation can be derived from gradients of the vertical deviation of the ocean topography with respect to its position of rest. The position of rest, observed in the hypothetic case of complete absence of ocean circulation, is an equipotential surface of gravity, the geoid. Aside from the equator and on timescales longer than a few days, the ADT of height H above the geoid is linked to the geostrophic part of the ocean circulation (u_g, v_g) by the geostrophic equilibrium equation (Fu and Chelton,

2001; Le Traon and Morrow, 2001; Rio and Hernandez, 2004):

$$u_g = -\frac{g}{f}\frac{\partial H}{\partial y} \qquad v_g = \frac{g}{f}\frac{\partial H}{\partial x} \tag{2.32}$$

where u_g and v_g are the horizontal East (zonal) and North (meridian) components of the geostrophic circulation velocity, x and y are the East and North directions, g is gravity and $f = 2\omega \sin\phi$ is the Coriolis parameter, with $\omega = 7.292115 \cdot 10^{-5}$ [rad·s^{-1}] the mean angular velocity of Earth's rotation and ϕ the geographic latitude. Geostrophic mean velocities (u_m, v_m) and geostrophic velocity anomalies (u_a, v_a) can be derived from (2.32), by inserting the MDT or the SLA as H, respectively. Analogous to the heights in (2.31), the three velocity fields are linked through the following equation:

$$u_a = u_g - u_m \qquad v_a = v_g - v_m \tag{2.33}$$

2.5.3 Mean Dynamic Topography of the Mediterranean Sea

The mean circulation in the Mediterranean Sea is largely unknown. It is characterised by smaller scales and less intensity than in the open ocean, making the interpretation of the variability observed from altimetric SLA rather difficult. The accurate knowledge of the Mediterranean MDT should help to correctly interpret the altimetric measurements and therefore to remove many remaining ambiguities on the Mediterranean variability (Rio et al., 2007). An exhaustive inventory of the main Mediterranean features from basin scale to mesoscale, mainly based on the analysis of sea surface temperature images, is given in (Millot, 1999) for the western Mediterranean basin and in (Hamad et al., 2005) for the eastern basin. Despite the fact that a correlation exists between the dynamic height and the surface temperature, such images are not always easy to interpret as they only contain surface information and therefore do not reflect the ocean dynamics (Rio et al., 2007).

The mean dynamic topography used in this project is the RioMed (Fig. 2.8a). RioMed was produced by CLS Space Oceanography Division and distributed by AVISO, with support from CNES (Rio et al., 2007). It is based on the Rio07 synthetic MDT of the Mediterranean Sea computed for the period 1993-1999. Values are given on a 1/8° regular grid. Besides the MDT, the RioMed product includes zonal and meridian components of the geostrophic mean circulation derived from to the MDT (Fig. 2.8b). The accuracy of the synthetic mean field obtained in areas covered by drifting buoys is directly linked to the number of buoy velocity observations used for the estimation (Rio et al., 2007). The smallest errors will be found for instance in the Ionian and Adriatic Seas, while larger errors will affect areas like the Balearic Sea or the Levantine basin. Inversely, where no buoy observations are available (mainly in the northern Levantine Sea and the North Aegean Sea), the accuracy is linked to the apriori model errors.

The Riomed MDT ranges from -0.17 to 0.27 m over the entire Mediterranean Sea (Fig. 2.8a). The Cretan area is characterised by a cyclonic (counter clockwise) circulation cell of the Cretan cyclone, centered at 25°E, 35°N (Fig. 2.8b). In the survey area around western Crete, the maximum effect of the MDT reaches -0.15 m (Fig. 2.9a). In the survey area in the North Aegean Sea, the effect of the MDT is small, with a maximum of only 0.05 m (Fig. 2.9b). The order of magnitude of the gradients of the RioMed MDT in the North Aegean Sea is in accordance with values found by other author, e.g. (Kourafalou and Tsiaras, 2007).

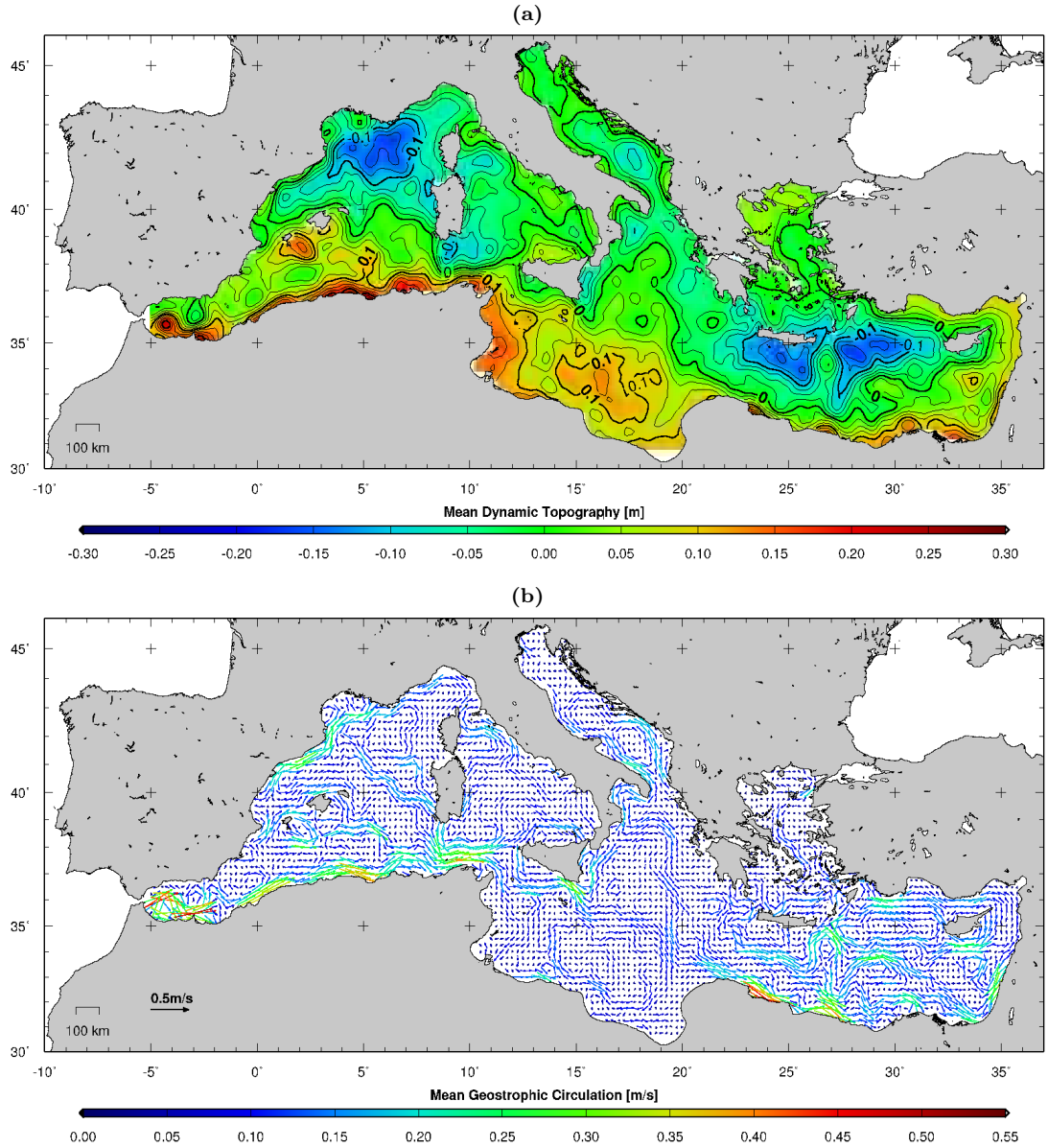

Figure 2.8: **(a)** RioMed mean dynamic topography of the Mediterranean Sea. Contour interval: 0.025 m. **(b)** RioMed mean geostrophic circulation.

2.6 Permanent Tide

2.6.1 Permanent Tidal Effects on Gravitational Potential and Earth's Crust

A considerable part of the tides does not vary periodically with time but is permanent (Ekman, 1989). This permanent deformation of the Earth caused by the presence of the Sun and the Moon is called permanent tide. The permanent tide complicates the definition of the geoid and mean sea surface. The Earth's own gravitational potential is perturbed by the action of the external tidal potential. The observed gravitational potential $W(t)_{obs}$ in the vicinity of the Earth is a combination of the Earth's own potential $W(t)_E$ and the tidal gravitational potential of external bodies (i.e. the Moon, the Sun, and the planets) (McCarthy and Petit, 2004). The external tidal potential

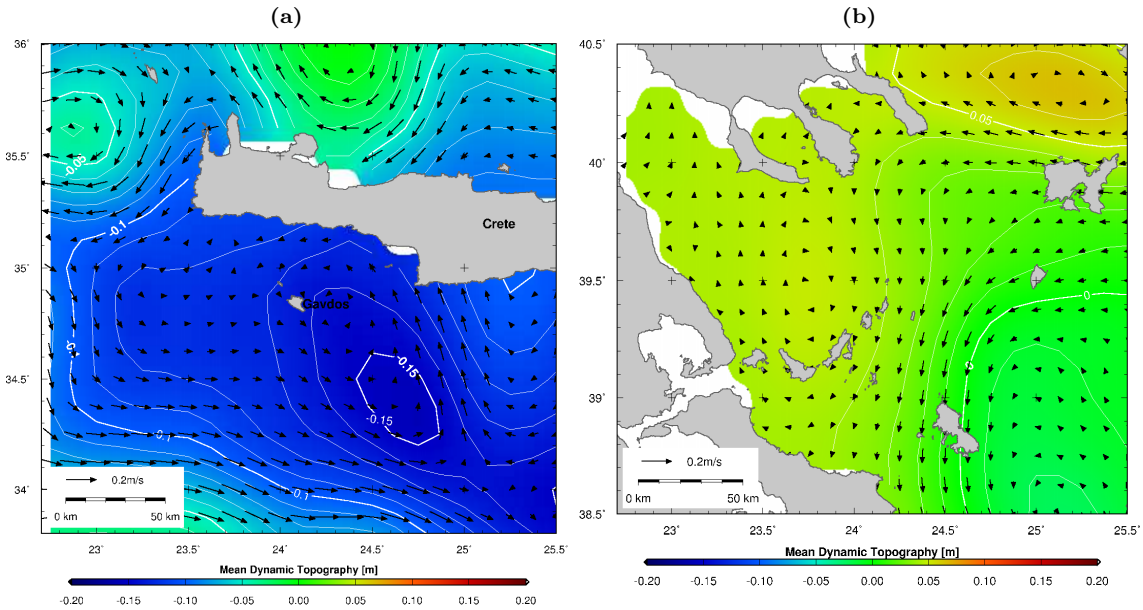

Figure 2.9: Extracts of the RioMed mean dynamic topography (surface) and mean geostrophic circulation (arrows) shown in Fig. 2.8 around Crete **(a)** and in the North Aegean Sea **(b)**. Contour interval: 0.01 m

contains both permanent and periodic parts (W_{ext} and $W(t)_{ext}$), and so does the tide-induced part of the Earth's own potential (W_{def} and $W(t)_{def}$):

$$W(t)_{obs} \;=\; W(t)_E \;+\; W_{ext} \;+\; W(t)_{ext} \;+\; W_{def} + \; W(t)_{def} \tag{2.34}$$

where

$W(t)_{obs}$	observed gravitational potential at a given position and time t
$W(t)_E$	gravitational potential of the Earth (not induced by tidal effects)
W_{ext}	permanent external tidal gravitational potential caused by external bodies (Moon, Sun and planets)
$W(t)_{ext}$	periodic external tidal gravitational potential caused by external bodies (Moon, Sun and planets)
W_{def}	permanent tide-induced gravitational potential, related to the permanent deformation of the Earth (permanent solid Earth tide) caused by the permanent external tidal potential W_{ext}
$W(t)_{def}$	periodic tide-induced gravitational potential, related to the periodic deformation of the Earth (periodic solid-Earth tide) caused by the periodic external tidal potential $W(t)_{ext}$

Similarly to the gravitational potential in (2.34), the observed site position is affected by displacements associated with solid Earth deformations produced by the tidal potential (McCarthy and Petit, 2004). Considering only the vertical site position $h(t)_{obs}$, we have:

$$h(t)_{obs} \;=\; h(t)_E \;+\; dh_{def} \;+\; dh(t)_{def} \tag{2.35}$$

where

$h(t)_{obs}$	observed site height at time t
$h(t)_E$	site height without solid Earth displacements caused by external tidal potential
dh_{def}	permanent vertical deformation of the crust caused by the permanent part of the external tidal potential W_{ext} (permanent solid Earth tide)
$dh(t)_{def}$	periodic vertical deformation of the crust caused by the periodic part of the external tidal potential $W(t)_{ext}$ (periodic solid Earth tide)

2.6.2 Mean-Tide, Zero-Tide and Tide-Free Systems

Consideration of the permanent tidal effects described in (2.34) has led to the definition of three types of gravitational potentials: mean-tide, zero-tide and tide-free (Lemoine et al., 1998). The mean-tide potential $W(t)_m$, zero-tide potential $W(t)_z$ and tide-free potential $W(t)_f$ are derived from (2.34) using the following equation:

$$W(t)_m = W(t)_{obs} - W(t)_{ext} - W(t)_{def} = W(t)_E + W_{ext} + W_{def} \quad (2.36)$$
$$W(t)_z = W(t)_m - W_{ext} = W(t)_E + W_{def} \quad (2.37)$$
$$W(t)_f = W(t)_z - W_{def} = W(t)_E \quad (2.38)$$

The mean-tide potential is obtained from (2.34) by removing the periodic parts of the tidal contributions from the observed potential (2.36). The permanent external tidal potential W_{ext} and the permanent potential W_{def}, associated with the permanent tidal deformation of the crust, are included in the mean-tide potential $W(t)_m$. The mean-tide potential is free of periodic variations due to tidal forces. The removal of the permanent external potential W_{ext} from the mean-tide potential in (2.36) results in the zero-tide potential (2.37), which is strictly a geopotential (Lemoine et al., 1998). The removal of the permanent potential W_{def}, related to the permanent tidal deformation, from the zero-tide potential in (2.37) results in the tide-free potential (2.38). In a tide-free quantity (e.g. potential), all tidal effects have been removed. Because the perturbing bodies are always present, a truly tide-free quantity cannot be observed (McCarthy and Petit, 2004).

The mean-tide, zero-tide and tide-free gravity can be derived from (2.36), (2.37) and (2.38):

$$g(t)_m = g(t)_{obs} - g(t)_{ext} - g(t)_{def} = g(t)_E + g_{ext} + g_{def} \quad (2.39)$$
$$g(t)_z = g(t)_m - g_{ext} = g(t)_E + g_{def} \quad (2.40)$$
$$g(t)_f = g(t)_z - g_{def} = g(t)_E \quad (2.41)$$

The mean-tide, zero-tide and tide-free geoid undulation are derived from (2.36), (2.37) and (2.38):

$$N(t)_m = N(t)_{obs} - N(t)_{ext} - N(t)_{def} = N(t)_E + N_{ext} + N_{def} \quad (2.42)$$
$$N(t)_z = N(t)_m - N_{ext} = N(t)_E + N_{def} \quad (2.43)$$
$$N(t)_f = N(t)_z - N_{def} = N(t)_E \quad (2.44)$$

The mean-tide geoid corresponds to the mean sea surface (MSS), exempt from non-gravitational disturbances (ocean currents, winds, air pressure, salinity, temperature), but including permanent tidal effects. The zero-tide geoid is obtained by removing the permanent direct effects of the Sun and Moon from the mean-tide geoid, while the indirect effects related to the elastic deformation of the Earth are retained. The tide-free geoid would exist for a tide-free Earth, with all (direct and indirect) effects of the Sun and Moon removed (Lemoine et al., 1998).

Analogous to the potential in (2.36), (2.37) and (2.38), the station height in the mean-tide, zero-tide and tide-free system can be derived from (2.35):

$$h(t)_m = h(t)_{obs} - dh(t)_{def} = h(t)_E + dh_{def} \quad (2.45)$$
$$h(t)_z = h(t)_m = h(t)_E + dh_{def} \quad (2.46)$$
$$h(t)_f = h(t)_m - dh_{def} = h(t)_E \quad (2.47)$$

When removing the periodic part of the tidal contributions from the observed station height in (2.35), the resulting station height $h(t)_m$ is on the mean-tide crust (2.45). The permanent part of the deformation produced by the tidal potential is still present in the mean-tide crust. The zero-tide crust $h(t)_z$ is identical to the mean-tide crust (2.46). If the permanent deformation due to the permanent tidal potential is removed from the mean-tide crust, the tide-free crust $h(t)_f$ is obtained (2.47).

2.6.3 Conversion between Permanent Tide Systems

The conversions between mean-tide gravity $g(t)_m$, zero-tide gravity $g(t)_z$ and tide-free gravity $g(t)_f$ are derived from (2.39), (2.40) and (2.41):

$$g(t)_m - g(t)_z = g_{ext} \quad (2.48)$$
$$g(t)_z - g(t)_f = g_{def} \quad (2.49)$$
$$g(t)_m - g(t)_f = g_{ext} + g_{def} \quad (2.50)$$

The difference between mean-tide gravity and zero-tide gravity (2.48) corresponds to the gravitation caused by the permanent external gravity g_{ext}. The difference between zero-tide gravity and tide-free gravity (2.49) corresponds to the gravitation g_{def} caused by the permanent solid Earth tide. The difference between mean-tide gravity and tide-free gravity (2.50) is the sum of g_{ext} and g_{def}. A numerical expression of the permanent tidal gravitation g_{ext}, associated with the permanent external tidal gravitational potential W_{ext}, caused by the Moon and the Sun, is given by (Ekman, 1989):

$$g_{ext} = -\frac{\partial W_{ext}}{\partial r} = -30.4 + 91.2 \sin^2\phi \quad [\mu\text{gal}] \quad (2.51)$$

where $\partial/\partial r$ is the radial derivative and ϕ is the geographic latitude. Numerical expressions for the conversions are obtained by inserting (2.51) into (2.48), (2.49) and (2.50) (Ekman, 1989):

$$g(t)_m - g(t)_z = -\frac{\partial W_{ext}}{\partial r} = -30.4 + 91.2 \sin^2\phi \quad [\mu\text{gal}] \quad (2.52)$$
$$g(t)_z - g(t)_f = -(\delta - 1)\frac{\partial W_{ext}}{\partial r} = (\delta - 1)(-30.4 + 91.2 \sin^2\phi) \quad [\mu\text{gal}] \quad (2.53)$$
$$g(t)_m - g(t)_f = -\delta \frac{\partial W_{ext}}{\partial r} = \delta(-30.4 + 91.2 \sin^2\phi) \quad [\mu\text{gal}] \quad (2.54)$$

with

$$\delta = 1 + \left(\frac{\partial W_{def}}{\partial r}\right) / \left(\frac{\partial W_{ext}}{\partial r}\right) \simeq 1.16 \quad (2.55)$$

The effects of the permanent tide on gravity, corresponding to (2.52), (2.53) and (2.54), are shown in Fig. 2.10a, as a function of latitude. The effect of the permanent external gravity g_{ext} (light grey line) is much more pronounced (factor of 6.25) than the gravitation g_{def} caused by the deformation

due to the permanent solid Earth tide (dark grey line). The effect of the permanent tide on gravity is more pronounced at the poles and at the equator than at mid-latitude. The difference between mean-tide gravity and tide-free gravity varies between -35.3 μgal at the equator and 70.5 μgal at the poles. The negative values near the equator indicate that g_{ext} and g_{def} are directed radially away from the center of the Earth, in opposite direction to the Earth's own gravitation. At the equator, the total gravity is decreased by the permanent tidal effects g_{ext} and g_{def}, while it is increased at the poles. The effects are zero at 35.26°N/S.

The conversions between mean-tide geoid $N(t)_m$, zero-tide geoid $N(t)_z$ and tide-free geoid $N(t)_f$ are derived from (2.42), (2.43) and (2.44):

$$N(t)_m \; - \; N(t)_z \; = \; N_{ext} \tag{2.56}$$
$$N(t)_z \; - \; N(t)_f \; = \; N_{def} \tag{2.57}$$
$$N(t)_m \; - \; N(t)_f \; = \; N_{ext} \; + \; N_{def} \tag{2.58}$$

The difference between mean-tide geoid and zero-tide geoid (2.56) corresponds to the geoid deformation N_{ext} caused by the permanent external potential W_{ext}. The difference between zero-tide geoid and tide-free geoid (2.57) corresponds to the geoid deformation N_{def}, associated with the permanent solid Earth tide. The difference between mean-tide geoid and tide-free geoid (2.58) is the sum of N_{ext} and N_{def}. A numerical expression of the permanent tidal deformation of the geoid N_{ext}, associated with the permanent external tidal potential W_{ext}, caused by the Moon and the Sun, is given by (Ekman, 1989):

$$N_{ext} \; = \; \frac{W_{ext}}{g} \; = \; 9.9 \; - \; 29.6 \; \sin^2 \phi \quad [\text{cm}] \tag{2.59}$$

where g is gravity and ϕ is the geographic latitude. Numerical expressions for the conversions are obtained by inserting (2.59) into (2.56), (2.57) and (2.58) (Ekman, 1989):

$$N(t)_m \; - \; N(t)_z \; = \; \frac{W_{ext}}{g} \; = \; 9.9 - \; 29.6 \; \sin^2 \phi \quad [\text{cm}] \tag{2.60}$$
$$N(t)_z \; - \; N(t)_f \; = \; k \; \frac{W_{ext}}{g} \; = \; k \; (9.9 - \; 29.6 \; \sin^2 \phi) \quad [\text{cm}] \tag{2.61}$$
$$N(t)_m \; - \; N(t)_f \; = (1+k) \; \frac{W_{ext}}{g} \; = (1+k) \; (9.9 - \; 29.6 \; \sin^2 \phi) \quad [\text{cm}] \tag{2.62}$$

with

$$k \; = \; \frac{W_{def}}{W_{ext}} \; \simeq \; 0.30 \tag{2.63}$$

where k is the (fundamentally unknowable) zero frequency Love number, usually taken as 0.30 (e.g. for the EGM96). Similar equations can be found in (Rapp, 1989). The effects of the permanent tide on the geoid deformation, corresponding to (2.60), (2.61) and (2.62), are shown in Fig. 2.10b, as a function of latitude. The deformation N_{ext} of the geoid caused by the permanent external potential (light grey line) is more pronounced (factor of 3.33) than the deformation N_{def} caused by the permanent solid Earth tide (dark grey line). The effect of the permanent tide on the deformation of the geoid is more pronounced at the poles and at the equator than at mid-latitude. The difference between mean-tide geoid and tide-free geoid varies between -25.6 cm at the poles and 12.9 cm at the equator. The positive values near the equator indicate that the permanent external potential W_{ext} and the potential caused by the permanent solid Earth tide W_{def} are increasing

the geoid undulation near the equator. At the poles, they have a decreasing effect on the geoid undulation. The effects are zero at 35.33°N/S.

Finally, the conversion of a GPS height above the ellipsoid on the tide-free crust to a GPS height on the mean-tide (or zero-tide) crust can be derived from (2.45), (2.46) and (2.47) (Ekman, 1989):

$$h(t)_m \; - \; h(t)_f \; = \; dh_{def} \; = \; h \; \frac{W_{ext}}{g} \; = \; h \; (9.9 \; - \; 29.6 \; \sin^2 \phi) \quad [\text{cm}] \tag{2.64}$$

where the Love number $h \simeq 0.62$. The difference is equal to the deformation dh_{def} of the crust due to the permanent part of the solid Earth tide. A similar equation can be found in the IERS Conventions 2003 (McCarthy and Petit, 2004):

$$h(t)_m \; - \; h(t)_f \; = \; [\; -0.1206 \; + \; 0.0001 \; P_2(\sin \phi) \;] \; P_2(\sin \phi) \quad [\text{m}] \tag{2.65}$$

with $P_2(\sin \phi) = (3 \sin^2 \phi - 1)/2$. Similar results are obtained using (2.64) and (2.65), with values of -12.21 and -12.05 cm at the poles, and 6.14 and 6.03 cm at the equator. The deformation of the crust caused by the permanent tide, corresponding to the difference between mean-tide (or zero-tide) and the tide-free crust heights (2.64) is shown in Fig. 2.10c, as a function of latitude. The difference varies between -12.2 cm at the poles and 6.1 cm at the equator. The effect is zero at 35.33°N/S.

2.6.4 Conversion of Sea Surface Heights

Most gravity models and their associated geoid undulations are referenced to a tide-free system. The undisturbed sea surface is a representation of the geoid in a mean-tide system, because it includes all the effects of the permanent tide on the water masses and on the Earth's crust. Sea surface heights observed by spaceborne radar altimetry are therefore referenced to a mean-tide system. In order to make comparisons between geoid undulations and sea surface heights, they have both to be referenced to the same permanent tide system, e.g. the tide-free system. The deformation of the sea surface due to the permanent tide is a combination of the deformation of the Earth's crust (sea bottom) and the deformation of the water masses above it. As shown in Section 2.6.3, the effects of the permanent tide are not the same on the Earth's crust than on the geoid or the sea surface, and have therefore to be treated separately.

As opposed to spaceborne radar altimetry, the sea surface heights determined in this project by airborne laser altimetry, shipborne ultrasound altimetry and GPS buoys all involve GPS observations, referenced to the tide-free ITRF reference frame. The GPS heights are therefore also related to the tide-free system. However, this definition only applies to the Earth's crust, but not to the sea surface. In a first step, in order to obtain consistent sea surface heights SSH_m in a mean-tide system, the observed heights SSH_{obs}, derived from GPS, have to be converted from the tide-free to the mean-tide system, using (2.64) or (2.65). Using (2.64) with $h_m = SSH_m$ and $h_f = SSH_{obs}$, the following corrections are obtained for the survey areas of Crete and North Aegean Sea:

$$\text{Crete (35.0°N)} : \; SSH_m \; = \; SSH_{obs} \; + \; 0.001 \quad [\text{m}] \tag{2.66}$$

$$\text{North Aegean (39.5°N)} : \; SSH_m \; = \; SSH_{obs} \; - \; 0.013 \quad [\text{m}] \tag{2.67}$$

Using the above equations, the sea surface heights determined in this project are made compatible with sea surface heights from spaceborne radar altimetry. The undisturbed sea surface heights in a mean-tide system are equivalent to geoid undulations N_m in a mean-tide system. In order to obtain sea surface heights SSH_f in a tide-free system, the mean-tide sea surface heights SSH_m have to be converted using (2.62), with $N_m = SSH_m$ and $N_f = SSH_f$:

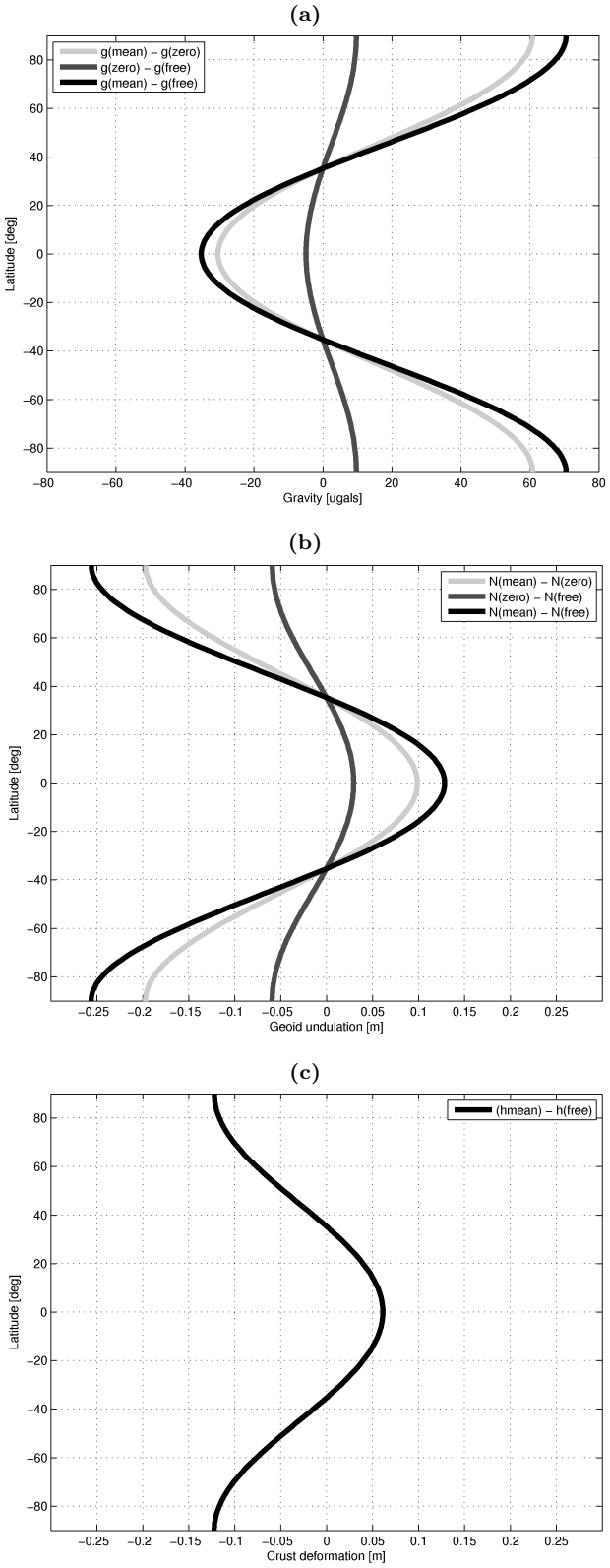

Figure 2.10: Effect of permanent tide, as a function of latitude, on **(a)** gravity, corresponding to (2.52), (2.53) and (2.54), **(b)** geoid height, corresponding to (2.60), (2.61) and (2.62) and **(c)** crust deformation, corresponding to (2.64).

$$\text{Crete (35.0°N)}: \quad SSH_f = SSH_m - 0.002 \ \text{[m]} \tag{2.68}$$

$$\text{North Aegean (39.5°N)}: \quad SSH_f = SSH_m + 0.027 \ \text{[m]} \tag{2.69}$$

Finally, the overall correction for converting observed sea surface heights SSH_{obs}, involving GPS observations, to sea surface heights SSH_f in a tide-free system, is given by the sum of (2.66) and (2.68), respectively the sum of (2.67) and (2.69):

$$\text{Crete (35.0°N)}: \quad SSH_f = SSH_{obs} - 0.001 \ \text{[m]} \tag{2.70}$$

$$\text{North Aegean (39.5°N)}: \quad SSH_f = SSH_{obs} + 0.014 \ \text{[m]} \tag{2.71}$$

These are the corrections that have to be applied to make the sea surface heights determined in this project using airborne laser altimetry, shipborne ultrasound altimetry and GPS buoys compatible with geoid heights in a tide-free system. It can be seen that the difference between the observed sea surface heights SSH_{obs} and sea surface heights SSH_f in a tide-free system are negligibly small, with values of 0.1 cm in the survey area around Crete and 1.4 cm in the North Aegean Sea. It has to be noted that the corrections to the observed sea surface heights using ocean tide models, like GOT00.2 or FES2004, only concern the periodic tides and that they do not affect the permanent tide systems, since in all three permanent tide systems (mean-tide, zero-tide and tide-free), the periodic tidal effects have previously been removed.

3 Geophysical Effects on Sea Surface Heights

3.1 Introduction

Instantaneous sea surface heights SSH_i, as obtained by satellite radar altimetry, airborne laser altimetry, shipborne ultrasound altimetry and GPS buoys, are affected by time-dependent geophysical effects, including ocean waves, astronomical tides, atmospheric pressure (inverse barometer effect) and wind stress. By subtracting these effects from SSH_i, time-independent sea surface heights SSH_c are obtained:

$$\begin{aligned} SSH_c \;=\; SSH_i \;&-\; \text{ocean waves} \\ &-\; \text{tide effects} \\ &-\; \text{inverse barometer effect} \\ &-\; \text{high frequency wind response} \end{aligned} \tag{3.1}$$

The resulting time-independent sea surface heights SSH_c can be interpolated in order to obtain a surface representing the time-independent sea surface topography. The correction for tidal effects has nowadays generally reached centimeter accuracy, whereas the effects associated with the forcing of wind and atmospheric pressure are less well known.

Other effects influencing sea surface heights, like precipitation, evaporation, river inflow, net flow at the strait of Gibraltar and from the Black Sea, changing ocean currents, salinity and steric sea level variations due to the volume change of water molecules related to water temperature change, are not considered directly (Fenoglio-Marc et al., 2006). This procedure is equivalent to the one applied by the official analysis centers of spaceborne radar altimetry data (Picot et al., 2003).

3.2 Ocean Waves, Sea State and Significant Wave Height

Ocean waves have typical amplitudes of half a meter to several meters in extreme cases. They are characterised by a succession of crests and troughs, as well as zero-upcrossings and zero-downcrossings (Fig. 3.1). The wave height H is the vertical distance between a trough and the next crest, or the vertical distance between the highest and the lowest value between two zero-downcrossings or upcrossings. The significant wave height $\bar{H}_{1/3}$ is given by the average height of the 1/3 highest waves in a record (WMO, 1998). It roughly approximates the visually estimated wave height. Details on waves can be found in (Coulson and Jeffrey, 1977; Lighthill, 1978; WMO, 1998).

The airborne and shipborne altimetry data, as well as the GPS buoy data, contain information on ocean waves. Wave characteristics (sea state) and significant wave heights can be derived from these data by signal filtering and wave modeling (Section 8.2.2, Fig. 8.4). Appropriate filter algorithms, based on cubic splines and windowed median, have been developed and applied in the framework of this project, allowing to separate the high-frequency wave component from the sea surface height signal (Sections 8.2.1 and 9.2).

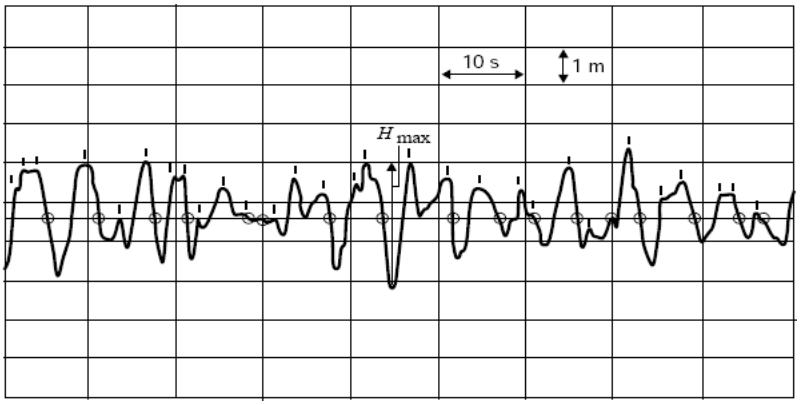

Figure 3.1: Typical sample of a wave record. Dashes: wave crests. Circles: zero-downcrossings. From (WMO, 1998).

3.3 Tides

3.3.1 Characteristics of Tides

Tidal effects are governed by Newton's law of gravitation, where the gravitational force $\vec{F}$ between two bodies of masses m and M, separated by a distance vector $\vec{r}$ is given by:

$$\vec{F} \;=\; G\,\frac{M\cdot m}{|\vec{r}|^3}\,\vec{r} \tag{3.2}$$

where $G = 6.6742\cdot 10^{-11}$ $[\mathrm{m^3{\cdot}kg^{-1}{\cdot}s^{-2}}]$ is Newton's universal gravitational constant. In the degree of approximation needed in the computation of tides, only the Moon and the Sun have an influence on the Earth: the Sun because of its huge mass ($M_{\mathrm{Sun}} = 3.33\cdot 10^5\ M_{\mathrm{Earth}}$) and the Moon because of its relatively small distance to the Earth ($3.84\cdot 10^8$ m).

The trajectories of the Moon and the Sun with respect to the Earth are highly complex. They have elliptic orbits contained in a plane which's inclination varies with respect to the terrestrial equatorial plane. In addition, interactions between the Moon, the Sun and the Earth are modifying the orbital trajectories. The tide generating force needs therefore to be separated into a sum of elementary forces.

The tide generating force can be derived from the tide generating potential. In the case of the system formed by the three bodies Earth, Moon and Sun, the total astronomic tide generating potential can be separated into the sum of the lunar and the solar potential. The result of the development of these potentials into Legendre polynomials is a series of harmonic components dependent on the time and the zenithal distance to the Moon or the Sun. In addition, the series is decomposed into a finite sum of simple periodic movements dependent on the celestial coordinates (declination, hour angle, terrestrial latitude).

There are several contributions to the tidal effect influencing the sea surface height: ocean tide, ocean loading tide, solid Earth tide and pole tide (Picot et al., 2003). The ocean tide (with respect to the ocean bottom), the ocean loading tide (of the ocean bottom) and the solid Earth tide are related to luni-solar forcing of the Earth (astronomical tides), either directly, as is the case of the ocean tide and solid Earth tide, or indirectly, as is the case of the ocean loading tide since it is forced by the ocean tide. The sum of the tidal contributions listed above is called the geocentric

tide:

$$\text{geocentric tide} \;=\; \text{ocean tide} \;+\; \text{ocean loading tide} \;+\; \text{solid Earth tide} \;+\; \text{pole tide} \qquad (3.3)$$

Tide-gauges directly observe the ocean tide, while satellite altimetry data includes the entire geocentric tide (3.3). Therefore, the geocentric tide must be removed to correct altimetric data for tidal effects. The same applies for airborne and shipborne altimetry data, but with special considerations concerning the solid Earth tide (Section 3.3.3).

3.3.2 Ocean Tide

The ocean tide of astronomic origin is the periodic variation of the sea surface height resulting from the actions of the celestial bodies (in particular the Moon and the Sun) moving around the Earth. The relative movements of the Moon and the Sun with respect to the Earth, combined with the Earth's own rotation, are generating periodic gravitational forces. Each of these elementary forces generates a periodic displacement of the water masses on Earth, resulting in sinusoidal variations of the sea surface (tidal waves), called harmonic tidal components.

The tide generating force is the differential force between the gravitational force of the Moon and the Sun at a given point of the sea surface and the gravitational force of the Moon and the Sun at the center of mass of the Earth (Fig. 3.2). The latter corresponds to the reciprocal of the rotational centrifugal force of the Earth-Sun-Moon system, since the Earth is in equilibrium. Hence, at the center of the Earth, the gravitational force towards the Moon/Sun and the centrifugal force away from the Moon/Sun are perfectly in balance. Assuming that the sea surface instantaneously adopts the equilibrium position corresponding to the acting gravitational forces of the attraction of the Moon and the Sun on the water particles and on the center of mass of the Earth, the equilibrium tide is obtained based on the tide generating force.

On the surface of the Earth nearest to the Moon/Sun, the gravitational force is stronger than the centrifugal force, resulting in a force towards the Moon/Sun causing a water bulge (Fig. 3.2). On the opposite side of the Earth, the gravitational force is weaker, since the Moon/Sun is further away, and the centrifugal force is dominant. Hence there is a resulting force away from the Moon/Sun, creating another water bulge (Fig. 3.2). At mid latitudes, the tide generating force is mainly horizontal.

When the Earth, Moon and Sun are in line (during new and full Moon), the bulges of water caused by the Moon and the Sun occur in the same place on the Earth's surface. The lunar and solar tides are reinforcing each other, which leads to higher than average high tides, and lower than average low tides. These are called spring tides. When the Earth, Moon and Sun form a right angle, the high water caused by the lunar tide coincides with the low water of the solar tide. This produces lower than average high waters and higher than average low waters, which are called neap tides. They occur approximately seven days after spring tides (source: Proudman Oceanographic Laboratory website).

Laplace's theory of dynamic response of the ocean suggests that the tide generating force induces a response of the ocean in form of oscillations with the same frequencies than the tide generating force (principle of forced oscillations), characterized by an amplitude and a phase. Based on Laplace's theory, the variation of the sea surface height $h_t(x,t)$ at location x and time t caused by the ocean tide is given by:

$$h_t(x,t) \;=\; \sum_{k=1}^{N} A_k(x)\;\cos\;[\;\omega_k\;t\;+\;V_k\;-\;G_k(x)\;] \qquad (3.4)$$

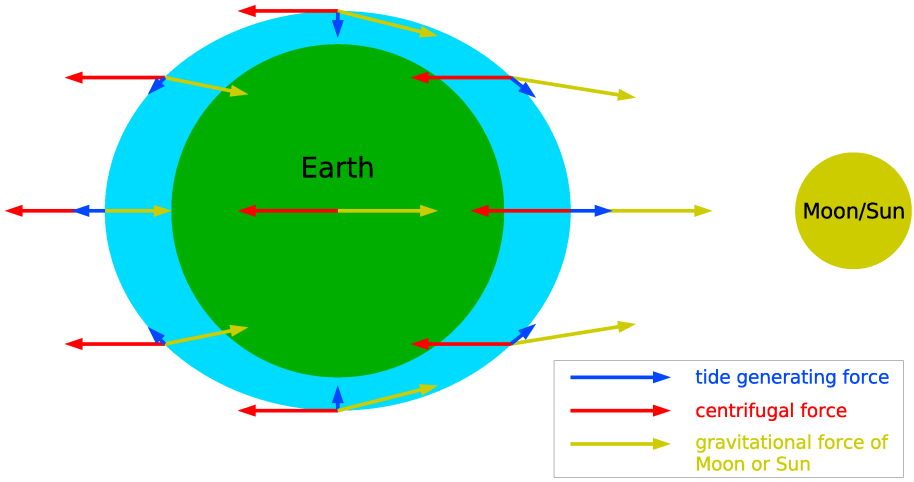

Figure 3.2: Schematic view of the forces governing the equilibrium ocean tide.

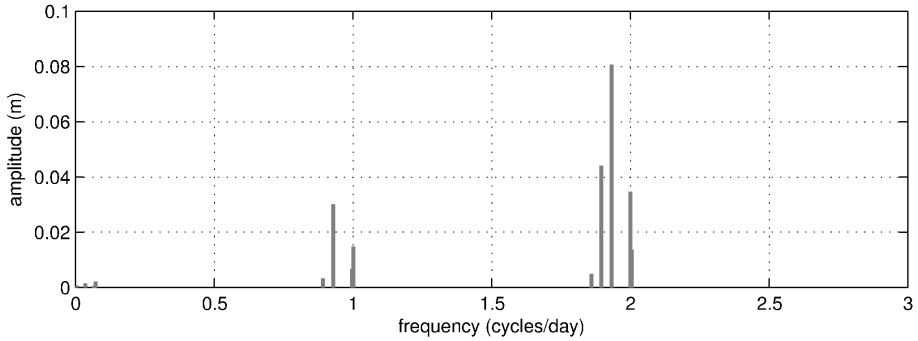

Figure 3.3: Spectrum of the tidal signal from FES2004 in the survey area in the North Aegean Sea.

where k is the tidal component with oscillation period ω_k, astronomical phase V_k, amplitude $A_k(x)$ and Greenwich phase lag $G_k(x)$. Hence, the tidal variation of the sea surface is constituted by the superposition of many oscillations generated by different phenomena (Le Provost, 2001).

The major components have diurnal or semi-diurnal periods (Fig. 3.3 and Tab. 3.1). The semi-diurnal waves have a period of about 12 hours. The M2 wave (M for Moon and 2 for semi-diurnal) is the most important semi-diurnal wave. It corresponds to the tide generated by the Moon uniformly moving around the Earth with a circular orbit in the equatorial plane. The S2 wave (S for Sun) corresponds to the same phenomena for the Sun. Its period is exactly 12 hours. There are other semi-diurnal waves due to the ellipsoidal shape of the orbits. The diurnal waves have a period of about 24 hours. The principal diurnal waves are the lunar-solar declination wave K1 and the lunar wave O1. In addition, there are waves with longer periods, e.g. the annual wave Sa caused by the annual variation of the distance Sun-Earth.

If the Earth was covered by a uniform water layer, the dynamic prediction of ocean tides at any location would be easy, since the astronomical periods, amplitudes and phases of all tidal constituents are known precisely (Chelton, 1988). However, the propagation speed of these oscillations depends on the water depth (bathymetry). In addition, they are reflected on the continental shelf, refracted and dissipated (Roblou, 2001). Hence, ocean tides are strongly influenced by the continental boundaries, the sub-marine topography (bathymetry), the complex sea floor topography in coastal regions, the shape of the coastline and the eigenfrequency of oceanic basins (Le Provost, 2001). These influences, which can locally produce tidal amplitudes of several meters, are making

Table 3.1: Major harmonic constituents of the astronomical tide.

Type	Name	Period	Origin
Semi-diurnal	M2	12h25	Mean movement of the Moon
	S2	12h00	Apparent mean movement of the Sun
	K2	11h59	Lunar-solar declination
	N2	12h39	Major lunar eccentricity effects
	L2	12h11	Minor lunar eccentricity effects
	2N2	12h54	Lunar eccentricity effects of 2^{nd} order
Diurnal	K1	23h56	Lunar-solar declination
	O1	25h49	Lunar declination
	P1	24h03	Solar declination
	Q1	26h56	Major lunar eccentricity effects
Long period	Mf	13.661 days	Semi-monthly lunar declination
	Mm	27.555 days	Monthly lunar declination
	Ssa	182.621 days	Semi-annual solar declination
	Sa	365.240 days	Annual variation of the distance Sun-Earth

purely dynamic predictions only marginally useful (Chelton, 1988).

In practice, ocean tides are therefore determined empirically at selected locations, based e.g. on hourly observations of the sea level from a tide-gauges, covering a period long enough (usually a few months to several years) to resolve the major tidal constituents. Tidal predictions are based on the harmonic analysis of the observed tidal signal, yielding amplitudes and phase lags of every harmonic constituent for the observations site. Dynamic models of global ocean tides are then constrained by the tidal amplitudes and phases empirically determined at the tide-gauges (Chelton, 1988). The harmonic analysis only allows to predict the tide at a location where it can be measured. Hence, the implementation of satellite altimetry is revolutionary, since for the first time, it offers the possibility to observe and predict the sea level at nearly every point of the ocean.

Amplitudes and phases of the major ocean tide constituents M2 and S2, as predicted for the Mediterranean Sea by the FES2004 model, are shown in Fig. 3.4. The amplitudes in the Mediterranean Sea are small as compared to the tidal effects encountered in the open sea, as can be seen from the amplitudes predicted in the Atlantic Ocean, adjacent to the Mediterranean Sea.

The ocean tide models used in this project are the FES2004, GOT00.2 and POL models:

- The FES2004 (Finite Element Solution) tide model is based on a based on a finite element hydrodynamic model and the assimilation of tide-gauge data and observations from TOPEX/Poseidon and ERS-2. FES2004 was produced by LEGOS and CLS Space Oceanography Division and distributed by AVISO, with support from CNES. The hydrodynamic model is based on the resolution of the tidal barotropic equations on a global finite element grid of approx. 1 million nodes. It is a global model, including 14 tidal constituents (M2, S2, K2, N2, 2N2, O1, P1, K1, Q1, Mf, Mtm, Mm, Msqm and M4), distributed on $1/8° \times 1/8°$grids of amplitude and phase lag. FES2004 tides are used as default tidal corrections for the altimetric products of TOPEX/Poseidon and Jason-1. Further details on the FES2004 model can be found in (Lyard et al., 2006; Letellier, 2004; Le Provost, 2001).
- The GOT00.2 model (Ray, 1999) used 286 cycles of TOPEX/Poseidon data, supplemented in shallow seas and in polar seas (latitudes above 66°) by 81 cycles of ERS-1 and ERS-2 data. The solution consists of independent near-global estimates of 8 major constituents (Q1, O1, K1, P1, N2, M2, S2, K2). FES94.1 was used as a priori hydrodynamic model, as well as several local hydrodynamic models. The tidal constituents are given on $0.5° \times 0.5°$grids. Since the GOT00.2 model was not available to the author, the model was only used under the form of tidal corrections along the flight-tracks of the airborne laser altimetry campaign around

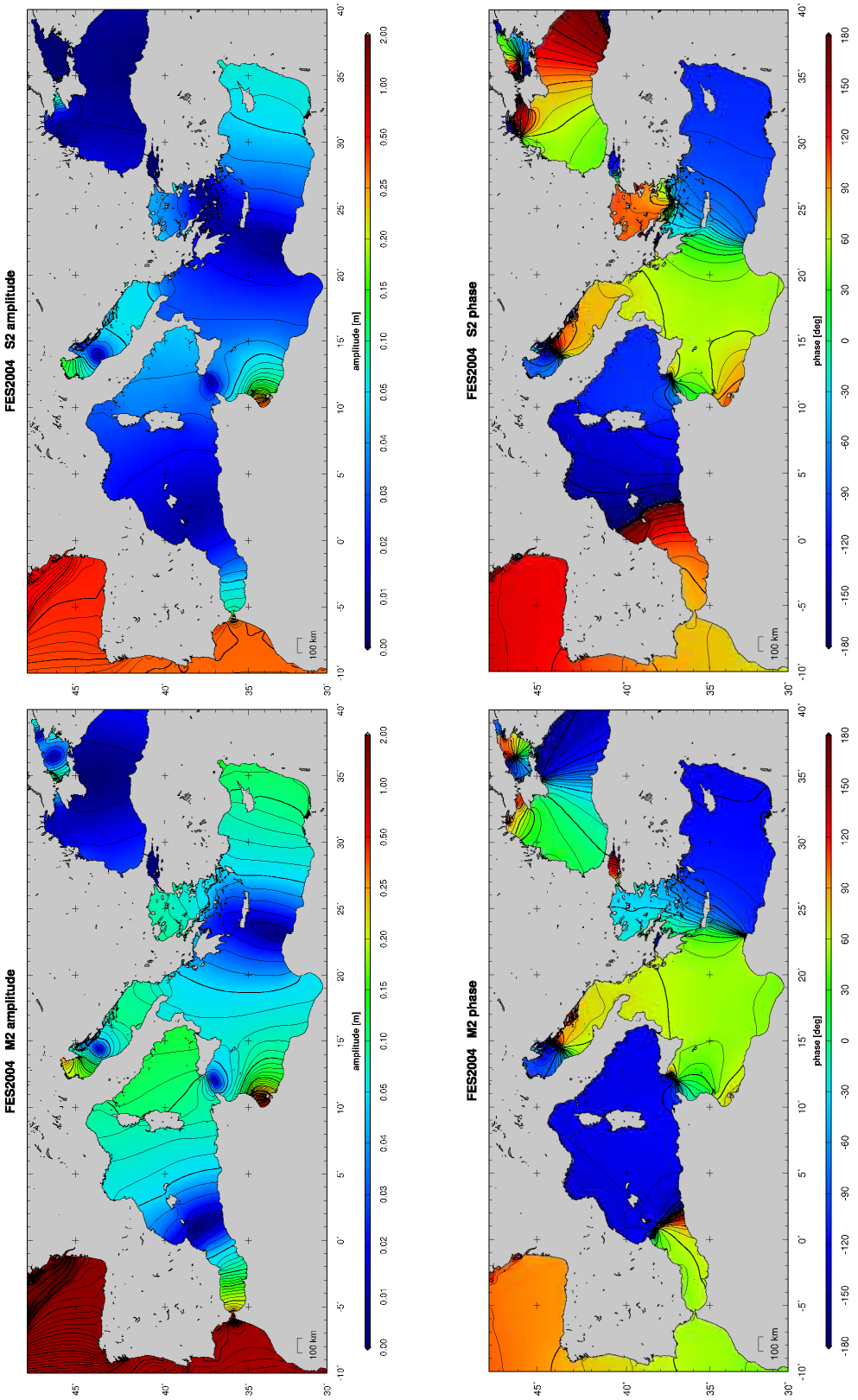

Figure 3.4: M2 and S2 ocean tide amplitude and phase from FES2004 in the Mediterranean Sea.

Crete, kindly provided by E.C. Pavlis from JCET.

- The POL model is a model for the Mediterranean Sea, developed by the Proudman Oceanographic Laboratory (POL) (Tsimplis et al., 1995). It is a high-resolution, two-dimensional hydrodynamic model forced by the equilibrium tide and the incoming tide at the Strait of Gibraltar. The model is based on depth-averaged equations of continuity and motion in spherical polar coordinates. The 4 most significant constituents M2, S2, K1, and O1 are included in the model. The model grid is $1/12^\circ \times 1/12^\circ$. The initial elevation parameters for all four harmonic constituents were tuned until the best agreement between the model predictions and the data of 63 coastal tide-gauges, including tide-gauges in the Aegean Sea and on Crete, was achieved.

The ocean tide is one of the most significant variations of the sea surface. Its amplitudes in the open ocean are typically 1 to 2 m. This means that the tidal amplitudes are often larger than the signals of interest in altimetric studies of ocean circulation or local geoid signals. Ocean tides need therefore to be removed from the observed sea surface heights. The variation of the sea surface due to ocean tides represents 80% of its variability in the open ocean (Le Provost, 2001), but much less in semi-enclosed seas like the Mediterranean. Further details on ocean tide can be found in (Le Provost, 2001).

3.3.3 Solid Earth Tide

The solid Earth tide is the elastic periodic deformation of the Earth's crust, including the ocean bottom, due to luni-solar forcing. The solid Earth responds to external gravitational forces similarly to the oceans (Picot et al., 2003). The response of the Earth is fast enough that it can be considered to be in equilibrium with the tide generating forces. Solid Earth tides have amplitudes of about 10-20 cm. Solid Earth tides occur at the same frequencies than the ocean tide, but can be modeled much more accurately (to approx. 1 cm) than ocean tides (Chelton, 1988). Since the movement of the ocean bottom due to solid Earth tides affects the height of the sea surface, it must be removed from spaceborne altimetric data.

In the case of sea surface height observations from airborne and shipborne altimetry, or from other techniques where the positioning of the altimetric sensor relies on differential GPS processing, the treatment of solid Earth tides has to be considered with care. Terrestrial GPS stations are affected by solid Earth tides. In the classical differential processing of a GPS baseline between two terrestrial stations of height h_1 and h_2, the solid Earth tide correction is given by the difference between the solid Earth tide at the two stations (Fig. 3.5a):

$$h_2 \;=\; h_1 \;+\; \Delta h_{obs}(t_i) \;+\; tide_1(t_i) \;-\; tide_2(t_i) \tag{3.5}$$

where h_1 is the height of the reference station without solid Earth tides, h_2 is the height of the second station without solid Earth tides, $\Delta h_{obs}(t_i)$ is the height difference between the two stations observed by differential GPS at time t_i, $tide_1(t_i)$ is the solid Earth tide at the reference station at time t_i and $tide_2(t_i)$ is the solid Earth tide at the second station at time t_i. The differential solid Earth tide correction becomes negligible if the baseline length is small.

In airborne altimetry, the height of the aircraft is not affected by solid Earth tides. In this case, the solid Earth tide correction that has to be applied to the laser ground point depends on whether or not solid Earth tides were considered during kinematic GPS baseline processing between the terrestrial reference station and the aircraft. If the solid Earth tide is considered, the real aircraft height h_a is obtained (Fig. 3.5b):

$$h_a(t_i) \;=\; h_r \;+\; \Delta h_{obs}(t_i) \;+\; tide_r(t_i) \tag{3.6}$$

where h_r is the height of the reference station without solid Earth tides, $\Delta h_{obs}(t_i)$ is the height difference between the aircraft and the reference stations observed by differential GPS at time t_i and $tide_r(t_i)$ is the solid Earth tide at the reference station at time t_i. In airborne altimetry, the laser sensor is measuring the range r between the real position of the aircraft, not affected by solid Earth tides, and the ground surface (sea or land), affected by solid Earth tides. Hence, by combining the observed range r with the real aircraft height h_a, the ground height h_g including the solid Earth tide effect $tide_g$ is obtained (Fig. 3.5b):

$$h_g \; + \; tide_g(t_i) \; = \; h_a(t_i) \; - \; r(t_i) \tag{3.7}$$

This means that if the solid Earth tide on the GPS reference station was corrected during kinematic GPS processing, the surface height obtained by airborne altimetry includes the full effect of the solid Earth tide at the ground point position, analogous to spaceborne altimetry. However, most kinematic GPS software do not consider solid Earth tide corrections. Thus, by fixing the baseline origin to the apriori coordinates of the reference station h_r, the tidal deformation $tide_r$ at the reference station propagates with opposite sign into the computed aircraft height $h_{a,\,c}$ (Fig. 3.5b), yielding vertical errors of up to 20 cm:

$$h_{a,\,c}(t_i) \; = \; h_r \; + \; \Delta h_{obs}(t_i) \; = \; h_a(t_i) \; - \; tide_r(t_i) \tag{3.8}$$

By combining the observed range r with the aircraft height $h_{a,\,c}$ falsified by the solid Earth tide effect $tide_r$ at the reference station, the obtained surface height is only affected by the differential solid Earth tide effect between the reference station and the laser ground point, analogous to the differential GPS positioning between terrestrial stations (3.5):

$$h_g \; + \; tide_g(t_i) \; - \; tide_r(t_i) \; = \; h_{a,\,c}(t_i) \; - \; r(t_i) \tag{3.9}$$

During the kinematic differential processing of the airborne GPS data used to compute sea surface heights by from airborne laser altimetry, no correction for solid Earth tides was applied. Hence, the solid Earth tide correction to be applied to the obtained sea surface heights is given by the differential solid Earth tide between the laser ground-point and the GPS reference station, according to (3.9). Thus, solid Earth tides were computed for both the reference station and the airborne data, both showing amplitudes in the order of 15 cm (Fig. 3.6). The resulting differential solid Earth tide, however, ranges only between -3 and 4 mm, even on baselines exceeding 100 km. This means that the major part of the solid Earth tide effect on the observed sea surface height was already indirectly eliminated during the differential GPS processing, and that the remaining part is negligible because it is about one order of magnitude smaller than the expected accuracy of the airborne laser altimetry system. On the other hand, removing the absolute value of the solid Earth tide, computed at the laser ground points, from the obtained sea surface heights would have induced a vertical error in the order of 15 cm.

Sea surface height observations by shipborne altimetry and GPS buoys, involving differential GPS processing, are similar to the case of two terrestrial GPS station (Fig. 3.5a). The ship and the buoy are both directly affected by the solid Earth tide, in the same way as a terrestrial station. Hence, (3.5) applies, meaning that the obtained sea surface heights are affected by the differential solid Earth tide between the reference station and the observation point, unless solid Earth tides were considered during GPS processing.

3.3.4 Ocean Loading Tide and Pole Tide

The ocean loading tide is the oscillation of the ocean bottom (and the adjacent continental shelf in coastal areas), caused by the tidal variations of the load of the water masses. Hence, the ocean

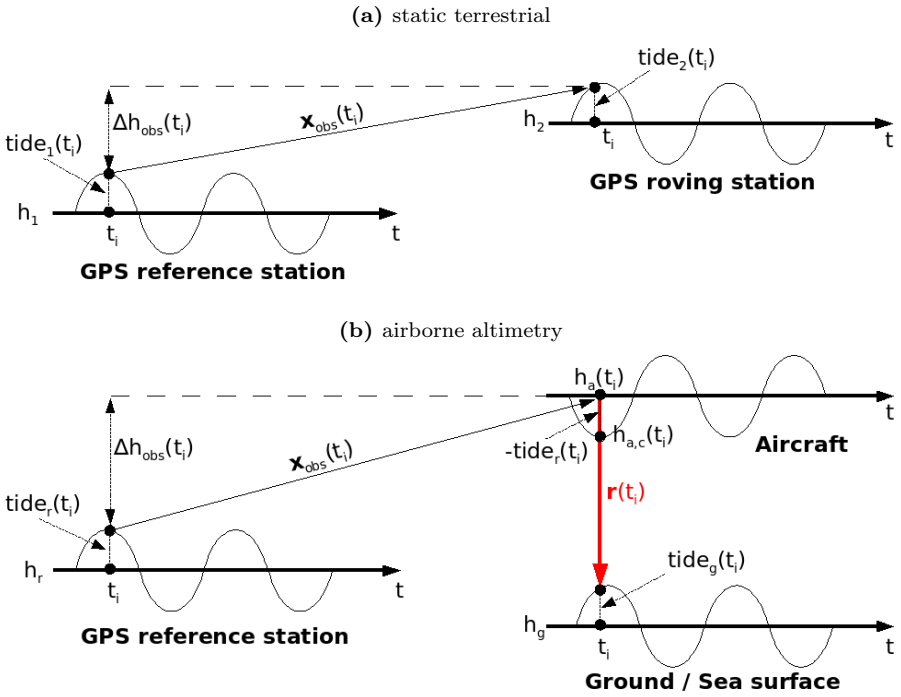

Figure 3.5: **(a)** Solid Earth tides in static differential GPS processing between two terrestrial stations. **(b)** Solid Earth tides in airborne altimetry and in kinematic differential GPS processing between a terrestrial reference station and the aircraft.

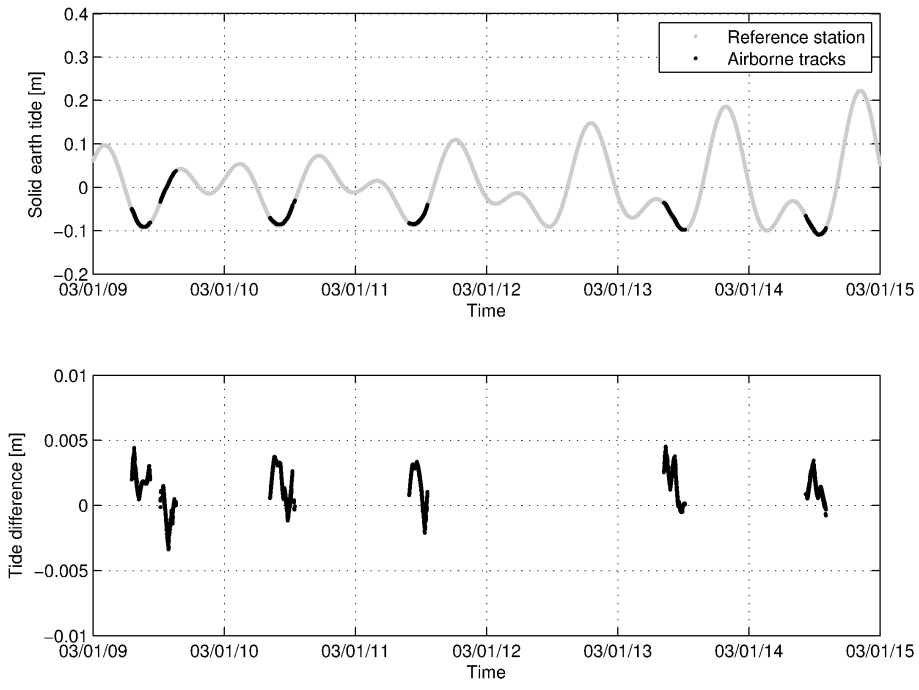

Figure 3.6: Top: time series of solid Earth tides at the GPS reference station TUC1 (grey) and along airborne altimetry tracks (black). Bottom: differences between solid Earth tides along airborne tracks and at the GPS reference station, corresponding to the correction to be applied to the observed sea surface heights.

loading tide is indirectly related to luni-solar forcing. The pole tide is unrelated to luni-solar forcing. In the case of the sea surface, it is a tide-like motion of the ocean surface as a response of both the solid Earth and the oceans to the centrifugal potential that is generated by small perturbations to the Earth's rotation axis (Picot et al., 2003). These perturbations primarily occur at periods of 433 days (called the Chandler wobble) and annually. Modeling the pole tide requires knowledge of proportionality constants, the so-called Love numbers, and a time series of perturbations to the Earth's rotation axis, a quantity that is now measured routinely with space techniques (Picot et al., 2003). Ocean loading and pole tide values were computed for the region of Crete and the North Aegean Sea using the GOT00.2 tide model. The ocean loading and pole tide effects were found to be below 1 cm in both survey areas, and were therefore not further considered.

3.4 Atmospheric Pressure and Wind Forcing

3.4.1 Inverse Barometer Effect

As atmospheric pressure increases and decreases, the sea surface tends to respond hydrostatically by falling or rising, respectively (Picot et al., 2003). This effect is referred to as the inverse barometer (IB) effect. The instantaneous IB effect on the sea surface height is given by (Dorandeu and Le Traon, 1999; Picot et al., 2003; Chelton, 1988):

$$IB \;=\; \frac{1}{\rho\, g}\;(\;P \;-\; P_{ref}\;) \;=\; -0.9948\;(\;P \;-\; P_{ref}\;) \tag{3.10}$$

where IB is the inverse barometer effect in [cm], $\rho = 1.025$ g/cm^3 is the density of sea water, $g = 980.7$ cm/s^2 is gravity, P is the atmospheric pressure at the sea surface in [hPa] and P_{ref} is the time varying mean global surface atmospheric pressure over the oceans in [hPa]. In many applications, P_{ref} is assumed to be constant, e.g. 1013.3 hPa. However, using a constant P_{ref} creates unrealistic signals: the mean correction is no longer zero, which is not consistent with ocean mass conservation (Dorandeu and Le Traon, 1999). The scale factor of -0.9948 implies that a local increase of 1 hPa in atmospheric pressure locally depresses the sea surface by about 1 cm.

The variation of the sea surface elevation in relation with atmospheric pressure changes does not result from a compression of water, but from a horizontal redistribution of the water masses in response to horizontal variations of the atmospheric pressure (Chelton, 1988). If the atmospheric pressure would change uniformly over an entire ocean basin, there would be no change in the sea level, except for a negligible variation due to the small compressibility of seawater. The response of the sea surface to atmospheric pressure loading depends both on the spatial and temporal scale of the pressure forcing (Wunsch, 1972). The adjustment to a change in atmospheric pressure propagates relatively rapidly by means of long gravity waves. The response is believed to be nearly isostatic for time scales between 2 days and 2 weeks (Wunsch, 1972). At shorter time scales, the response of ocean is too slow to compensate for rapid pressure changes. At longer time scales, the ocean responds dynamically in the form of geostrophic currents and Rossby waves. The detailed wavenumber-frequency characteristics of the transfer function between sea surface elevation and atmospheric pressure loading is not known (Chelton, 1988). It is likely that the transfer function varies geographically, with e.g. different behaviours in coastal and open ocean regions.

The IB correction is presently a major source of error in altimetric studies of dynamic ocean topography (Chelton, 1988). Its accuracy is limited by the uncertainty in the atmospheric surface pressure field over the oceans and by the uncertainty in the transfer function between sea surface elevation and atmospheric pressure loading. The uncertainty in the atmospheric pressure is typically about 3 hPa, corresponding to an uncertainty of 3 cm in the IB correction. The uncertainty may be higher by a factor of two or more in the case of intense storms and in the southern hemisphere,

where atmospheric pressure fields are not well resolved by meteorological models (Chelton, 1988). A detailed review of the theoretical background on atmospheric loading and the oceanic inverted barometer effect is given in (Wunsch and Stammer, 1997).

3.4.2 MOG2D Dynamic Atmospheric Corrections

The ocean response to meteorological forcing is poorly accounted for by simply applying the inverted barometer (IB) correction (Wunsch and Stammer, 1997), described in Section 3.4.1. The classic IB correction formulates the static response of the ocean to atmospheric pressure forcing, while wind effects are totally ignored (Carrère and Lyard, 2003). The validity of the IB assumption depends on the temporal and spatial scales considered. The ocean has a dynamic response (differing from the IB response) to atmospheric pressure forcing at high frequencies (periods below 3 days) and at high latitudes. Thus, the high frequency variability needs to be corrected from an independent model. Wind effects prevail particularly around the 10 days period (Carrère and Lyard, 2003).

The corrections for atmospheric pressure and wind forcing used in this project are the dynamic atmospheric corrections (DAC) produced by CLS Space Oceanography Division using the MOG2D model from LEGOS and distributed by AVISO, with support from CNES. The corrections are composed of two parts. The correction of the low frequency (above 20 days) response of the ocean to atmospheric forcing is computed using an IB correction developed by CLS, assuming a static response and neglecting wind effects. The correction of the high frequency (below 20 days) ocean response to atmospheric pressure and wind forcing is computed using the MOG2D barotropic model (Carrère and Lyard, 2003) developed by LEGOS/CNRS.

MOG2D (2D Gravity Waves model) is a barotropic non-linear model derived from (Lynch and Gray, 1979). The model is governed by the classic shallow water continuity and momentum equations and it can include tides (Carrère and Lyard, 2003). It is based on a finite elements space discretization, which allows to increase the resolution in areas of interest with strong topographic gradients or shallow waters. The grid size ranges from 400 km in the deep sea to 20 km in coastal, shallow areas (Carrère and Lyard, 2003). In shallow water, the MOG2D model shows an oceanic response very different from the classic IB response (Carrère and Lyard, 2003). The simulation domain includes the Mediterranean Sea and other semi-enclosed seas. The model is forced by atmospheric pressure and 10 m wind speeds from ECMWF analysis data, with a temporal resolution of 6 hours and a spatial resolution of $0.25^\circ \times 0.25^\circ$. MOG2D dynamic atmospheric corrections are provided via the AVISO web site as global grids with a temporal resolution of 6 hours and a spatial sampling of $0.25^\circ \times 0.25^\circ$. An example of MOG2D correction grids during the airborne laser altimetry campaign around Crete is shown in Appendix G. Corresponding ECMWF atmospheric pressure fields at sea level are shown in appendix F. More details on MOG2D can be found in (Carrère and Lyard, 2003; Letellier, 2004; Mourre, 2004; Roblou, 2001).

4 Airborne Laser Altimetry Technique

4.1 Introduction

Airborne laser altimetry has become a powerful method serving a wide range of important applications in remote sensing, geodesy, geophysics and geodynamics (Luthcke et al., 2002). These applications include the determination of digital terrain models and the monitoring of changing surfaces like landslides and glaciers. During the last decades, advances in airborne laser altimetry have enabled the production of very precise digital surface models on an operational level, with accuracies better than 20 cm. The potential of airborne laser altimetry especially lies in regions where conventional methods encounter serious problems due to a lack of sufficient texture or fast deforming terrain, where the establishment of reliable ground control points is difficult or impossible. In oceanography-related projects, airborne laser altimetry is mainly aimed at sea level determination in coastal areas to bridge deep sea satellite radar altimetry data with coastal tide-gauge stations.

Airborne laser altimetry provides 3D coordinates of ground surface points. It is based on range measurements between an aircraft and the ground surface using a laser distance measurement device. Since the laser device measures the slant range between an aircraft and the ground surface, the position of the ground point can only be determined if the position and orientation of the laser system are permanently known with respect to an absolute coordinate system. Precise knowledge of position and attitude are crucial for the production of accurate data. Thus, for the determination of ground surface points, the laser system has to be supported by a positioning and orientation system, providing autonomous and accurate position and attitude of the aircraft without further ground information. The laser data was processed using GPS-based aircraft trajectories and attitudes, yielding sea surface heights with vertical accuracies below 10 cm. Details on the computation of laser ground point coordinates based on direct georeferencing of airborne laser altimetry data are given in Chapter 7.

4.2 Instumental Setup

4.2.1 Overview

The airborne laser altimetry surveys were carried using the DeHavilland Twin-Otter of the Swiss Federal Office of Topography (swisstopo), operated by the Swiss airforce (Fig. 4.1). The aircraft was equipped with the following instruments:

- Optech 501 SA Rangefinder laser profiler, sampling rate 1-2 kHz (Fig. 4.2)
- Riegl LMS-Q140i-60 laser scanner[1]
- 4 GPS receivers for position and attitude determination, sampling rate 2 Hz (Fig. 4.1)
- Honeywell H-764G INS[1], sampling rate 50 Hz, coupled with GPS (Fig. 4.2a)
- LaCoste Romberg S-meter sea/air gravimeter[2]

[1]Provided by KMS.
[2]Provided by the University of Bergen.

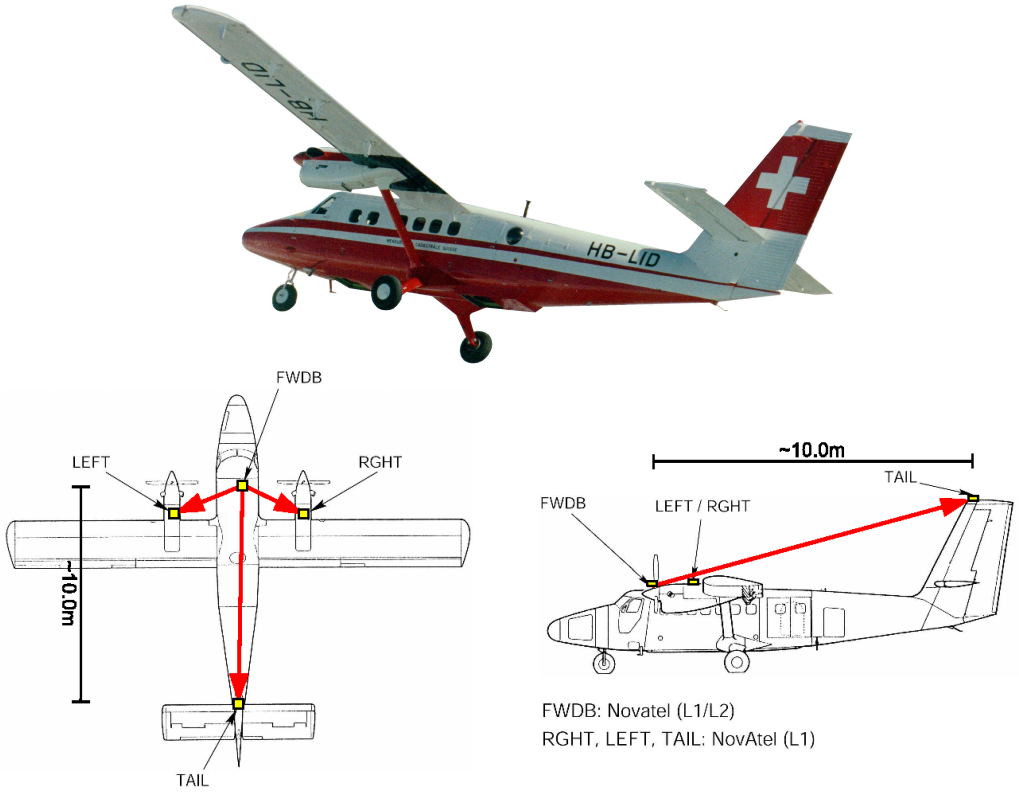

Figure 4.1: DeHavilland Twin-Otter survey aircraft owned by the Swiss Federal Office of Topography (swisstopo), with array of four GPS antennas/receivers and resulting baseline vectors for attitude determination.

Since the aircraft is mainly used for photogrammetric survey missions, the downward-looking laser sensors could easily be mounted in the photogrammetric shaft (Fig. 4.2). All instruments had to be integrated into the measuring system and synchronized with GPS time. For gravity surveys, a LaCoste Romberg Sea/Air gravimeter provided information on the Earth's gravity field.

4.2.2 Laser Profiler

The Optech 501 SA Rangefinder is a pulsed laser ranging instrument designed to give high accuracy readings on a single-shot basis (Fig. 4.2 and Tab. 4.1) (Optech, 1989). The unit uses a GaAs laser diode to generate optical pulses. A high precision time interval counter measures the time-of-flight of the laser pulse to and from the target. The time-of-flight is converted into range by a microprocessor. The GaAs diode in the transmitter module generates 15-20 ns wide optical pulses of near-infrared radiation at a wavelength of 904 nm, triggered by the internal trigger circuit or an external trigger source. The transmitter lens assembly collimates the outgoing infrared radiation into a narrow beam which propagates to the target.

The laser beam has a diameter of 8 cm at the exit of the aperture of the instrument and a nominal divergence of 0.25% (= 2.5 mrad = 0.143°). This means that the beam diameter increases by 0.25 m/100 m. Hence, for a flight height of 200 m above ground, the laser footprint has a diameter of 0.58 m. The instrument can be operated at pulse repetition rates between 1 Hz and 2 kHz, with a range resolution of 1 cm and an operating range of 10-500 m.

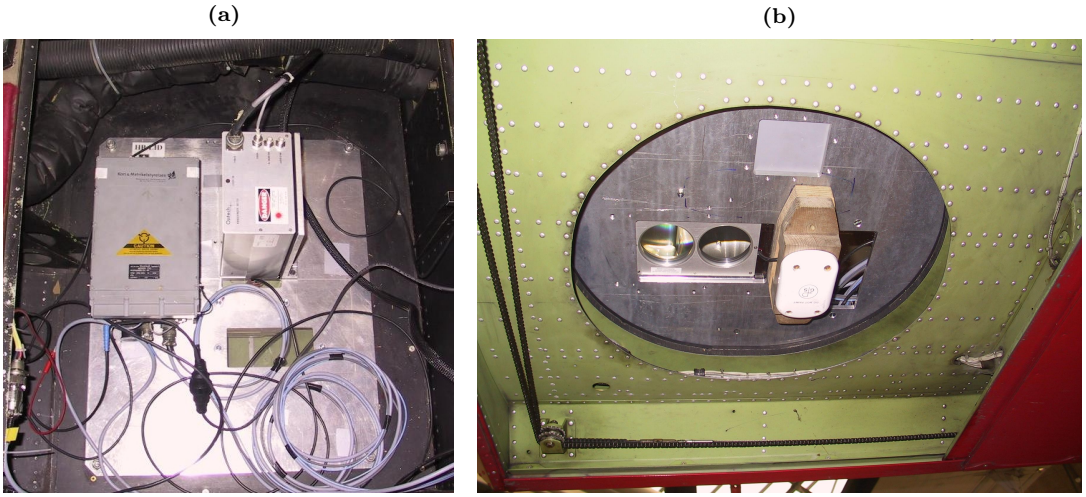

Figure 4.2: **(a)** Optech 501 SA laser profiler (right) and Honeywell H-764G INS (left), mounted on the same platform installed in the photogrammetric camera shaft of the aircraft. **(b)** Outside view of the photogrammetric camera shaft with downward-looking laser profiler optics.

Table 4.1: Technical specifications of Optech 501 SA laser profiler and Riegl LMS-Q140i-60 laser scanner.

	Optech 501 SA	Riegl LMS-Q140i-60
Wavelength	904 nm (near infrared)	900 nm (near infrared)
Range	10 - 500 m[1]	2 - 350 m[2]
Accuracy	0.20 m[3]	0.025 m
Range resolution	0.01 m	0.025 m
Initial beam diameter	0.08 m	?
Beam divergence	2.5 mrad (0.25%)	3.0 mrad (0.30%)
Footprint diameter @ 200 m	0.58 m	0.60 m
Pulse repetition rate	1 - 2 kHz (max. 2 kHz)	25 kHz (max. 30 kHz)
Scan angle range	-	60°
Scan speed	-	40 scans/s
Angle step width	-	0.288°
Angle readout accuracy	-	0.036°
Pulse peak power	160 W	?[4]
Pulse duration / width	15-20 ns	?[4]

[1] The maximum range of 500 m is based on a target reflectance of 20%, in daylight under clear weather conditions, at an ambient temperature of 20°C.
[2] The maximum range is 150 m and 350 m under a target reflectance of 10% and 80%, respectively.
[3] Achieved when ranging to a target from 10 to 500 m, under a 20% reflectance and over the operating temperature range of -20°C to 40°C.
[4] Details on pulse width and peak power are not provided by the manufacturer.

4.2.3 Laser Scanner

A Riegl LMS-Q140i-60 linear laser mirror scanner (Tab. 4.1), provided by KMS, has been used as additional equipment for the recovery of the sea state data. The scanner is designed for high speed line scanning applications. It is based upon the principle of time-of-flight measurement of short laser pulses in the near-infrared (900 nm). An electrical pulse generator periodically drives a semiconductor laser diode sending out infrared light pulses, which are collimated by the transmitter lens. Via the receiver lens, part of the echo signal reflected by the target hits a photodiode which generates an electrical receiver signal. The time interval between transmitted and received pulses

are counted by a quartz-stabilized clock frequency and processed by the internal microcomputer.

The laser beam divergence is 0.30% (= 3 mrad = 0.172°). Hence, for a flight height of 200 m above ground, the laser footprint has a diameter of 0.60 m. The nominal maximum range is 350 m under a target reflectance of 80% and 150 m under a target reflectance of 10%. These are typical values for average conditions. In bright sunlight, the operational range is considerably shorter than under overcast sky. The range resolution and nominal accuracy (1 σ) are 2.5 cm.

The angular deflection of the laser beam is realized by a rotating polygon mirror wheel. Polygonal mirrors are rotated continuously at a fixed speed to provide repetitive unidirectional scans. The scanner has a scan angle range of 60°. The scanner was operated at a scan speed of 40 scans/s and a pulse repetition rate of 25 kHz, leading to an angle step width of 0.288°.

4.2.4 Multi-Antenna GPS Configuration

The aircraft was equipped with an array of four GPS antennas adequately mounted on the aircraft's top side (Fig. 4.1) and connected to four independent GPS receivers. One dual-frequency receiver was used for trajectory recovery and as reference for moving baseline processing. The other three receivers were single-frequency receivers, acting as remote receivers in the moving baseline processing, yielding three vectors used for attitude determination. The obtained baseline lengths are 5.5 m between the engine-antennas and 10 m between the forward and rear antenna. This setup allowed highly precise 3D positioning (trajectography) of the aircraft in combination with terrestrial GPS reference stations, as well as autonomous attitude determination, both needed for georeferencing the ultrasound ground point Chapter 7.

4.2.5 Inertial Navigation System

The inertial unit used in this project is a Honeywell H-764G INS (Fig. 4.2a), provided by KMS. It is a tactical-grade INS used on military aircrafts and helicopters. It is based on accelerometers and digital ring-laser gyros, and is coupled with GPS. The INS was used for attitude recovery at a sampling rate of 50 Hz, independent of the multi-antenna GPS system.

4.3 Laser Ranging

In laser ranging, two major principles are used: continuous wave (CW) lasers, which continuously emit light, or pulsed lasers (Wehr and Lohr, 1999). The CW principle is based on measuring the phase difference between the transmitted signal and the received signal backscattered from the object surface. In current ranging laser systems, mostly pulsed lasers are used. The principle of pulsed lasers is based on determining the time-of-flight of a light pulse by measuring the traveling time t between the emitted and received pulse. The distance r between the ranging unit and the target is then given by:

$$r = \frac{1}{2} c\, t \tag{4.1}$$

where c is the speed of light (299'792.458 km/s in the vacuum). The range determination is complicated by the atmospheric refraction of light, discussed in Section 4.5. From (4.1), the range resolution Δr, which is directly proportional to the time resolution Δt of the ranging unit, can be derived (Wehr and Lohr, 1999):

$$\Delta r = \frac{1}{2} c\, \Delta t \tag{4.2}$$

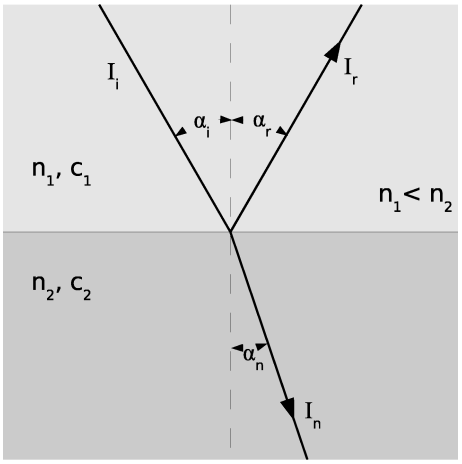

Figure 4.3: Refraction and reflection at a medium boundary with refractive index $n_1 < n_2$.

For example, to achieve a range resolution Δr of 1 cm, a time resolution Δt of 0.07 ns is required in the vacuum.

4.4 Laser Backscatter from Ocean Surface

4.4.1 Refraction and Reflection at Air-Water Boundary

In airborne laser altimetry onto a sea surface, the optical radiation incident from the atmosphere is partially reflected from the ocean surface because of the refractive index discontinuity at the air-water interface (Bufton et al., 1983). The velocity of light changes depending on the refractive index of the medium. When light (e.g. a laser beam) passes from a transparent medium (e.g. air) with refractive index n_1 into another transparent medium (e.g. water) with refractive index n_2, one part of the incident light is refracted and penetrates into the second medium, while the other part is reflected at the surface, due to the discontinuity of the refractive index at the medium boundary Fig. 4.3. According to the law of specular reflection, the incident light is always reflected in a plane normal to the surface at an angle of reflection α_r opposite to the angle of incidence α_i (Fig. 4.3):

$$a_i \;=\; -\,a_r \tag{4.3}$$

The relation between the angle of incidence α_i and the angle of refraction α_n is given by the law of diffraction, also called Snell's law (Fig. 4.3):

$$\frac{\sin\alpha_i}{\sin\alpha_n} \;=\; \frac{n_2}{n_1} \;=\; \frac{c_1}{c_2} \tag{4.4}$$

where α_i is the angle of incidence, relative to the normal of the medium boundary, α_n is the angle of refraction, relative to the normal of the medium boundary, n_1 and n_2 are the refractive indices of medium 1 and 2 and c_1 and c_2 are the speed of light in medium 1 and 2. The intensity distribution of the diffraction phenomena (Fig. 4.3) is given by:

$$I_i \;=\; I_r \;+\; I_n \tag{4.5}$$

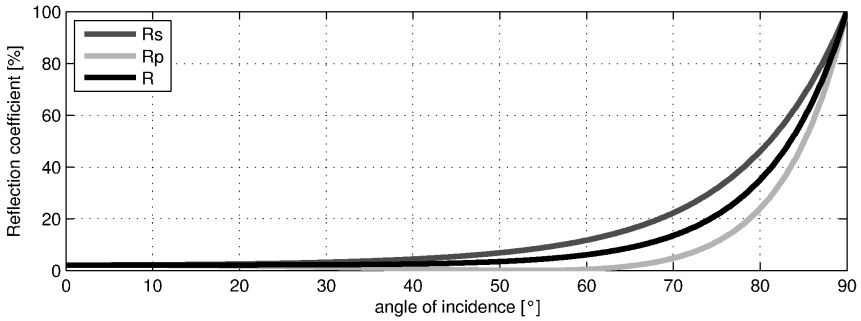

Figure 4.4: Reflection coefficients ρ_s (labeled Rs) of light polarized in the plane perpendicular to the plane of incidence, ρ_p (labeled Rp) of light polarized in the plane of incidence and ρ (labeled R) of unpolarized light (4.6), as a function of the angle of incidence, at an air-seawater boundary ($n_1 = 1.000278$, $n_2 = 1.338$).

where I_i is the intensity of the incident light, I_r is the intensity of the reflected light and I_n is the intensity of the refracted light penetrating into the second medium. The relation between the intensity of the incident light and the intensity of the reflected light, called reflection coefficient ρ (or reflectivity, or reflectance), depends on the refractive indices, the angle of incidence and the polarization of the incident ray. The reflection coefficient ρ of unpolarized light (containing an equal mix of s- and p-polarizations) is given by:

$$\rho \;=\; \frac{I_r}{I_i} \;=\; \frac{\rho_p \;+\; \rho_s}{2} \tag{4.6}$$

where ρ_p is the reflection coefficient for energy polarized in the plane of incidence and ρ_s is the reflection coefficient for energy polarized in the plane perpendicular to the plane of incidence. For a normal or near-normal incidence ($\alpha_i < 20°$), ρ, ρ_p and ρ_s have similar values (Fig. 4.4), and (4.6) yields the following simplified expression for the reflection coefficient:

$$\rho = \rho_s = \rho_p = \frac{I_r}{I_i} = \left(\frac{n_1 - n_2}{n_1 + n_2}\right)^2 \tag{4.7}$$

The refractive index n is proportional to the density of the medium. The refractive index n_{air} of dry air at 15°C and 1013.25 hPa is approx. 1.000278. The refractive index of water is affected by its temperature, as well as the concentration of dissolved and particulate matter. The refractive index increases with increasing salinity and turbidity but decreases with increasing temperature (Bufton et al., 1983). The refractive index n_{water} of pure water at 20°C, 760 Torr, and 500 nm is approx. 1.336 (Tradowsky, 1975), while the refractive index $n_{seawater}$ of uncontaminated seawater is 1.338 (Cox and Munk, 1954). Thus, the refraction at an air-water boundary is characterized by Fig.4.3. In the case of an air-water boundary, (4.7) yields a reflection coefficient $\rho = 2\%$ at normal incidence ($\alpha_i = 0$), meaning that only 2% of the incident light is directly reflected by the water surface ($I_r = 0.02\ I_i$). The remaining 98% of incident light penetrate into the water, where absorption and scattering occurs (Section 4.4.4). The reflection coefficient has its lowest value at normal incidence and is nearly constant for angles of incidence up to 45° (Fig. 4.4). Beyond 45°, the reflectivity increases, but the probability of receiving a return signal from the water surface in airborne applications decreases rapidly (Section 4.4.6). From an optical point of view, the air-water boundary is comparable to an air-glass boundary, with $n_{glass} = 1.5$ and $I_r = 0.04\ I_i$. In the case of reflection at an $n_1 < n_2$ boundary (e.g. air-water), the reflected part of the incident wave incurs a phase jump of half its wavelength during reflection (Tradowsky, 1975). This phenomena is important when using a continuous wave laser which tracks the phase difference between the transmitted and received signal (Section 4.3).

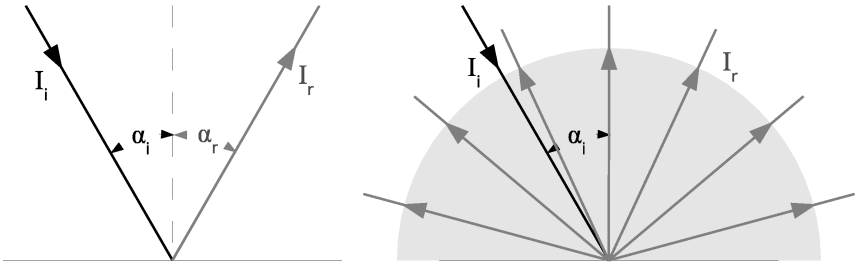

Figure 4.5: Specular (coherent) reflection (left) and diffuse reflection (right).

4.4.2 Specular and Diffuse Reflection

In laser ranging, two types of reflection on the target surface may occur: specular (coherent, mirror) reflection or diffuse reflection (Fig. 4.5). Specular reflection is the reflection of electromagnetic energy without scattering or diffusion, as from a surface that is smooth in relation to the wavelengths of incident energy. In the case of specular reflection, the laser beam is reflected following the law of specular reflection (4.3). Examples of specular surfaces include calm water or paved roads, as well as mirrors and geodetic corner reflectors. Diffuse reflection is the type of reflection obtained from a relatively rough surface (in terms of wavelength of the electromagnetic radiation), where the reflected rays are scattered in all directions (Fig. 4.5). Diffuse reflecting surfaces are e.g. natural forest canopies or agricultural fields. Even a narrow-width laser beam reflects from a diffuse surface at any angle.

In reflector-less laser ranging applications, the target surface needs to have diffuse reflection properties, unless the surface is oriented perfectly normal to the laser beam. In airborne laser altimetry, the major factors that determine the character of the reflection (specular or diffuse) of the incident radiation by the sea surface are (Zissis, 1993):

1. the surface geometry and wave slope distribution, influencing the surface reflection
2. the optical properties of water, influencing the subsurface reflection

4.4.3 Impact of Sea Surface Geometry on Laser Return

In the case of a completely flat water surface, the part of the incident laser beam directly reflected at the surface would be reflected as it would from a mirror (specular reflection), with an angle of reflection α_r opposite to the angle of incidence α_i (Fig. 4.3). The probability that such a coherently-reflected laser beam reaches the receiver aboard the aircraft is virtually zero. In order to receive a return signal from the water surface, the incident laser beam would need to be very close to normal ($\alpha_i \approx 0°$), to the sea surface. The tolerance for the deviation of the angle of incidence from normal is in the order of half the beam divergence, corresponding to approx. 0.09°, independently of the range. The small deviation tolerance underlines the necessity of diffuse reflection conditions in laser ranging onto targets like water surfaces.

In most cases, the sea surface is affected by wind and waves, implicating that the surface is composed of a multitude of little facets, each of them acting like a small mirror with specular reflection. The slope of a small water facet in any direction is assumed to be independent of the wind direction and the cumulative probability distribution for slopes is approximated by a Gaussian distribution (Hooper and Gerber, 1983). If the surface of the laser footprint is large enough to contain a large number of facets, a multitude of specular reflections in many different directions occur. As a consequence, the larger the footprint, the higher the probability of signal

returns. The resulting integral reflection can be considered as a pseudo-diffuse reflection, with a significantly higher probability of signal return to the receiver. Thus, the equivalent Lambertian reflection coefficient of water is strongly dependent on its surface state and varies from less than 1 % when its surface is very smooth to greater than 20 % when it is rough (Optech, 1989). However, the inherent specular reflection coefficient of the water surface remains unchanged (e.g. 2 % for an angle of incidence of 0°), regardless if the sea surface is flat or rough (Cox and Munk, 1954). On the other hand, if the laser footprint is smaller or of similar size than the surface facets, specular reflection occurs despite the faceted surface structure and the signal reception probability is drastically lowered. This may be the case if the distance between the laser source and the sea surface is very small, e.g. in shipborne measurements.

The effects of wind-stress on the optical properties of the ocean surface have been studied for several decades (Tratt et al., 1996). In particular, the classic study of (Cox and Munk, 1954), linking sea surface wind fields to wave slope statistics provides a phenomenology by which the sea surface wind velocity can be estimated from direct measurements of the wave-modulated surface reflectance.

4.4.4 Absorption, Scattering, Penetration Depth and Backscattering

In laser ranging onto water surfaces, the major part of the incident light, that is about 98%, penetrates into the water volume, where it is affected by absorption and scattering, both depending on the wavelength of the light and the water characteristics. When traveling through a medium (e.g. water), the intensity of a laser beam is continuously weakened by absorption and scattering. The optical transparency of a medium at a given wavelength is given by:

$$T \;=\; \frac{I}{I_0} \;=\; e^{\,-(a+b)d} \;=\; e^{\,-cd} \tag{4.8}$$

where T is the optical transparency of the medium at wavelength λ, I is the intensity [W/cm^2] of laser beam after a traveling distance L (e.g. in air), I_0 is the initial intensity [W/cm^2] of laser beam, a is the spectral absorption coefficient [m^{-1}] of the medium, b is the scattering coefficient [m^{-1}] of the medium, d is the distance [m] traveled by laser beam in the medium and c is the attenuation coefficient [m^{-1}] regrouping absorption and scattering of the medium. Coefficients a and b, and hence coefficient c and the transparency T are a function of the wavelength of laser beam.

The penetration depth and the intensity of the light reemerging from the second medium are depending on absorption and scattering, and thus on the wavelength and type of medium. The penetration depth is usually defined as the depth at which the collimated beam has been attenuated by a factor of e^{-1} (= 37%) (Welch et al., 1989). Thus, the penetration depth d_p can be derived from (4.8):

$$d_p \;=\; \frac{1}{a \;+\; b} \;=\; \frac{1}{c} \tag{4.9}$$

Natural water bodies contain both solutes and particulates in suspension. In this case, the spectral attenuation coefficient c is a measure of the decrease of downward-welling radiation from the combined effects of the absorption of the solution and particulates, as well as the scattering due to the particulates. Because of multiple scattering and particulates absorption, the attenuation coefficient is not necessarily the simple sum of the absorption coefficient of the solution and the scattering coefficient of the particulates as assumed in (4.8) and (4.9) (Zissis, 1993). When the medium's absorptive capacity is very high relative to the scattering ability, the laser beam remains highly collimated and the penetration depth is given by the reciprocal of the wavelength-dependent absorption coefficient $1/a$ (Welch et al., 1989).

Backscattered laser radiation from the water volume must be considered in addition to surface backscatter for predicting pulse energy reaching the laser receiver (Bufton et al., 1983). Volume backscatter is strongly dependent on the wavelength of the laser: it has an important effect at 532 and 337 nm laser wavelengths but is e.g. negligible at 9.5 μm because of essentially no surface penetration at this wavelength (Bufton et al., 1983). A concise method for treating volume backscatter is obtained by defining the parameter $R(0-)$, the subsurface irradiance reflectivity for zero depth, given by the ratio of upwelling to downwelling irradiance just beneath the water surface at zero depth (Gordon, 1977). This enables the water volume to be handled as an hypothetical Lambertian reflector of reflectivity $R(0-)$ located just beneath the surface. $R(0-)$ is related to the inherent optical properties of water. A simple relation for the subsurface irradiance reflectivity for zero depth $R(0-)$ is given by (Morel and Prieur, 1977):

$$R(0-) \;=\; 0.33\,\frac{b_b}{a} \tag{4.10}$$

where b_b is the volume backscatter coefficient and a the volume absorption coefficient. The variation of $R(0-)$ with wavelength yields the ocean color observed from high altitude under solar illumination (Bufton et al., 1983). In airborne laser altimetry, the natural solar background is negligible compared to laser backscatter. Hence, $R(0-)$ only needs to be considered at the respective laser wavelength. For example, at the two laser wavelengths 337 and 532 nm, $R(0-) \approx 1\%$, while it is negligible at 9.5 μm, where absorption is strong (Bufton et al., 1983).

In laser ranging with a pulsed laser to a diffuse reflecting target, the power of the return signal (or backscattered pulse energy) arriving at the receiver is given by:

$$P_r \;=\; P_e\,\frac{S_r}{d^2}\,e^{\,-2\beta_\lambda d}\,R \tag{4.11}$$

where P_r is the power [W] returning to the receiver, P_e is the power [W] emitted by the pulsed laser, S_r is the effective surface of the receiver, d is the one way distance [m] traveled by the laser beam, c is the attenuation coefficient [m^{-1}] regrouping absorption and scattering of the medium at wavelength λ, $e^{-2\beta_\lambda d}$ is the two-way atmospheric transmission and R is the optical reflectivity of the target. The backscatter properties of the ocean surface are modeled by the target term R, which is given by (Bufton et al., 1983):

$$R \;=\; \frac{\rho}{\Omega} \tag{4.12}$$

where ρ is specular surface reflectivity (4.7) and Ω is a solid angle that models the pattern of reflected radiation for backscatter (Bufton et al., 1983). Both ρ and Ω are functions of the angle of incidence α_i. In (4.11), the power arriving in the receiver is proportional to the emitted power and the surface of the receiver. The effective surface of the receiver has to be as large as possible in order to maximize the exploitation of the reflected intensity. The propagation of light after diffuse reflection at the target follows Lambert's law, meaning that the intensity decreases with the square of the traveled distance. Additionally, the attenuation from absorption and scattering in the atmosphere results in a large loss of intensity. The strong attenuation can be counteracted using high-power laser sources.

4.4.5 Optical Properties of Water in the Optical and Infrared Range

In pure water, the attenuation of light by absorption and scattering is much higher than in the atmosphere (Tradowsky, 1975). The absorption coefficient $a(\lambda)$ of pure water in the visible and infrared band is shown in Fig. 4.6a, as a function of the wavelength λ. The spectral absorption

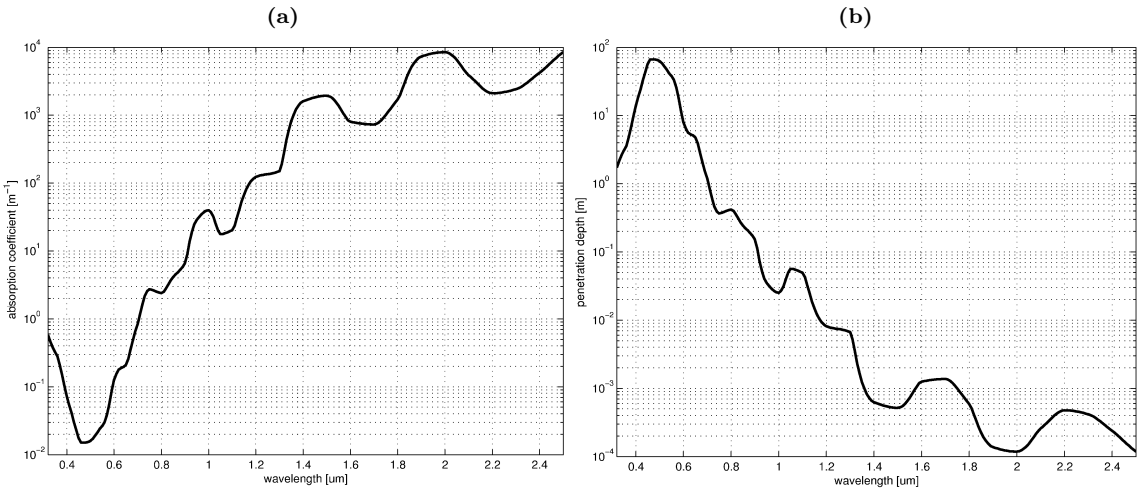

Figure 4.6: (a) Absorption coefficient [m^{-1}] of pure water at wavelengths between 0.32 and 2.50 μm. Values from (Zissis, 1993). **(b)** Penetration depths [m] into pure water at wavelengths between 0.32 and 2.50 μm, computed from absorption coefficients in (a).

coefficient of pure water falls to relatively low values of 0.015 - 0.840 m^{-1} in the visible band between 0.4 and 0.7 μm (Fig. 4.6a). At these wavelengths, light transmits quite well trough water (Welch et al., 1989). Pure water shows a broad absorption minimum in the blue and green spectral range (440 - 540 nm) (Fig. 4.6a). At blue and green wavelengths, the amount of absorption and scattering is about equal, yielding a considerable penetration depth (Fig. 4.6a). The absorption coefficient reaches its absolute minimum of 0.015 m^{-1} at blue wavelengths between 460 and 480 nm, corresponding to a penetration depth of 67 m.

For the red and near-infrared wavelengths (630 - 1400 nm), scattering is predominant in the water. At a near-infrared wavelength of 900 nm, the absorption coefficient of pure water is 6.55 m^{-1}, corresponding to a penetration depth of 0.15 m (Fig. 4.6b). At a near-infrared wavelength of 1060 nm, the absorption coefficient of pure water is 17.70 m^{-1}, corresponding to a penetration depth of 0.06 m. At this wavelength, 30 - 50% of the light that penetrates into the water reemerges from the water due to subsurface scattering (Welch et al., 1989). Water is essentially opaque to infrared radiation with wavelengths above 1.4 - 3.0 μm. Due to the absorptive properties (very high absorption coefficient and very small penetration depth) of water at infrared wavelengths above 1.4 μm, any contribution to the total reflectance due to subsurface scatter can be neglected (Tratt et al., 1996).

Seawater and coastal water have similar optical properties than pure water. Seawater also has an absorption minimum in the blue and green spectral range, although it is less pronounced than for pure water due to solute salts, particulates and plankton (Tradowsky, 1975). Consequently, blue and green radiation can penetrate deeply into the seawater and will scatter from suspended particulates and even be reflected by the bottom (Zissis, 1993). Red and infrared light is characterized by a much weaker penetration from air into water. It is nearly entirely reflected at the water surface. There are bathymetric lasers, that are based on the same principles as the topographic lasers, but emit in two wavelengths, usually 1064 nm (near infrared) and 532 nm (green). The infrared wavelength is reflected on the water surface, while the green one penetrates the water and is reflected by the bottom surface or other objects in the water (Wehr and Lohr, 1999).

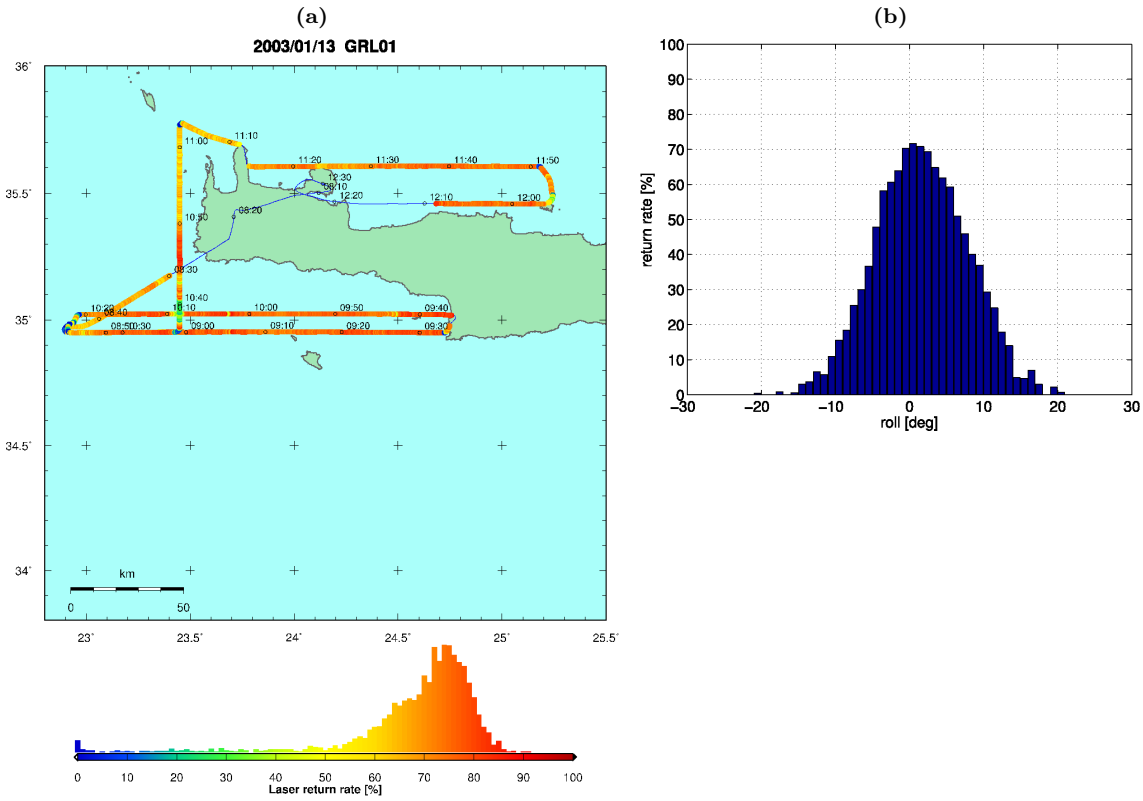

Figure 4.7: **(a)** Laser pulse return rate from laser profiler during survey flight GRL01 and distribution of return rate. **(b)** Mean laser profiler pulse return rate distribution as a function of the off-nadir (roll) angle of the aircraft during survey flight GRL01.

4.4.6 Case Study: Backscatter Intensity and Return Rate from Ocean Surface

During airborne laser altimetry surveys onto the ocean surface using the Optech laser profiler (Section 4.2.2) at a sampling rate of 1 kHz, showed that during flight operations with a roll angle of apporx. zero, the rate of obtained laser pulse returns is on the order of 80% and hardly ever reaches 100% (Fig. 4.7a). During turns, the return rate is drastically reduced and can reach 0%. Depending on the sea state, the return rate can vary among the entire range from 0 to 100%. An interesting feature in the return rate on flight GRL01 is the exceptionally low return rate around the crossing point of the flight trajectory around 10:10 and 10:40, where a similar low return rate was observed twice in the same area. The mean return rate at a sampling rate of 1 kHz and during a straight flight-line does usually not exceed 70% (Fig. 4.7b). For off-nadir (roll) angles of 5°, the expected return rate drops under 50%, whereas for off-nadir angles of 10°, the expected return rate is only 20%. For off-nadir angles above 15°, the expected return rate is practically zero. These values are strongly depending on the sea state. Slightly lower return rates were observed on the Riegl laser Scanner (Section 4.2.3) data (Fig. 4.9b). The mean return rate at nadir during a flight-line of 150 km was 40%. The return rate rapidly drops with increasing off-nadir angles. As for the laser profiler, the expected return rate is practically zero for off-nadir angles above 15°. The difference between laser ranging on water surfaces and laser ranging on land surfaces is shown during the overflight of the port of Agia Galini (Fig. 4.8 and Fig. 8.5). On water, the transverse range of scanner is very limited as compared to ground-points on land. The narrowest range is observed on calm water inside the port, where specular reflection predominates.

Beside range observations, the Riegl laser scanner also provides relative intensity data of the returned signal (Fig. 8.5). Normalized mean backscatter intensities were analyzed with respect to the off-nadir angle on a flight line of 150 km (Fig. 4.9a). As for the return rate (Fig. 4.9b), an extremely smooth distribution is obtained. A slight deviation of the distribution with respect to the normal distribution is observed. The distribution is centered at 0.32°. These values were obtained without boresight misalignment calibration of the laser scanner. A calibration of the scanner with the method described in Section 7.5.4, a boresight misalignment on the scanner angle of 0.39°was determined.

4.5 Tropospheric Refraction of Light

4.5.1 Basic Principles

The atmosphere of the Earth is not completely penetrable for light. Absorption, diffusion and refraction of light in the atmosphere depend on the temperature, water vapor content and other impurities, as well as on the wavelength of the light, The result are very complex dependencies, enhanced by the fact that these parameters strongly vary on a daily and seasonal basis. When traveling through the atmosphere, electromagnetic waves experience velocity changes and associated changes of their direction (bending), called refraction. These changes depend on the physical state of the gas quantities in the traversed atmosphere. The propagation velocity v in the atmosphere deviates from the velocity c in the vacuum by the refractive index n:

$$v = \frac{c}{n} \tag{4.13}$$

Instead of the refractive index n, the refractivity is often used to quantify the atmospheric refraction. The refractivity N is the departure of the refractive index n from unity, commonly multiplied by 10^6 to obtain N in units of [ppm], corresponding to 1 mm delay per km of measured range:

$$N\ [\text{ppm}] = (n-1) \cdot 10^6 \tag{4.14}$$

The refraction has a different behavior in the troposphere and the ionosphere. Since laser ranging in airborne laser altimetry is only affected by tropospheric effects, ionospheric effects are not considered here. The tropospheric refraction is the path delay caused by the neutral (non-ionized) part of the Earth's atmosphere. In the troposphere, the refractive index of air depends on temperature, pressure and humidity. The refractive index n is proportional to the density of air and therefore decreases with increasing altitude and becomes approx. 1 at an altitude of 40 km. Since $n > 1$ in the atmosphere, the velocity v in the atmosphere is always smaller than the velocity of light in the vacuum c. Since the troposphere is a dispersive medium for optical frequencies, the refractive index also depends on the wavelength of the considered electromagnetic waves. The range r measured through air is given by the integral along the curved signal path (Hopfield, 1979):

$$r = \int_{path} n \, dr \tag{4.15}$$

In distance measurements through the atmosphere using optical methods like lasers, refraction and change of propagation velocity of electromagnetic waves due to the atmospheric effects result in a delay of the laser beam. This delay yields an range error Δs, given by the difference between the

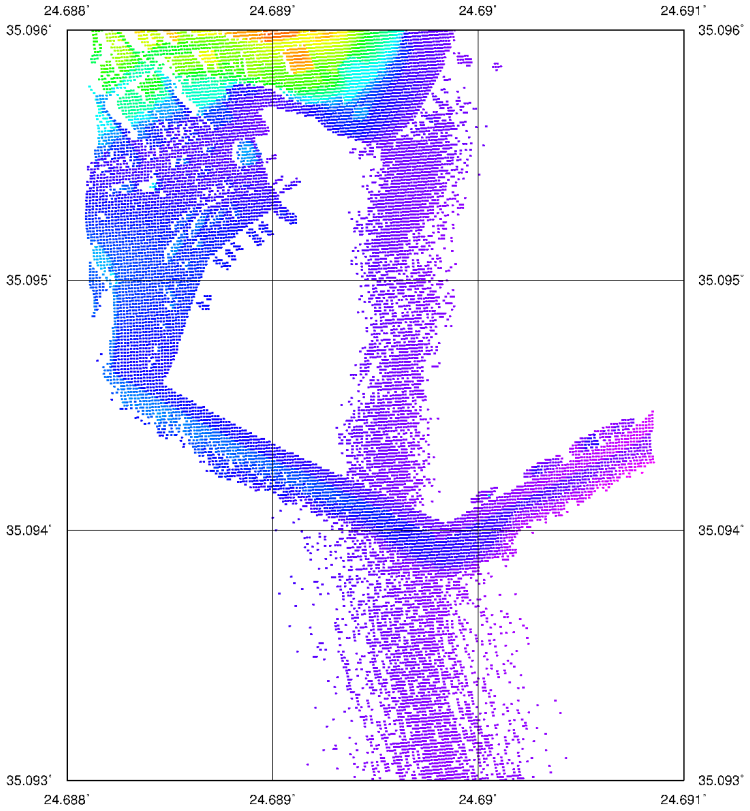

Figure 4.8: Airborne laser scanner ground-points during overflight of the port of Agia Galini (Fig. 8.5), with color-coded dimensionless intensity of the return signal (blue = low intensity, red = high intensity).

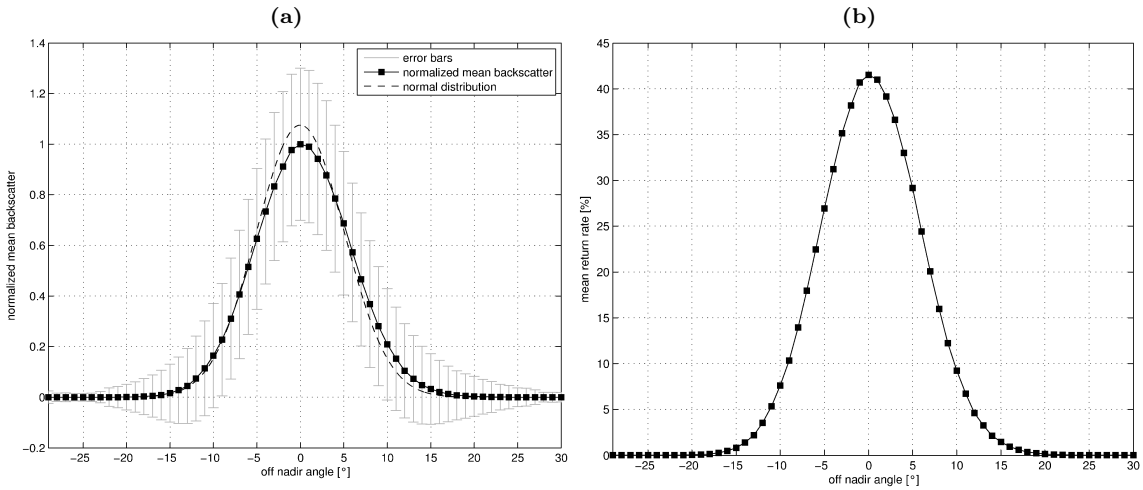

Figure 4.9: **(a)** Normalized mean backscatter intensity of airborne laser scanner data as a function of off-nadir angle, during a survey flight-line of 150 km. Error bars indicate standard deviations for each bin. A normal distribution of the same surface is indicated by the dashed line. **(b)** Mean laser scanner return rate distribution as a function of off-nadir angle during the same flight as in (a).

optic and geometric distance between the laser site and laser target (Hopfield, 1979):

$$\Delta s \;=\; r \;-\; s \;=\; \int\limits_{path} n\; dr \;-\; \int_0^s ds \;=\; \int_0^s (n-1)\; ds \;+\; \int\limits_{path} n\; dr \;-\; \int_0^s n\; ds \tag{4.16}$$

where r is the optical path length measured along the beam trajectory (optical range) and s is the slant range between the end points of the path, i.e. the distance of a line connecting the initial and terminal point of the beam trajectory. The first term on the right hand side is the range error produced by the reduced traveling speed in the atmosphere and the associated longer traveling time. The second term represents the effect of the bending of the beam trajectory on the measured length. If the bending of the signal path is negligible, the integral can be taken along the slant range vector (Hopfield, 1979), yielding:

$$r \;=\; \int\limits_{path} n\; dr \;=\; \int_0^s n\; ds \tag{4.17}$$

Using (4.17) in (4.16), it follows that the range error Δs is only affected by the reduced traveling speed along the slant range vector:

$$\Delta s \;=\; \int_0^s (n-1)\; ds \tag{4.18}$$

For short distances, the refractive index can be considered as constant, and (4.17) and (4.18) yield the following simple formulas for the range error Δs and the real slant range s:

$$\Delta s \;=\; r \;-\; s \;=\; (n-1)\; s \;=\; \frac{n-1}{n}\; r \tag{4.19}$$

$$s \;=\; r \;-\; \Delta s \;=\; \frac{1}{n}\; r \;=\; \frac{c}{n}\; \frac{\Delta t}{2} \tag{4.20}$$

where r is the optical range provided by an uncalibrated EDM (Electronic Distance Measurement) instrument (4.1). Usually, geodetic EDM instruments are calibrated in order to provide correct distances under standard atmospheric conditions. The measured range r_0 given by a calibrated instrument, the range error Δs_0, caused by the deviation of the actual refraction from the refraction during calibration, and the slant range s are given by:

$$r_0 \;=\; \frac{1}{n_0}\; r \;=\; \frac{c}{n_0}\; \frac{\Delta t}{2} \tag{4.21}$$

$$\Delta s_0 \;=\; r_0 \;-\; s \;=\; \left(\frac{n}{n_0} - 1\right)\; s \;=\; \frac{n-n_0}{n}\; p_0 \tag{4.22}$$

$$s \;=\; r_0 \;-\; \Delta s \;=\; \frac{n_0}{n}\; r_0 \;=\; \frac{1}{n}\; r \;=\; \frac{c}{n}\; \frac{\Delta t}{2} \tag{4.23}$$

where n_0 is the refractive index associated with the atmospheric conditions during calibration. Note that in of all the above equations, the distances s, r and r_0 correspond to the one-way range between the source and the target, covered during half the traveling time Δt.

In airborne laser altimetry, vertical range measurements are carried out between the aircraft and the ground. In that case, a linear approximation $n(h)$ along the vertical range can be used and

the range error Δs becomes:

$$\Delta s \;=\; \int_{h_b}^{h_a} (n(h)-1)\; dh \;=\; \int_{h_b}^{h_a} \left(n_b + \frac{n_a - n_b}{h_a - h_b}(h - h_b) - 1 \right)\; dh \;=\; \left(\frac{n_a + n_b}{2} - 1 \right) s \quad (4.24)$$

where n_a and n_b are the refractive indices at the altitude h_a of aircraft and at altitude h_b of the laser ground point, respectively.

4.5.2 Group Refractivity

In most geodetic surveys, EDM instruments use intensity-modulated or pulsed light, which can be considered as a superposition of waves of different wavelengths forming short groups of waves. The velocity v in (4.13) represents the phase velocity of a monochromatic carrier wave, whereas the center of a group of waves, as used by most EDM instruments, travels at the group velocity v_g:

$$v_g \;=\; v \;-\; \lambda \, \frac{dv}{d\lambda} \quad (4.25)$$

where λ is the wavelength. In a dispersive medium like the troposphere, the refractive index n depends on the wavelength and hence $\frac{dv}{d\lambda} \neq 0$. Therefore, the knowledge of the group refractivity rather than the phase refractivity is required. The group refractivity N_g is given by (Marini and Murray, 1973):

$$N_g \;=\; \frac{d\,(f\;N)}{df} \;=\; N \;-\; \lambda \, \frac{dN}{d\lambda} \quad (4.26)$$

where f is the operational frequency of laser beam, λ is the corresponding wavelength, N is the phase refractivity.

4.5.3 Refraction Model Recommended by the IAG

In Appendix A, an non-exhaustive overview of former refraction models is given, namely the (Barrell and Sears, 1939) model, the (Barrell, 1951) model, the (Edlén, 1966) model and the (Birch and Downs, 1994) model. In the last few years, the computation of the refractive index at optical wavelengths has received special attention. As a consequence, the International Association of Geodesy (IAG) has established a working group to develop equations better suited to the very wide ranges of atmospheric conditions and wavelengths required in geodetic surveying (McCarthy and Petit, 2004). As part of that effort, a new set of equations was developed, based on more recent equations and recently reported measurements for density and dispersion in the visible and the near-infrared regions (Ciddor, 1996).

The IAG recommended in 1999 (IUGG, 1999) that the group refractive index in air for EDM to better than 1 ppm with visible and near infrared waves in the atmosphere be computed using the computer procedure published by (Ciddor and Hill, 1999) and (Ciddor, 1996). Since this procedure is rather complex as compared to the former equations given in Appendix A, the IAG also recommended the following closed formulae be adopted for the computation of the group refractive index in air for EDM to within 1 ppm with visible and near infrared waves in the atmosphere (IUGG, 1999):

$$N \;=\; (n-1)\cdot 10^6 \;=\; N_g \; \frac{273.15}{T} \; \frac{p}{1013.25} \;-\; \frac{11.27}{T} \; e \quad (4.27)$$

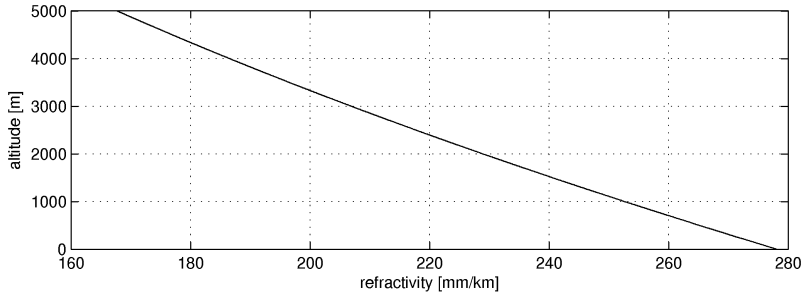

Figure 4.10: Refractivity N [mm/km] from the IAG (1999) model, as a function of altitude for a standard atmosphere and a wavelength of 900 nm (near infrared), computed from (4.27) and (B.1).

where

$$N_g \;=\; (n_g - 1) \cdot 10^6 \;=\; 287.6155 \;+\; \frac{4.88660}{\lambda^2} \;+\; \frac{0.06800}{\lambda^4} \tag{4.28}$$

with

N	refractivity of visible and near infrared light in ambient moist air, for atmospheric conditions t, p, e and wavelength λ
n	corresponding refractive index
N_g	group refractivity of standard air at T=273.15 K (0°C), p=1013.25 hPa, e=0.0 hPa and 0.0375 % CO_2 content
n_g	corresponding group refractive index
T	temperature [K] at the laser site in the ITS-90, with T = 273.15 + t [°C]
p	total atmospheric pressure [hPa] at the laser site
e	partial water vapor pressure [hPa] at the laser site
λ	carrier wavelength of the EDM signal in the vacuum [μm]

(4.27) and (4.28) reveal the complex dependency of the refractive index on the wavelength, temperature, air pressure and water vapor content. The computation of the refractive index is complicated by atmospheric condition changing in space and time, depending e.g. on the time of day and the cloudiness. Especially the near-ground temperature can change rapidly. The input values in (4.27) and (4.28) for temperature, atmospheric pressure and water vapor pressure are usually measured *in situ* at the measurement site. In airborne laser altimetry, this is normally not possible. In that case they can be derived from a standard atmosphere model, as a function of the altitude of the laser site and using reference values for a reference altitude (Appendix B). The decrease of refractivity with increasing altitude, computed from (4.27) and (B.1), is shown in Fig. 4.10.

4.5.4 Impact of Refraction in Airborne Laser Altimetry

In airborne laser altimetry, ranges do usually not exceed 1000 m. In sea surface height measurements, the range does even usually not exceed 300 m because of the sparse to inexistent return from water surfaces in case at longer distances. For a flight altitude of 300 m and a vertical distance of 300 m covered by the laser signal, the variation of the refractivity is only 7.7 ppm, or 2.3 mm along the covered distance of 300 m (Fig. 4.10). The short ranges in airborne laser altimetry, as compared to e.g. ranges of several thousand kilometers in satellite laser ranging (SLR), reduce the impact of atmospheric refraction errors, since the range error is proportional to the range itself. The required absolute range accuracy in the airborne laser altimetry surveys conducted in this project is in the order of one to a few centimeters.

Under the above considerations, all the models considered in Appendix A and in Section 4.5.3 produce very similar refractivity values, with a predicted relative range error (refractivity) of

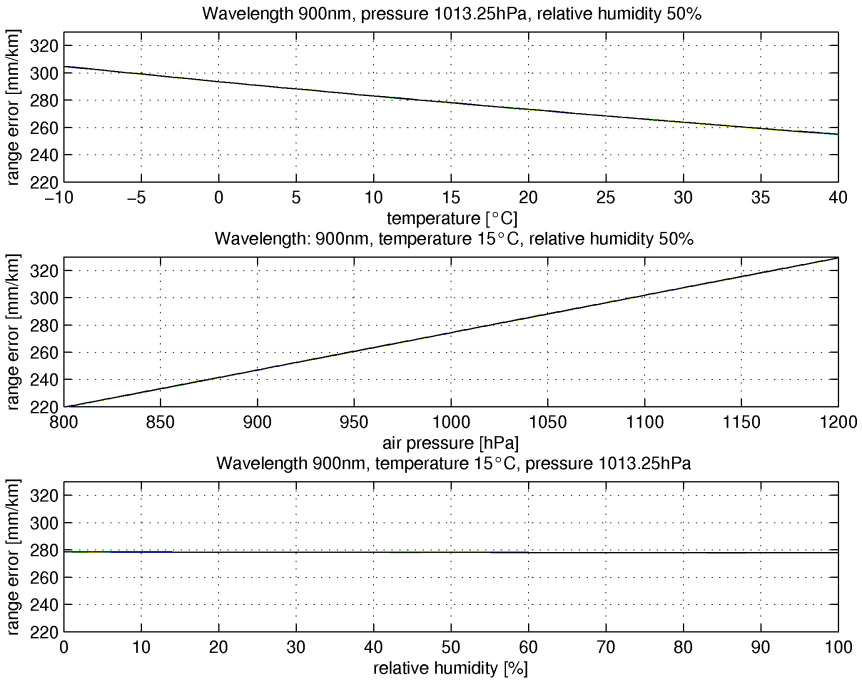

Figure 4.11: Relative range error (refractivity N) in mm/km (ppm) for a wavelength of 900 nm (near infrared). Top: range error as a function of temperature, for an atmospheric pressure of 1013.25 hPa and a relative humidity of 50%. Center: range error as a function of atmospheric pressure, for a temperature of 15°C and a relative humidity of 50%. Bottom: range error as a function of relative humidity, for a temperature of 15°C and an atmospheric pressure of 1013.25 hPa.

about 280 mm/km (ppm) under the standard atmospheric conditions of 15°C, 1013.25 hPa and 50% relative humidity (Fig. 4.11). Since in the (Barrell and Sears, 1939), (Barrell, 1951), (Edlén, 1966) and (Birch and Downs, 1994) models, the refractive indices of standard air were originally related to phase velocities, they had to be converted to group refractive indices using 4.26. Note that Fig. 4.11 contains an overlay of the data of all the considered models. The average variation of the range error as a function of temperature and as a function of atmospheric pressure is -1 ppm/°C and 0.275 ppm/hPa, respectively (Fig. 4.11). The variation of the range error as a function of relative humidity is negligible compared to the influence of temperature and pressure, with a decrease of only 0.6 ppm over the entire humidity range of 0-100% (Fig. 4.11). Within the considered range of atmospheric conditions, the models are not deviating more than 0.35 mm/km from each other (Fig. 4.12). Hence it can be concluded that the models produce no noticeable difference in refractivity in the considered order of magnitude.

For a vertical range measurement of 300 m, absolute range errors of 7-9 cm can be expected (Fig. 4.13, top) that have to be considered if cm-accuracy is sought. However, if a calibrated instrument is used, the range error caused by refraction consists only of the deviation of the actual refraction from the reference refraction during calibration (4.22). In this case, the residual range error varies only between -2 and 2 cm over the wide range of atmospheric conditions considered (Fig. 4.13, bottom). It can be concluded that for applications like airborne laser altimetry for sea surface height observations, with ranges of 200-300 m and accuracy requirements of 1-5 cm, the application of additional refractivity corrections is not needed if the ranging instrument was calibrated under conditions similar to the operating conditions (where similar means ±100 hPa air pressure and ±20°C air temperature.

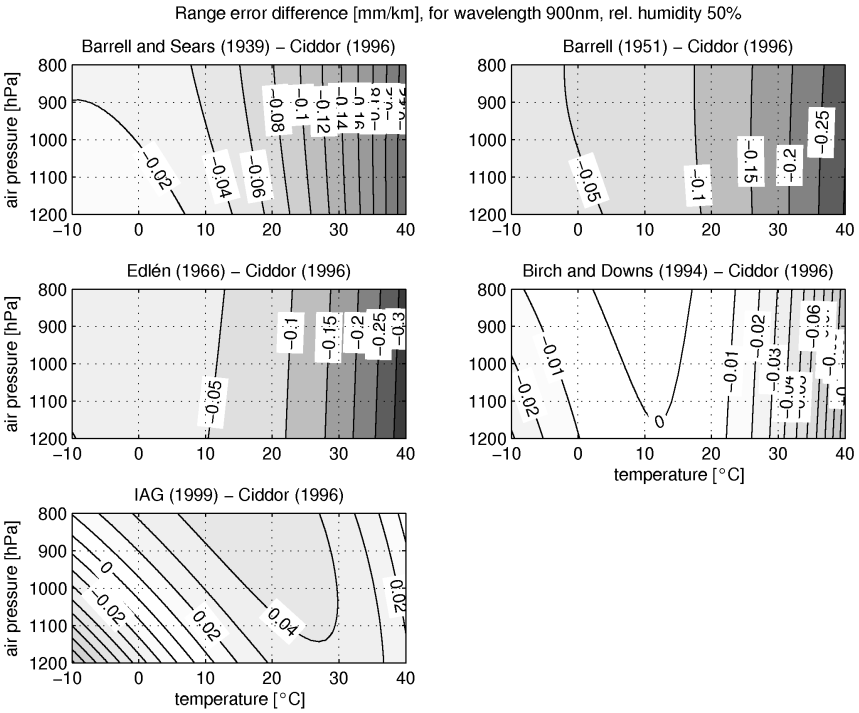

Figure 4.12: Relative range error differences in mm/km (ppm) with respect to the (Ciddor, 1996) model, as a function of temperature and atmospheric pressure, for a wavelength of 900 nm (near infrared) and a relative humidity of 50%.

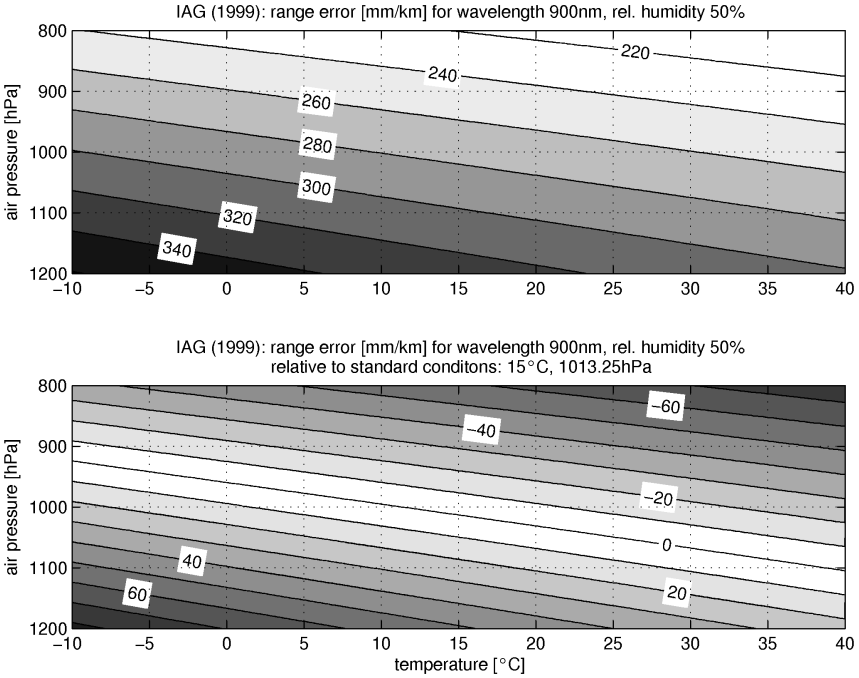

Figure 4.13: Relative range error [mm/km] from the (IUGG, 1999) model, as a function of temperature and atmospheric pressure, for a wavelength of 900 nm (near infrared) and a relative humidity of 50%. Top: range error (refractivity N) [mm/km]. Bottom: range error [mm/km] relative to standard atmospheric conditions (equivalent to range error produced by an instrument calibrated under standard conditions).

5 Shipborne Ultrasound Altimetry Technique

5.1 Introduction

Since airborne laser altimetry is very cost-intensive, a major aim of this thesis was the development of an alternative method for precise local-scale sea surface topography determination. Since the GPS-equipped buoys (Chapter 6) only provide useful data when they are deployed under drifting conditions or towed at very low speed, they can only be used for punctual sea surface height observations. In order to be able to cover larger areas, a novel method of shipborne sea surface height measurements was developed in the framework of this project. The method relies on one or two low-cost industrial ultrasonic distance sensors mounted on a boat, providing continuous measurements of the distance to the sea surface with an observation rate of approx. 10 Hz. In combination with the position and attitude information from a multi-antenna GPS system installed on the boat, this method allows for highly reliable sea surface height determination by direct georeferencing (Chapter 7). Due to its analogy to airborne laser altimetry (Chapter 4), the method is called shipborne ultrasound altimetry. The successful implementation of the new technique during several survey campaigns proved that shipborne ultrasound altimetry is a powerful method for providing offshore sea surface height measurements, even under rough sea conditions. Hence, the method provides a low-cost alternative to airborne laser altimetry.

5.2 Instrumental Setup

5.2.1 Overview

The setup of the sailing-yacht for shipborne ultrasound altimetry, developed and deployed in the framework of this project, is composed of the following instruments (Fig. 5.1):

- 2 ultrasonic distance sensors, sampling rate 10 Hz (Fig. 5.2)
- 4 - 5 GPS receivers for position and attitude determination, sampling rate 1 - 2 Hz (Fig. 5.3)
- 1 inertial AHRS (Attitude and Heading Reference System), sampling rate 20 Hz (Fig. 5.4)

All instruments had to be integrated into the measuring system and synchronized with GPS time (Section 5.4).

5.2.2 Ultrasonic Distance Sensors

The two ultrasonic distance sensors used in this project are the Pepperl+Fuchs UC4000-30GM-IUR2-V15 and UC6000-30GM-IUR2-V15 (Fig. 5.2). They are industrial low-cost sensors, with a nominal detection range of 4 and 6 m, respectively. A data logger with an analog-to-digital (A/D) converter was used to record the analog signal of the sensors. Technical details of the sensors are discussed in Section 5.3 and the technical specifications are listed in Appendix C. The sensors were

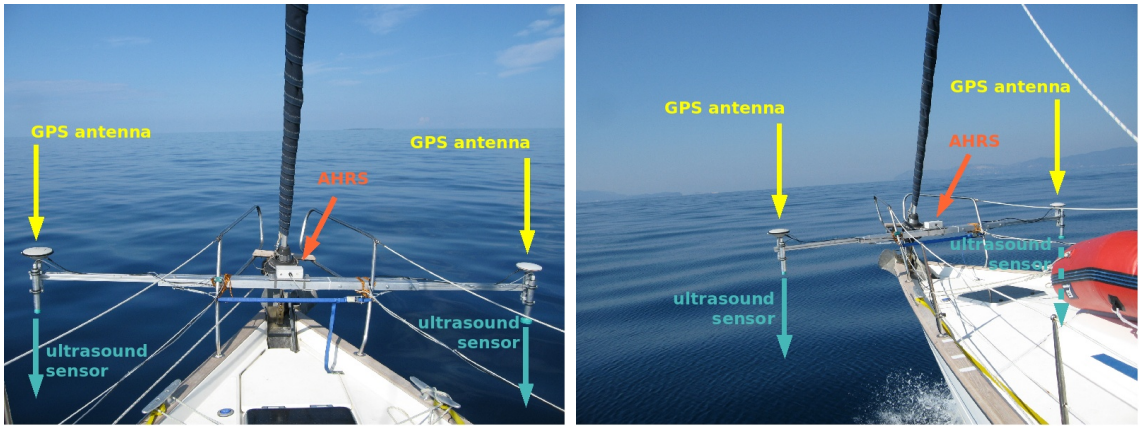

Figure 5.1: Main components of the ultrasound altimetry system mounted at the bow of a sailing-yacht, including two ultrasonic distance sensors, two GPS antennas and an inertial AHRS.

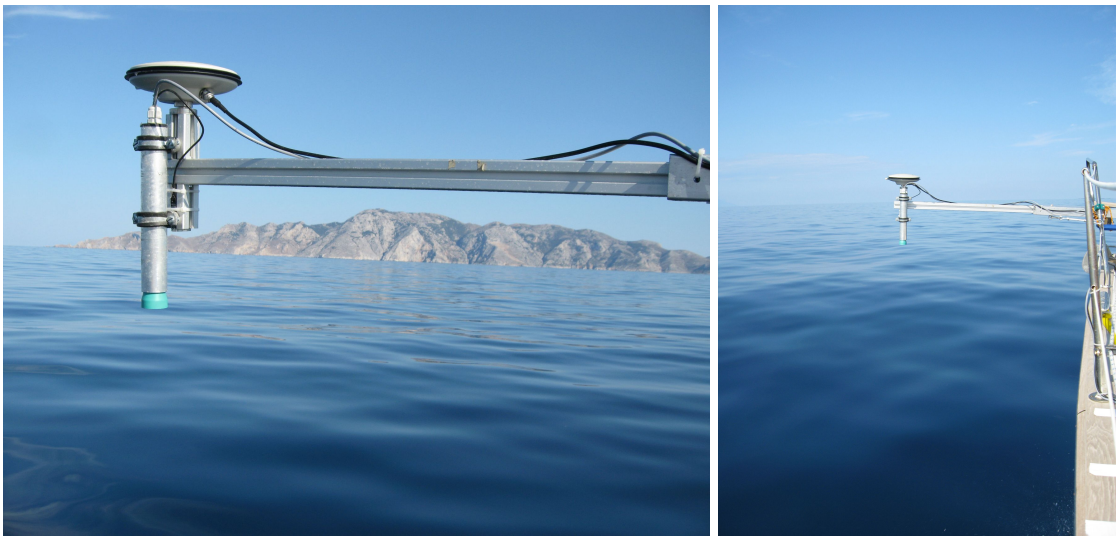

Figure 5.2: Portside ultrasonic distance sensor and GPS antenna.

mounted at the bow of the boat, in a way that the target water surface was not disturbed by the boat (Fig. 5.1).

5.2.3 GPS Antenna Configuration

The boat was equipped with an array of four to five GPS antennas (Fig. 5.3). All antennas were connected to independent dual-frequency GPS receivers. The obtained baseline lengths are 2.7 m between the portside and the starboard antennas, and 12.5 m between the stern and bow antennas. This setup allowed highly precise 3D positioning (trajectography) of the boat in combination with terrestrial GPS reference stations, as well as autonomous determination of the attitude of the boat, both needed for georeferencing the ultrasound ground point Chapter 7.

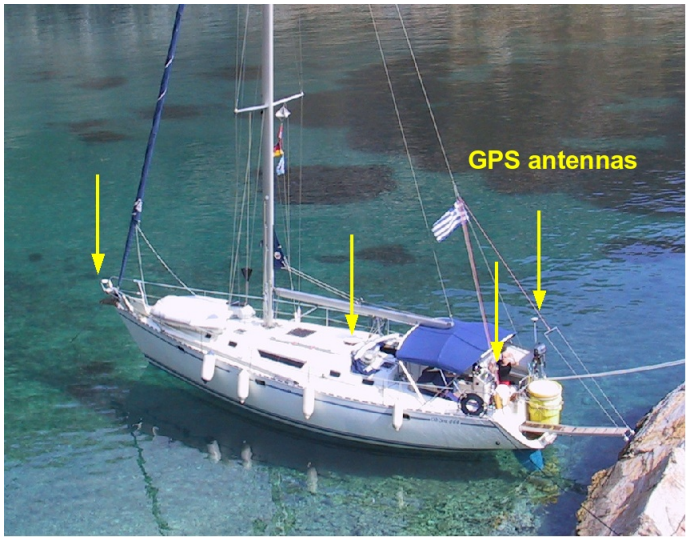

Figure 5.3: GPS antenna configuration on the sailing-yacht.

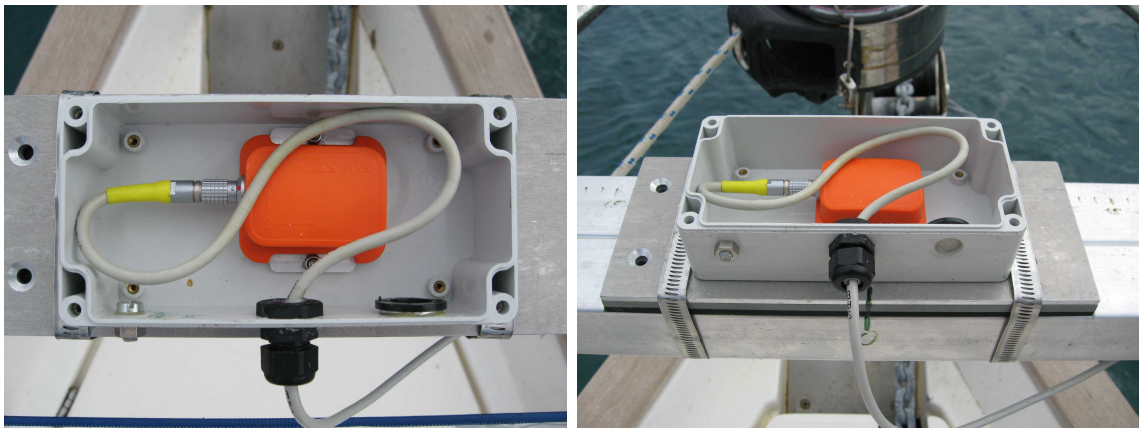

Figure 5.4: Xsens MTi inertial AHRS (Attitude and Heading Reference System).

5.2.4 Inertial Attitude and Heading Reference System (AHRS)

During the latest campaigns, the reliable, yet laborious multi-antenna GPS system used for attitude determination was augmented with an inertial measurement unit. With the use of the inertial unit, only one GPS receiver for positioning is needed. The multi-antenna GPS array and the inertial system were operated in parallel aboard the boat, in order to compare the benefits of both attitude determination methods in shipborne applications.

The inertial unit used in this project is an Xsens MTi miniature, gyro-enhanced Attitude and Heading Reference System (AHRS) (Fig. 5.4). It is based on solid state miniature MEMS (Micro-Electro-Mechanical Systems) inertial sensors, including 3-axis gyroscopes, 3-axis accelerometers and 3-axis magnetometer (3D compass), providing 3D rate of turn, 3D acceleration and 3D magnetic field data. The Xsens sensor fusion algorithm allows to compute absolute 3D orientation (attitude) in real-time. The data of the accelerometers and magnetometers are used to compensate for the drift errors from the integration of rate of turn gyro data. The AHRS was operated at a sampling rate of 20 Hz. Details on the performance of the AHRS, based on comparisons with the results from the multi-antenna GPS system, can be found in Section 7.4.6.

5.3 Ultrasound Ranging

This section is mainly based on information from the manufacturer of the ultrasonic distance sensors used in this project (Pepperl+Fuchs, 2006).

5.3.1 Basic Principles

Analogous to pulsed laser sensors, ultrasonic sensors determine the distance to an object by measuring the time delay between the sending of a package of ultrasonic pulses and the reception of the returned echo reflected by the object (Fig. 5.5):

$$2\tau = \frac{2d}{c_s} \tag{5.1}$$

where 2τ is the propagation time, d is the distance between the sensor and the reflecting object and c_s is the speed of sound ($\simeq$ 344.0 m/s at 20°C, 331.6 m/s at 0°C). Hence, for a distance of 1 m to the target, the propagation time 2τ is approx. 5.8 ms.

The ultrasonic sensors used in this project operate with a piezoelectric transducer as the sound emitter and receiver. A patented decoupling layer is used to decouple the ultrasonics from air, which is an acoustically thin medium. The ultrasonic transducer is embedded, watertight, in polyurethane foam and integrated into the sensor housing. The technical specification of the ultrasonic sensors are given in Appendix C. Both sensors have two analog outputs, as well as switching outputs. Since they operate with only one sound transducer acting alternately as transmitter and receiver, the transmitted pulse duration and the attenuation time of the sonic transducer result in an unusable area, called blind range, in which targets cannot be detected (Fig. 5.5). The blind range d_b is a function of the sum of the pulse duration Δt and the attenuation time t_a of the sonic transducer:

$$d_b \;<\; \frac{c_s}{2}\,(\Delta t + t_a) \tag{5.2}$$

The pulse duration Δt of the sensors are configurable between 0.04 and 0.55 ms. For the UC6000, $\Delta t + t_a = 2.0$ ms, corresponding to a blind range d_b of 35 cm. For the UC4000, $\Delta t + t_a = 1.1$ ms, corresponding to a blind range d_b of 20 cm.

The detection range of the sensor depends on the sound reflection properties of the object. Good reflectors can be detected from up to double the nominal detection range. On the other hand, an object situated close to the sensor can produce multiple return signals, since the ultrasonic package may propagate several times back and forth between the target and the sensor. This can lead to erroneous distance estimation if the object is situated within the blind range and only the second echo is recognized as the first return signal. Blind range and detection range are both functions of the energy contained in the pulse. The higher the energy, the larger the detection range, but in parallel, the attenuation time and thus the blind range also increase. The spatial dimension of the sound cone emitted by the sensor is defined by the opening angle of the ultrasonic beam, which is approx. 5° for the sensors used in this project. Fig. 5.6 shows the response ranges of typical objects. Within these ranges, the sensor can detect the specific object.

After the transmission of the ultrasonic pulse, the sensor waits for a time equivalent to twice the nominal detection range, since it can receive echoes from distances beyond the detection range under favorable reflection conditions. This waiting phase limits the maximum sampling rate of the sensor. For the UC6000 and UC4000, the nominal detection ranges of 6 m and 4 m result in waiting phases of 70 ms and 47 ms, corresponding to maximum sampling rates of 14 Hz and 21 Hz, respectively. In this project, both sensors were operated in self-synchronization mode (Section 5.4.1), yielding a sampling interval of 0.15 s (7 Hz) for each sensor.

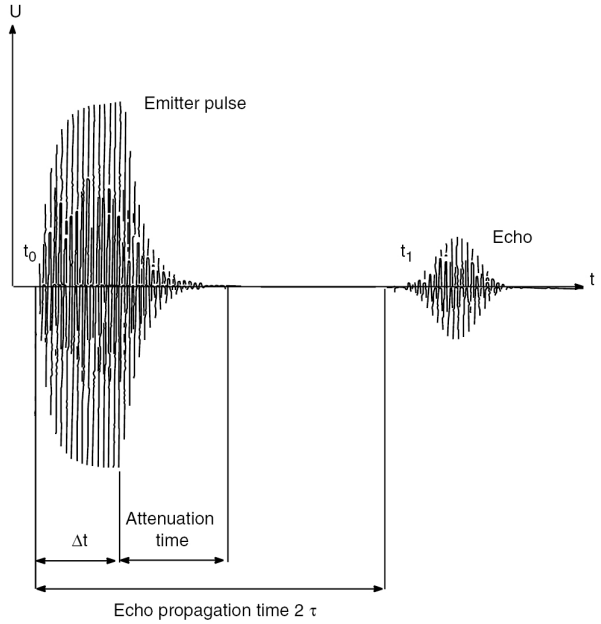

Figure 5.5: Transmitted and received signal in ultrasound ranging. From (Pepperl+Fuchs, 2006).

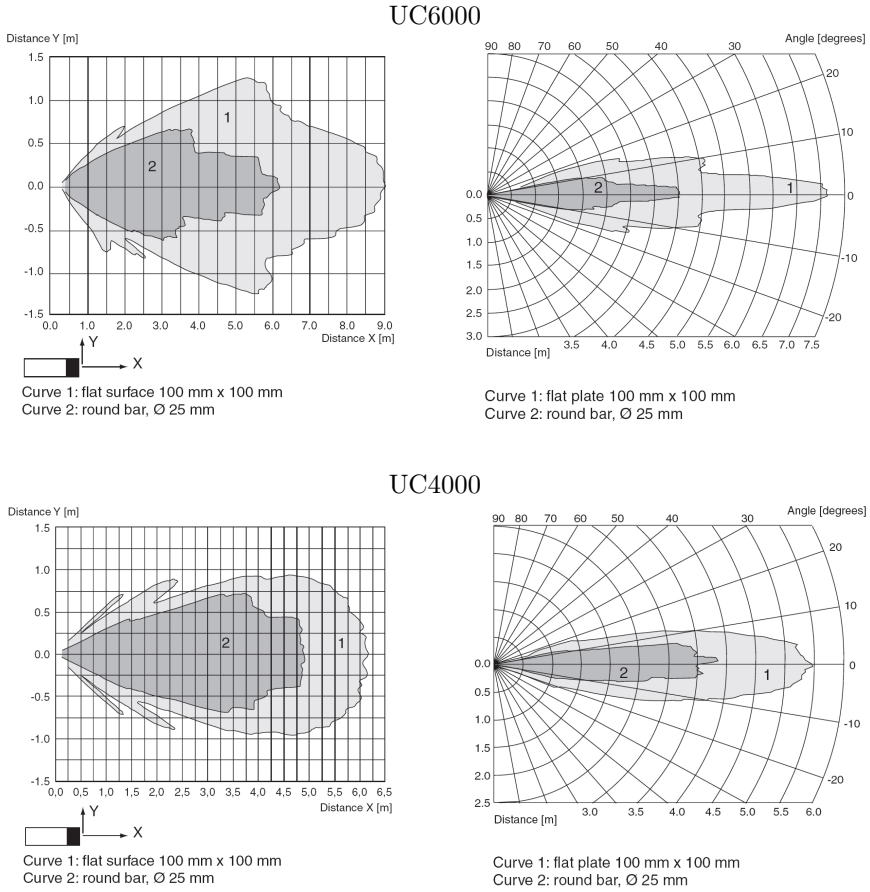

Figure 5.6: Response curves of UC6000 and UC4000 ultrasonic sensors. From (Pepperl+Fuchs, 2006).

5.3.2 Range Resolution and Accuracy

The ultrasonic sensors are equipped with an integrated 12-bit D/A (digital-to-analog) converter, converting the determined range in a 0-10 V or a 4-20 mA signal. A resolution of 12 bits corresponds to $2^{12} = 4096$ available values. The propagation time of an ultrasonic pulse is determined with a resolution of 1 μs, given by he clock rate of the micro-controller and corresponding to a range resolution of 0.172 mm. However, this maximum range resolution is only available if the measuring window (distance between the lower and the upper range limits) is smaller than $4096 \cdot 0.172$ mm = 705 mm. The measuring window of the sensor is configurable. For a measuring window above 705 mm, the range resolution dr is limited by the 12-bit D/A converter, according to the relation:

$$dr = \frac{\text{upper limit} - \text{lower limit}}{4096} \tag{5.3}$$

In this project, the sensor limits were set between 0.5 and 4.0 m, yielding a resolution of 0.85 mm.

In order to determine the absolute accuracy of the range measured by an ultrasonic sensor, factors such as temperature, atmospheric pressure, relative humidity (Section 5.3.3), turbulences, hot spots in the air surrounding the sensor, and sensor in hot operating status must be taken into consideration. In addition, tolerances of the electronic components and differences in the response characteristic of the ultrasonic sensor due to varying signal strengths of the sound reflected by the object also have an effect. Under consideration of all these influences, an accuracy of better than 2 cm/m can generally be achieved, along with a repeatability and linearity of better than 2 mm/m (Pepperl+Fuchs, 2006).

5.3.3 Atmospheric Influences

Due to the physical properties of sound propagation, the sound propagation velocity and the detection range depend on the physical properties of the carrier medium. In the case of a gas-air mixture, the propagation velocity and detection range depend on air temperature, relative humidity and barometric pressure (Fig. 5.7). Temperature changes greatly affect the velocity of sound, whereas air pressure and humidity are less important factors. The temperature influence on the measured range is approx. -0.17 %/°C. For a temperature increase of 1°C, this corresponds to a decrease of the measured range by 0.17 cm/m with respect to the real range. Due to the strong temperature dependency, the ultrasonic sensors used in this project are temperature-compensated, based on an electrical temperature probe connected to the sensors. From Fig. 5.7b, the increased maximum detection range at low temperatures, independent of the relative humidity, is apparent. The reduced detection range at higher temperatures, however, is strongly influenced by the relative humidity.

5.3.4 Ultrasonic Target Reflection

Objects detectable by ultrasonic sensors can be solid, liquid or powdery. The echo is influenced by the characteristics of the object's surface. Even and smooth surfaces, arranged at a right angle to the sound cone, provide an ideal reflection. Reliable detection is still obtained for angular deviations of the measuring plate by 3°. Material properties such as transparency, color or surface finish have no effect on detection reliability.

The roughness of the surface, together with the sensor-specific transducer frequency, determines whether the reflection of the ultrasonic pulse is specular or diffuse (Tab. 5.1). If the sound wavelength is longer than the peak-to-valley height of the surface roughness, specular reflection prevails. If it is shorter, diffuse reflection prevails. The transition from specular to diffuse reflection is continuous. Roughness depths in-between the values in Tab. 5.1 will result in reflections with diffuse

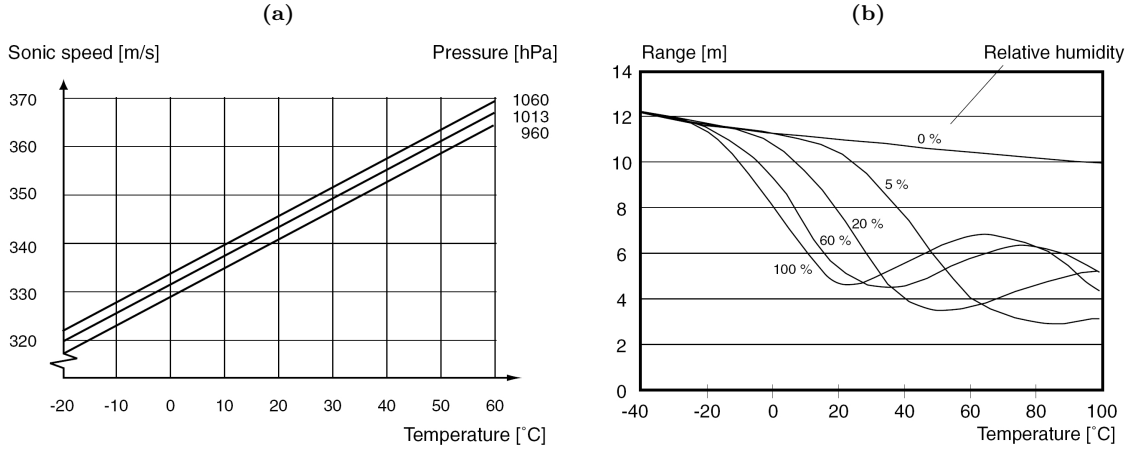

Figure 5.7: (a) Theoretical relationship between air temperature, pressure and velocity of sound. **(b)** Theoretical relationship of the maximum detection range with respect to air temperature and relative humidity, for the UC6000-30GM. The nominal detection range at an ambient temperature of 20°C and a relative humidity of 50% is 6 m. Both graphs from (Pepperl+Fuchs, 2006).

Table 5.1: Ultrasound transducer frequencies and wavelengths, and associated degrees of surface roughness (peak-to-valley height) for specular and diffuse reflection. Values from (Pepperl+Fuchs, 2006).

Transducer sonic frequency	Transducer sonic wavelength	Surface roughness causing a predominately specular reflection	Surface roughness causing a predominately diffuse reflection
65 kHz	5.3 mm	$<$ 1.0 mm	$>$ 25 mm
85 kHz	4.0 mm	$<$ 0.8 mm	$>$ 20 mm
120 kHz	2.9 mm	$<$ 0.5 mm	$>$ 13 mm
175 kHz	2.0 mm	$<$ 0.4 mm	$>$ 10 mm
375 kHz	0.9 mm	$<$ 0.2 mm	$>$ 5 mm

and specular shares. Objects with pronounced surface roughness and associated diffuse reflection will result in a reduction of the detection range. On the other hand, pronounced surface roughness allows larger deviations of the angle of incidence from the normal, due to predominately diffuse reflection. As a consequence, filling level or pouring cones of coarse-grained material can e.g. be detected (at reduced sensing range) at an angular deviation of up to 45°.

The following objects are well-suited for detection:

- smooth and solid objects that are aligned at a right angle to the axis of the sound cone
- solid objects with degrees of surface roughness that cause a diffuse reflection and which are to a large extend independent of their alignment
- liquid surfaces, if the surface is not inclined by more than 3° perpendicular to the axis of the sound cone

The following materials are poorly suited for detection:

- materials absorbing ultrasonic waves such as felt, cotton, wool, coarse textiles or plastic foam
- materials at temperatures above 100°C

The transducer frequencies of the sensors used in this project are 65 and 85 kHz, respectively. Since natural water surfaces like oceans are usually characterized by a peak-to-valley height above 25 mm

within the ultrasound footprint of approx. 1 m diameter, the resulting reflection is predominately diffuse, leading to good signal returns even for off-nadir angles above 3°.

5.4 Sensor Synchronization

5.4.1 Self-Synchronization between Ultrasonic Sensors

Mutual interference between ultrasonic sensors can occur if they are not separated by a minimum distance. The necessary minimum distance can be relatively large, depending on the nominal detection range, the distance to the object and the site conditions. Interference can be effectively prevented by synchronizing the sensors. For this purpose, the sensors are equipped with a synchronization input/output interface. Synchronization pulses sent to the sensor initiate each measuring cycle and the transmission of a single ultrasonic pulse. The two sensors used in this project were self-synchronized by interconnecting their synchronization inputs/outputs, causing the sensors to alternately transmit ultrasonic pulses.

5.4.2 Hardware Synchronization of Ultrasonic Sensors with GPS

The self-synchronization pulses described above were also used to synchronize the ultrasonic sensors with the GPS system, by simultaneously transmitting the pulses to the data logger recording the range of the sensors, as well as to a GPS receiver. Every pulse coincides with a data sample of an ultrasonic sensor. The data logger associates a time-tag to every pulse, and hence to every range observation, in his internal time system. The GPS receiver attributes a time-tag in GPS time to the same pulses, providing a precise absolute time-tag for every ultrasonic range measurement.

5.4.3 Software Synchronization of Ultrasonic Sensors with GPS

Due to sporadic dropouts of the hardware synchronization during the early deployment of the ultrasound altimetry system, an algorithm relying on a purely mathematical synchronization was developed to avoid unusable data. The system is based on 2D cross-correlation between the absolute height of the GPS antenna mounted close to the ultrasonic sensor and the range observed by the sensor. The antenna height is determined by GPS processing and is given in precise GPS time. The sensor range is recorded in the time frame of the data logger. The synchronization between the two time frames is defined by an offset and a scale factor. The offset accounts for the offset of the time frame of the data logger with respect to the absolute GPS time frame, whereas the scale factor accounts for a constant drift of the logger time frame. Drift variations are neglected.

Since the GPS antenna and the ultrasonic sensor are rigidly mounted on the boat, the movement produced by the boat equally affects the height of the GPS antenna and the ultrasonic range (Fig. 5.8). The 2D cross-correlation, where the first dimension is the offset, and the second is the scale factor, allows to identify the offset and scale factor for which the maximum correlation between the GPS height and the ultrasound range is obtained (Fig. 5.9). The method did not suffer from the fact that the range signal is additionally affected by the undulation of waves at the target water surface. The only case where the synchronization method would not provide a solution is in the absence of vertical movement of the boat. This condition is actually never verified, even when the boat is floating in calm water. Hence, correct synchronization was obtained even when the boat was lying in a calm port. Theoretically, the maximum synchronization accuracy that can be obtained is governed by the minimum sampling rate of the GPS or ultrasound records. However, since both signals are smooth oscillating movements, they can be interpolated to a much higher sampling rate, e.g. using cubic polynomial or spline interpolation.

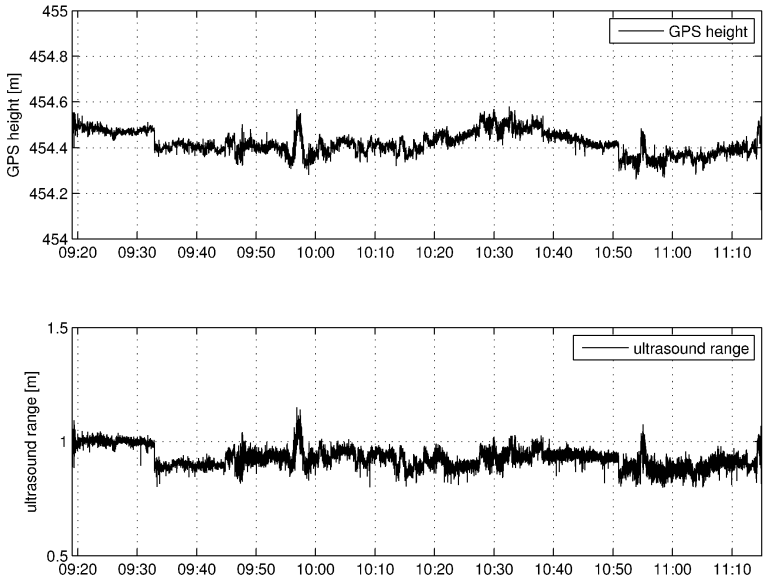

Figure 5.8: Example of mathematical synchronization under calm conditions on the lake of Zurich, Switzerland, with height of GPS antenna (top) and ultrasonic range (bottom).

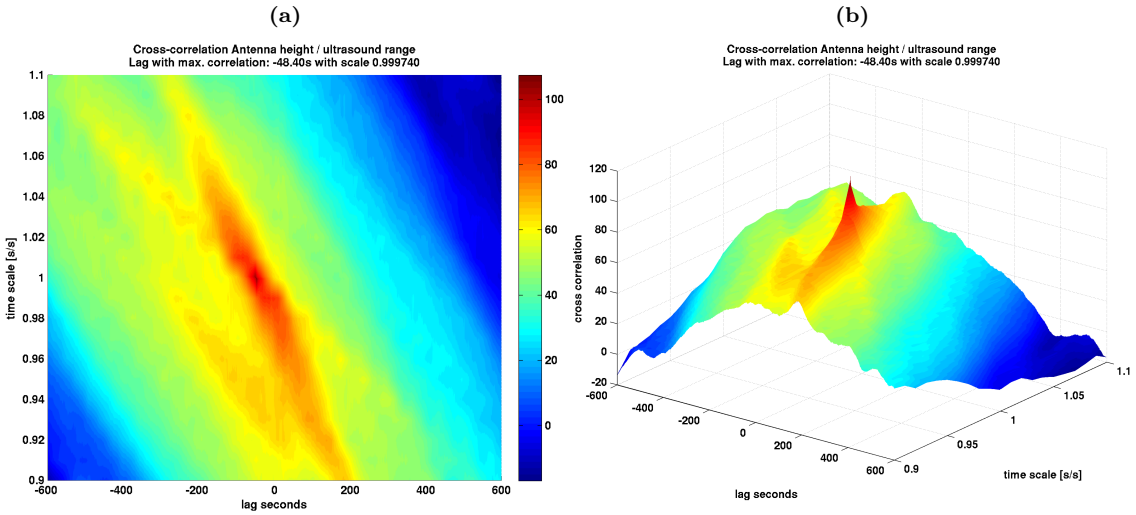

Figure 5.9: **(a)** 2D cross-correlation of the two signals in Fig. 5.8, with offset (lag) along the x-axis and scale factor along the y-axis. The (dimensionless) correlation values are color-coded. A distinct peak of maximum correlation can be identified. **(b)** 3D view of (a).

6 GPS-Equipped Buoys

6.1 Introduction

GPS-equipped buoys provide ground-truth information on the instantaneous sea surface height, enabling the determination of sea state parameters, the integration in early-warning systems for Tsunamis and the calibration of spaceborne, airborne and shipborne altimetry systems. Depending on the application, different types of buoys and concepts have been developed by different institutions. An overview of worldwide specialized buoy activities is given by (Schöne, 2003).

6.2 GPS-Equipped Buoys developed by the GGL

For offshore hydrodynamic investigations and ground-truth measurements of the sea surface height, the GGL has designed and constructed lightweight GPS buoys (Fig. 6.1). The buoys weight 10 kg including the equipment and have a diameter of 0.40 m, facilitating their handling. The shell of the buoys is fabricated from microwave-transparent polycarbonate, so they can be waterproof sealed containing the GPS receiver, GPS antenna and power supply. The dimension of the buoys and the weight of the equipment were optimally chosen and designed in order to reach an exact floating balance. No ballast is needed to stabilize the buoy or to reach the foreseen floating line in the middle of the spherical buoy. Their small weight allows to follow the movements of the waves. The operation autonomy is about 24 hours. The buoys are equipped with Novatel DL–4 dual-frequency GPS receivers.

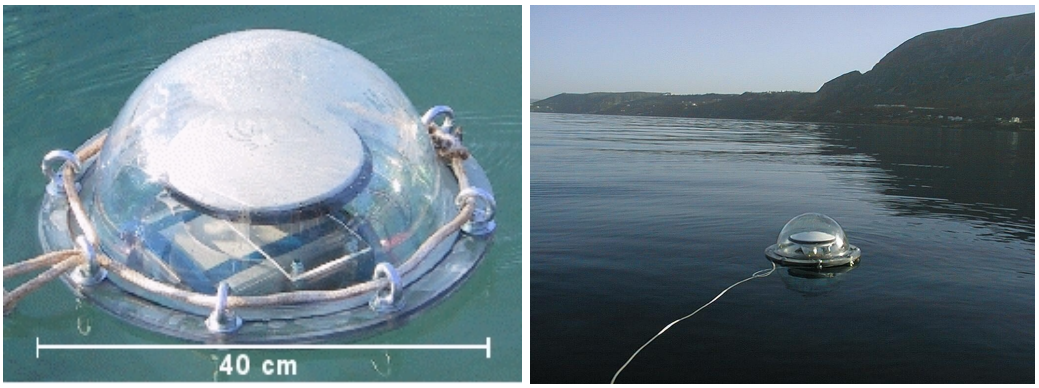

Figure 6.1: GPS-equipped buoy deployed in coastal region, containing GPS receiver, GPS antenna and battery.

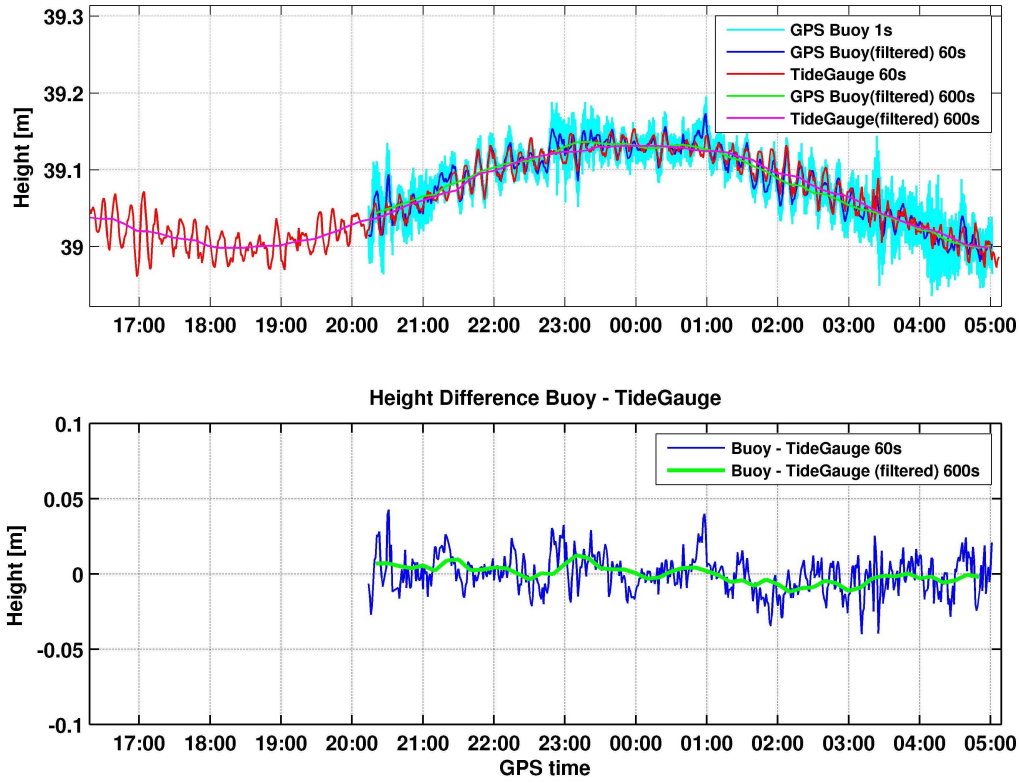

Figure 6.2: Comparison between sea surface heights from GPS buoy and pressure tide-gauge in the same bay.

6.3 Case Study: Ocean Tide Observations with GPS Buoys

Apart from providing calibration data for spaceborne, airborne and shipborne altimetry systems, GPS buoys can be used to observe ocean tides. Onshore tide-gauges have the disadvantage to produce data only in coastal regions, whereas GPS buoys can be deployed offshore, thus providing accurate ground-truth ocean tide data for the open sea. Field measurements with GPS buoys carried out in this project produced very promising results, as is shown by comparing them to pressure tide-gauge data. In this case study (Fig. 6.2), both systems were operated in the same bay. The buoy data with an original sampling rate of 1 Hz (Fig. 6.2 top, cyan line) were first low-pass filtered and resampled to the 60 s sampling interval of the tide-gauge data (Fig. 6.2 top, blue line). In this example, the difference between GPS and tide-gauge data (Fig. 6.2 bottom, blue line) shows an RMS of 1.3 cm. Both methods have observed a special wave characterized by a period of approx. 11 minutes and an amplitude of approx. 2 cm, best distinguishable between 1:00 and 3:00 GPS time. For tidal analysis purposes, focusing on periods of 12 hours and more, both datasets were low-pass filtered and resampled to a sampling interval of 600 s (Fig. 6.2 top, green and magenta lines). The filtered datasets show a very good agreement (Fig. 6.2 bottom, green line), with an RMS of only 0.5 cm.

7 Direct Georeferencing

7.1 Introduction

In this chapter, an approach for direct georeferencing is shown, valid for both airborne laser altimetry (Chapter 4) and shipborne ultrasound altimetry (Chapter 5). The GPS based trajectory and attitude recovery is discussed, and comparisons with attitude solutions from inertial units are made. In addition, a calibration method for boresight misalignment in airborne laser altimetry is presented. Error models of the platform and the laser or ultrasound device are important issues. The quality of the trajectory of the airplane or the boat determined by differential GPS, and their attitude determined by a multi-antenna GPS array or by inertial systems, are of utmost importance. These issues will be analysed in Sections 7.3 and 7.4, respectively. Another critical element is the determination of the boresight misalignment between the frame of the laser device and the body frame. This misalignment affects the georeferencing of the laser data systematically. Since they are rather difficult to measure directly, their determination is not trivial. In Section 7.5, the impact of boresight misalignment on computed terrain heights will be analysed and a boresight self-calibration method is presented. Considerations on the effect of tropospheric refraction in laser ranging were discussed in Section 4.5. Most of the elemnts in this chapter are focused on airborne laser altimetry, but unless not explicitly stated, they also apply in shipborne ultrasound altimetry. The approach of direct georeferencing described in this chapter is based on (Favey, 2001).

7.2 Basic Principle

7.2.1 Direct Georeferencing Equation

The key problem in airborne laser altimetry consists in integrating all necessary elements for georeferencing the laser beam, yielding a 3D vector between the aircraft and the ground-point in an absolute coordinate system (Fig. 7.1). For each range measurement r by the laser device, the corresponding ground-point is computed, involving the GPS position of the aircraft and its attitude. The measurements from all devices have to be synchronized with respect to GPS time and interpolated to the corresponding measuring epochs. The observation equation for direct georeferencing in airborne laser altimetry can be written as (Favey, 2001):

$$\boldsymbol{x}^G \;=\; \boldsymbol{a}^G \;+\; \boldsymbol{R}_{G/L}\;\boldsymbol{R}_{L/B}\;\left(\;\boldsymbol{R}_{B/S}\;r\;\boldsymbol{s}^S \;+\; \boldsymbol{b}^B\;\right) \tag{7.1}$$

or in vector notation:

$$\begin{bmatrix} X \\ Y \\ Z \end{bmatrix}^G \;=\; \begin{bmatrix} X_a \\ Y_a \\ Z_a \end{bmatrix}^G \;+\; \boldsymbol{R}_{G/L}\;\boldsymbol{R}_{L/B}\;\left(\;\boldsymbol{R}_{B/S}\;r\;\begin{bmatrix} s_x \\ s_y \\ s_z \end{bmatrix}^S \;+\; \begin{bmatrix} b_x \\ b_y \\ b_z \end{bmatrix}^B\;\right)$$

where:

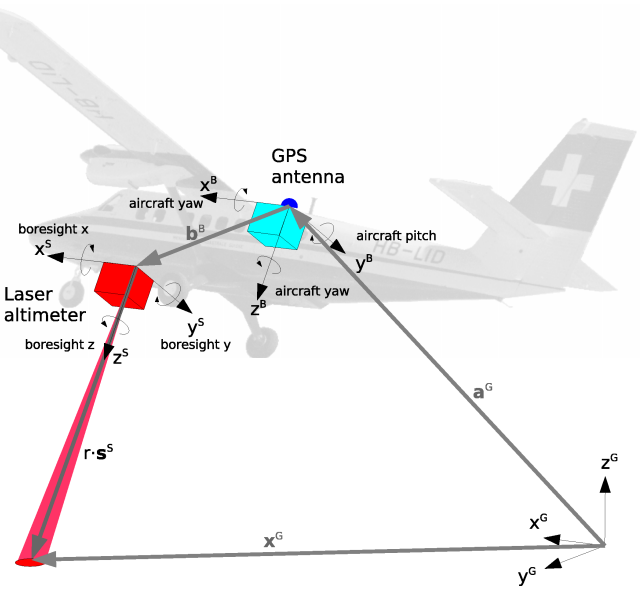

Figure 7.1: Direct georeferencing elements in airborne laser altimetry.

$\boldsymbol{x}^G$	geocentric position of laser ground-point (to be determined)
$\boldsymbol{a}^G$	geocentric position of GPS antenna (measured by GPS trajectography)
$\boldsymbol{R}_{G/L}$	rotation matrix from topocentric to geocentric system, defined by the aircraft's latitude and longitude
$\boldsymbol{R}_{L/B}$	rotation matrix from body frame to topocentric system, defined by the attitude angles roll (a_x), pitch (a_y) and yaw (a_z)
$\boldsymbol{R}_{B/S}$	boresight rotation matrix between laser device and body frame, defined by the boresight angles β_x, β_y, β_z and the boresight misalignment angles $d\beta_x$, $d\beta_y$, β_z (to be determined by calibration)
r	slant laser range (measured by laser device)
$\boldsymbol{s}^S$	laser vector giving the beam direction in laser device coordinate frame
$\boldsymbol{b}^B$	lever arm (offset) between laser device and GPS antenna (measured with terrestrial methods)

The laser vector $\boldsymbol{s}^S$ in the laser device coordinate frame is given by:

$$\boldsymbol{s}^S = (\sin\sigma_x \cos\sigma_z,\ \sin\sigma_x \sin\sigma_z,\ \cos\sigma_x)^T \tag{7.2}$$

where σ_x is the off-nadir angle with respect to the vertical as defined in the laser frame and σ_z is the horizontal angle (azimuth) with respect to the laser frame. For a profiler, $\sigma_x = \sigma_z = 0$ and $\boldsymbol{s}^S = (0, 0, 1)^T$. For a cross-section linear scanner, σ_x is the time-varying off-nadir scan angle, σ_z = -90° and $\boldsymbol{s}^S = (0, -\sin\sigma_x, \cos\sigma_x)^T$. The signs of σ_z and $\sin\sigma_x$ depend on the definition of the sens of the scan rotation.

The rotation matrix from local level north oriented NED (North, East, Down) coordinate frame to the geocentric system (Appendix D.2) depends on the aircraft's latitude (φ) and longitude (λ), determined by GPS trajectography :

$$\boldsymbol{R}_{G/L} = \boldsymbol{R}_3(-\lambda)\ \boldsymbol{R}_2\left(\varphi + \frac{\pi}{2}\right) = \begin{bmatrix} -\sin\varphi\cos\lambda & -\sin\lambda & -\cos\varphi\sin\lambda \\ -\sin\varphi\sin\lambda & \cos\lambda & -\cos\varphi\sin\lambda \\ \cos\varphi & 0 & -\sin\varphi \end{bmatrix} \tag{7.3}$$

The rotation matrix from the body frame to the local level NED frame depends on the attitude angles roll (α_x), pitch (α_y) and yaw (α_z) of the aircraft:

$$\begin{aligned}\boldsymbol{R}_{L/B} &= \boldsymbol{R}_3(-\alpha_z)\ \boldsymbol{R}_2(-\alpha_y)\ \boldsymbol{R}_1(-\alpha_x) \\ &= \begin{bmatrix} \cos\alpha_y \cos\alpha_z & -\cos\alpha_x \sin\alpha_z + \sin\alpha_x \sin\alpha_y \cos\alpha_z & \sin\alpha_x \sin\alpha_z + \cos\alpha_x \sin\alpha_y \cos\alpha_z \\ \cos\alpha_y \sin\alpha_z & \cos\alpha_x \cos\alpha_z + \sin\alpha_x \sin\alpha_y \sin\alpha_z & -\sin\alpha_x \cos\alpha_z + \cos\alpha_x \sin\alpha_y \sin\alpha_z \\ -\sin\alpha_y & \sin\alpha_x \cos\alpha_y & \cos\alpha_x \cos\alpha_y \end{bmatrix}\end{aligned} \tag{7.4}$$

The boresight rotation is described by three rotation angles (β_x, β_y, β_z) around the three axes of the laser device frame. Approximate values (β_x^0, β_y^0, β_z^0) of the boresight rotation angles are known from mechanical alignment. The actual angles can slightly differ from these nominal values. This deviation is called boresight misalignment. The boresight misalignment angles ($d\beta_x$, $d\beta_y$, $d\beta_z$) are unknown and have to be determined by calibration. The boresight rotation matrix depends on the boresight angles ($\beta = \beta^0 + d\beta$):

$$\begin{aligned}\boldsymbol{R}_{B/S} &= \boldsymbol{R}_3(-\beta_z)\ \boldsymbol{R}_2(-\beta_y)\ \boldsymbol{R}_1(-\beta_x) \\ &= \begin{bmatrix} \cos\beta_y \cos\beta_z & -\cos\beta_x \sin\beta_z + \sin\beta_x \sin\beta_y \cos\beta_z & \sin\beta_x \sin\beta_z + \cos\beta_x \sin\beta_y \cos\beta_z \\ \cos\beta_y \sin\beta_z & \cos\beta_x \cos\beta_z + \sin\beta_x \sin\beta_y \sin\beta_z & -\sin\beta_x \cos\beta_z + \cos\beta_x \sin\beta_y \sin\beta_z \\ -\sin\beta_y & \sin\beta_x \cos\beta_y & \cos\beta_x \cos\beta_y \end{bmatrix}\end{aligned} \tag{7.5}$$

In many applications, the coarse boresight angles β^0 are zero from mechanical alignment, and the rotation matrix $\boldsymbol{R}_{B/S}$ only depends on the unknown misalignment angles $d\beta$. Usually, the boresight misalignment angles are small differential angles $< 1°$, and the rotation matrix $\boldsymbol{R}_{B/S}$ can be simplified using the properties of small angles close to 0 ($\sin d\beta \approx d\beta$ and $\cos d\beta \approx 1$):

$$\boldsymbol{R}_{B/S} = \begin{bmatrix} 1 & -d\beta_z & d\beta_y \\ d\beta_z & 1 & -d\beta_x \\ -d\beta_y & d\beta_x & 1 \end{bmatrix} \tag{7.6}$$

Further details on rotation matrices are given in Appendix D.

7.2.2 Vertical Component of Direct Georeferencing Equation

In boresight misalignment calibration (Section 7.5), or when estimating the impact of erroneous attitudes angles onto terrain height (Section 7.2.3), the vertical component of the laser ground-point in the direct georeferencing equation (7.1) is of particular interest. Therefore, we want to first express the coordinates of the ground-point in topocentric coordinates by left-multiplying (7.1) with $\boldsymbol{R}_{G/L}^{-1}$:

$$\begin{aligned}\begin{bmatrix} N \\ E \\ D \end{bmatrix}^L &= \begin{bmatrix} N_a \\ E_a \\ D_a \end{bmatrix}^L + \boldsymbol{R}_{L/B} \left(\boldsymbol{R}_{B/S}\ r \begin{bmatrix} s_x \\ s_y \\ s_z \end{bmatrix}^S + \begin{bmatrix} b_x \\ b_y \\ b_z \end{bmatrix}^B \right) \\ &= \begin{bmatrix} N_a \\ E_a \\ D_a \end{bmatrix}^L + \begin{bmatrix} r_{11} & r_{12} & r_{13} \\ r_{21} & r_{22} & r_{23} \\ r_{31} & r_{32} & r_{33} \end{bmatrix}^{L/B} \left(\begin{bmatrix} r_{11} & r_{12} & r_{13} \\ r_{21} & r_{22} & r_{23} \\ r_{31} & r_{32} & r_{33} \end{bmatrix}^{B/S} r \begin{bmatrix} s_x \\ s_y \\ s_z \end{bmatrix}^S + \begin{bmatrix} b_x \\ b_y \\ b_z \end{bmatrix}^B \right)\end{aligned} \tag{7.7}$$

For the case of a **cross-section linear scanner**, $\boldsymbol{s}^S = (0, -\sin\sigma_x, \cos\sigma_x)^T$. Considering only the vertical down component D in (7.7) and by substituting the terms of the rotation matrices from

(7.3), (7.4) and (7.6) in (7.7), the true height difference Δh^L_{true} between the GPS antenna and the laser ground-point is obtained:

$$\begin{aligned}\Delta h^L_{true} \;=\; D^L \;-\; D^L_a \;=\; &-\; \sin\alpha_y \left(r\; d\beta_z\; \sin\sigma_x \;+\; r\; d\beta_y\; \cos\sigma_x \;+\; b^B_x\right)\\ &+\; \sin\alpha_x\; \cos\alpha_y \left(-r\; \sin\sigma_x \;-\; r\; d\beta_x\; \cos\sigma_x \;+\; b^B_y\right)\\ &+\; \cos\alpha_x\; \cos\alpha_y \left(-r\; d\beta_x\; \sin\sigma_x \;+\; r\; \cos\sigma_x \;+\; b^B_z\right)\end{aligned} \tag{7.8}$$

This equation can be reformulated using the true height of the laser ground-point h^L_{true} and the ellipsoidal height of the GPS antenna h^L_a in the classical ENU (East, North, Up) coordinate system:

$$\begin{aligned}h^L_{true} \;=\; h^L_a \;-\; \Delta h^L_{true} \;=\; h^L_a \;&+\; \sin\alpha_y \left(r\; d\beta_y\; \cos\sigma_x \;+\; r\; d\beta_z\; \sin\sigma_x \;+\; b^B_x\right)\\ &-\; \sin\alpha_x\; \cos\alpha_y \left(-r\; \sin\sigma_x \;-\; r\; d\beta_x\; \cos\sigma_x \;+\; b^B_y\right)\\ &-\; \cos\alpha_x\; \cos\alpha_y \left(r\; \cos\sigma_x \;-\; r\; d\beta_x\; \sin\sigma_x \;+\; b^B_z\right)\end{aligned} \tag{7.9}$$

For the special case of a **laser profiler**, $\boldsymbol{s}^S = (0,0,1)^T$ and (7.9) is further simplified to:

$$h^L_{true} = h^L_a - \left[\cos\alpha_x \cos\alpha_y \left(r + b^B_z\right) \;-\sin\alpha_x \cos\alpha_y \left(r\; d\beta_x - b^B_y\right) \;-\sin\alpha_y \left(r\; d\beta_y + b^B_x\right)\right] \tag{7.10}$$

In the case of a cross-section linear scanner, the vertical component does not depend on the yaw angle α_z (7.9). In the case of a laser profiler, the vertical component does not depend on the yaw angle α_z, nor on the yaw component $d\beta_z$ of the boresight misalignment (7.10).

7.2.3 Impact of Attitude Error onto Ground-Point Height

Erroneous attitude angles can occur due to inaccurate attitude measurements or a misalignment of the attitude measurement system. Assuming that the roll and pitch angles α_x and α_y are affected by the errors $d\alpha_x$ and $d\alpha_y$, (7.10) for a profiler becomes:

$$\begin{aligned}h^L_{true} \;=\; h^L_a \;&-\; \cos\left(\alpha_x + d\alpha_x\right) \cos\left(\alpha_y + d\alpha_y\right) \left(r + b^B_z\right)\\ &+\; \sin\left(\alpha_x + d\alpha_x\right) \cos\left(\alpha_y + d\alpha_y\right) \left(r\; d\beta_x - b^B_y\right)\\ &+\; \sin\left(\alpha_y + d\alpha_y\right) \left(r\; d\beta_y + b^B_x\right)\end{aligned} \tag{7.11}$$

Since attitude errors are usually small angles ($< 1°$), (7.11) can be simplified using the properties of small angles (for $d\alpha_i \to 0$, $\sin d\alpha_i \approx d\alpha_i$, $\cos d\alpha_i \approx 1$ and $d\alpha_i \cdot d\alpha_i \approx 0$):

$$\begin{aligned}h^L_{true} \;=\; h^L_a \;&-\; \left(\cos\alpha_x \cos\alpha_y - d\alpha_x \sin\alpha_x \cos\alpha_y - d\alpha_y \cos\alpha_x \sin\alpha_y\right) \left(r + b^B_z\right)\\ &+\; \left(\sin\alpha_x \cos\alpha_y + d\alpha_x \cos\alpha_x \cos\alpha_x - d\alpha_y \sin\alpha_x \sin\alpha_y\right) \left(r d\beta_x - b^B_y\right)\\ &+\; \left(\sin\alpha_y + d\alpha_y \cos\alpha_y\right) \left(r d\beta_y + b^B_x\right)\end{aligned} \tag{7.12}$$

By subtracting (7.10) from (7.12), the effect dh of roll and pitch errors $d\alpha_x$ and $d\alpha_y$ on the ground-point height is obtained (using $d\alpha_i \cdot d\beta_i \approx 0$ and $d\alpha_i \cdot b^B_i \approx 0$):

$$dh \;=\; r\; \left(d\alpha_x\; \sin\alpha_x\; \cos\alpha_y \;+\; d\alpha_y\; \cos\alpha_x\; \sin\alpha_y\right) \tag{7.13}$$

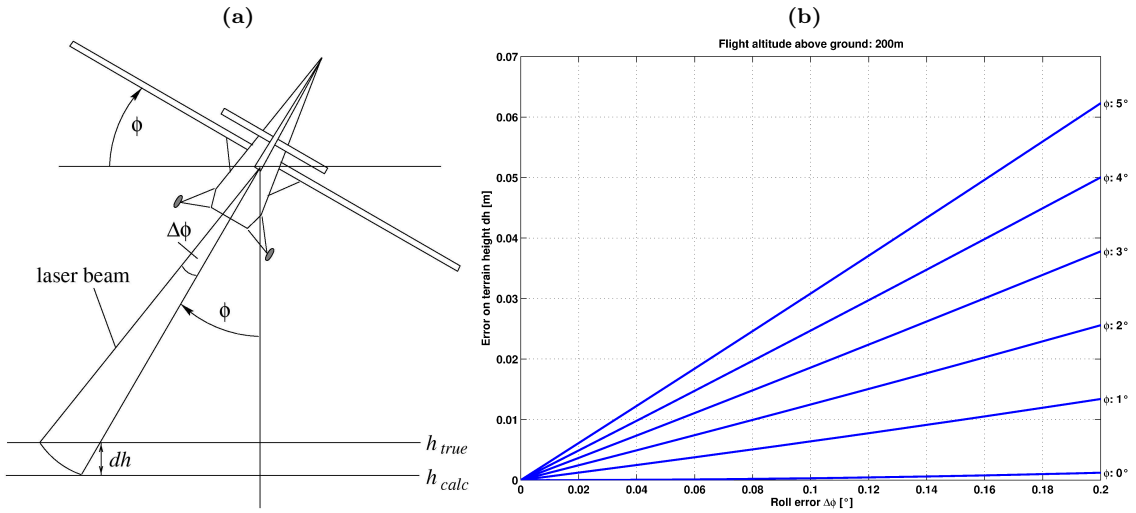

Figure 7.2: **(a)** Impact dh of roll error $\Delta\phi$ onto ground-point height height, illustrating (7.14) (Graph by E. Favey). **(b)** Height error dh from (7.14) as a function of roll error $\Delta\phi$, for roll angles ϕ from 0-5° and a laser range r ($\approx$ flight height above ground) of 200 m.

Thus, the impact of roll and pitch attitude errors on the ground-point height dh depends on the laser range r ($\approx$ flight height above ground) and on the attitude angles themselves. Considering e.g. only the roll angle ($\alpha_y = 0,\ d\alpha_y = 0$), an intuitive formula can be derived for the height error dh from (7.13) (Fig. 7.2):

$$dh \;=\; r\ d\alpha_x\ \sin\alpha_x \;=\; r\ [\ \cos\alpha_x \;-\; \cos\left(\alpha_x + d\alpha_x\right)\ ] \tag{7.14}$$

For example in airborne laser altimetry, for a roll angle α_x of 3°, a roll error $d\alpha_x$ of 0.2° and a laser range r of 200 m, (7.14) yields a height error dh of 4 cm. In shipborne altimetry, the impact of an erroneous roll/pitch angle onto height determination is much smaller as compared to airborne applications, due to the small range (usually less than 3 m) between the ultrasound distance sensor and the sea surface. For the same roll angle α_x of 3°, the same roll error $d\alpha_x$ of 0.2° and an ultrasound range r of 3 m, (7.14) yields a height error dh below 1 mm.

7.2.4 Required Attitude Accuracy in Airborne and Shipborne Applications

Using (7.13), the required attitude accuracy $d\alpha$ for roll or pitch angles can be computed as a function of the height above ground ($\approx$ range r), the maximal roll/pitch angle α_{max} during the survey and the desired height accuracy dh_{max}. In (7.13), the worst case leading to the heaviest impact on the height occurs when $\alpha_x = \alpha_y = \alpha_{max}$ and $d\alpha_x = d\alpha_y = d\alpha$. Thus, the following expression for the required attitude accuracy is obtained:

$$d\alpha \;=\; \frac{dh_{max}}{2\ r\ \sin\alpha_{max}\ \cos\alpha_{max}} \tag{7.15}$$

In the airborne altimetry application, the flight height above ground (sea) r is about 200 m, and the roll and pitch angles α_{max} on a flight-line are below 3°. The maximum height error dh_{max} can be fixed to 4 cm, which corresponds to the maximum vertical accuracy achievable by kinematic differential GPS positioning, used for the determination of the absolute altitude of the aircraft.

Under the above conditions, the required accuracy $d\alpha$ for the roll and pitch angles using (7.15) is 0.11°.

In the shipborne altimetry application, the required accuracy for the roll and pitch angles is much lower than in airborne altimetry, due to the smaller range between the distance sensor and the sea surface. For a range r of 3 m, maximum roll and pitch angles α_{max} of 10° on a survey track and a desired height accuracy dh_{max} of 4 cm, the required accuracy $d\alpha$ for the roll and pitch angles using (7.15) is 3.9°.

7.3 Kinematic GPS Positioning

7.3.1 Basic Principle

The methods of airborne and shipborne altimetry, as well as GPS buoy measurements, rely on precise kinematic positions determined by GPS. E.g. in airborne laser altimetry, the absolute position of the aircraft has to be known at any moment during a survey flight in order to georeference the laser ground-point. Thus, the trajectory of the aircraft has to be tracked continuously. This is achieved by kinematic GPS measurements aboard the aircraft, referred to as kinematic GPS positioning or GPS trajectography. GPS trajectography supplies $\boldsymbol{a}^G$ and $\boldsymbol{R}_{G/L}$ of the direct georeferencing equation (7.1). Precise trajectography is one of the major issues in airborne and shipborne altimetry, since the computed position of the laser or ultrasound ground-point directly depends on the position of the aircraft. Positioning errors propagate one-to-one into the ground-point positions and directly affect the observed sea surface heights.

High-precision kinematic GPS positioning relies on differential carrier phase measurements, achieved by simultaneously operating at least one GPS receiver aboard the moving vehicle (e.g. aircraft or ship) and several terrestrial GPS reference stations. The coordinates of the reference stations have to be known or determined with respect to the International Terrestrial Reference Frame (ITRF). The trajectory of the aircraft is computed through kinematic differential GPS carrier phase processing with respect to the reference stations. A sampling rate of at least 1 Hz is usually required on the roving receiver as well as on the reference stations. For high-precision positioning, the resolution of phase ambiguities and cycle slip detection are important issues. The quality of the GPS solutions can be degraded by various factors like tropospheric and ionospheric refraction, radio frequency interference, obstruction of satellite visibility and multi-path effects. Since the baselines between the reference stations and the moving receiver on the aircraft or ship can exceed 100 km, the use of dual-frequency receivers is mandatory to mitigate ionospheric influences.

The software primary used in this work to process kinematic GPS data is a software package for baseline-wise differential kinematic GPS processing developed at the GGL (Cocard, 1995). Investigations were made to assess the kinematic potential of Bernese GPS Software version 5 (Beutler et al., 2007) and its capabilities to estimate tropospheric path delays in kinematic mode (Section 7.3.3).

7.3.2 Atmospheric Influences

GPS phase observations and code pseudoranges are affected by systematic errors due to ionospheric and tropospheric refraction. The ionosphere is a dispersive medium at microwave frequencies, thus the refractive index for GPS signals is frequency-dependent. To the first order, ionospheric refraction is inversely proportional to the square of the frequency of the electromagnetic signal. In the case of dual-frequency GPS measurements, the relation between the ionospheric effect I_1 on the L1 carrier of frequency f_1 and the ionospheric effect I_2 on the L2 carrier of frequency f_2 is

given by (Beutler et al., 2007):

$$I_2 = \frac{f_1^2}{f_2^2} I_1 \tag{7.16}$$

Ionospheric refraction delays the GPS code measurements and advances the carrier phases. The effect has the same absolute value for code and phase measurements, but with opposite signs. Based on 7.16, the effect of ionospheric refraction can be largely mitigated by the use of dual-frequency receivers.

Two kinds of tropospheric biases can be distinguish (Beutler et al., 2007):

- Relative troposphere biases caused by errors of (mismodeled) tropospheric refraction at one endpoint of a baseline relative to the other endpoint.
- Absolute troposphere biases caused by errors of (mismodeled) tropospheric refraction common to both endpoints of a baseline.

Relative troposphere biases cause primarily biased station heights, whereas absolute troposphere biases produce scale biases of the estimated baseline lengths (Beutler et al., 2007). In airborne or shipborne altimetry applications involving differential kinematic GPS data, the relative troposphere biases between the reference station and the aircraft or ship is important, due to its direct impact on the computed sea surface heights. To a first order, the station height bias dh due to a relative troposphere error can be computed as (Beutler et al., 2007):

$$dh = \frac{dr_r}{\cos z_{max}} \tag{7.17}$$

where dr_r is the relative tropospheric zenith delay error and z_{max} is the maximum zenith angle of the observation scenario. In this order of magnitude formula, it is assumed that the satellites are uniformly distributed in the sky above the observing sites. It indicates that a relative troposphere bias of only 1 cm leads to an error of approx. 3 cm in the estimated relative station height for an elevation cutoff angle of 20°. This error increases to 19 cm for an elevation cutoff angle of 3° (Beutler et al., 2007).

Due to the availability of high accuracy orbits from IGS, orbit errors need no longer be considered as an important error source (Beutler et al., 2007). The propagation delay of GPS signals due to atmospheric water vapor in the troposphere are probably the ultimate accuracy-limiting factor for geodetic applications (Beutler et al., 2007; Dodson et al., 1996). At the moment, the major error source in kinematic GPS positioning, and especially in height determination, is the insufficient modeling of the influence of tropospheric path delays. The impact of tropospheric mismodeling on kinematic relative positioning is increased by the height difference between the reference ground station and the moving receiver on the aircraft. An example of the impact of relative troposphere biases on airborne kinematic GPS data is shown in Section 7.3.3.

7.3.3 Case Study: Impacts of Reference Station and Troposphere on Airborne GPS Heights

Aircraft trajectories were computed for the six flights of the GAVDOS airborne campaign around Crete (Section 8.1), using three reference stations (TUC1, GALI and RTHY), yielding three baselines with respect to the aircraft. Stations TUC1 and RTHY are situated at the northern coast of Crete, while station GALI is situated at the southern coast. The altitudes of stations TUC1, GALI and RTHY are 178 m, 34 m and 38 m, resepctively, while the average flight height of the aircraft

Table 7.1: Mean aircraft height differences dh and their standard deviations (std) between trajectory determined with reference stations GALI and TUC1 and with RTHY and TUC1.

Date	Flight	GALI - TUC1 mean dh ± std [m]	RTHY - TUC1 mean dh ± std [m]
2003/01/09	GRL06	-	0.13 ± 0.02
2003/01/09	GRL02	-0.26 ± 0.05	0.05 ± 0.04
2003/01/10	GRL03	-0.16 ± 0.20	0.03 ± 0.11
2003/01/11	GRL05	-0.21 ± 0.06	0.03 ± 0.12
2003/01/13	GRL01	-0.02 ± 0.04	0.03 ± 0.03
2003/01/14	GRL04	-0.04 ± 0.04	0.00 ± 0.04

during surveys was 215 m. During the processing, only a priori altitude-dependent tropospheric path delay corrections where applied, based on the Saastamoinen tropospheric refraction model together with standard atmosphere values, without any in situ meteorological information.

In Fig. 7.3 to Fig 7.7, height differences between baseline-wise trajectories of the same moving antenna aboard the aircraft, obtained using three reference stations, are shown for five flights in chronological order. A summary of the aircraft height differences is given in Tab. 7.1. The height differences range between -0.40 m and 0.25 m (Fig. 7.3 to Fig 7.7). The differences clearly depend both on the used reference station and on the flight day (Tab. 7.1). Two different behaviours can be distinguished. On the first three days of the campaign (2003/01/09, 2003/01/10 and 2003/01/11, flights GRL02, GRL03 and GRL05), the differences between the aircraft heights obtained with GALI and TUC1 show mean differences of up to -0.26 m and standard deviations of up to 0.20 m (Fig. 7.3a to Fig 7.5a). The aircraft heights obtained with RTHY and TUC1 show mean differences around 0.05 m and standard deviations of up to 0.12 m (Fig. 7.3b to Fig 7.5b). Especially for the differences RTHY-TUC1 on flights GRL03 and GRL05, the distributions of height differences show several peaks, indicating inconsistent ambiguity resolutions between different flight sections. On the 2003/01/12, flight operations were cancelled due to bad weather conditions. As can be seen from the atmospheric pressure grids from ECMWF (European Centre for Medium-Range Weather Forecasts) over the Mediterranean Sea (Appendix F), these four days are characterised by a large atmospheric depression over the Mediterranean basin, accompanied by strong pressure gradients around Crete and the entire region. These gradients are obviously producing inhomogeneous tropospheric path delays between the reference stations and the moving receiver, strongly deviating from the a priori troposphere model. On the last two days of the campaign (2003/01/13 and 12003/01/14, flights GRL01 and GRL04), the differences between GALI and TUC1 and between RTHY and TUC1 are in good agreement, with non-significant mean offsets between -0.04 and 0.03 m and near normal distributions with standard deviations below 0.04 m (Fig. 7.6 and Fig 7.7). These two days are characterised by a high pressure regime and small pressure gradients (Appendix F), indicating a more homogeneous troposphere that is better approximated by the a priori troposphere mdoel.

The height differences of the aircraft determined with different reference stations correspond in a very good approximation to the height differences that were directly obtained by kinematic processing of the static baselines between the reference stations, since the airborne data and influences on the airborne data are largely cancelled out in the difference. Hence, errors on the height differences of the aircraft primary reflect errors of mismodelled effects between the two reference stations. Hence, in order to further asses the origin of these height differences, tropospheric zenith path delays (ZPD) at the reference stations, estimated during the static network processing using Bernese GPS software, were analysed. The impacts of these ZPD on the baselines between the reference stations were computed based on (Geiger, 1987), by considering the elevations and azimuths of the satellites used the in airborne GPS processing. These impacts correspond to the theoretical impacts of tropospheric influences on the differences of aircraft positions computed with respect to the different reference stations (Fig. 7.8 and Fig. 7.9, black line). A strong correlation is observed with respect to the obtained position differences of the aircraft (Fig. 7.8 and Fig. 7.9,

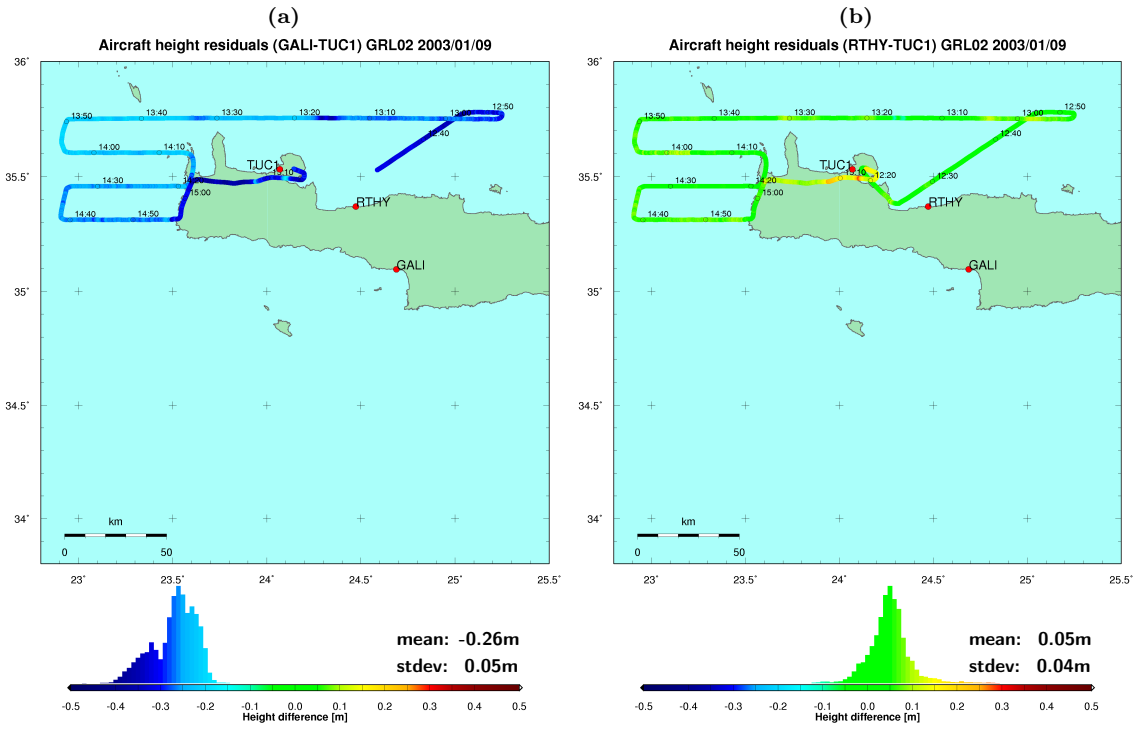

Figure 7.3: Aircraft height differences on 2003/01/09 (flight GRL02) between trajectory determined with reference stations **(a)** GALI and TUC1 and **(b)** RTHY and TUC1.

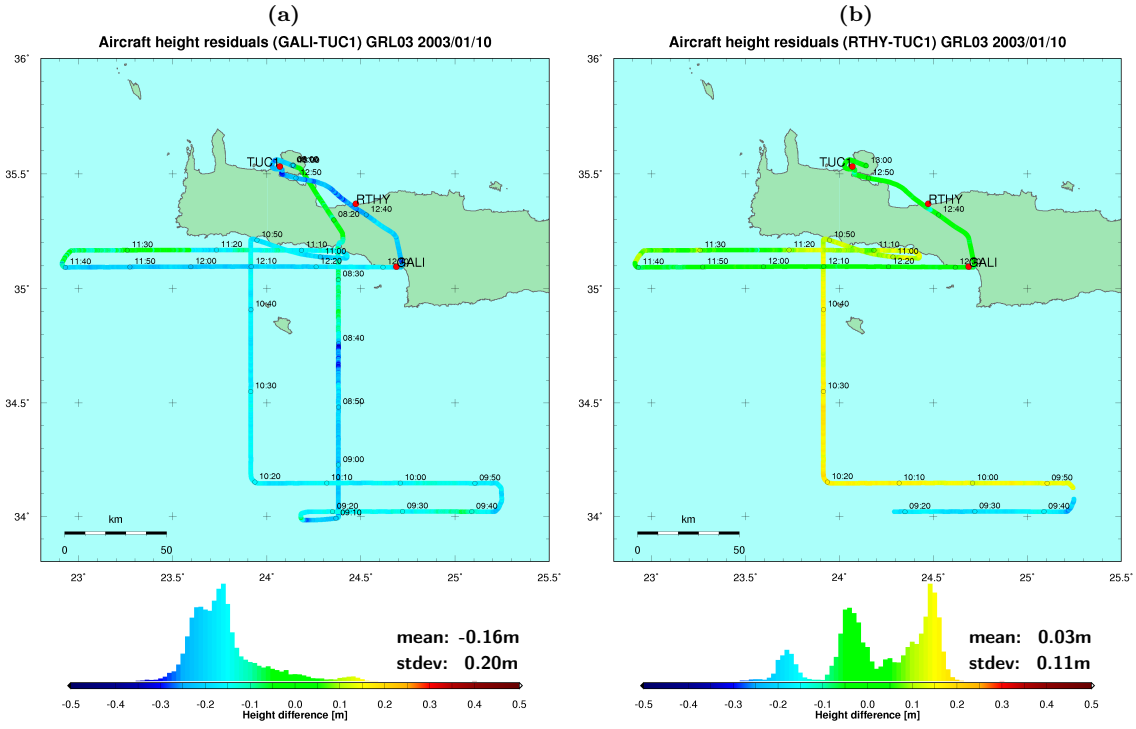

Figure 7.4: Aircraft height differences on 2003/01/10 (flight GRL03) between trajectory determined with reference stations **(a)** GALI and TUC1 and **(b)** RTHY and TUC1.

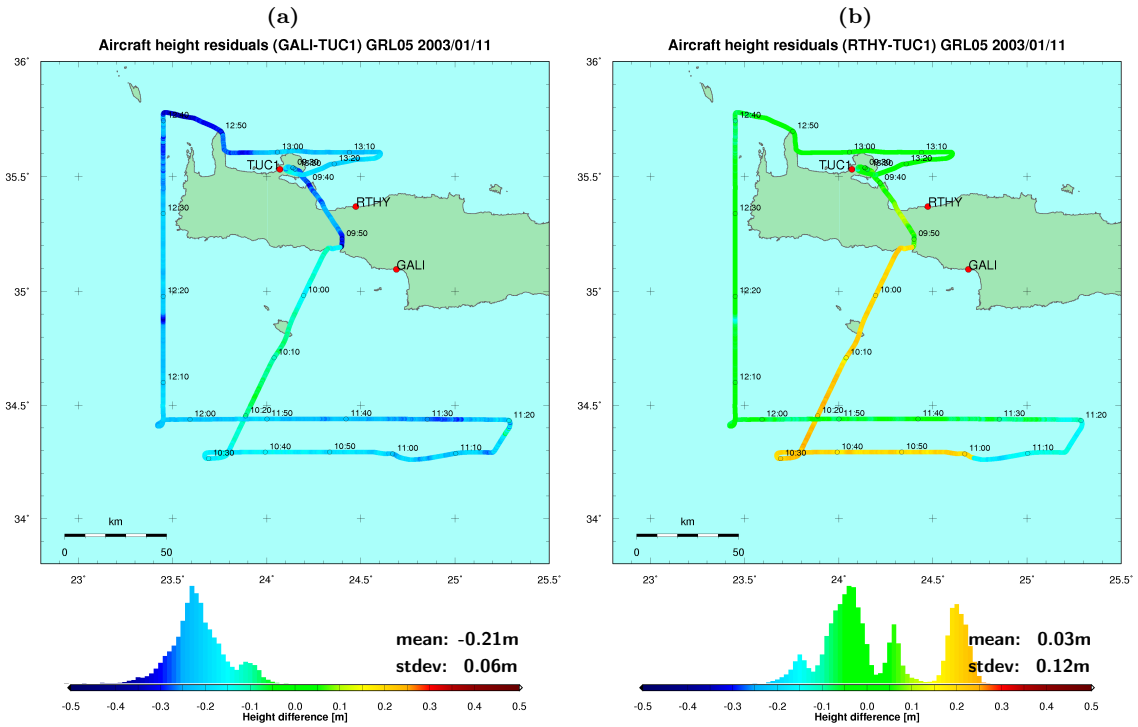

Figure 7.5: Aircraft height differences on 2003/01/11 (flight GRL05) between trajectory determined with reference stations **(a)** GALI and TUC1 and **(b)** RTHY and TUC1.

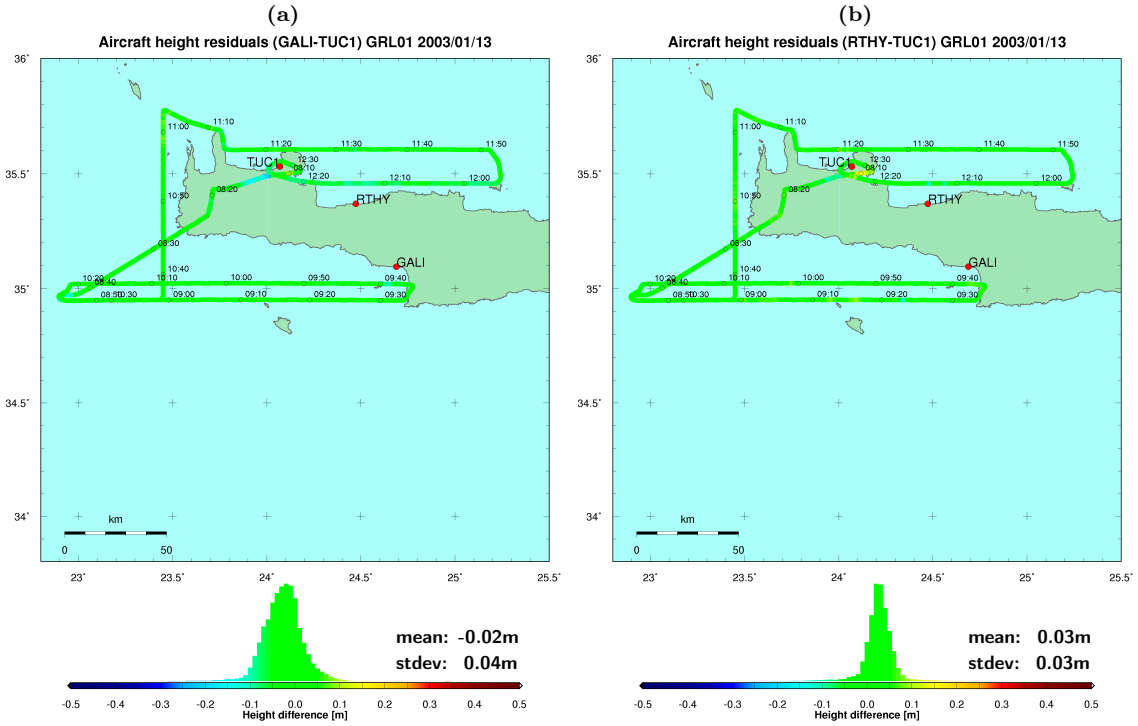

Figure 7.6: Aircraft height differences on 2003/01/13 (flight GRL01) between trajectory determined with reference stations **(a)** GALI and TUC1 and **(b)** RTHY and TUC1.

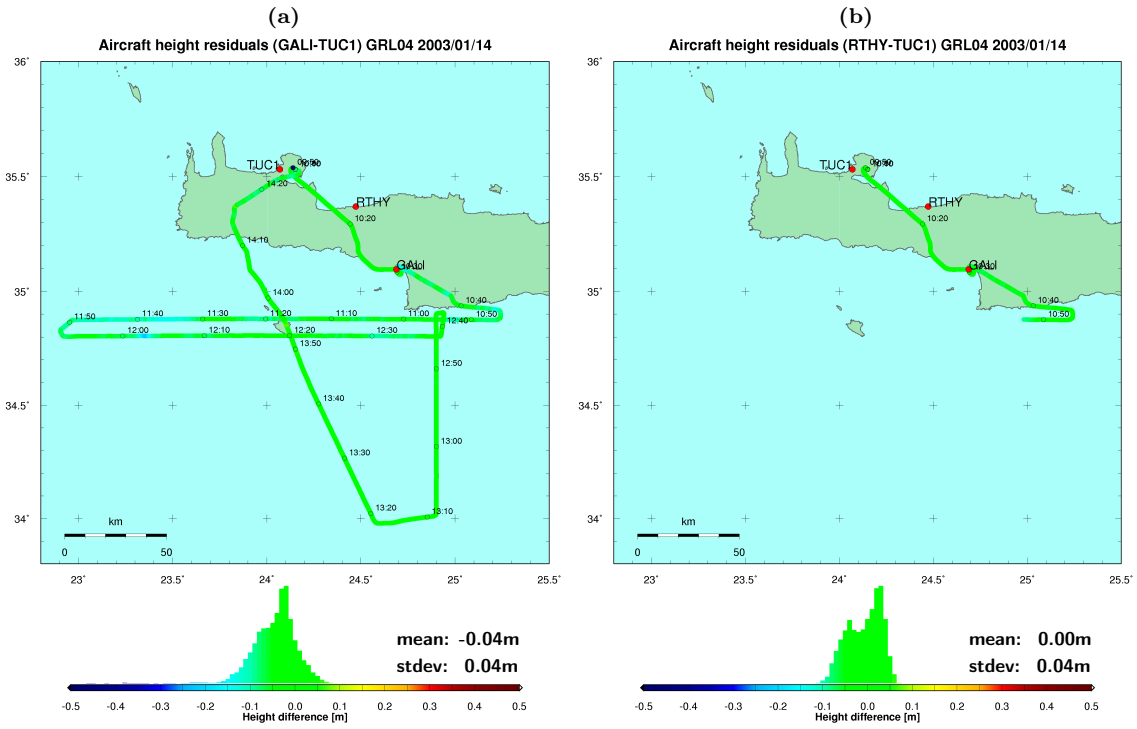

Figure 7.7: Aircraft height differences on 2003/01/14 (flight GRL04) between trajectory determined with reference stations **(a)** GALI and TUC1 and **(b)** RTHY and TUC1.

grey line). Jumps on the theoretical impacts (black line) are produced by abrupt changes in the satellite constellation (rise or fall of a satellite). The observed height differences are not always following these abrupt changes, since the GPS solution is stabilised over longer time periods by the phase ambiguities of satellites constantly tracked. This aspect also explains part of the deviations between the observed differences and the modeled impacts.

Based on the conclusions stated above, investigations were made to assess the kinematic potential of the Bernese GPS Software version 5 (Beutler et al., 2007) and its capabilities of estimating tropospheric path delays in kinematic mode. The Bernese GPS Software is a very powerful state-of-the-art GPS processing software, widely approved by the geodetic community for static processing of permanent GPS networks. The existing source code had to be adapted to the estimation of path delays in kinematic mode. Results similar to the classic solution with path delays predicted from an a priori model were obtained under homogeneous atmospheric conditions. Under extreme tropospheric conditions, differences between the two solutions could easily reach 0.5 m. The analysis of resulting sea surface height differences at crosspoints showed, that with the estimation of tropospheric parameters, it was possible to locally improve the solution, but the overall agreement was always degraded. The analysis also showed that under such conditions, the Bernese solution including the estimation of tropospheric path delays was extremely sensitive to the parameter settings, like e.g. the interval of the piecewise linear tropospheric parameters and their relative constraints, but also a priori weights of observations and parameters. Small changes of the parameters could induce height differences of 1 m. The instability of the solution leads to the conclusion that the algorithms used to model the troposphere are not sophisticated enough to provide a realistic representation of extreme inhomogeneous atmospheric conditions (e.g. atmospheric inversion) in kinematic mode.

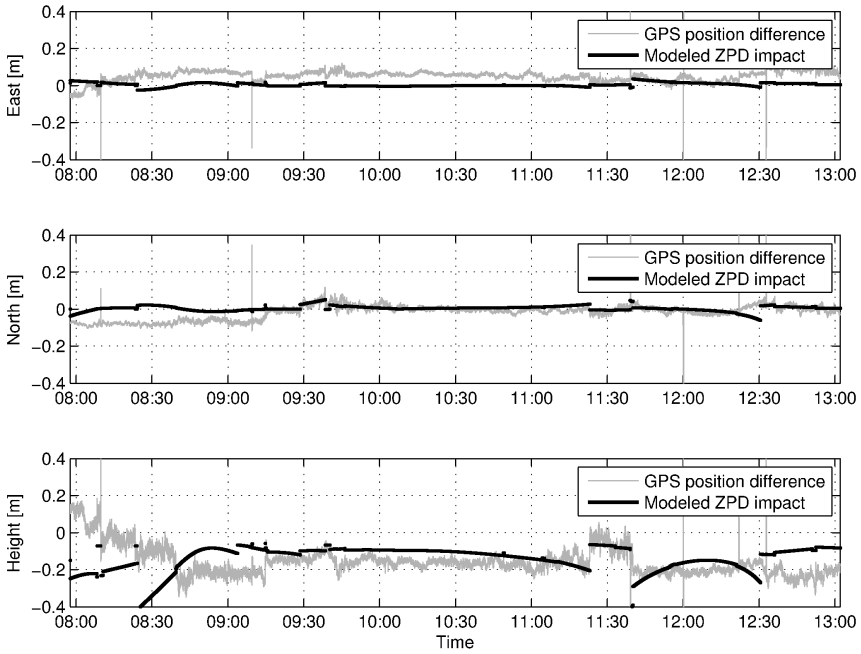

Figure 7.8: Aircraft position differences (grey line) on 2003/01/10 (flight GRL03) between trajectory determined with reference stations GALI and TUC1 (corresponding to Fig. 7.4a), and modeled theoretical impact of tropospheric zenith path delays estimated at the reference stations (black line).

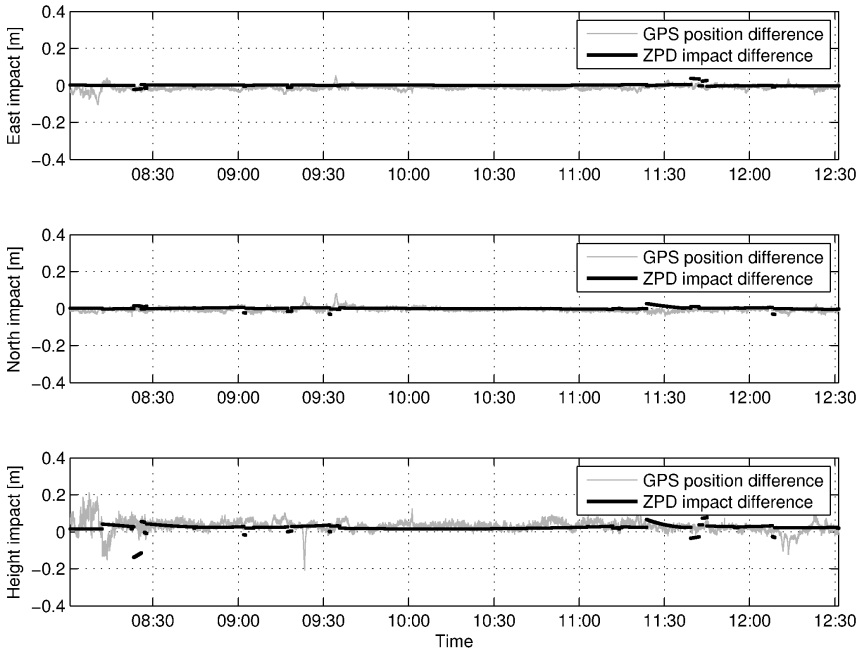

Figure 7.9: Aircraft position differences (grey line) on 2003/01/13 (flight GRL01) between trajectory determined with reference stations RTHY and TUC1 (corresponding to Fig. 7.6b), and modeled theoretical impact of tropospheric zenith path delays estimated at the reference stations (black line).

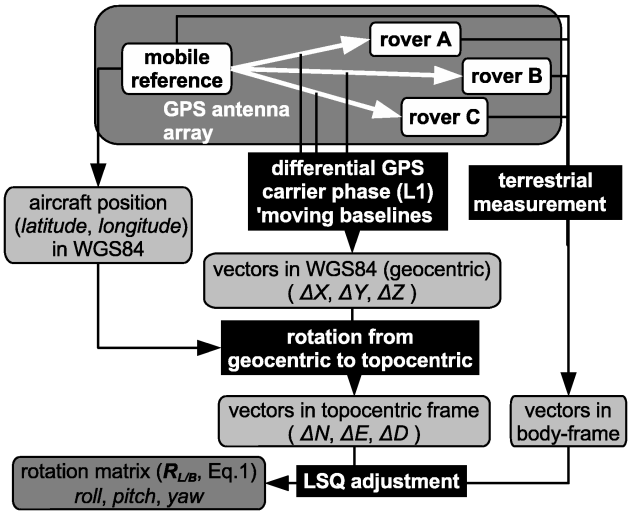

Figure 7.10: Attitude determination with multi-antenna GPS array.

7.4 Multi-Antenna GPS Attitude Determination

7.4.1 Basic Principle

The attitude of an aircraft or of any other vehicle or platform is given by its roll, pitch and yaw angles, which constitute the rotation matrix $\boldsymbol{R}_{L/B}$ of (7.1) and (7.4). Whereas many systems acquire the attitude of a platform using a very accurate, yet expensive inertial measuring unit (IMU) in conjunction with a single GPS receiver for trajectory recovery, another approach for attitude determination is based on a multiple-antenna GPS array. Since three points on a platform determine its movement completely, the relative position of at least three points on the platform needs to be continuously monitored in order to derive its attitude. This is achieved by equipping the platform with an array of at least three GPS antennas, adequately mounted on the platform's topside, so that they form non-collinear baseline vectors between each other. The approach of attitude determination by multi-antenna GPS described in this section is based on (Favey, 2001).

After time-adjusting the resulting moving vectors of the antenna array, they are first rotated from the geocentric GPS reference frame to a topocentric, north oriented frame, using the latitudes and longitudes given by the moving reference antenna (7.3). As the antennas are rigidly mounted on the aircraft, their coordinates are also known in the body frame by terrestrial calibration measurements. Thus, the core problem of attitude determination using a multiple-antenna array can be formulated as follows (Favey, 2001): Given two or more non-collinear vectors in the topocentric coordinate frame L and in the body frame B, find the rotation matrix $\boldsymbol{R}_{L/B}$ (7.4) that transforms the vectors from the body frame into the topocentric frame (Fig. 7.10).

Acquiring attitude information from GPS or IMU shows properties individual to each method (Favey, 2001). As the GPS attitude solution is computed on a per epoch basis, independently from subsequent epochs (except the link through GPS carrier phase ambiguities), the major advantage of the GPS attitude is that it is exempt from random walk (drift) effects. Regarding the IMU attitude, epochs are correlated and suffer from typical drift effects, that have to be corrected by coupling a GPS receiver to the IMU. The major advantage of IMU is its higher sampling rate.

7.4.2 Processing of Moving GPS Baselines

The relative positions of the GPS antennas used to compute the vectors for attitude determination are obtained by so-called 'moving baselines processing'(Fig. 7.10). Like in conventional differential kinematic GPS processing, moving baselines processing is based on differential GPS carrier phase processing, with the only difference that the two receivers forming a baseline are moving. During processing, one of the moving receivers is defined as reference. The coordinates of its antenna are fixed to an approximate kinematic position (e.g. stande-alone code solution), since only the relative vector is of interest. The reference receiver is used to compute the relative positions of the other antennas by differential GPS carrier phase processing. Since the lengths of the baselines are usually less than 10 m, relative atmospheric path delay errors between the reference and remote receiver are negligible and ambiguity resolution usually causes no major problem, unless severe interferences or lack of satellite visibility are encountered. Since the lengths of the vectors are theoretically constant and known by terrestrial measurements, they may be introduced in the GPS baseline processing as additional information. The obtained GPS vectors are corrected for differential clock bias using (E.8) (Appendix E) in an intermediate step before computing the LSQ adjustment for attitude retrieval (Section 7.4.3). The approach of moving baselines processing used in this project is based on (Favey, 2001).

7.4.3 Algorithm for Multi-Antenna GPS Attitude Determination

Approximate Attitude Solution from Two Vectors

An approximate attitude solution can be calculated using two vectors. Considering two vectors $\boldsymbol{k}_1^L$ and $\boldsymbol{k}_2^L$ obtained from three GPS antennas in the topocentric frame L, and the corresponding vectors $\boldsymbol{k}_1^B$ and $\boldsymbol{k}_2^B$ determined by terrestrial calibration measurements in the body frame B (Fig. 7.11), the basic equation can be written as (Favey, 2001):

$$\boldsymbol{k}_i^L \;=\; \boldsymbol{R}_{L/B}\,\boldsymbol{k}_i^B \tag{7.18}$$

The approximate solution for the rotation matrix $\boldsymbol{R}_{L/B}$ in (7.18) is obtained by:

$$\boldsymbol{R}_{L/B} \;\approx\; \boldsymbol{L}\boldsymbol{B}^T \;=\; \boldsymbol{R}_0 \tag{7.19}$$

where $\boldsymbol{R}_0$ is the obtained approximated rotation matrix, and $\boldsymbol{L}$ and $\boldsymbol{B}$ are rotation matrices given by:

$$\boldsymbol{L} \;=\; \left(\boldsymbol{i}_1^{L'},\, \boldsymbol{i}_2^{L'},\, \boldsymbol{i}_3^{L'}\right), \quad \boldsymbol{B} \;=\; \left(\boldsymbol{i}_1^{B'},\, \boldsymbol{i}_2^{B'},\, \boldsymbol{i}_3^{B'}\right) \tag{7.20}$$

with

$$\boldsymbol{i}_1^{L'} = \frac{\boldsymbol{k}_1^L}{\left\|\boldsymbol{k}_1^L\right\|}, \quad \boldsymbol{i}_2^{L'} = \boldsymbol{i}_3^{L'} \times \boldsymbol{i}_1^{L'}, \quad \boldsymbol{i}_3^{L'} = \frac{\boldsymbol{k}_1^L \times \boldsymbol{k}_2^L}{\left\|\boldsymbol{k}_1^L \times \boldsymbol{k}_2^L\right\|} \tag{7.21}$$

$$\boldsymbol{i}_1^{B'} = \frac{\boldsymbol{k}_1^B}{\left\|\boldsymbol{k}_1^B\right\|}, \quad \boldsymbol{i}_2^{B'} = \boldsymbol{i}_3^{B'} \times \boldsymbol{i}_1^{B'}, \quad \boldsymbol{i}_3^{B'} = \frac{\boldsymbol{k}_1^B \times \boldsymbol{k}_2^B}{\left\|\boldsymbol{k}_1^B \times \boldsymbol{k}_2^B\right\|} \tag{7.22}$$

The approximate attitude angles roll (α_x), pitch (α_y) and yaw (α_z) are derived directly from the elements r_{ij} of the resulting rotation matrix $\boldsymbol{R}_{L/B}$ (7.4):

$$\alpha_x \;=\; \arctan\left(r_{32}/r_{33}\right), \quad \alpha_y \;=\; \arcsin\left(r_{31}\right), \quad \alpha_z \;=\; \arctan\left(r_{21}/r_{11}\right) \tag{7.23}$$

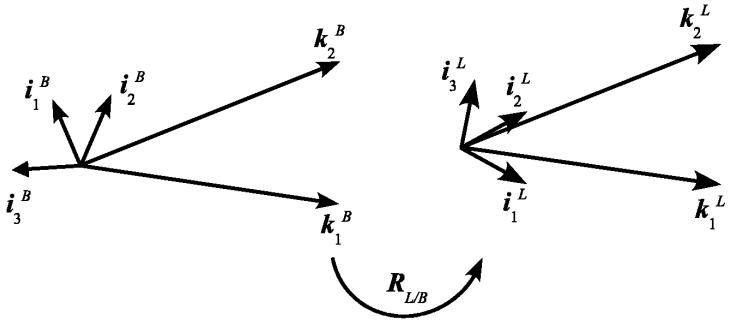

Figure 7.11: Rotation of a two-vector array from body frame B to topocentric frame L using rotation matrix $\boldsymbol{R}_{L/B}$.

Attitude Estimation from Least-Squares Adjustment

If more than two vectors (more than three antennas) are available, an optimal solution can be estimated by least-squares (LSQ) adjustment. An LSQ model for every epoch is obtained by taking (7.18) as the observation equation of a parametric LSQ adjustment for each vector i (Favey, 2001):

$$\boldsymbol{k}_1^L \; - \; \boldsymbol{v}_i \; = \; \boldsymbol{R}_{L/B} \; \boldsymbol{k}_i^B \tag{7.24}$$

which is of the general form $\boldsymbol{l} - \boldsymbol{v} = F(\boldsymbol{x})$. In this equation, the vectors $\boldsymbol{k}_i^L$ in the topocentric frame L, derived from GPS moving baseline processing, are considered as the observations l, with residuals $\boldsymbol{v}$. The unknown parameters $\boldsymbol{x}$ are the attitude angles forming the rotation matrix $\boldsymbol{R}_{L/B}$ (7.4). The vectors $\boldsymbol{k}_i^B$ in the body frame, determined by terrestrial calibration measurements, are considered as error-free. Linearization of (7.24) near the approximate values yields:

$$\boldsymbol{k}_1^L \; - \; \boldsymbol{v}_i \; = \; \boldsymbol{R}_0 \; \boldsymbol{k}_i^B \; + \; \boldsymbol{A}_i \; \delta\boldsymbol{x} \tag{7.25}$$

which is of the general form:

$$\boldsymbol{l} \; - \; \boldsymbol{v} \; = \; F(\boldsymbol{x}_0) \; + \; \left|\frac{\partial F(\boldsymbol{x})}{\partial \boldsymbol{x}}\right|_{\boldsymbol{x}_0} (\boldsymbol{x} - \boldsymbol{x}_0) \; = \; F(\boldsymbol{x}_0) \; + \; \boldsymbol{A} \; \delta\boldsymbol{x} \tag{7.26}$$

where $\boldsymbol{x}_0$ are the approximate attitude angles from (7.23), $\delta x = (\boldsymbol{x} - \boldsymbol{x}_0)$ are the increments of the parameters, $\boldsymbol{R}_0 = \boldsymbol{R}_{L/B}(\boldsymbol{x}_0)$ is the approximate rotation matrix calculated from two vectors (7.19) and $\boldsymbol{A}_i$ is the design matrix of the LSQ adjustment, with:

$$\boldsymbol{A}_i \; = \; \left|\frac{\partial F_i}{\partial \boldsymbol{x}}\right|_{\boldsymbol{x}_0} = \; \left|\frac{\partial (\boldsymbol{R}_{L/B} \; \boldsymbol{k}_i^B)}{\partial \boldsymbol{x}}\right|_{\boldsymbol{x}_0} \approx \; \left|\frac{\partial \boldsymbol{R}_0 \; \boldsymbol{k}_i^B \; + \; \boldsymbol{R}_0 \; \boldsymbol{K}_i^B \; \delta\boldsymbol{x}}{\partial \boldsymbol{x}}\right|_{\boldsymbol{x}_0} = \; \boldsymbol{R}_0 \; \boldsymbol{K}_i^B \tag{7.27}$$

In (7.27), only the rotation matrix $\boldsymbol{R}_{L/B}$ is a function of $\boldsymbol{x}$. Thus, the expression to be differentiated in (7.27) was linearized using:

$$\boldsymbol{R}_{L/B} \; \boldsymbol{k}_i^B = \; \boldsymbol{R}(\boldsymbol{x}_0 + \delta\boldsymbol{x}) \; \boldsymbol{k}_i^B \; = \; \boldsymbol{R}_0 \; \boldsymbol{R}(\delta\boldsymbol{x}) \; \boldsymbol{k}_i^B \approx \; \boldsymbol{R}_0 \; (\boldsymbol{I} + \boldsymbol{\Omega}) \; \boldsymbol{k}_i^B \; = \; \boldsymbol{R}_0 \; \boldsymbol{k}_i^B + \boldsymbol{R}_0 \; \boldsymbol{K}_i^B \; \delta\boldsymbol{x} \tag{7.28}$$

with

$$\boldsymbol{\Omega}\ \boldsymbol{k}_i^B \ = \ \begin{pmatrix} 0 & \delta x_3 & -\delta x_2 \\ -\delta x_3 & 0 & \delta x_1 \\ \delta x_2 & -\delta x_1 & 0 \end{pmatrix} \begin{pmatrix} k_{i,1}^B \\ k_{i,2}^B \\ k_{i,3}^B \end{pmatrix} \ = \ \begin{pmatrix} 0 & -k_{i,3}^B & k_{i,2}^B \\ k_{i,3}^B & 0 & -k_{i,1}^B \\ -k_{i,2}^B & k_{i,1}^B & 0 \end{pmatrix} \begin{pmatrix} \delta x_1 \\ \delta x_2 \\ \delta x_3 \end{pmatrix} \ = \ \boldsymbol{K}_i^B\ \delta\boldsymbol{x} \quad (7.29)$$

where $\boldsymbol{K}_i^B$ is a skew symmetric matrix containing the elements of $\boldsymbol{k}_i^B$. The solution of the LSQ adjustment for one epoch is finally given by (Favey, 2001):

$$\delta\boldsymbol{x} \ = \ \left(\sum_i \ \boldsymbol{A}_i^T\ \boldsymbol{P}_i\ \boldsymbol{A}_i \right)^{-1} \cdot \sum_i \ \boldsymbol{A}_i^T\ \boldsymbol{P}_i\ \boldsymbol{v}_{0,i} \quad (7.30)$$

where $\boldsymbol{P}_i$ is the weight matrix and $\boldsymbol{v}_{0,i}$ are the approximate residuals obtained by:

$$\boldsymbol{v}_{0,i} \ = \ \boldsymbol{l}_i \ - \ F_i\left(\boldsymbol{x}_0\right) \ = \ \boldsymbol{k}_i^L \ - \ \boldsymbol{R}_0\ \boldsymbol{k}_i^B \quad (7.31)$$

Since the observation equation (7.24) is nonlinear, the LSQ adjustment needs to be iterated a few times with $\boldsymbol{R}_0$ improved as $\boldsymbol{R}_{L/B}(\boldsymbol{x}_0 + \delta\boldsymbol{x})$ (Favey, 2001).

7.4.4 Accuracy Estimation of Multi-Antenna GPS Attitude

The attitude of the aircraft and boat was determined using the multi-antenna GPS arrays (Fig. 4.1 and Fig. 5.3), operated at a sampling rate of 2 Hz. The accuracy σ_a of the estimation by multi-antenna GPS array depends on:

- the differential GPS ranging error σ_r (7.32)
- the baseline length l (7.32)
- the antenna vector geometry (optimal configuration in case of orthogonal vectors)

Since the multi-antenna GPS attitude estimation is computed using GPS baseline vectors, its accuracy σ_a depends on the antenna vector geometry. The configuration is optimal in the sense of minimizing attitude errors when the antennas are arranged to build orthogonal vectors, which is almost impossible on an aircraft or a boat. Another strategy to reduce the attitude error σ_a consists in increasing the baseline lengths, since the attitude error directly depends on the differential GPS positioning error σ_r and the baseline length l, according to the following formula (Fig. 7.12):

$$\sigma_a \ = \ \frac{\sigma_r}{l} \quad [rad] \quad (7.32)$$

For example, in order to reach an attitude accuracy σ_a of 0.01°, with a vector accuracy σ_r of 1 cm, a baseline length l of about 57 m would be required. The antenna configurations in the used setups (Fig. 4.1 and Fig. 5.3) were chosen to have the vectors as orthogonal as possible with maximum possible lengths.

The attitude accuracy obtained during a survey flight cannot be measured directly, but it can be quantified by different methods (Tab. 7.2). First, the accuracy can be assessed using (7.32). In the airborne application, two antennas were mounted on the wing-engines (Fig. 4.1), in order to reach the best compromise between wing-flexure effects and baseline length. Maximizing baseline lengths by mounting the antennas on the wing-tips would reduce the accuracy, since the wing-flexure on the tips can easily exceed 10 cm. In the chosen setup, the distance between the engine antennas, relevant for the roll angle, is 5.5 m, whereas the baseline length between the forward

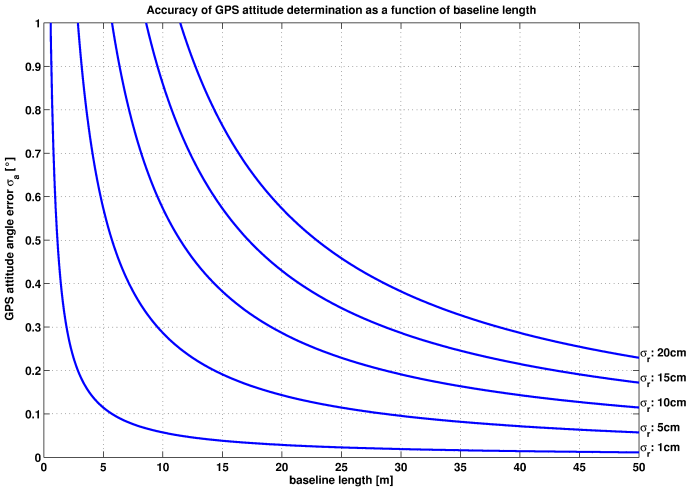

Figure 7.12: Error σ_a of attitude determined by multi-antenna GPS, according to (7.32), as a function of baseline length l, for differential GPS positioning errors σ_r from 1 to 20 cm.

and tail antennas, relevant for the pitch and yaw angles, is 10.0 m. During the flights studied here, the RMS of the difference between the baseline lengths determined by GPS and the terrestrially calibrated lengths is in the order of 0.9 cm, yielding theoretical attitude accuracies of 0.08° for the roll and 0.05° for the pitch and yaw (Tab. 7.2), based on (7.32). The average attitude standard deviations estimated by the LSQ adjustment during attitude determination are in the same order of magnitude (Tab. 7.2). Finally, the standard deviation of differences between attitudes determined with GPS and INS are in the order of 0.11° for the roll and pitch, and 0.06° for the yaw. The differences between GPS and INS attitude are analysed in more detail in Section 7.4.5. It can be concluded that the obtained attitude accuracies are in the order of 0.10° and that they meet the required accuracy value of 0.11° established in Section 7.2.4.

Similar to the airborne case, the obtained attitude accuracy of the boat was quantified by different methods (Tab. 7.2). The shipborne data analysed in Tab. 7.2 corresponds to 18 survey-tracks during the 2007 campaign. For the shipborne antenna setup (Fig. 5.3), the baseline length between the portside and starboard antennas, relevant for the roll angle, is 2.7 m, whereas the baseline length between the bow and stern antennas, relevant for the pitch and yaw angle, is 12.5 m. The RMS of the difference between the baseline lengths determined by GPS and the terrestrially calibrated lengths is 0.9 cm, yielding theoretical attitude accuracies of 0.19° for the roll and 0.04° for the pitch and yaw (Tab. 7.2), based on (7.32). The obtained attitude accuracies from LSQ adjustment are about twice the theoretical values (Tab. 7.2). This is most likely due to inaccurate, because hard to measure, bodyframe coordinates on the boat. Nevertheless, it can be concluded that the obtained accuracies easily meet the required value of 3.9° established in Section 7.2.4. The differences between GPS and IMU attitude are discussed in Section 7.4.6.

7.4.5 Case Study: Airborne Multi-Antenna GPS vs. Tactical-Grade INS

Two independent systems for attitude determination were operated aboard the aircraft: the multi-antenna GPS array (Section 4.2.4, Fig. 4.1) and a Honeywell H-764G tactical-grade inertial navigation system (INS), coupled with GPS (Section 4.2.5, Fig. 4.2a). The simultaneous operation of the two systems allowed to directly compare their performance under the given conditions (Tab. 7.3 and Fig. 7.13).

Significant offsets between the GPS and INS attiude solutions were observed, persisting throughout the campaign (Tab. 7.3). Mean offsets are 0.50° on the roll, -0.91° on the pitch and -0.42° on

Table 7.2: Estimated accuracy of attitude determined by multi-antenna GPS array, for the airborne and the shipborne setup.

	ROLL		PITCH		YAW	
	airborne	shipborne	airborne	shipborne	airborne	shipborne
baseline RMS [m][1]	0.008	0.009	0.009	0.009	0.009	0.009
theor. attitude SD [°][2]	0.08	0.19	0.05	0.04	0.05	0.04
GPS LSQ SD [°][3]	0.14	0.31	0.05	0.08	0.06	0.08
GPS-INS SD [°][4]	0.11	0.32	0.11	0.22	0.08	0.38

[1] average RMS of differences between baseline lengths determined by GPS and by terrestrial calibration
[2] average attitude standard deviation (SD) from (7.32) using baseline RMS
[3] average attitude standard deviation (SD) estimated during LSQ adjustment
[4] average standard deviation (SD) of differences between GPS and INS attitude

the yaw. These offsets are of similar size as those observed by (Favey, 2001) using the same GPS antenna array on the same aircraft, but a different inertial system. The offsets reveal that there is a misalignment between the body frames defined by the GPS antennas and the INS. The coordinates of the GPS antennas with respect to the aircraft body frame were measured using a terrestrial tachymeter setup (Favey, 2001). For this purpose, the aircraft was jacked up and levelled out in the hangar. Highly precise antenna coordinates in the aircraft frame were obtained, showing a standard deviation below 1 mm. If the offsets were produced by wrong coordinates of the GPS antennas, the offset of 0.50° on the roll would correspond to a vertical error of 4.8 cm on the 5.5 m baseline between the wing antennas, and the offset of -0.91° on the pitch would correspond to a vertical error of 15.9 cm on the 10.0 m baseline between the front and tail antennas. Since such large errors on the terrestrial measurements can be excluded, the offsets must be produced by a misalignment between the INS and the aircraft body frame. Since the INS unit and the laser profiler were mounted on the same rigid platform (Fig. 4.2a), it can be assumed that the aircraft body frame as defined by the INS is more consistent with the frame of the laser device than the body frame defined by the GPS antenna array. This assumption was confirmed during the boresight misalignment calibration, where smaller misalignements were obtained between the laser frame and INS body frame (Section 7.5.5).

Apart from the offsets, a very good agreement was observed between the attitude solutions provided by the two independent systems, with mean standard deviations of 0.11° on the roll and pitch, and 0.08° on the yaw (Tab. 7.3). The standard deviations are of the same order of magnitude as the expected accuracy of the multi-antenna GPS attitude determination (Section 7.4.4, Tab. 7.2). Furthermore, the differences between the attitudes as determined by the two systems revealed no noticeable drift effect on the INS, demonstrating the efficiency of the coupling with GPS. Given the excellent agreement between the two independent attitude systems, the GPS attitude solution could be merged with the INS data in a loosely-coupled implementation for enhancement purposes.

7.4.6 Case Study: Shipborne Multi-Antenna GPS vs. MEMS-based AHRS

Two independent systems for attitude determination were operated aboard the boat during the 2007 campaign: the multi-antenna GPS array (Section 5.2.3, Fig. 5.3) and an Xsens MTi miniature MEMS-based AHRS (Attitude and Heading Reference System) (Section 5.2.4, Fig. 5.4). The simultaneous operation of the two independent systems allowed to directly compare their performance under the given conditions (Tab. 7.4 and Fig. 7.15). Due to the good agreement between the multi-antenna GPS system and the Honeywell H-764G tactical-grade INS (Section 7.4.5), the GPS derived attitude can be considered as reference solution for the AHRS.

Significant offsets between the GPS and AHRS attitude solutions were observed, persisting throughout the campaign (Tab. 7.4). Mean offsets are -2.67° on the roll and -4.83° on the pitch. These

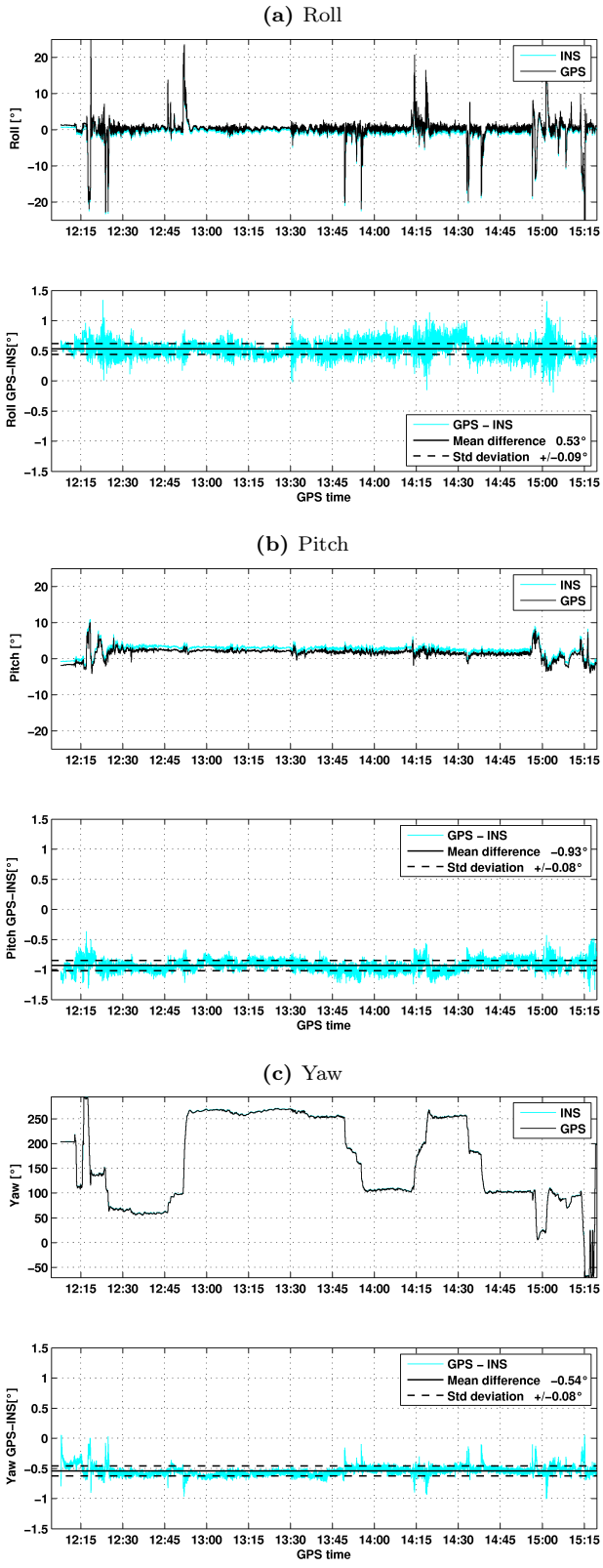

Figure 7.13: Example of attitude angles from the Honeywell H-764G tactical-grade INS and the multi-antenna GPS array, and their differences, during survey-flight GRL02.

Table 7.3: Mean differences and standard deviations (std) between airborne attitude angles from multi-antenna GPS array and Honeywell H764G tactical-grade INS.

Date	Flight	Roll GPS-INS Mean ± std [°]	Pitch GPS-INS Mean ± std [°]	Yaw GPS-INS Mean ± std [°]
09/01/2003	GRL06	0.50 ± 0.09	-0.88 ± 0.12	-0.50 ± 0.07
09/01/2003	GRL02	0.53 ± 0.09	-0.93 ± 0.08	-0.54 ± 0.08
10/01/2003	GRL03	0.53 ± 0.12	-0.92 ± 0.13	-0.32 ± 0.07
11/01/2003	GRL05	0.50 ± 0.12	-0.92 ± 0.11	-0.35 ± 0.09
13/01/2003	GRL01	0.45 ± 0.15	-0.89 ± 0.10	-0.34 ± 0.07
14/01/2003	GRL04	0.38 ± 0.25*	-0.90 ± 0.09	-0.49 ± 0.10
	Mean	**0.50 ± 0.11**	**-0.91 ± 0.11**	**-0.42 ± 0.08**

* GPS attitude computed without left-wing receiver due to receiver breakdown, yielding poor roll angle determination. This roll information was excluded from mean computation.

Table 7.4: Mean differences and standard deviations (std) between shipborne attitude angles from multi-antenna GPS array and Xsens MTi miniature AHRS.

Date		Roll GPS-AHRS Mean ± std [°]	Pitch GPS-AHRS Mean ± std [°]	Yaw GPS-AHRS Mean ± std [°]	Yaw GPS-AHRS[2] Mean ± std [°]
08/09/2007	moving	-2.61 ± 0.28	-4.97 ± 0.20	6.16 ± 1.02[1]	4.61 ± 0.46[2]
08/09/2007	static	-2.60 ± 0.37	-4.85 ± 0.16	1.86 ± 0.33[1]	4.73 ± 0.33[2]
08/09/2007	static	-2.69 ± 0.32	-4.81 ± 0.16	1.92 ± 0.32[1]	4.78 ± 0.33[2]
09/09/2007	moving	-2.58 ± 0.49	-4.89 ± 0.27	4.63 ± 2.29[1]	4.44 ± 0.47[2]
09/09/2007	static	-2.68 ± 0.21	-4.81 ± 0.14	3.85 ± 2.02[1]	4.79 ± 0.42[2]
09/09/2007	moving	-2.57 ± 0.32	-4.86 ± 0.21	4.30 ± 2.57[1]	4.69 ± 0.42[2]
10/09/2007	static	-2.72 ± 0.23	-4.79 ± 0.14	5.50 ± 2.05[1]	4.79 ± 0.30[2]
10/09/2007	moving	-2.65 ± 0.24	-4.88 ± 0.19	4.74 ± 2.34[1]	4.47 ± 0.39[2]
10/09/2007	static	-2.61 ± 0.22	-4.87 ± 0.12	3.80 ± 1.35[1]	4.82 ± 0.24[2]
11/09/2007	moving	-2.70 ± 0.32	-4.88 ± 0.23	3.75 ± 1.86[1]	4.62 ± 0.41[2]
	Mean			**4.05 ± 1.62**[1]	**4.67 ± 0.38**[2]
15/09/2007	moving	-2.74 ± 0.38	-4.63 ± 0.23	4.83 ± 0.85[3]	5.53 ± 0.64[4]
16/09/2007	moving	-2.64 ± 0.48	-4.95 ± 0.32	4.87 ± 1.27[3]	4.63 ± 0.97[4]
17/09/2007	moving	-2.63 ± 0.31	-4.80 ± 0.18	6.12 ± 0.51[3]	5.53 ± 0.52[4]
18/09/2007	moving	-2.65 ± 0.35	-4.80 ± 0.22	5.37 ± 0.76[3]	4.80 ± 0.67[4]
19/09/2007	moving	-2.90 ± 0.33	-4.80 ± 0.54	4.91 ± 0.88[3]	5.51 ± 0.60[4]
20/09/2007	static	-2.72 ± 0.30	-4.74 ± 0.18	4.98 ± 0.44[3]	5.38 ± 0.41[4]
	Mean	**-2.67 ± 0.32**	**-4.83 ± 0.22**	**5.18 ± 0.79**[3]	**5.23 ± 0.64**[4]

[1] Uncalibrated AHRS yaw anlge
[2] AHRS yaw anlge calibrated with GPS reference yaw based on (7.33) (Fig. 7.14)
[3] AHRS yaw anlge calibrated by instrumental magnetometer calibration
[4] AHRS yaw anlge calibrated by instrumental magnetometer calibration and GPS reference yaw

offsets are produced by the approximate mechanical alignement of the AHRS with respect to the boat axes and the horizontal plane. The offsets are in accordance with roll an pitch misalignments of 2.7° and 4.1° with respect to the horizontal plane, approximately measured with a clinometer.

The offset on the yaw angle depends on the calibration method used for the AHRS data. Since the yaw (heading) determination of the AHRS mainly relies on 3D magnetometer data, it suffers from disturbances of the Earth magnetic field. In shipborne applications, the disturbances are mainly produced by the magnetic field caused by the structure and machinery of the ship. The deviation of a magnetic compass can be modeled by (NGA, 2004):

$$\Delta\omega = A + B\sin\omega + C\cos\omega + D\sin 2\omega + E\cos 2\omega \tag{7.33}$$

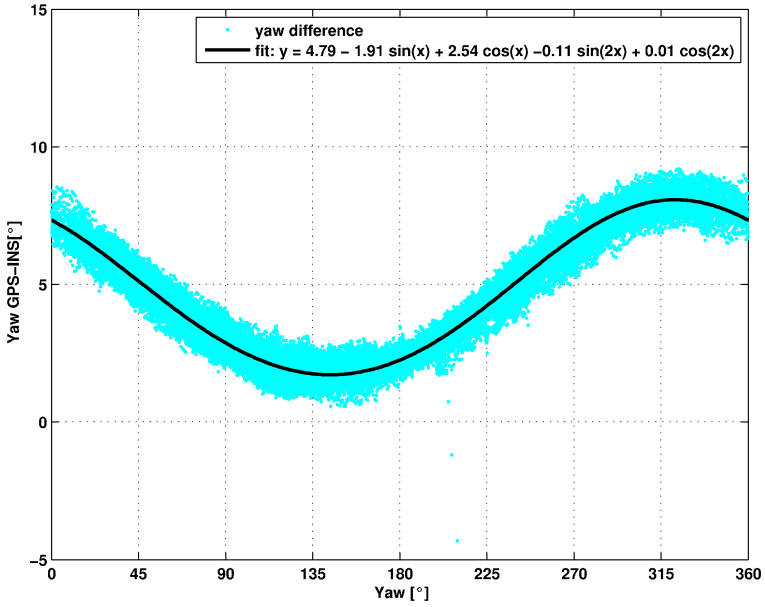

coefficient	value [°]	std [°]
A	4.786	0.0013
B	-1.908	0.0018
C	2.544	0.0019
D	-0.113	0.0017
E	0.007	0.0018

Figure 7.14: Example of difference between yaw (heading) from shipborne multi-antenna GPS array and Xsens MTi AHRS (labeled INS) as a function of yaw angle, over a period of 10 hours. A heading deviation curve of the AHRS was estimated by an least-squares adjustment based on (7.33). The five magnetic deviation coefficients and their standard deviation (std) are shown on the right.

where ω is the heading angle and $\Delta\omega$ is the heading error or deviation. Coefficient A accounts for a permanent offset, while coefficients B and C account for effects produced by the hard-iron portions of the ship's structure. Hard-iron portions behave like permanent magnets and retain their polarity as the ship rotates (Kayton and Fried, 1997), causing a magnetic disturbance with a period of 360°. Electrical equipment, motors and wiring aboard the ship produce fixed magnetic fields that rotate with the ship and have the same effect as hard iron (Kayton and Fried, 1997). However, the magnetic field depends on the power-on status of the electrical equipment. Coefficients D and E account for effects produced by the soft-iron portions of the ship's structure, made of highly-permeable magnetic material. Soft iron is magnetized by the Earth by induction. As the ship rotates, the soft iron remains polarized so that its north-facing poles always face the north pole (Kayton and Fried, 1997), causing a magnetic disturbance with a period of 180°.

Using the yaw determined by the multi-antenna GPS system as a reference, the heading deviation $\Delta\omega$ between the GPS and AHRS solution can be computed for every yaw angle ω. If observations were made under a large number of different headings, a heading deviation curve given by the five coefficients of (7.33) can be estimated using a least-squares adjustment (Fig. 7.14). As for the roll and pitch angles, the yaw offset (coefficient A in (7.33)) is caused by the misalignement between the AHRS and the body frame. Since the yaw angles of the GPS system and the AHRS are referenced to the geographic and the magnetic North, respectively, the yaw offset also includes the difference between the magnetic and geographic North (magnetic declination). For the given location and time, the magnetic declination is 3.5°, yielding a remaining yaw misalignement of 1.3°for the given example (Fig. 7.14). In Tab. 7.4, four types of AHRS yaw angles have to be distinguished:

[1] uncalibrated AHRS yaw. The yaw deviation of the AHRS depends on the yaw angle itself, yielding variable mean offsets with resepct to the GPS yaw (Tab. 7.4), irregular distributions of the differences (Fig. 7.15c) and consequently a high mean standard deviation of 1.62°.

[2] AHRS yaw calibrated in post-processing with the yaw from GPS, based on (7.33) (Fig. 7.14).

The calibrated yaw deviation no longer depends on the yaw angle, yielding a mostly constant offset with resepct to the yaw from GPS (Tab. 7.4) and a normal distribution of the differences (Fig. 7.15d). The calibration allowed to reduce the mean standard deviation to 0.38°.

[3] AHRS yaw determined with anterior magnetometer calibration using the Xsens Magnetic Field Mapper software. The calibration is obtained by performing a complete heading rotation of the ship with the sensor mounted in its final position. Because this calibration does not rely on a reference yaw, this case corresponds to the expected yaw accuracy that can be obtained with the Xsens MTi in stand-alone operation. The mean standard deviation of 0.79°with respect to the GPS solution is less good than the results with the yaw calibration (case [2]). However, a clear improvement with respect to the uncalibrated heading (case [1]) is obtained.

[4] AHRS yaw determined with calibrated magnetometers (case [3]), followed by the post-processing yaw calibration (case [2]). The post-processing calibration allowed to reduce the mean standard deviation to 0.64°, but not to the same degree as in case [2].

Apart from the offsets, a very good agreement between the attitude solutions provided by the two independent systems was observed, with mean standard deviations of 0.32° on the roll and 0.22° on the pitch (Tab. 7.4). For the yaw, standard deviations of 0.38° can be obtained, depending on the calibration (Tab. 7.4). As opposed to the multi-antenna GPS system, there is no reason for an inhomogeneous accuracy between the roll an pitch determined with the AHRS. Furthermore, the standard deviation of the roll differences is very similar to the standard deviation of 0.31° of the roll estimation with the multi-antenna GPS system (Tab. 7.2). Hence, the roll agreement is limited by the weak roll determination of the GPS system, due to the short distance between the starboard and portside antennas. On the other hand, the standard deviation of the pitch differences is about three times higher than the standard deviation of 0.08° of the pitch estimation with the multi-antenna GPS system (Tab. 7.2). Considering the strong pitch estimation by the GPS system, due to the longer distance between the bow and stern antennas, the pitch agreement is rather limited by the accuracy of the AHRS. The differences between the attitudes determined by the two systems revealed no noticeable drift effects on the AHRS, demonstrating the efficiency of the stabilization of the gyro data with the magnetometer and accelerometer data in the Xsens sensor fusion algorithm.

7.5 Boresight Misalignment Calibration in Airborne Altimetry

7.5.1 Introduction

Critical elements in the direct georeferencing equation (7.1) for airborne laser altimetry are the inner orientation parameters (Favey, 2001), and especially the boresight misalignment angles between the body frame B and the laser frame S. Boresight misalignment can affect the georeferencing of the laser data systematically, yet it is not trivial to determine. Boresight misalignment is usually assumed to remain constant during the whole flight, tough it may be subject to vibrations and aircraft deformations to a small degree. The aim of boresight misalignment calibration is the estimation of the boresight misalignment angles $(d\beta_x, d\beta_y, d\beta_z)$ in order to form he boresight misalignment rotation matrix $\boldsymbol{R}_{B/S}$ of the direct georeferencing equation (7.1).

7.5.2 Impact of Boresight Misalignment on Ground-Point Height

In order to estimate the boresight misalignment angles, their effect on the ground-point position, and especially on its vertical component, have to be modeled. (7.9) gives the true height $h^L_{x,true}$ of

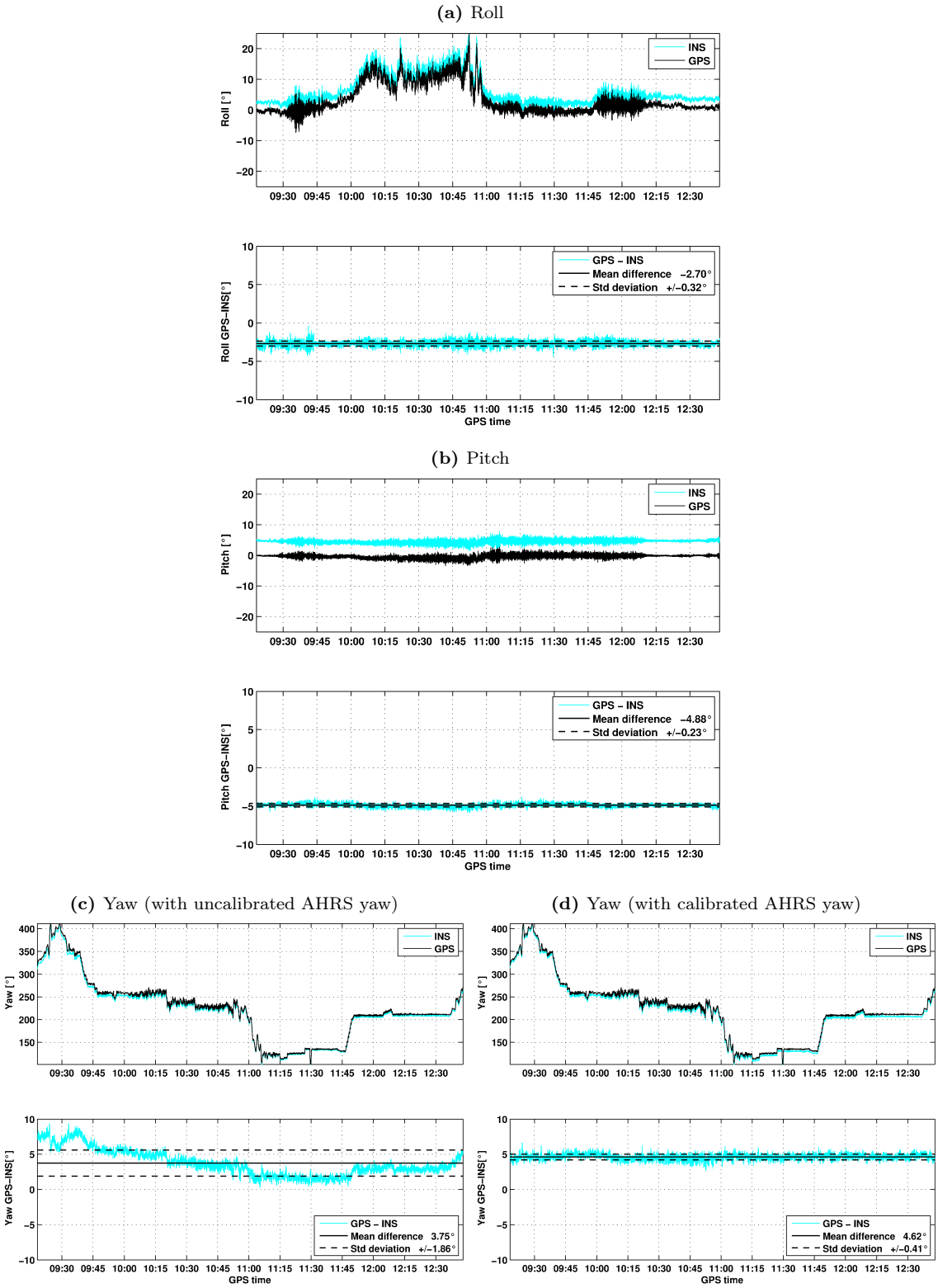

Figure 7.15: Example of attitude angles from the Xsens MTi miniature AHRS (labeled INS) and the multi-antenna GPS array, and their differences, during a survey-track on 2007/09/11.

the laser ground-point for the case of a **cross-section linear scanner**. If boresight misalignment is not considered, e.g. in a preliminary data processing before calibration, the approximate height $h^L_{x,0}$ of the laser ground-point becomes, based on (7.9):

$$h^L_{x,0} \;=\; h^L_a \;-\; \left[\cos\alpha_x \cos\alpha_y \left(r\cos\sigma_x + b^B_z\right) \;-\; \sin\alpha_x \cos\alpha_y \left(r\sin\sigma_x - b^B_y\right) \;-\; b^B_x \sin\alpha_y\right] \quad (7.34)$$

Thus, the effect dh_β of boresight misalignment on the height is given by the difference between the true height $h^L_{x,true}$ from (7.9) and the approximate height $h^L_{x,0}$ (without considering boresight misalignment) from (7.34):

$$dh_\beta \;=\; r\;\left[\left(\cos\alpha_x \sin\sigma_x + \sin\alpha_x \cos\sigma_x\right) d\beta_x \cos\alpha_y \;+\; \sin\alpha_y \left(d\beta_y \cos\sigma_x + d\beta_z \sin\sigma_x\right)\right] \quad (7.35)$$

For the special case of a **laser profiler**, $\boldsymbol{s}^S = (0,0,1)^T$, and (7.34) and (7.35) can be simplified using $\sin\sigma_x = 0$ and $\cos\sigma_x = 1$:

$$h^L_{x,0} \;=\; h^L_a \;-\; \left[\cos\alpha_x \cos\alpha_y \left(r + b^B_z\right) \;+\; b^B_y \sin\alpha_x \cos\alpha_x \;-\; b^B_x \sin\alpha_y\right] \quad (7.36)$$

$$dh_\beta \;=\; h^L_{x,true} \;-\; h^L_{x,0} \;=\; r\;\left(d\beta_x\;\sin\alpha_x\;\cos\alpha_y \;+\; d\beta_y\;\sin\alpha_y\right) \quad (7.37)$$

7.5.3 Impact of Simplification for Small Boresight Misalignment Angles

Without the simplification for small boresight misalignment angles (7.6), the true height $h^L_{x,true}$ of the laser ground-point for the case of a **laser profiler** becomes, based on (7.7):

$$\begin{aligned} h^L_{x,true} \;=\; h^L_a \;&-\; \cos\alpha_x\;\cos\alpha_y\;\left(r\;\cos d\beta_x\;\cos d\beta_y \;+\; b^B_z\right) \\ &+\; \sin\alpha_x\;\cos\alpha_y\;\left(r\;\sin d\beta_x\;\cos d\beta_y \;-\; b^B_y\right) \\ &+\; \sin\alpha_y\;\left(r\;\sin d\beta_y \;+\; b^B_x\right) \end{aligned} \quad (7.38)$$

and the non-simplified impact dh_β of boresight misalignment on the height would be given by the difference between (7.38) and (7.36):

$$dh_\beta \;=\; r\;\left(\sin\alpha_x \cos\alpha_y \sin d\beta_x \cos d\beta_y \;+\; \sin\alpha_y \sin\beta_y \;-\; \cos\alpha_x \cos\alpha_y \cos d\beta_x \cos d\beta_y\right) \quad (7.39)$$

and the impact $dh_{\beta,simp}$ of the simplification of the boresight misalignment on the height of the laser ground-point is given by the difference between (7.38) and (7.10):

$$\begin{aligned} dh_{\beta,simp} \;&=\; r\;\cos\alpha_x\;\cos\alpha_y\;\left(1 \;-\; \cos d\beta_x\;\cos d\beta_y\right) \\ &+r\;\sin\alpha_x\;\cos\alpha_y\;\left(\sin d\beta_x\;\cos d\beta_y \;-\; d\beta_x\right) \\ &+r\;\sin\alpha_y\;\left(\sin d\beta_y \;+\; d\beta_y\right) \end{aligned} \quad (7.40)$$

Hence, the impact of the boresight simplification on the height is proportional to the laser range r. Assuming the simple case where the roll and pitch angles are perfectly zero on a flight line ($\alpha_x = \alpha_y = 0$), (7.40) becomes:

$$dh_{\beta,simp} \;=\; r\;\left(1 \;-\; \cos d\beta_x\;\cos d\beta_y\right) \quad (7.41)$$

Table 7.5: Impact [cm] of boresight misalignment simplification on ground-point height from (7.41), for roll = pitch = 0° and $d\beta_x = d\beta_y$

boresight	flight height above ground				
angles	100 m	200 m	300 m	500 m	1000 m
0.10°	0.0	0.1	0.1	0.2	0.3
0.25°	0.2	0.4	0.6	1.0	1.9
0.50°	0.8	1.5	2.3	3.8	7.6
0.75°	1.7	3.4	5.1	8.6	17.1
1.00°	3.0	6.1	9.1	15.2	30.5

The impact for different flight heights above ground ($\approx$ laser range r) and boresight misalignment angles are given in Tab. 7.5, for the simple case where $\alpha_x = \alpha_y = 0$ (7.41). Note that this case represents the minimum impact for boresight misalignment, and that in case of roll and pitch angle deviating from zero, or in case of a laser scanner, the impact would drastically increase. Tab. 7.5 shows that for high flight heights and relatively large expected boresight misalignment angels, the simplification of the boresight rotation matrix is not recommended in high-accuracy applications. In this case, (7.38) should be used rather than (7.10) to compute ground-point heights.

7.5.4 Self-Calibration based on Piecewise Polynomial Fit of Water Surfaces

Although several well-developed boresight calibration approaches for airborne camera systems exist, e.g. (Škaloud and Schaer, 2003), the correct recovery of airborne laser scanner misalignments still remains elusive (Škaloud and Lichti, 2006). In airborne laser scanning, the usual approach to estimate boresight misalignment angles relies directly on the laser distance measurements, using a least squares adjustment. This self-calibration techniques are based on the assumption that laser ground-points from different shots close to each other have the same height when the scanned area is rather continuous and planar (Škaloud and Lichti, 2006). In this case, the data from one scan subset should have the same characteristics as the data from an adjacent scan subset covering the same area. Difference are then functionally modeled to be an error induced by the boresight angles.

The methods described above are based on the assumption that the target surface remains the same between two overflights of the same target, or between the forward and backward scan within the same flight line. This assumption does not hold for water surfaces, especially oceans, where the topography of the surface permanently changes with time, e.g. due to waves. Thus, the same surface height can never be observed twice at the same position. This means that in self-calibration techniques based on water surfaces, an adapted model for surface characteristics has to be applied.

In the following, a method for boresight misalignment calibration based on water surfaces is described. It is applicable for airborne laser profilers and scanners. The method is based on former investigations at the GGL (Peter, 1994; Geiger et al., 1994). The method described below is directly based on ellipsoidal water surface heights as provided by airborne laser altimetry. Ellipsoidal water surfaces cannot be satisfactorily modeled by a single horizontal or inclined plane over large distances, due to geoid undulations. Hence, the true water surface of height $h^L_{x,true}$ in (7.9) and (7.10) is modeled by piecewise planar surfaces::

$$h^L_{x,true} \;=\; a_i\; x \;+\; b_i\; y \;+\; c_i \tag{7.42}$$

where (x, y) are the horizontal coordinates of the laser ground-point, and a_i, b_i and c_i are the planar coefficients of the piecewise interval i, leading to one set of polynomial parameters for every chosen interval of e.g. 5-10 km flight distance. Additionally, the piecewise polynomials are constrained

from one interval to the next with a continuity condition:

$$h^L_{x_{0,i},true} \;=\; a_{i-1}\, x_{0,i} \;+\; b_{i-1}\, y_{0,i} \;+\; c_{i-1} \;=\; a_i\, x_{0,i} \;+\; b_i\, y_{0,i} \;+\; c_i \;=\; c_i \tag{7.43}$$

If the aircraft is flying on a more or less straight line during an interval i, the planar fit is weakly determined because an infinite number of planes can be defined by a single line. To avoid this problem, the coordinates (x, y) are defined in a local coordinate system, the origin (x_0, y_0) being the first ground-point of the interval, and the x-axis defined in flight direction. Using this coordinate system, the parameter b_i can be constrained to zero on a straight flight-line, leading to a linear fit of the sea surface in flight direction. If the interval comprises a turn between two flight-lines, a planar polynomial is used. In the case of a laser profiler, the latter intervals contain the most significant information on boresight misalignment, especially for the roll angle, due to the banking of the aircraft. Hence, a special algorithm has been setup to obtain an ideal interval distribution with intervals centered around the turns.

The boresight misalignment calibration model is given the following general observation equation:

$$h^L_{x,0} \;=\; h^L_{x,true} \;-\; dh_\beta \;=\; F(x) \tag{7.44}$$

The observations are the approximate ground-point heights $h^L_{x,0}$ without considering boresight misalignment. $h^L_{x,true}$ is the true but unknown surface height that is modeled by the polynomials (7.42). dh_β is the effect of boresight misalignment on the ground-point height. A least-squares (LSQ) adjustment of (7.44) attributes the difference between the approximate ground-point heights and the true height modeled by the surface polynomials (i.e. the deviations from the piecewise planar surfaces) upon the effect of the boresight misalignment angles ($d\beta_x$, $d\beta_y$, $d\beta_z$). For **cross-section linear laser scanners**, (7.34), (7.42) and (7.35) are inserted in (7.44), yielding the following observation equation:

$$\begin{aligned} &h^L_a - \left[\cos\alpha_x \cos\alpha_y \left(r\cos\sigma_x + b^B_z\right) - \sin\alpha_x \cos\alpha_y \left(r\sin\sigma_x - b^B_y\right) - b^B_x \sin\alpha_y\right] \\ &= \\ &= a_i x + b_i y + c_i - r\left[\left(\cos\alpha_x \sin\sigma_x + \sin\alpha_x \cos\sigma_x\right) d\beta_x \cos\alpha_y + \sin\alpha_y \left(d\beta_y \cos\sigma_x + d\beta_z \sin\sigma_x\right)\right] \end{aligned} \tag{7.45}$$

It is seen from (7.9) and (7.45) that the surface height does not depend on the yaw angle a_z. The unknown parameters x_i for an interval i are the three boresight calibration angles ($d\beta_x$, $d\beta_y$, $d\beta_z$) (the same for every interval), plus three surface polynomial coefficients (a_i, b_i, c_i). Thus, the total number of unknowns is $3 + 3ni$, where ni is the number of polynomial intervals. Compared to the huge number of observations at a sampling rate of 1 kHz, over-determination is always guaranteed, even when opting for short polynomial intervals. The unknowns can be estimated by conventional LSQ approach. Since the observation equation (7.45) is linear with respect to the parameters, the corresponding design matrix $\boldsymbol{A}$ is relatively simple, given here for one observation:

$$\begin{aligned} \boldsymbol{A}_i &= \left[\frac{\partial F_i}{\partial a}, \frac{\partial F_i}{\partial b}, \frac{\partial F_i}{\partial c}, \frac{\partial F_i}{\partial d\beta_x}, \frac{\partial F_i}{\partial d\beta_y}, \frac{\partial F_i}{\partial d\beta_z}\right] \\ &= \left[x,\; y,\; 1,\; -r\cos\alpha_y \left(\cos\alpha_x \sin\sigma_x + \sin\alpha_x \cos\sigma_x\right),\; -r\sin\alpha_y \cos\sigma_x,\; -r\sin\alpha_y \sin\sigma_x\right] \end{aligned} \tag{7.46}$$

For boresight misalignment calibration of airborne **laser profilers**, (7.36), (7.42) and (7.37) are inserted in (7.44), yielding the following observation equation:

$$h_a^L \; - \; \left(r + b_z^B\right) \; \cos\alpha_x \; \cos\alpha_y \; + \; b_x^B \; \sin\alpha_y \; - \; b_y^B \; \sin\alpha_x \; \cos\alpha_y \tag{7.47}$$
$$=$$
$$a_i x \; + \; b_i y \; + \; c_i \; - \; r \; d\beta_x \; \sin\alpha_x \; \cos\alpha_y \; - \; r \; d\beta_y \; \sin\alpha_y$$

It is seen from (7.10) and (7.47) that the surface height depends neither on the yaw angle α_z, nor on the yaw boresight misalignment angle $d\beta_z$. Hence, the yaw boresight misalignment angle $d\beta_z$ cannot be estimated for laser profilers by this method. Thus, the number of unknowns is decreased by one as compared to the scanner model, yielding the following design matrix $\boldsymbol{A}$ for one observation:

$$\begin{aligned} \boldsymbol{A}_i &= \left[\frac{\partial F_i}{\partial a}, \; \frac{\partial F_i}{\partial b}, \; \frac{\partial F_i}{\partial c}, \; \frac{\partial F_i}{\partial d\beta_x}, \; \frac{\partial F_i}{\partial d\beta_y}\right] \\ &= [x, \; y, \; 1, \; -r \; \sin\alpha_x \; \cos\alpha_y, \; -r \; \sin\alpha_y] \end{aligned} \tag{7.48}$$

In order to enhance the estimation, the aircraft may fly at different levels and do banking turns. Note that if the scan angle $\sigma_x = 0$, the (7.45) and (7.47) for the scanner and profiler are identical. It has to be noted that the models described above ((7.45) and (7.47)) do not allow to distinguish between boresight misalignment and systematic errors on the attitude angles, as caused by a misalignment between the attitude measurement system and the body frame. Attempts to introduce constant roll and pitch offsets as additional parameters in the calibration models revealed very high negative correlations of more than 99.99% with the boresight misalignment parameters, due to the small size of the lever arm vector $\boldsymbol{b}^B$ as compared to the laser range r.

The boresight misalignment calibration method for airborne laser altimetry described above is a truly self-calibrating technique, in the sense that the calibration exclusively relies on the sea surface height observations themselves. There is no need for overflying specially selected calibration surfaces. Additionally, the method relies directly on subsequent measurements within the same flight-line, with no need for overflying the same area more than once. Furthermore, the calibration algorithm is completely independent of any a priori information about the relief of the measured water surface, like e.g. geoid heights. The calibration method allowed to estimate boresight misalignment angles with an accuracy better than 0.1° (Section 7.5.5), corresponding to the expected order of magnitude of boresight misalignment variations during flight operations, as well as to the estimated attitude accuracy (Section 7.4.4). Due to the small ranges of less than 3 m in shipborne ultrasound altimetry, and the comparably large size of the footprint, there was no need for boresight misalignment calibration in shipborne ultrasound altimetry.

7.5.5 Case Study: Airborne Laser Profiler Calibration

The attitude of the aircraft was determined using two independent systems: a multi-antenna GPS array and a Honeywell H764G tactical-grade INS coupled with GPS (Section 7.4.5). The laser data was georeferenced separately using both attitude solutions. The two ground-point solutions were then entered separately into the boresight calibration algorithm described in the Section 7.5.4, yielding two sets of boresight misalignment angles. The results of the flight-wise boresight misalignment calibration using the two independent attitude solutions are summarized in Tab. 7.6 and Tab. 7.7. The roll and pitch misalignment angles obtained from one solution on all 6 flights agree better than 0.1°, except for two outliers on the pitch angle on flights GRL03 and GRL05 for both the GPS and INS solutions. The outliers are due to a complete lack of significant pitch maneuvers on these specific flights. In general, the pitch misalignment estimation suffers from larger standard deviations due to less significant pitch maneuvers as compared to roll maneuvers during the survey

Table 7.6: Boresight misalignment angles estimated from calibration using attitudes from the multi-antenna GPS system. The * are marking 3-sigma outliers.

Date	Flight	droll [°]	std [°]	dpitch [°]	std [°]
09/01/2003	GRL06	-0.71	±0.006	0.53	±0.010
09/01/2003	GRL02	-0.73	±0.007	0.61	±0.018
10/01/2003	GRL03	-0.77	±0.007	0.42*	±0.018
11/01/2003	GRL05	-0.76	±0.009	0.68*	±0.022
13/01/2003	GRL01	-0.70	±0.008	0.57	±0.017
14/01/2003	GRL04	-0.65	±0.006	0.53	±0.009
	Mean	**-0.72**	**±0.007**	**0.56**	**±0.016**
	std	**±0.045**		**±0.087**	

Table 7.7: Boresight misalignment angles estimated from calibration using INS attitudes. The * are marking 3-sigma outliers.

Date	Flight	droll [°]	std [°]	dpitch [°]	std [°]
09/01/2003	GRL06	-0.21	±0.006	-0.28	±0.010
09/01/2003	GRL02	-0.20	±0.007	-0.23	±0.018
10/01/2003	GRL03	-0.25	±0.007	-0.37*	±0.018
11/01/2003	GRL05	-0.25	±0.009	-0.12*	±0.022
13/01/2003	GRL01	-0.20	±0.007	-0.25	±0.016
14/01/2003	GRL04	-0.23	±0.005	-0.32	±0.008
	Mean	**-0.22**	**±0.007**	**-0.26**	**±0.015**
	std	**±0.021**		**±0.086**	

flights. The estimated standard deviations of the GPS and INS solutions are very similar. This shows that the slightly higher accuracy and the higher sampling rate of the INS does not result in a significant advantage during boresight calibration and that the efficiency of the calibration is primary governed by the characteristics of the aircraft maneuvers during a survey-flight.

The differences between the boresight angels of the GPS and INS solution are listed in Tab. 7.8. Theoretically, these differences should correspond to the mean attitude differences obtained by the two systems (Tab. 7.3). For the roll angle, both differences are identical, while for the pitch angle, a deviation of 0.09° was observed. Obviously, the attitude differences must be of opposite sign than the boresight differences.

An example of boresight misalignment calibration using attitudes from the multi-antenna GPS system on survey-flight GRL01 is shown in Fig. 7.16 to 7.18. Fig. 7.16 shows the attitude of the

Table 7.8: Differences between boresight misalignment angles estimated using attitudes from the multi-antenna GPS system and INS.

Date	Flight	droll GPS-INS [°]	dpitch GPS-INS [°]
09/01/2003	GRL06	-0.50	0.81
09/01/2003	GRL02	-0.53	0.85
10/01/2003	GRL03	-0.53	0.79
11/01/2003	GRL05	-0.51	0.79
13/01/2003	GRL01	-0.50	0.82
14/01/2003	GRL04	-0.42	0.86
	Mean	**-0.50**	**0.82**
	std	**±0.041**	**±0.028**
Mean from Tab. 7.3		**0.50**	**-0.91**

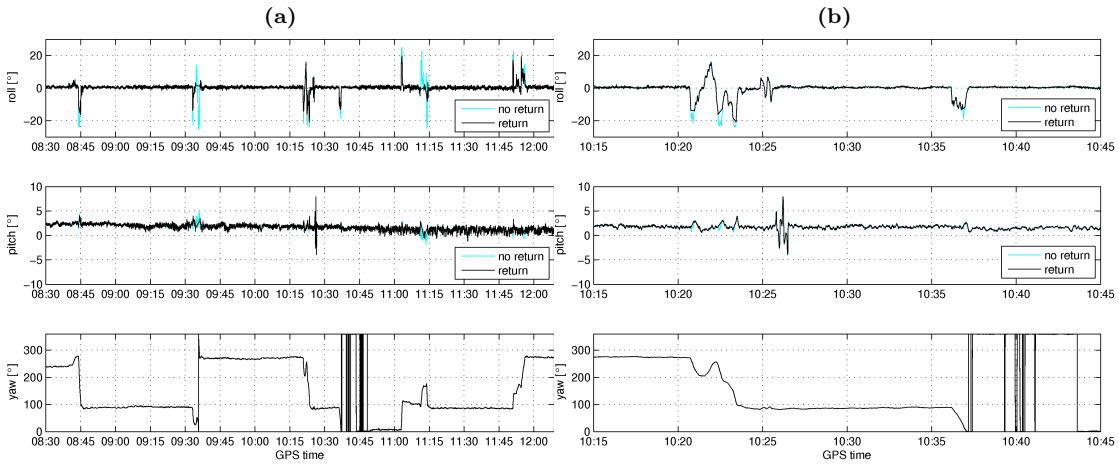

Figure 7.16: **(a)** Attitude of the aircraft during flight GRL01 from multi-antenna GPS. Light line on roll and pitch: attitudes where no returns of the laser pulse were obtained. **(b)** Zoom into part of (a), with special roll and pitch maneuvers without heading change (constant yaw) around 10:26.

aircraft during the flight. It is seen that during strong roll maneuvers, the laser altimeter receives no return from the sea surface, whereas the pitch movements on survey flights are not strong enough to produce a lack of laser return. Fig. 7.17 shows the approximate sea surface heights without considering boresight misalignment (7.36), as well as the compensated sea surface heights obtained by LSQ adjustment, given by the difference between the approximate sea surface heights and the residuals from the LSQ adjustment. The compensated sea surface heights clearly reveal the effect of the boresight misalignment during the turns, characterised by oversized variations of the sea surface heights. The residuals contain the non-modeled part of the sea surface height, mainly formed by ocean waves, as well as residual system noise. The residuals are normally distributed around zero (Fig. 7.17, bottom), underlining the conformity of the model. The good performance of the model is demonstrated by its capability of separating the waves, considered as residuals, from the approximate sea surface heights affected by boresight misalignment effects.

The effect of the boresight misalignment correction on ground-point height can reach 1 m during turns, due to large roll angels in the order of 20° (Fig. 7.18, bottom). A common approach to avoid strong boresight misalignment effects consists in considering only data on straight flight-lines and neglecting data during turns or other roll and pitch maneuvers. On flight GRL01, the effect of the pitch angle decreasing from 2.5° at the beginning of the flight to 1° towards the end of the flight (Fig. 7.16) results in a vertical boresight effect decreasing from 5 to 2.5 cm (Fig. 7.18, bottom). This underlines the necessity of boresight calibration even in the case were only line-data is considered. Even on the straight lines, aircrafts usually fly at a constant pitch angle (different from 0), or they may fly at constant roll angle due to strong side winds. This would cause systematic ground-point errors of several centimeters if boresight misalignment is not considered. Systematic vertical effects of up to 10 cm were observed in this study.

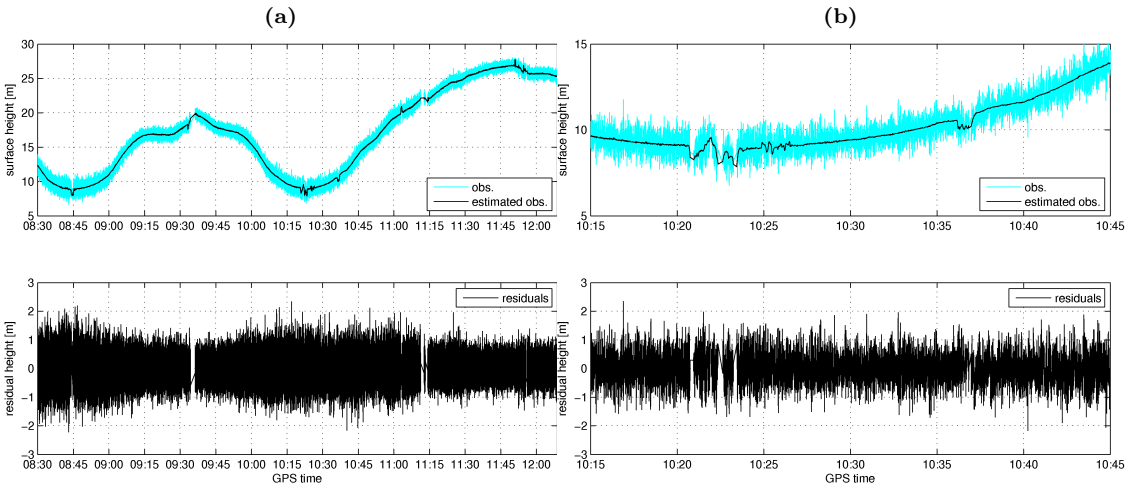

Figure 7.17: **(a)** Boresight misalignment calibration during flight GRL01 using the attitude solution from multi-antenna GPS. Top: Approximate sea surface height without considering boresight misalignment (light line) and compensated sea surface heights obtained by LSQ adjustment (black line), given by the difference between the approximate sea surface heights and the residuals from the LSQ adjustment. Bottom: Residuals on sea surface heights obtained by LSQ adjustment. **(b)** Zoom into part of (a), with special roll and pitch maneuvers around 10:26.

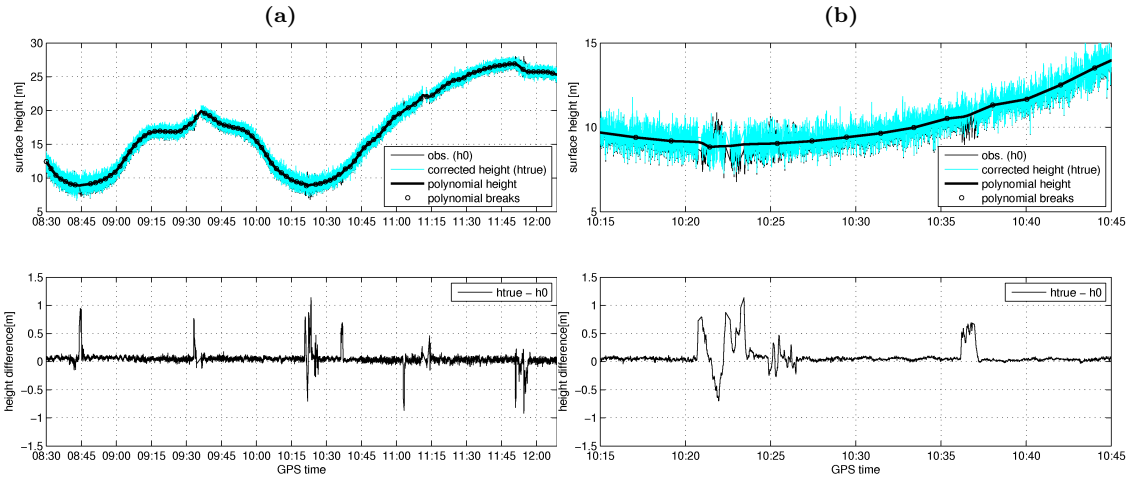

Figure 7.18: **(a)** Boresight misalignment calibration during flight GRL01 using the attitude solution from multi-antenna GPS. Top: Sea surface heights corrected for boresight misalignment obtained by the LSQ adjustment (light line), approximate sea surface heights without boresight misalignment correction (black line in the background) and piecewise polynomial fit used to model the sea surface heights (black line with circles indicating polynomial breaks). Bottom: Difference between sea surface heights corrected for boresight misalignment and approximate sea surface heights without boresight misalignment correction, corresponding to the estimated effect of boresight misalignment on sea surface heights. **(b)** Zoom into part of (a), with special roll and pitch maneuvers around 10:26.

8 Sea Surface Heights by Airborne Laser Altimetry around western Crete

8.1 GAVDOS Airborne Laser Altimetry Campaign

The GAVDOS project, supported by the European Union (EU), formed an integral part of an international effort to establish European absolute sea level monitoring facilities and calibration sites for radar altimetry satellites (Pavlis et al., 2004). The isle of Gavdos, situated south of Crete (Greece), was selected to host the facilities due to its offshore location under a crossover point of two ground-tracks of the radar altimetry missions TOPEX/Poseidon and Jason-1. The GAVDOS project was an international cooperation between the following institutions:

- Technical University of Crete (TUC), Laboratory of Geodesy & Geomatics Engineering, Greece
- Joint Center for Earth Systems Technology (JCET), University of Maryland Baltimore County, USA
- Aristotle University of Thessaloniki (AUTH), Department of Geodesy and Surveying, Greece
- Institute of Marine Biology of Crete (IMBC), Department of Oceanography, Heraklion, Greece (now Hellenic Center for Marine Research, HCMR)
- Austrian Space Research Institute, Department of Satellite Geodesy, Austrian Academy of Sciences
- National Survey and Cadastre of Denmark (KMS), Geodynamics Department, Denmark
- Observatoire de la Cote d'Azur (OCA), France
- Centre d'Etudes et de Recherches en Géodynamique et Astrométrie (CERGA), CNRS, France
- Hellenic Navy Hydrographic Service, Athens, Greece
- University of Bergen, Institute of Solid Earth Physics, Norway

During the GAVDOS project (2001-2004), coordinated survey campaigns were carried out in the area around Gavdos and Crete, with the primary aim to calibrate Jason-1 observations. The project included data collected from tide-gauges, satellite radar altimeter, airborne laser altimetry, airborne gravimetry, GPS buoys, hydrodynamic leveling, direct altimeter transponder observations and continuous GPS measurements. Observations for ultra-precise orbit determination have been carried out on the site at Gavdos after the end of the validation period for Jason-1, using satellite laser ranging (SLR) and the DORIS radio positioning system.

In order to reference the radar altimeter measurements over the calibration facility and to study the regional sea current circulation, detailed regional models of the geoid and sea surface topography are required. This task was achieved by carrying out a regional flight campaign for airborne gravimetry and laser altimetry. A high-resolution geoid has been derived from the gravimetric data (Tziavos et al., 2004).

The airborne campaign took place during 7 consecutive days, from 2003/01/09 to 2003/01/15, with a total of 35 survey flight hours. An area of approx. 200 by 200 km was covered with two different flight levels around Gavdos and the western part of Crete, in the vicinity of the

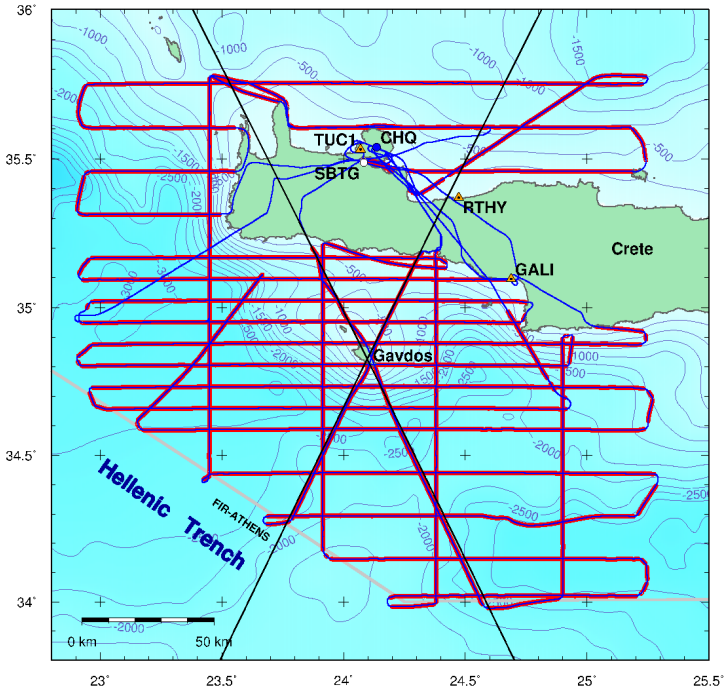

Figure 8.1: Low altitude (700 ft) flight lines of the GAVDOS combined airborne gravimetry and laser altimetry campaign around Crete, with aircraft trajectories (thin blue line) and laser data (thick red line). Black diagonal lines: Jason-1 radar altimeter ground-tracks. Orange triangles: GPS reference stations (TUC1, GALI, RTHY). White circle: Souda Bay tide-gauge (SBTG). Blue circle: Chania Airport (CHQ). Gray line: boundary of FIR-Athens. Background: bathymetry in [m].

Hellenic Trench. The higher flight level, with 8 flight lines at 11500 ft (3500 m) altitude, was reserved for gravimetric surveying. The lower flight level, with 24 lines at 700 ft (215 m) altitude flown in 6 consecutive days was a combined gravimetric and laser altimetry survey over the sea (Fig. 8.1). Three GPS reference stations (TUC1, GALI, RTHY) were operated on the island of Crete during flight operations. Data from the permanent tide-gauge station in Souda Bay (SBTG), operated by the Hellenic Navy Hydrographic Service, was available. All flights were flown out of Chania Airport (CHQ), Crete, and remained within the Athens Flight Information Region (FIR-Athens) (Fig. 8.1). The campaign was carried out in close cooperation with the National Survey and Cadastre of Denmark (KMS) and the Institute of Solid Earth Physics of the University of Bergen. The survey-vessel Pytheas of Hellenic Navy Hydrographic Service (HNHS) took part in the campaign. There has been a close collaboration and help received by the Hellenic Military Geographic Service, Civil and Military Aviation Control Authorities and Chania Airport.

8.2 Instantaneous Sea Surface Height Profiles

8.2.1 Sea Surface Heights from Airborne Altimetry around Crete

Sea surface height profiles were computed based on airborne laser profiler data, aircraft trajectories and attitudes, using the direct georeferencing method described in Chapter 7 (Fig. 8.2 and Fig. 8.3). The original sea surface height results from airborne laser altimetry, with a sampling rate of 1 kHz, were low-pass filtered using a robust one dimensional spline filter with a cut-off wavelength of 10 km (Fig. 8.2 and Fig. 8.3). The spline filter algorithm used in this project has several advantages over filter methods in the frequency domain based on Fourier transforms. The spline filter algorithm is

robust against outliers and is capable of processing the enormous amount of data points yielded by the 1 kHz laser measurements. In addition, as opposed to filter algorithms based on Fourier transforms, the spline filter is indifferent to data gaps as observed throughout the laser datasets. Further information on spline filters can be found in (Goto et al., 2005; Hernla, 2000; Numada et al., 2007; Törnig and Spellucci, 2000).

8.2.2 Significant Wave Heights

Due to the high sampling rate of the airborne laser altimetry data, the residuals between the original and filtered data correspond to the ocean wave undulations, neglecting system noise. Based on these wave undulations, significant wave heights $\bar{H}_{1/3}$ (Section 3.2) were computed from the airborne laser altimetry data (Fig. 8.4). For each significant wave height sample, an overlapping data interval of 10 km was considered in the computation. During the airborne campaign, the sea surface was characterized by a wide variety of sea states, with significant wave heights ranging from 0.3 m to 2.8 m. Significant wave heights from a dedicated profile are compared to significant wave heights from Jason-1 GDR data in Section 10.2.

8.2.3 Calibration of Airborne Altimetry Data with GPS Buoys

GPS-equipped buoys were deployed offshore and in coastal regions, simultaneously with the airborne laser altimetry campaign. They provide ground-truth instantaneous sea surface heights for the verification and calibration of the airborne laser altimetry system. Two lightweight buoys (Section 6.2) were used at a sampling rate of 1 Hz. The GPS data of the buoys was processed by double-differenced carrier phase, using stations TUC1 and GALI as reference stations (Fig. 8.1). Several overflights of the buoys were performed. Two verifications of airborne laser altimetry results with GPS Buoy measurements during flight GRL04 are presented in this section.

A first calibration measurement was performed in the port of Agia Galini (GALI in Fig. 8.1) during an overflight of the survey-aircraft (Fig. 8.5). The buoy heights reveal the presence of a wave with a period of approximately 10 minutes and an amplitude of about 2 cm inside the port (Fig 8.6b). The laser data also indicates the presence of a wave, since the filtered heights are not constant inside the port (Fig 8.6a). Due this wave, in conjunction with the large horizontal offset of 87 m between the laser profile and the buoy, the comparison between the two datasets at the closest approach makes no sense. Therefore, the mean buoy height observed during 1 hour and the mean laser height over the entire cross-section of the port basin were considered in the comparison. A height difference of 4.3 cm is observed, which lies within the expected accuracies, regarding the noisy laser data inside the port.

In order to obtain offshore calibration measurements, a GPS buoy was deployed in the open sea, south of Crete, at approx. 35.17°N and 23.90°E. The buoy was deployed under drifting conditions by the survey-vessel Pytheas of the Hellenic Navy Hydrographic Service, during an overflight of the survey aircraft (Fig. 8.7). The horizontal distance between the buoy and the laser profile during the overflight (closest approach) was only 26 m. Both datasets were smoothed using a spline filter with the same cut-off wavelength of 2 km. A very good agreement was obtained between the two independent observations, with a height difference of only 0.2 cm (Fig 8.8). In addition similar wave amplitudes of around 0.5 m were observed by both systems.

The good agreement between ground-truth GPS buoy observations and airborne laser altimetry enabled the validation of the laser altimetry system and direct georeferencing processing algorithm, without any further calibration.

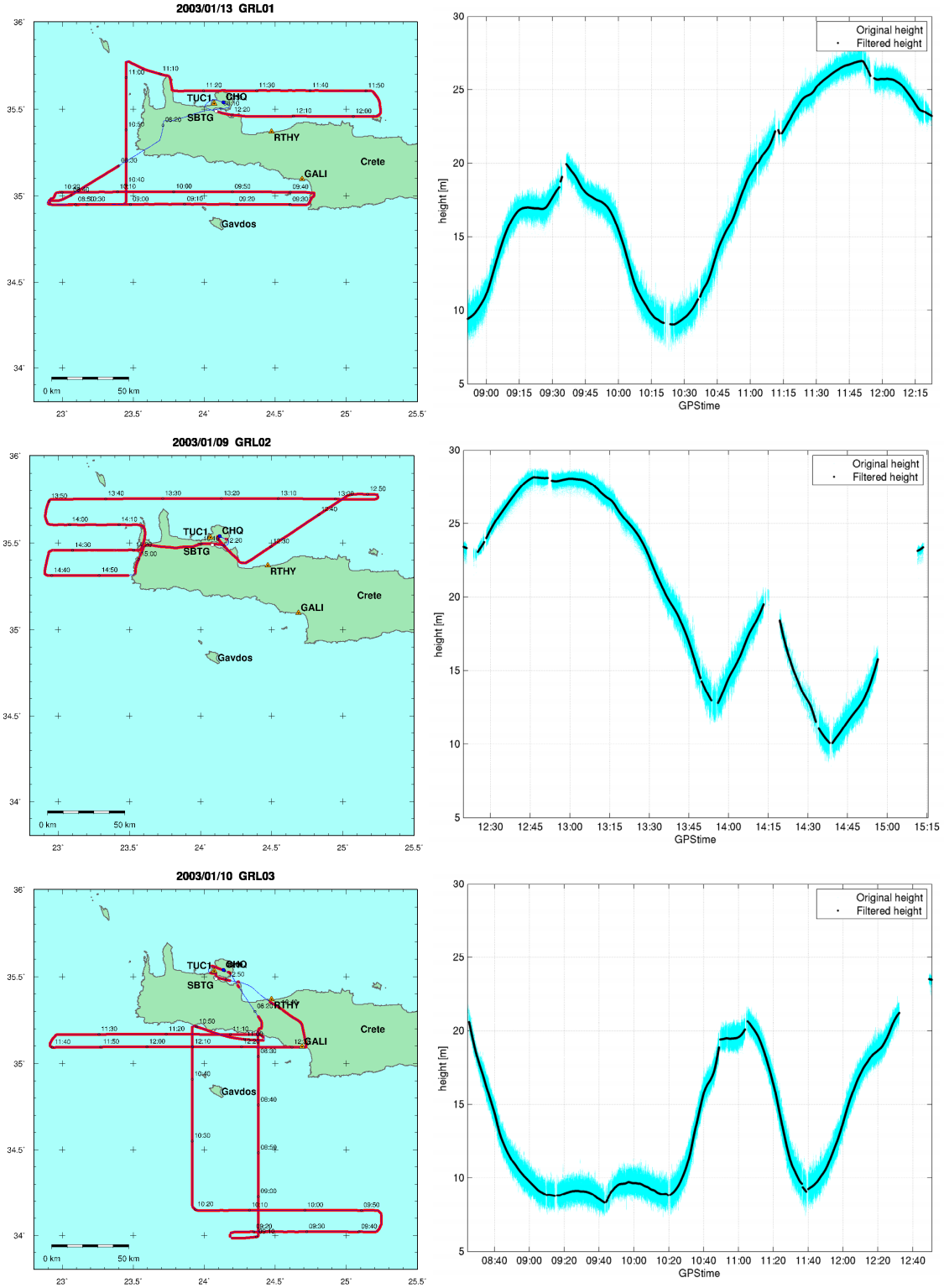

Figure 8.2: Sea surface height results of flights GRL01, GRL02 and GRL03. Left: flight-tracks with aircraft trajectory (thin blue line) and laser data (thick red line). Right: corresponding ellipsoidal sea surface height profiles from airborne laser altimetry, with original sampling rate of 1 kHz (cyan dots) and heights smoothed using a spline filter with a cut-off wavelength of 10 km (black dots). Time indications on the left-hand graphs correspond to the time axis of the right-hand graphs.

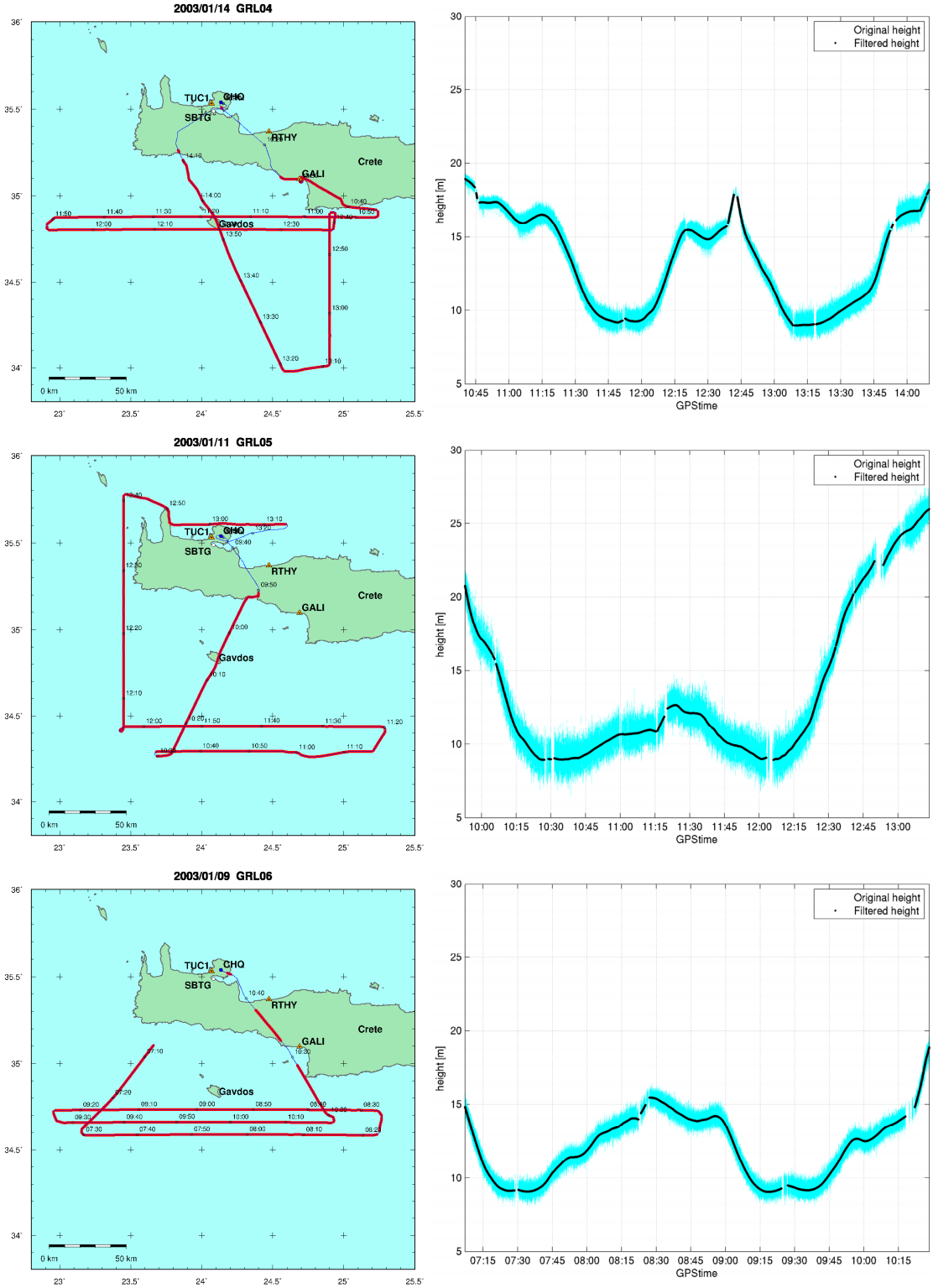

Figure 8.3: Sea surface height results of flights GRL04, GRL05 and GRL06. Left: flight-tracks with aircraft trajectory (thin blue line) and laser data (thick red line). Right: corresponding ellipsoidal sea surface height profiles from airborne laser altimetry, with original sampling rate of 1 kHz (cyan dots) and heights smoothed using a low-pass spline filter with a cut-off wavelength of 10 km (black dots). Time indications on the left-hand graphs correspond to the time axis of the right-hand graphs.

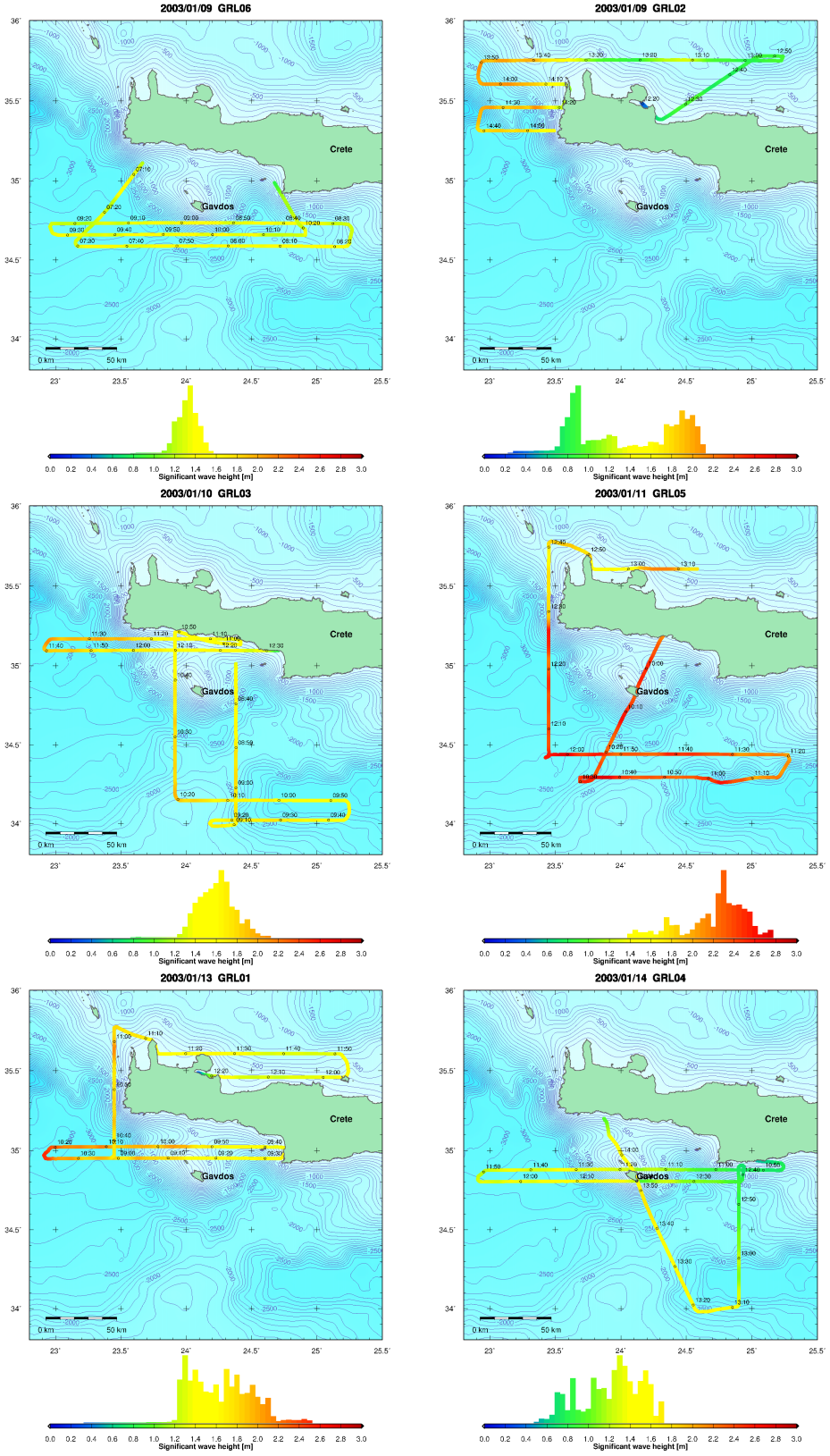

Figure 8.4: Significant wave heights estimated from airborne laser altimetry.

Figure 8.5: **(a)** Overflight of the port of Agia Galini as seen from the aircraft. **(b)** GPS Buoy deployed in the port of Agia Galini during overflight.

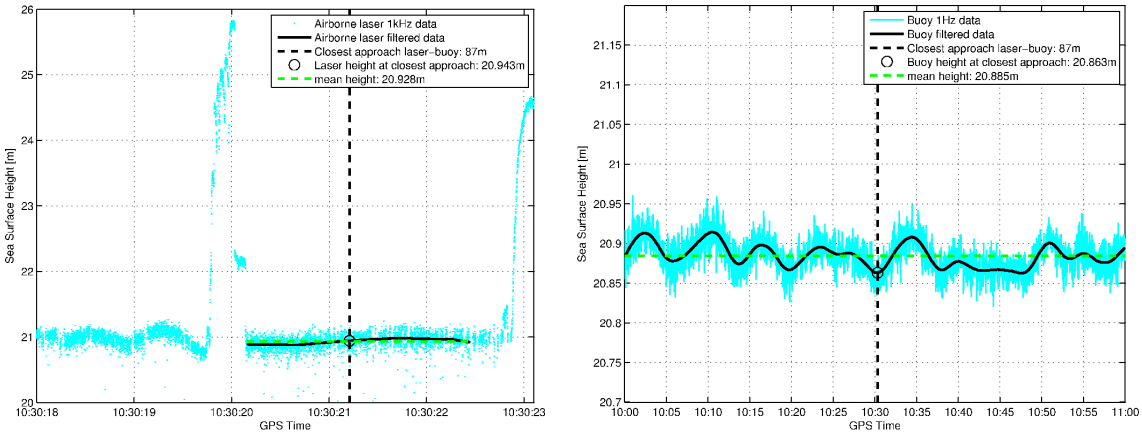

Figure 8.6: **(a)** Height profile from airborne laser altimetry during overflight of the port of Agia Galini. Cyan dots: original data (sampling rate 1 kHz). From the left to the right, the laser data shows the sea surface outside the port, the wave-breaker, the sidewalk, the sea surface inside the port and the pear. The cross-section of the port corresponds to 150 m, covered in 2.5 s. Black line: low-pass filtered heights inside the port. Green dashed line: mean height inside the port. Black dashed line: closest approach between the buoy and the laser profile. **(b)** Sea surface height from GPS Buoy in the port of Agia Galini during 1 hour centered around the overflight. Cyan line: original data (sampling rate 1 Hz). Black line: low-pass filtered height. Green dashed line: mean height inside the port. Black dashed line: closest approach between the buoy and the laser profile.

8.3 Sea Surface Height Corrections

8.3.1 Ocean Wave Correction

The oscillation effects of ocean waves were eliminated by the low-pass filtering described in Section 8.2.1. More details on ocean waves are given in Section 3.2.

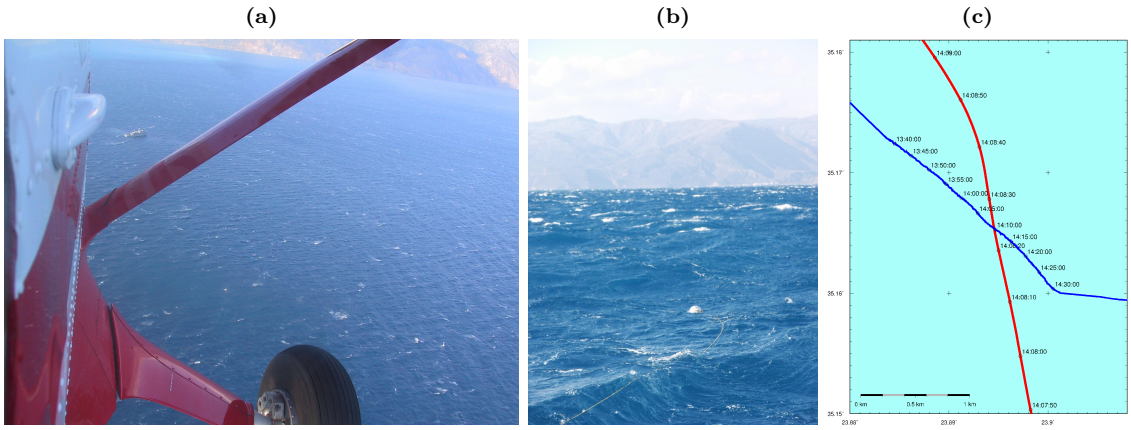

Figure 8.7: **(a)** Overflight of the survey-vessel Pyhteas as seen from the aircraft. **(b)** GPS Buoy deployed during overflight, under rough sea conditions. (c) Situation of the overflight with airborne laser altimetry profile (red line), with time indications corresponding to Fig. 8.8a and (GPS buoy trajectory (blue line), with time indications corresponding to Fig. 8.8b.

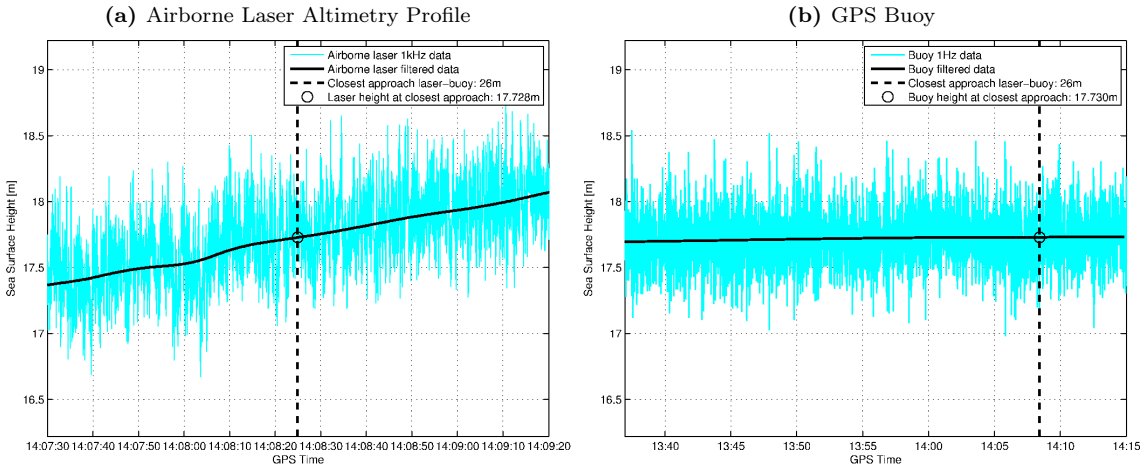

Figure 8.8: **(a)** Sea surface height profile from airborne laser altimetry during offshore buoy overflight. Cyan line: original data (sampling rate 1 kHz). Black line: low-pass filtered heights. The laser data covers 120 s centered on the overflight, corresponding to a distance of 5 km. Black dashed line: closest approach between the buoy and the laser profile. **(b)** Sea surface height from GPS Buoy during overflight, covering 40 minutes and corresponding to a drifted distance of 1.5 km. Cyan line: original data (sampling rate 1 Hz). Black line: low-pass filtered height. Black dashed line: closest approach between the buoy and the laser profile.

8.3.2 Ocean Tide Correction

The amplitudes of the major ocean tide constituents M2 and S2 are below 2 cm in the survey area around Crete (Fig. 3.4). Hence, only very small tidal effects are to be expected in this region. Tidal corrections along the airborne laser altimetry tracks were computed based on the two global tide models FES2004 (Fig. 8.9a) and GOT00.2[1] (Fig. 8.9b), as well as on the POL (Proudman Oceanographic Laboratory) model for the Mediterranean Sea (Fig. 8.9c). Further details on the three ocean tide models can be found in Section 3.3.2. All three models predict ocean tides below

[1]Tide corrections based on the GOT00.2 model were kindly provided by E.C. Pavlis from JCET.

2.5 cm. However, the predictions are highly contradictory, since the differences between the models reach up to 3 cm (Fig. 8.9d). Especially the predictions from FES2004 are very different from the predictions of GOT00.2 and POL. Considering the small size of the encountered tidal amplitudes and of the differences between the models, the choice of the tide model is not crucial for the accuracy of the corrected sea surface heights.

Nevertheless, in order to select the most appropriate model for the considered survey area, a validation of the tidal corrections obtained from the three models was performed, based on tide-gauge observations and on crosspoints analysis. The validation of FES2004 and POL with local tide-gauge data showed that the POL predictions agree better with in-situ observations (Section 8.3.4). Since the tidal amplitudes and the differences between the predictions of the three models are in the same order of magnitude as the expected accuracy of the sea surface height observations from airborne laser altimetry, it was not possible to discredit one model in favor of another based on the crosspoints analysis (Section 8.4.2). Similar validations were performed for the shipborne data in the North Aegean Sea (Section 9.3.4 and Section 9.4.1). Due to the fact that tidal amplitudes are higher in that survey area, the POL model was clearly identified to agree best with the in-situ observations. This model was therefore used to correct the shipborne sea surface height data of the North Aegean Sea campaign. For consistency reasons, the POL model was also chosen to correct the airborne sea surface height data around western Crete.

8.3.3 Correction for Atmospheric Pressure and Wind Forcing

Corrections for the effect of atmospheric pressure and wind forcing on sea surface heights were computed from MOG2D correction grids (Fig. G.1 to Fig. G.3) for the airborne laser altimetry data around Crete. Corrections along the airborne tracks were obtained by temporal and spatial interpolation of the MOG2D grids (Fig. 8.10). At the tide-gauge station in Souda Bay (SBTG), the atmospheric effect varied between -18 and 4 cm during 9 consecutive days of the survey campaign (Fig. 8.10b, light line). The maximum positive effect occurred during the morning of January 12^{th}, coinciding with the passage an atmospheric depression (Fig. F.1 to Fig. F.3, appendix F). The atmospheric effects along the flight tracks ranged from -10 to -2 cm, and variations of up to 5 cm were encountered during the same flight (Fig. 8.10a and Fig. 8.10b dark line). Small deviations between the station corrections in Souda Bay and the flight track corrections are produced by the geographical distance between the aircraft and the tide-gauge station (Fig. 8.10b). For the area and period of the considered dataset, the effect of atmospheric pressure and wind forcing (Fig. 8.10) is larger than the ocean tide effect (Fig. 8.9).

8.3.4 Validation of Tidal and Atmospheric Models with Tide-Gauge Data

A validation of the FES2004 and POL tide models, as well as the MOG2D atmospheric forcing model, was carried out using observations from Souda Bay tide-gauge station (SBTG, Fig. 8.1), operated by the Hellenic Navy Hydrographic Service. The GOT00.2 model was not validated since the model was not available to the author. The sea surface heights recorded by tide-gauges are affected by astronomic ocean tides and the forcing of atmospheric pressure and wind. In order to compare tide-gauge data to the predictions obtained from tide models, the effects of atmospheric forcing have to be removed from tide-gauge data.

Tide data of 9 consecutive days of the airborne campaign were analyzed (Fig. 8.11). In a first step, the atmospheric effect from MOG2D correction grids (corresponding to Fig. 8.10b, light line) were removed from the tide-gauge observations (Fig. 8.11a). In a second step, a remaining low frequency trend (period >48 h) was removed from the observations. This trend mainly represents the remaining local effect of atmospheric forcing, not resolved by MOG2D. In particular during the last two days, MOG2D underestimates the depression of the sea surface by up to 6.5 cm (Fig. 8.11a). Differences between the corrected tide-gauge observation (Fig. 8.11a, bottom) and predications of

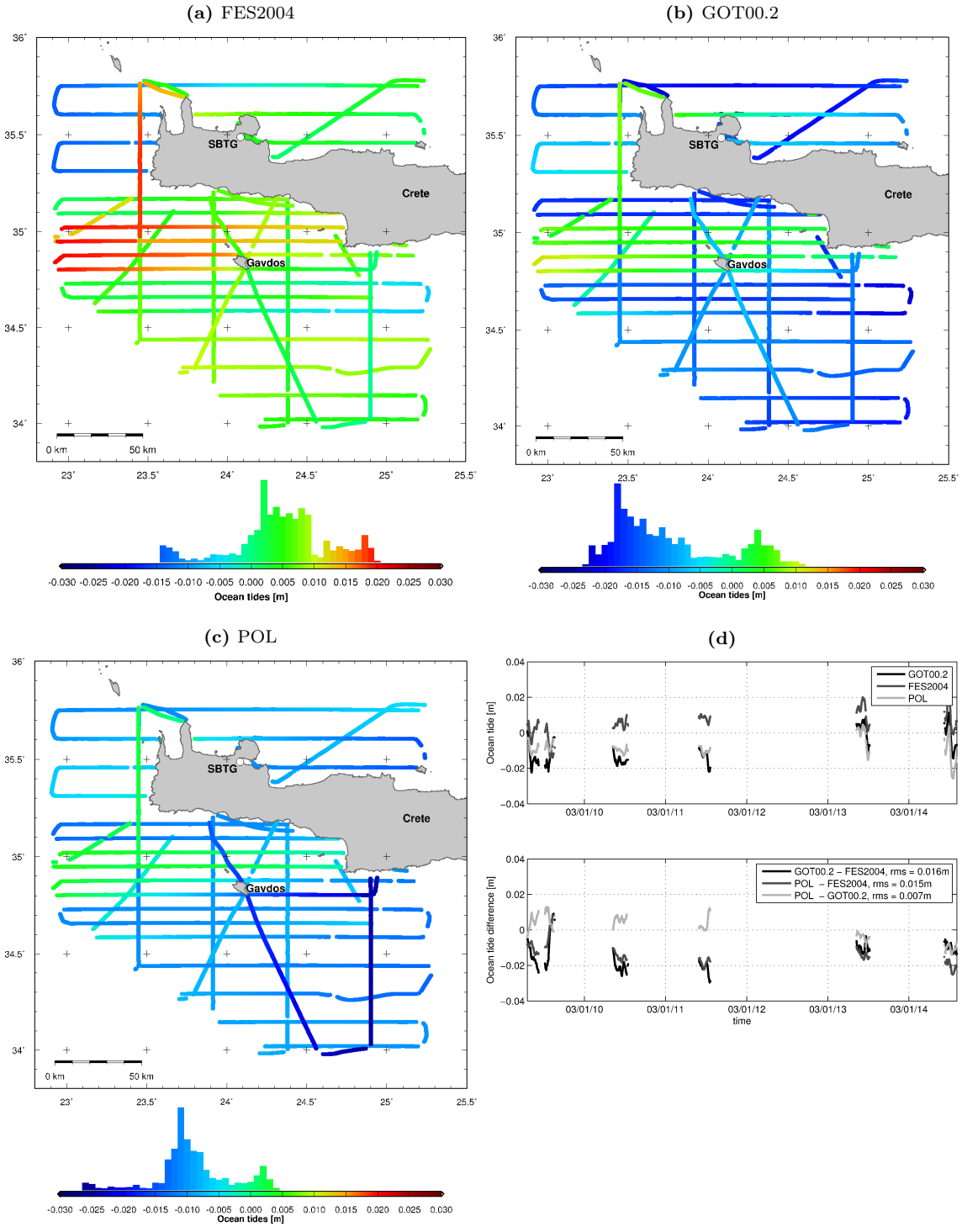

Figure 8.9: Ocean tides along airborne laser altimetry tracks predicted by the models **(a)** FES2004, **(b)** GOT00.2 and **(c)** POL (Proudman Oceanographic Laboratory). **(d)** Top: time series of ocean tides along airborne laser altimetry tracks from FES2004 (dark grey line, corresponding to (a)), GOT00.2 (black line, corresponding to (b)) and POL (light grey line, corresponding to (c)). (d) Bottom: differences between the models.

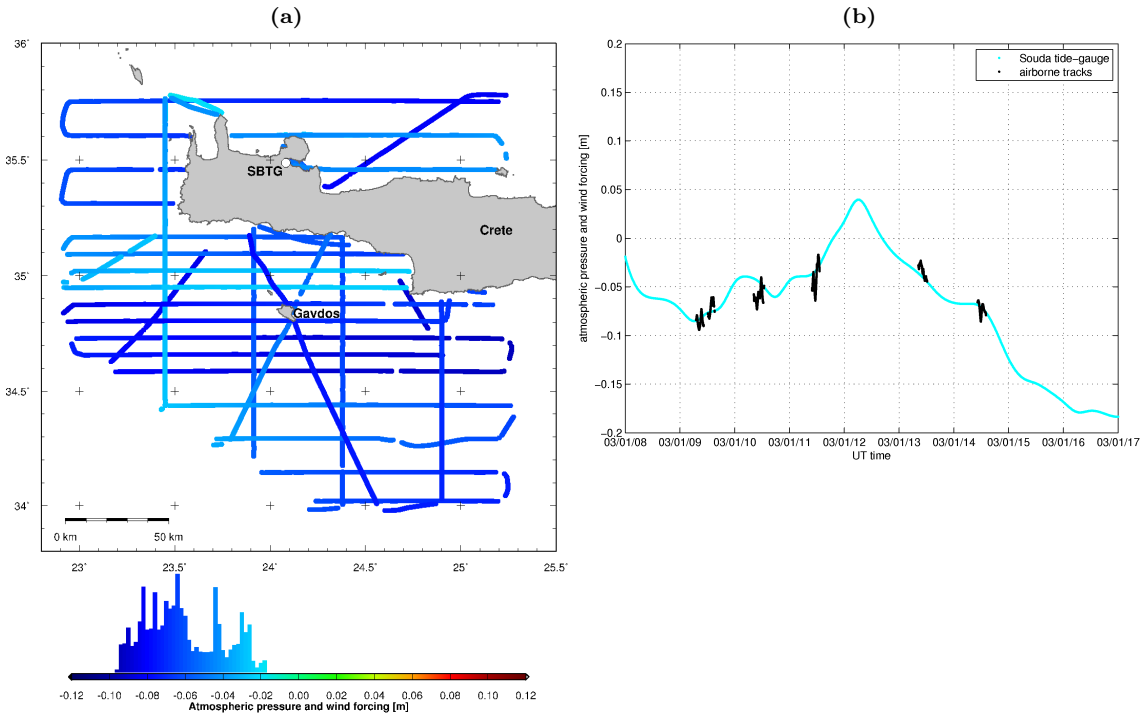

Figure 8.10: **(a)** Effect of atmospheric pressure and wind forcing on sea surface height along airborne laser altimetry tracks, based on MOG2D correction grids. **(b)** Time series of effect of atmospheric pressure and wind forcing. Dark line: effect along flight tracks, corresponding to (a). Light line: effect on Souda Bay tide-gauge station.

FES2004 show a standard deviation of 2.0 cm and maximum values of up to 5 cm (Fig. 8.11b). Differences with respect to the POL model were found to have a smaller standard deviation of 1.3 cm and maximum values of up to 3 cm (Fig. 8.11b), yielding a slightly better prediction than FES2004. But the differences with respect to both tide models still contain periodic signals, meaning that both models do not match the observed tide. The discrepancies between the tide-gauge observations and both the models for tidal and atmospheric forcing are most likely due to local coastal effects in Souda Bay, not resolved by the models. It can be assumed that the models would perform better offshore, in the absence of strong and hardly predictable coastal effects.

8.3.5 Sea Level Anomaly Correction

Sea level anomalies (SLA) were computed for the survey area around Crete during the airborne campaign, based on the SSALTO/DUACS sea level anomalies (Section 2.4). For the considered area and period (1 week), the SLA values ranged from -2 to 18 cm (Fig. 8.12). The average sea surface height in the area was higher than the reference height, with positive mean SLA values of 10.9 cm and 4.5 cm for 2003/01/08 and 2003/01/15, respectively. Hence, during only one week, an important decrease of the mean SLA by 6.3 cm and local SLA variations of up to 12 cm were observed in the survey area (Fig. 8.12c).

The SLA values show that the sea surface topography cannot be considered as constant during the six days of the airborne campaign. Thus, an additional sea surface height correction was computed along the flight-tracks, based on the SSALTO/DUACS sea level anomalies, by spatial and temporal interpolation (Fig. 8.12d). The SLA corrections take significant values between -1 cm and 15 cm. These corrections, however, should only be applied when the resulting sea surface heights are meant

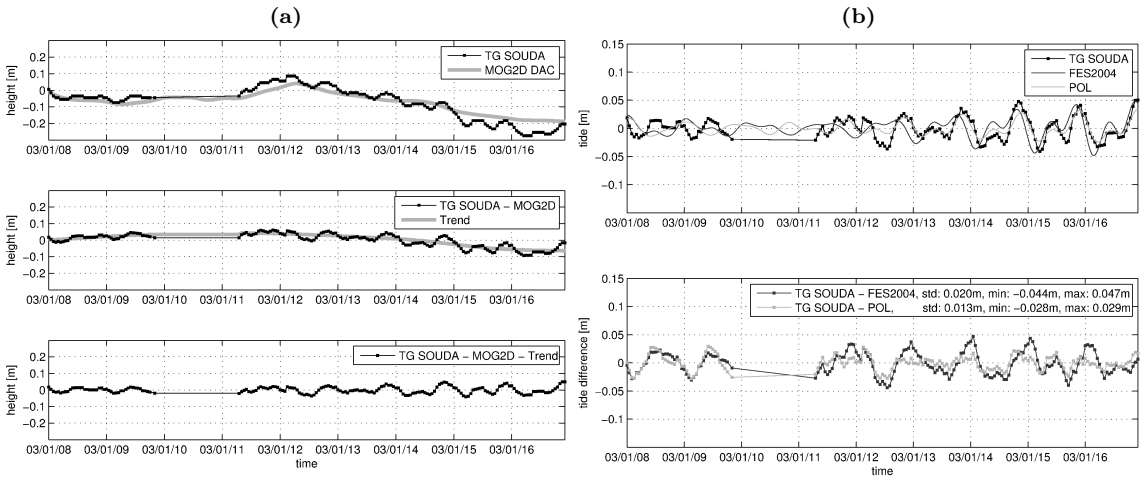

Figure 8.11: (a) Top: Sea level observations from Souda Bay tide-gauge station, Crete (black line, with data-gap on 2003/01/10), during 9 consecutive days of the airborne campaign, and dynamic atmospheric correction (DAC) from MOG2D (grey line). Center: Tide-gauge data corrected with MOG2D DAC (black line) and remaining trend (grey line). Bottom: Tide-gauge data corrected with MOG2D DAC and with remaining trend removed. **(b)** Top: Sea level observations from Souda Bay tide-gauge station (black line), corrected with MOG2D DAC and with remaining trend removed (corresponding to (a) bottom), as well as tidal predictions of both FES2004 (dark grey line) and POL models (light grey line). Bottom: Difference between tide-gauge data and both FES2004 (dark grey line) and POL models (light grey line).

to represent the mean sea surface MSS, as defined in (2.2) and (2.30). They must not be applied when the resulting sea surface heights are meant to represent corrected sea surface heights SSH_c, including the variable part of the dynamic topography, as defined in (2.1) and (2.29).

8.4 Repeatability Analysis

8.4.1 Analysis of Repeated Tracks

Good indicators for the repeatability of the airborne laser altimetry system are height differences on repeated tracks. Repeated tracks have the advantage to provide information on the repeatability and on the behavior of the height difference along a whole track, rather than only at punctual cross-overs. Three repeated tracks were flown. The first one is a repeated track flown during flight GRL01 (Fig. 8.13a), the second and the third ones are repeated tracks between flights GRL01 and GRL05 (Fig. 8.13b and Fig. 8.13c). Cross-track distances between the repeated tracks were mainly below 100 m. Statistics on the height differences using different combinations of tidal and atmospheric sea surface height corrections are shown in Tab. 8.1. Good agreements were obtained between the repeated tracks, with the majority of the height differences below 10 cm. Strong winds and heavy turbulences were encountered on flight GRL05, which could be a reason for a degradation of the obtained sea surface height on this flight.

The tidal and atmospheric corrections did not allow to substantially improve the height differences (Fig. 8.13), since the order of magnitude and the frequency of the height differences are higher than the estimated corrections. This confirms the conclusion of Section 8.4.2, where no significant improvement at the crosspoints was obtained using the different combinations of tidal and atmospheric corrections, since the order of magnitude of the tidal and atmospheric effects are small compared to the accuracy of the airborne laser altimetry method.

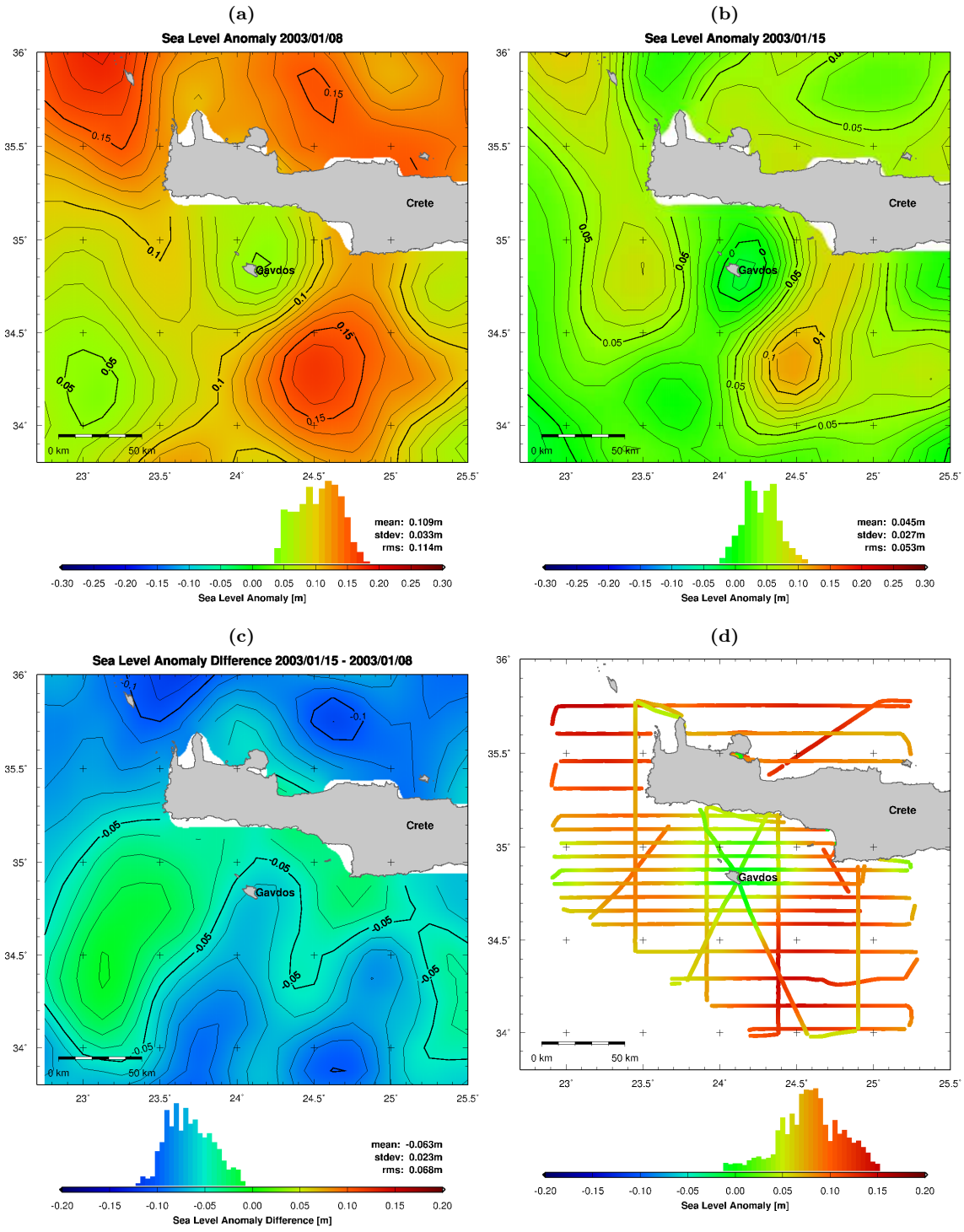

Figure 8.12: Weekly sea level anomaly *SLA* from SSALTO/DUACS merged multi-mission altimetric data around Crete, on 2003/01/08 **(a)** and 2003/01/15 **(b)**. Contour interval: 0.01 m. **(c)** Sea level anomaly *SLA* difference between the two consecutive weekly datasets in (a) and (b). Contour interval: 0.01 m. **(d)** Sea level anomalies along airborne laser altimetry tracks, based on SSALTO/DUACS sea level anomalies in (a) and (b).

Table 8.1: Height differences on repeated tracks for solutions with different combinations of tidal and atmospheric sea surface height corrections.

	Tidal/Atmospheric sea surface height correction							
Tidal	-	FES2004	GOT00.2	POL	-	FES2004	GOT00.2	POL
Atmospheric	-	-	-	-	MOG2D	MOG2D	MOG2D	MOG2D
Repeated track GRL01-GR0L1 (Fig. 8.13a)								
Mean [m]	-0.054	-0.048	-0.053	-0.055	-0.059	-0.052	-0.058	-0.060
StD [m]	0.017	0.017	0.018	0.018	0.017	0.017	0.018	0.018
RMS [m]	0.057	0.051	0.056	0.058	0.061	0.055	0.060	0.062
Min [m]	-0.075	-0.069	-0.075	-0.077	-0.080	-0.074	-0.079	-0.081
Max [m]	-0.017	-0.010	-0.015	-0.016	-0.022	-0.015	-0.020	-0.021
Repeated track GRL01-GR0L5 1 (Fig. 8.13b)								
Mean [m]	0.015	0.026	0.037	0.028	-0.000	0.011	0.022	0.013
StD [m]	0.069	0.069	0.072	0.069	0.063	0.063	0.066	0.063
RMS [m]	0.070	0.074	0.081	0.074	0.063	0.064	0.070	0.064
Min [m]	-0.140	-0.130	-0.122	-0.127	-0.144	-0.133	-0.125	-0.131
Max [m]	0.150	0.161	0.179	0.163	0.126	0.137	0.155	0.139
Repeated track GRL01-GR0L5 2 (Fig. 8.13c)								
Mean [m]	-0.003	-0.003	-0.024	-0.005	0.013	0.013	-0.008	0.011
StD [m]	0.047	0.048	0.049	0.048	0.046	0.047	0.047	0.047
RMS [m]	0.047	0.048	0.054	0.049	0.048	0.049	0.048	0.048
Min [m]	-0.067	-0.069	-0.091	-0.072	-0.058	-0.054	-0.074	-0.056
Max [m]	0.068	0.070	0.050	0.068	0.080	0.082	0.062	0.080

8.4.2 Crosspoint Analysis

The airborne laser altimetry profiles yield a total of 102 crosspoints, where the sea surface height was measured twice at the same geographic position (Fig. 8.15a). Height differences at crosspoints are a good indicator for the repeatability and the accuracy of the airborne laser altimetry system. An analysis of height differences at crosspoints using different combinations of tidal and atmospheric sea surface height corrections, as well as sea level anomaly (SLA) corrections, was carried out (Tab. 8.2 and Fig. 8.14). The various combinations yield no significant difference, with RMS values of the height differences varying by less than 0.7 cm. Furthermore, no significant improvement at the crosspoints, and even a small degradation, is observed using the different combinations of tidal and atmospheric corrections. This is a consequence of the fact that the orders of magnitude of the tidal and atmospheric effects are small compared to the accuracy of the airborne laser altimetry method. The beneficial impact on sea surface height differences at crosspoints of the same corrections applied to the shipborne data in the North Aegean Sea is shown in Section 9.4.1.

After the application of tidal, atmospheric and SLA corrections, the final RMS value of the height differences at the 102 crosspoints is in the order of 8.5 cm. The RMS at 19 inner-flight crosspoints is about 6.5 cm, whereas the RMS at the remaining 83 inter-flight crosspoints is slightly higher, with a value of 9.0 cm. For the solution using POL tidal corrections, MOG2D atmospheric corrections and SLA correction (Fig. 8.15), the height difference remains below 10 cm at 76% of the crosspoints, below 15 cm at 89% and below 20 cm at 99% of the crosspoints. The maximum observed height difference is 21.6 cm.

A final outlier rejection was only carried out during the surface generation and data gridding (Section 8.5). An outlier removal would further improve the height differences at crosspoints and eliminate most of the differences above 15 cm. At this stage, however, the objective of the crosspoint analysis was not to give the best possible result by eliminating all outliers, but to give a realistic impression of the accuracy and repeatability of the airborne laser altimetry method, prior to a thorough outlier removal.

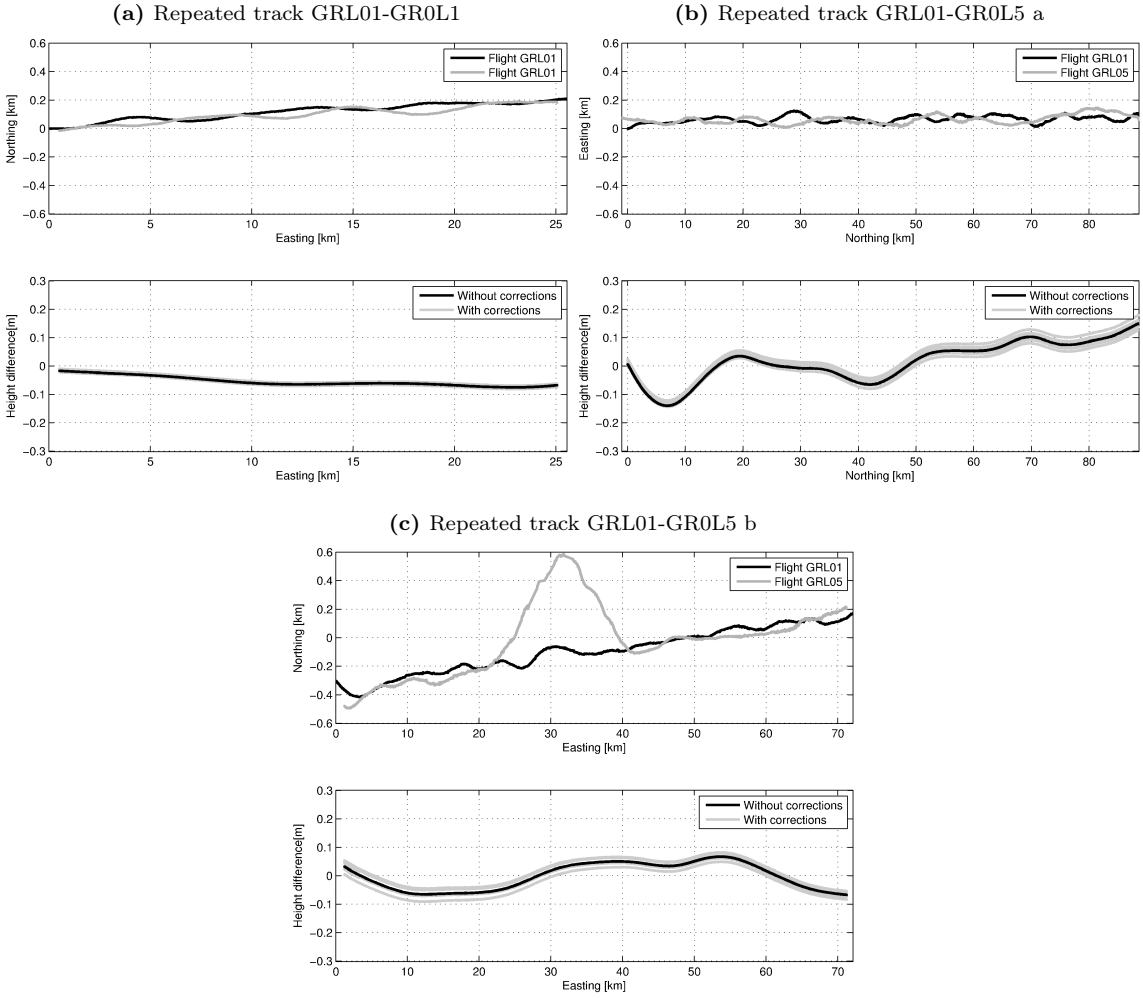

Figure 8.13: Repeated tracks on flights GRL01 and GRL05. Top of (a), (b), (c): along-track horizontal coordinate of repeated tracks against cross-track coordinate. Bottom of (a), (b), (c): height difference between repeated tracks without sea surface height corrections (black line) and with different combinations of sea surface heigtht corrections (grey lines), corresponding to Tab. 8.2.

8.4.3 LSQ Adjustment based on Crosspoints

After the application of all corrections (Section 8.4.2), a relatively large amount (24%) of height differences at crosspoints remained above 10 cm. These misfits would cause severe problems during surface generation (Section 8.5). Hence, as a final correction, an LSQ adjustment of the profiles was carried out, estimating a linear correction for every flight-line that reduces the height differences at crosspoints in a least-squares sense. The LSQ adjustment largely benefits from the grid-like configuration of the densely-spaced flight-tracks. Corrections of up to 15.7 cm were obtained by the LSQ adjustment, providing a significant improvement of the height differences (Tab. 8.2 and Fig. 8.15). Using POL tidal corrections, MOG2D atmospheric corrections and *SLA* corrections in combination with the LSQ adjustment, the RMS of the height differences was reduced to 4.5 cm, corresponding to an improvement of 50%. After the LSQ adjustment, height differences remain below 5 cm at 77% of the 102 crosspoints and below 10 cm at 98% of the crosspoints. The maximum observed height difference was reduced from 21.6 to 14.9 cm. The beneficial impact of the LSQ adjustment for the surface generation procedure is shown in Section 8.5.

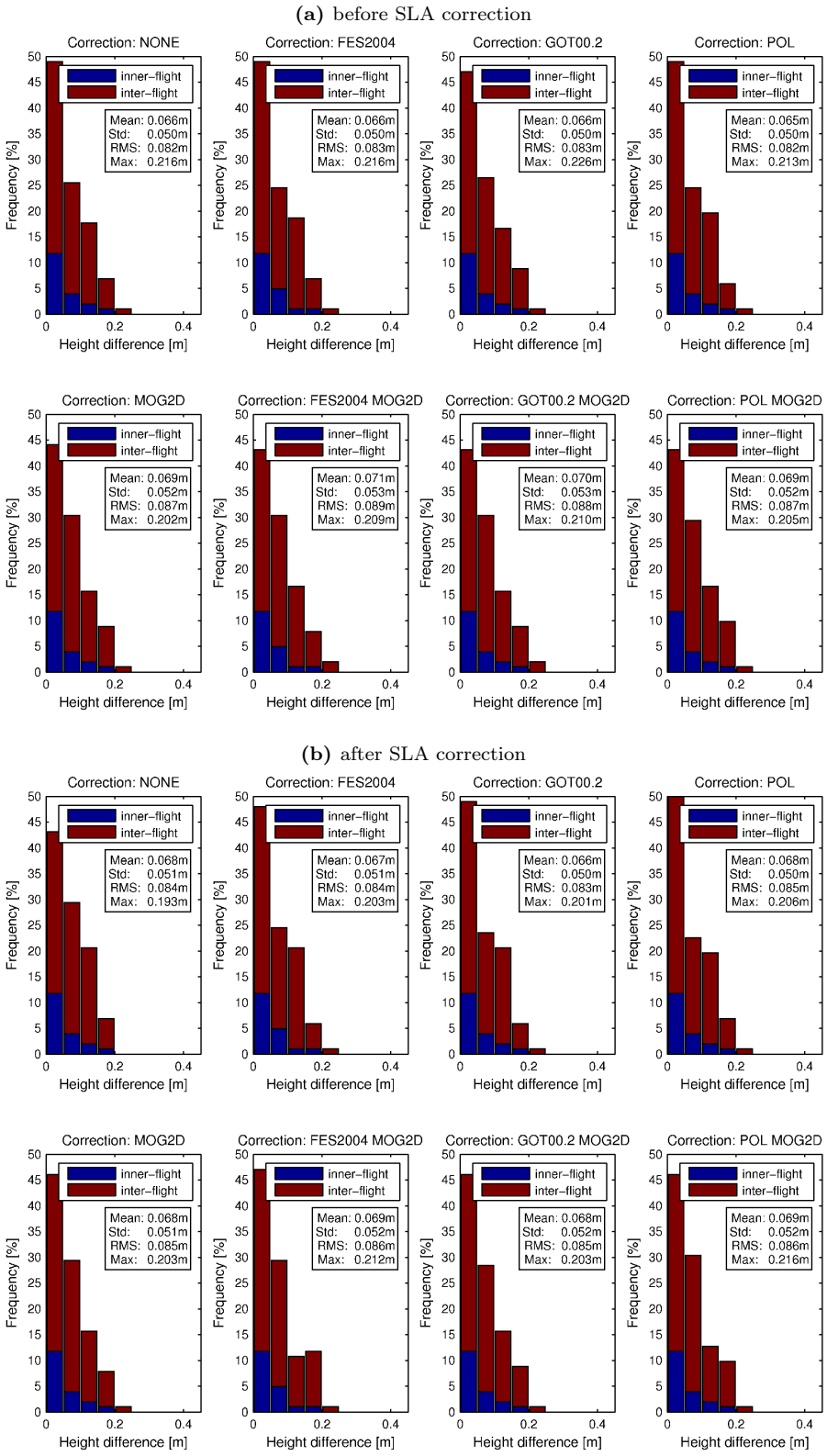

Figure 8.14: Distributions of height differences at crosspoints using different combinations of tidal and atmospheric corrections (corresponding to Tab. 8.2), without **(a)** and with **(b)** sea level anomaly (SLA) correction. Blue: inner-flight crosspoints. Red: inter-flight crosspoints.

Table 8.2: RMS [m] of height differences at crosspoints for solutions with different combinations of tidal and atmospheric sea surface height corrections, without sea level anomaly (SLA) correction, with SLA correction and with combined SLA correction and LSQ adjustment.

	Tidal/Atmospheric sea surface height correction							
Tidal	-	FES2004	GOT00.2	POL	-	FES2004	GOT00.2	POL
Atmospheric	-	-	-	-	MOG2D	MOG2D	MOG2D	MOG2D
All 102 crosspoints								
RMS [m]	0.082	0.083	0.083	0.082	0.087	0.089	0.088	0.087
RMS [m] (SLA)	0.084	0.084	0.083	0.085	0.085	0.086	0.085	0.086
RMS [m] (SLA+LSQ)	-	-	-	-	-	-	-	0.045
Inner-flight 19 crosspoints								
RMS [m]	0.066	0.066	0.065	0.065	0.066	0.065	0.065	0.065
RMS [m] (SLA)	0.066	0.065	0.065	0.065	0.066	0.065	0.064	0.064
RMS [m] (SLA+LSQ)	-	-	-	-	-	-	-	0.050
Inter-flight 83 crosspoints								
RMS [m]	0.086	0.086	0.086	0.086	0.091	0.093	0.092	0.091
RMS [m] (SLA)	0.088	0.087	0.087	0.089	0.089	0.091	0.089	0.090
RMS [m] (SLA+LSQ)	-	-	-	-	-	-	0.045	0.044

8.5 Time-Independent Sea Surface Topography

By subtracting the time-dependent corrections (Section 8.3) from the low-pass filtered instantaneous sea surface heights (Section 8.2.1, Fig. 8.2 and Fig. 8.2), time-independent sea surface height profiles are obtained (Fig. 8.16). The sea surface heights are heights above the WGS84 ellipsoid. Based on the analysis of sea surface height corrections in Section 8.4.2, the observed sea surface heights were corrected using POL tidal corrections, MOG2D atmospheric corrections and SLA corrections from SSALTO/DUACS. Furthermore, the sea surface heights were corrected using an LSQ adjustment of the profiles in order to reduce the height differences at crosspoints (Section 8.4.3).

The resulting punctual time-independent sea surface heights were interpolated onto a regular grid using a bicubic spline interpolation with continuous curvature and adjustable tension. In a second step, the obtained gridded sea surface heights were low-pass filtered using a 2D FFT filter with a cut-off wavelength of 10 km. The cut-off wavelength of the FFT filter was optimally chosen in order to keep the residuals small, without obtaining an unrealistically rough surface. The final gridded data are forming a surface representing the time-independent sea surface topography (Fig. 8.17).

A final indication for the accuracy of the sea surface heights is given by the residuals between the time-independent sea surface height profiles (Fig. 8.16) and the gridded sea surface topography (Fig. 8.17). Without the LSQ adjustment (Section 8.4.3), the along-track residuals have a standard deviation of 4.1 cm and large local values of up to 28.5 cm (Fig. 8.18a). After the LSQ adjustment, the residuals are significantly improved (Fig. 8.19a). The standard deviation was reduced to 3.1 cm, but large residuals of up to 26.6 cm locally remained. In order to avoid unrealistic strong gradients in the gridded sea surface topography, it is advisable to eliminate along-track data presenting large residuals prior to the surface generation. Using the LSQ adjustment, less observations had to be removed (Fig. 8.18b and Fig. 8.19b). After the removal of the outliers, the final residuals are all below 10 cm, with a standard deviation of 2.9 cm only (Fig. 8.19b).

The sea surface height results reveal very strong gradients, with heights decreasing from 28 m above the reference ellipsoid in the north-eastern part of the survey area down to 8 m towards the Hellenic Trench in the southern part, along a distance of only 200 km (Fig. 8.17). Further analysis and interpretation of the observed sea surface heigths are treated in Chapter 11.

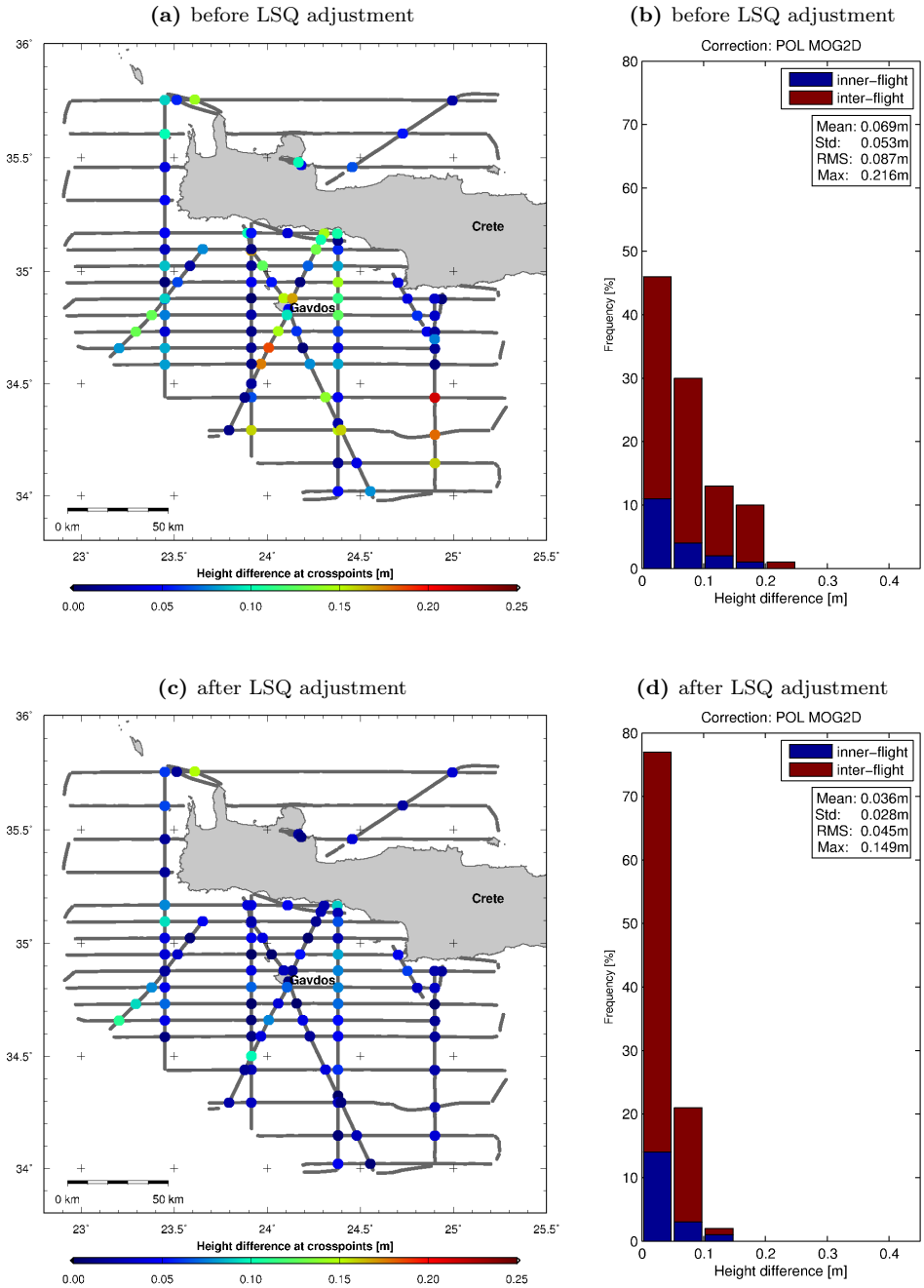

Figure 8.15: **(a)** Crosspoints of sea surface height profiles with color-coded height differences, for the solution using POL tidal corrections, MOG2D atmospheric corrections and SSALTO/DUACS sea level anomaly (SLA) corrections. **(b)** Distribution of height differences. Blue: inner-flight crosspoints. Red: inter-flight crosspoints. **(c)** Same as (a), but with LSQ adjustment of flight-lines based on crosspoints. **(d)** Same as (b), but with LSQ adjustment of flight-lines.

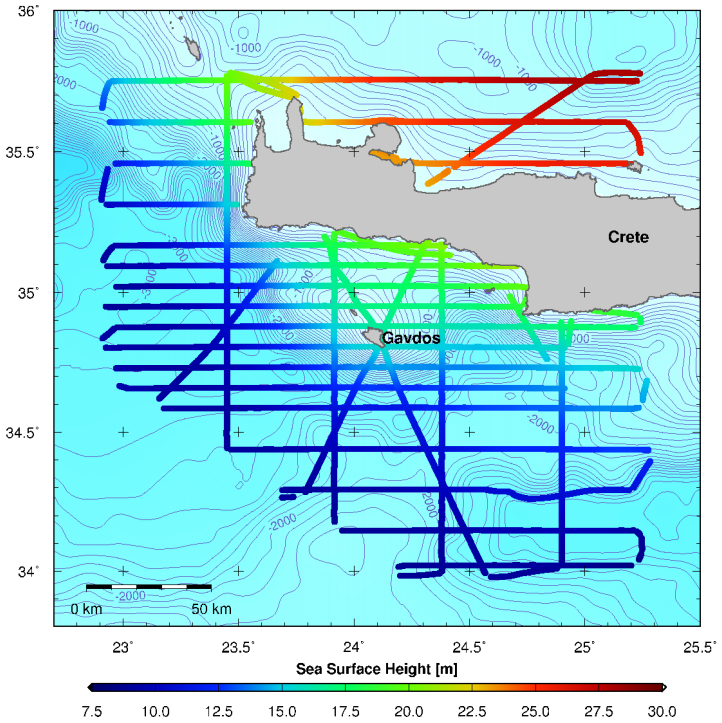

Figure 8.16: Time-independent sea surface height profiles (color-coded) from airborne laser altimetry around the island of Crete. The sea surface height profiles were low-pass filtered using a 1D spline filter with a cut-off wavelength of 10 km. Background: bathymetry in [m] (contour interval 100 m).

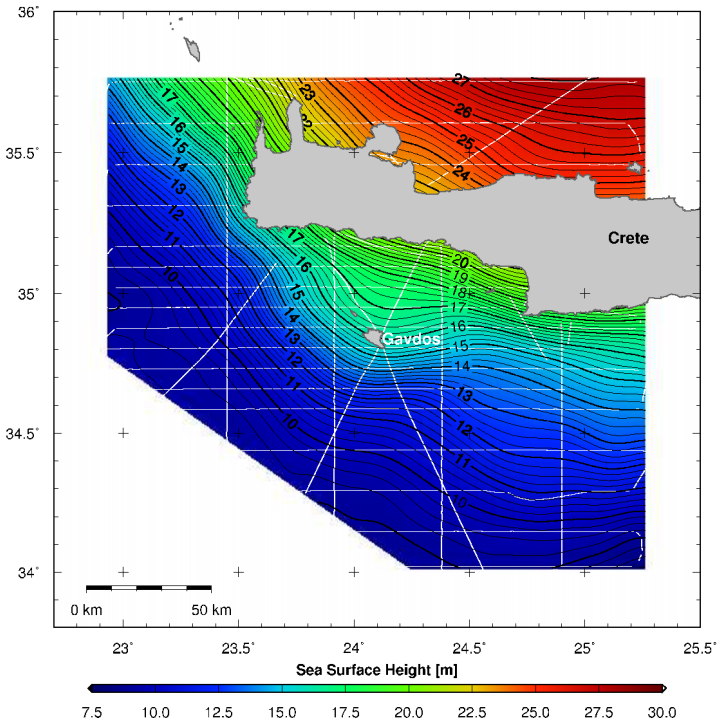

Figure 8.17: Sea surface topography obtained from airborne laser altimetry profiles around Crete (Fig. 8.16) by bicubic spline interpolation. The sea surface topography was low-pass filtered using a 2D FFT filter with a cut-off wavelength of 10 km. White lines: flight-tracks. Contour interval: 0.25 m.

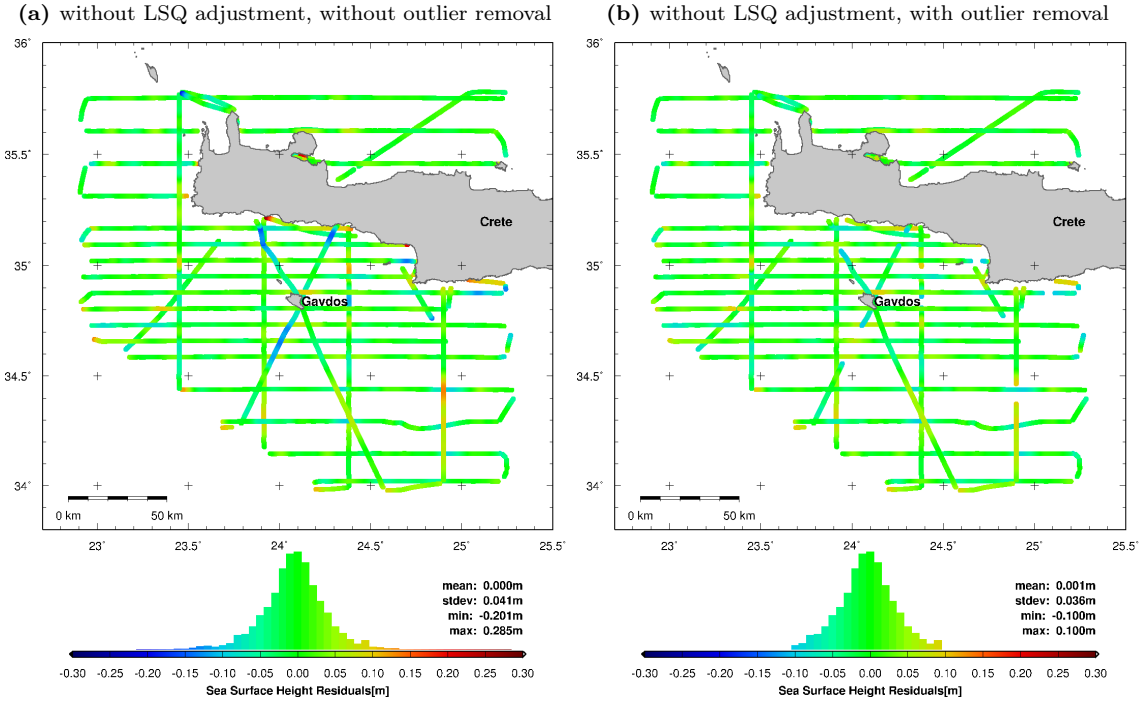

Figure 8.18: Residuals between along-track sea surface heights (Fig. 8.16) and gridded sea surface topography (Fig. 8.17), without correction from LSQ adjustment, before **(a)** and after **(b)** outlier removal.

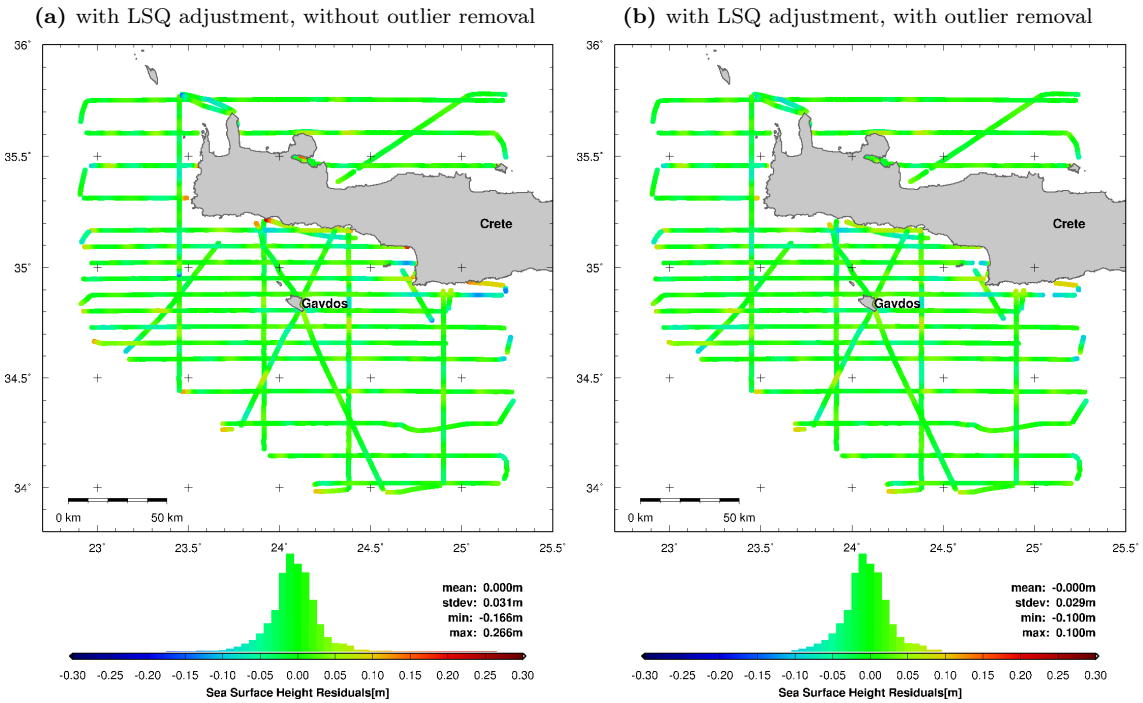

Figure 8.19: Residuals between along-track sea surface heights (Fig. 8.16) and gridded sea surface topography (Fig. 8.17), with correction from LSQ adjustment, before **(a)** and after **(b)** outlier removal.

9 Sea Surface Heights by Shipborne Ultrasound Altimetry in the North Aegean Sea

9.1 Shipborne Ultrasound Altimetry Campaigns

The survey area is situated in the North Aegean Sea and covers part of the North Aegean Trough (NAT), which is a tectonic graben-like feature characterized by a zone of deep water reaching 1500 m and trending from north-east to south-west in the North Aegean Sea. The North Aegean Trough is considered to form the western continuation of the seismically active North Anatolian Fault Zone (McNeill et al., 2004). For calibration and validation purposes of radar altimeter missions, the survey area was chosen in the vicinity of Jason-1 ground-tracks, including the cross-over of Jason-1 ascending track 33 and descending track 94 (Fig. 9.1, black diagonal lines).

Five successful campaigns for shipborne sea surface height surveys were carried out in the North Aegean Sea from 2004 to 2008, totaling more than 2000 nautical miles of ship-tracks (Fig. 9.1). The campaigns were carried out in Sept. 2004, June 2005, Sept. 2006, Sept. 2007 and July 2008. The campaigns involved a multi-antenna GPS array of 4 - 5 receivers aboard the boat, 1 - 2 ultrasonic distance sensors, 1 - 2 GPS-buoys and an inertial AHRS (Attitude and Heading Reference System). Dedicated GPS-buoy measurements were performed on Jason-1 ground-tracks and at other key spots, including deployments with simultaneous Jason-1 cross-over. Five GPS reference stations, situated on the islands of Alonissos (ALON), Agios Efstratios (EFST), Limnos (LIMS) and Skiros (NSKS), as well as in Neohori (NEOH), were operated at a sampling rate of 1 Hz during the shipborne campaign. In June 2005 and Sept. 2007, the permanent tide-gauge stations PELAS and PELAN were installed in the survey area and operated since then (Fig. 9.1).

9.2 Instantaneous Sea Surface Height Profiles

Sea surface profiles were computed based on shipborne GPS and ultrasound altimetry data, ship trajectories and attitudes, using the direct georeferencing method described in Chapter 7 (Fig. 9.2 and Fig. 9.3). During the shipborne campaigns, sea surface height data was collected while the ship was at rest or moving with varying velocity. This made inadequate the use of the spline filter algorithm, developed and applied for sea surface height observations by airborne laser altimetry (Section 8.2.1). Hence, a robust windowed median filter algorithm, allowing to switch between window sizes in the time and distance domain, was developed. The shipborne sea surface height results, with sampling rates of 1 Hz and 10 Hz, were low-pass filtered using the median filter with a moving-window size of 30 minutes or 500 m, depending on whether the ship was at rest or moving. The windowed median filter algorithm used in this project has several advantages over filter methods in the frequency domain based on Fourier transforms. It is robust against outliers and is capable of processing the enormous amount of data points yielded by the 10 Hz ultrasound measurements. In addition, as opposed to filter algorithms based on Fourier transforms, the windowed median filter is indifferent to data gaps as observed throughout the ultrasound datasets.

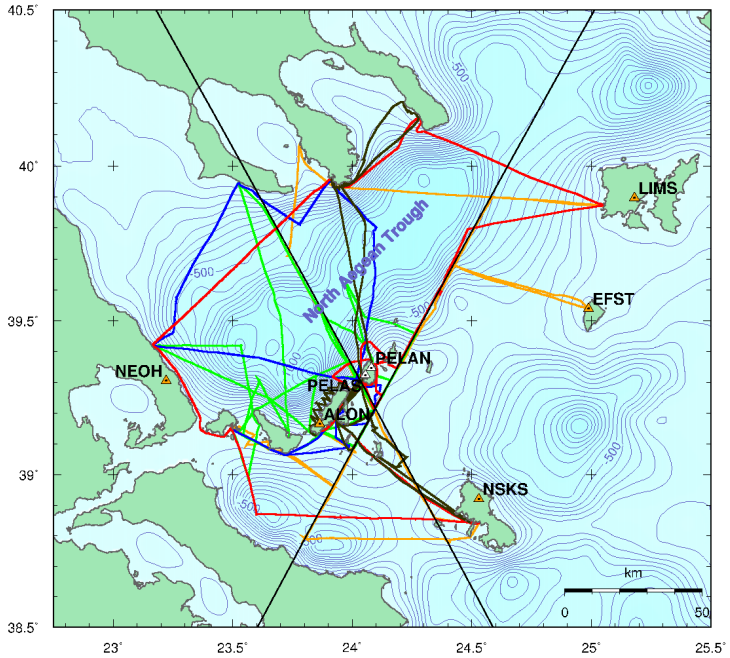

Figure 9.1: Shipborne sea surface height campaigns in the North Aegean Sea. Boat tracks from the 2004 (orange line), 2005 (green line), 2006 (blue line), 2007 (red line) and 2008 (brown line) campaigns. Black diagonal lines: Jason-1 tracks 33 (ascending) and 94 (descending). Orange triangles: GPS reference stations (ALON, EFST, LIMS, NSKS, NEOH). White triangles: tide-gauge stations (PELAS, PELAN). Background: bathymetry in [m] with contour interval 50 m.

9.3 Sea Surface Height Corrections

9.3.1 Ocean Wave Correction

The oscillation effects of ocean waves are eliminated by the low-pass filtering described in Section 9.2. More details on ocean waves are given in Section 3.2.

9.3.2 Ocean Tide Correction

In the North Aegean Sea, the amplitudes of the major ocean tide constituents M2 and S2 are in the order of 15 cm and 10 cm, respectively (Fig. 3.4). The tidal effects to be expected in the North Aegean Sea are thus stronger than in the survey area around Crete. Tidal corrections along the shipborne altimetry tracks were computed based on the global tide model FES2004 (Fig. 9.4a) and on the POL (Proudman Oceanographic Laboratory) model for Mediterranean (Fig. 9.4b). Further details on the two ocean tide models can be found in Section 3.3.2. Both models predict ocean tide amplitudes in the order of 15-20 cm. However, the predictions are contradictory, since the differences between the models can reach 20 cm (Fig. 9.4). Considering the size of the encountered tidal amplitudes and of the differences between the models, the choice of the tide model is crucial for the accuracy of the corrected sea surface heights.

In order to select the most appropriate model for the considered survey area, a validation of the tidal corrections obtained from the two models was performed, based on tide-gauge observations (Section 9.3.4) and on crosspoints analysis (Section 9.4.1). The POL model was identified to agree better with the in-situ observations and was therefore chosen to correct the shipborne sea surface height data of the North Aegean Sea campaign.

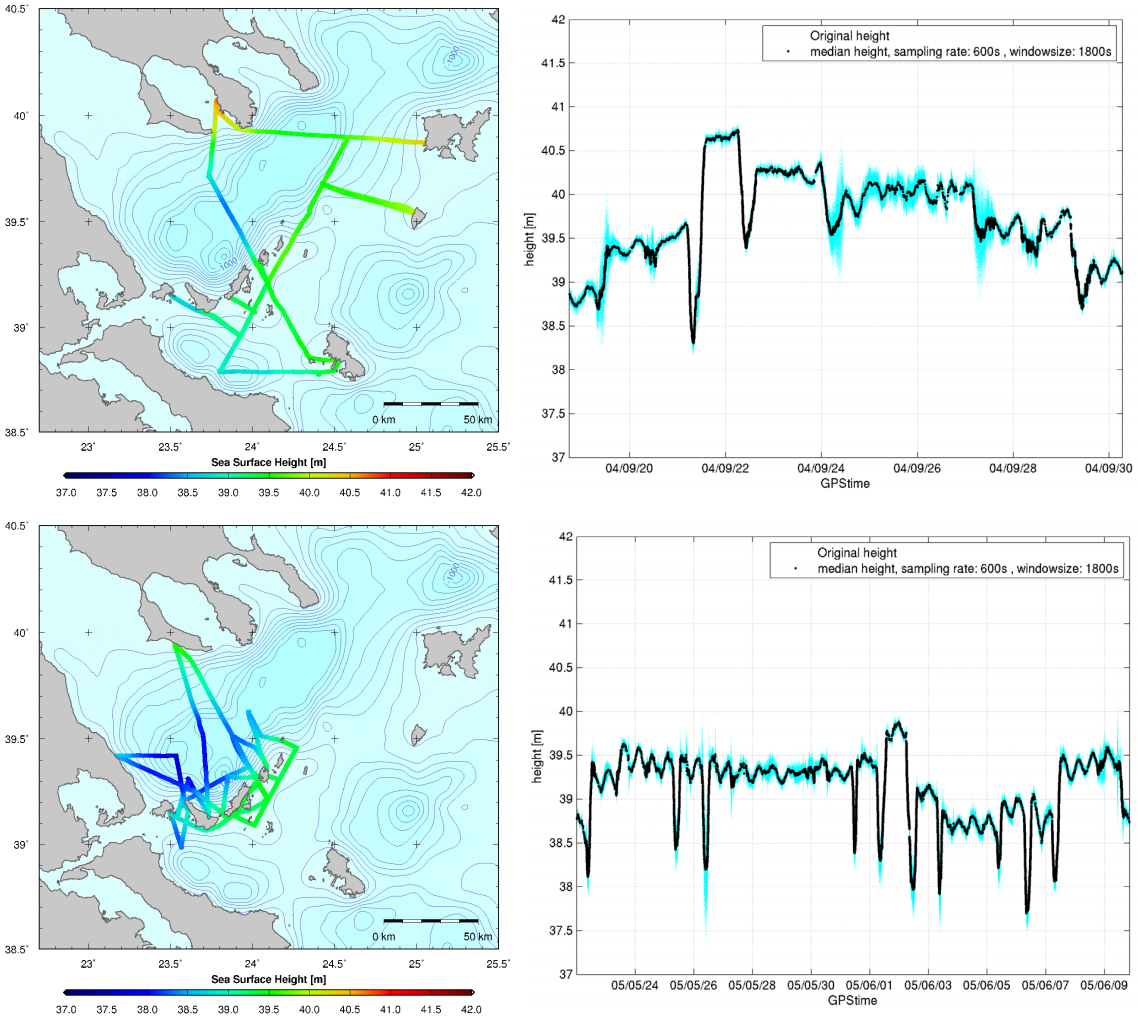

Figure 9.2: Sea surface height results of shipborne GPS campaigns in 2004 (top) and 2005 (bottom). Left: ship-tracks with color-coded instantanenous sea surface heights. Right: corresponding time-series of ellipsoidal sea surface height profiles, with original sampling rate of 1 Hz (cyan dots) and filtered heights.

9.3.3 Correction for Atmospheric Pressure and Wind Forcing

Corrections for the effect of atmospheric pressure and wind forcing on sea surface heights were computed from MOG2D correction grids for the shipborne data in the North Aegean Sea. Corrections along the shipborne tracks are obtained by temporal and spatial interpolation of the MOG2D grids. The atmospheric effects along the ship tracks ranged from -16 to 12 cm during the five survey campaigns (Fig. 9.5). Extreme variations of the atmospheric effect of up to 10 cm/day were encountered. Small deviations below 2 cm between the corrections at the tide-gauge station PELAN situated in the center of the survey area (Fig. 9.5a to Fig. 9.5e, grey line) and the ship track corrections (Fig. 9.5a to Fig. 9.5e, black line) are produced by the geographical distance between the ship and the tide-gauge station. For the area and period of the considered dataset, the effect of atmospheric pressure and wind forcing reached values similar to the amplitudes of the ocean tide (Fig. 9.4).

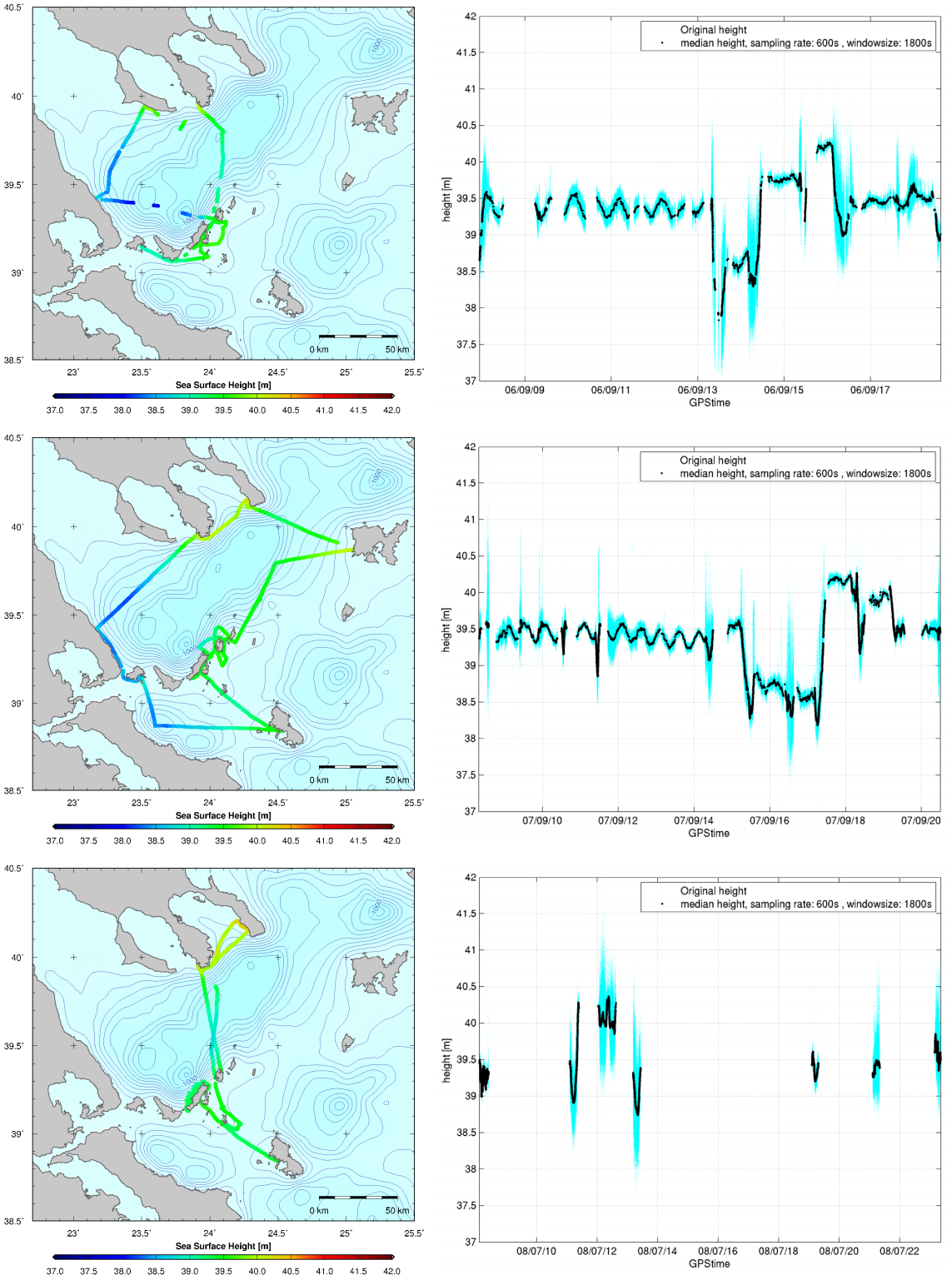

Figure 9.3: Sea surface height results of shipborne ultrasound altimetry campaigns in 2006 (top), 2007 (middle) and 2008 (bottom). Left: ship-tracks with color-coded instantaneous sea surface heights. Right: corresponding time-series of ellipsoidal sea surface height profiles, with original sampling rate of 10 Hz (cyan dots) and filtered heights.

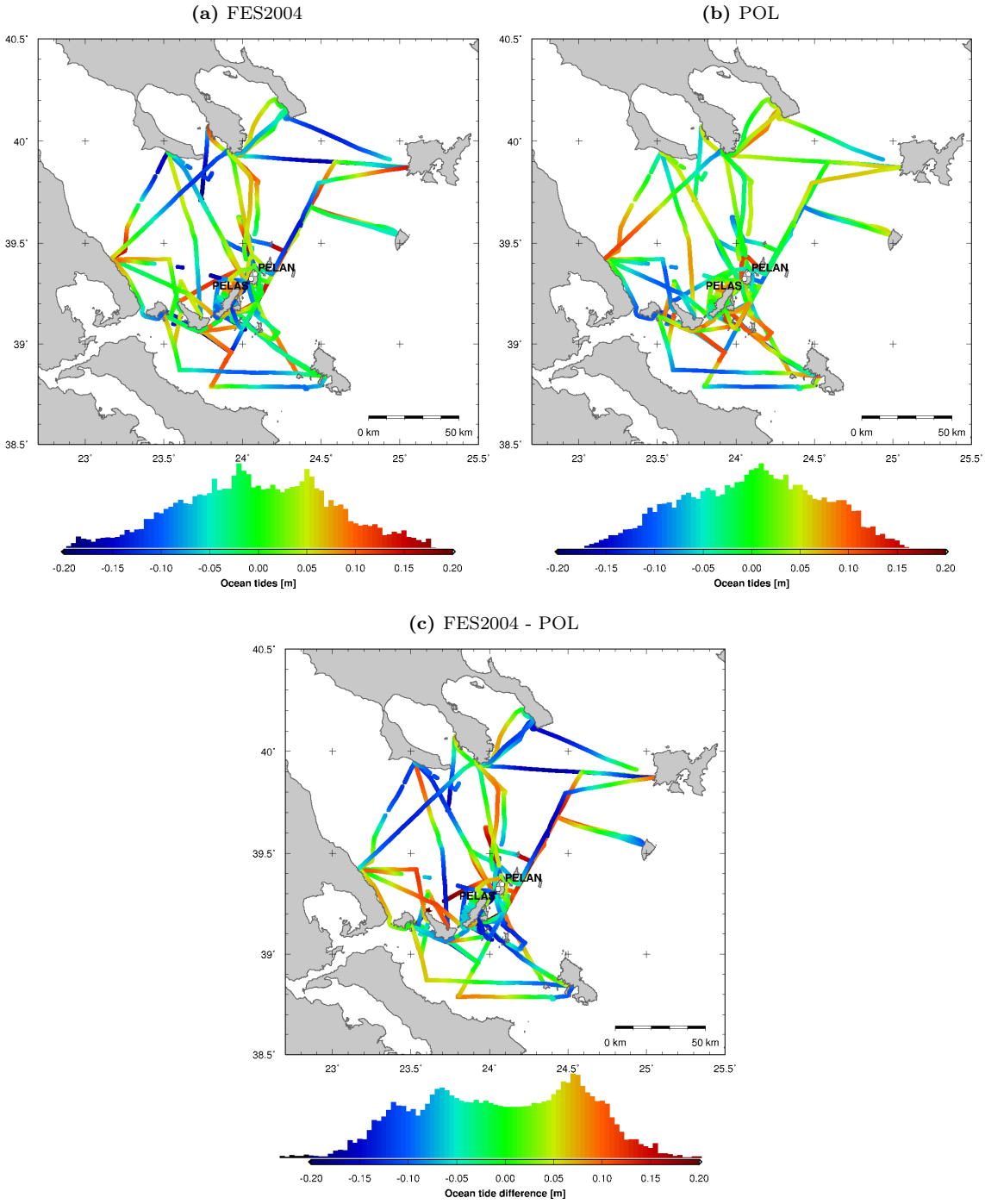

Figure 9.4: Ocean tides along shipborne tracks predicted by the models **(a)** FES2004 and **(b)** POL (Proudman Oceanographic Laboratory). **(c)** Differences between the tide predictions from FES2004 and POL.

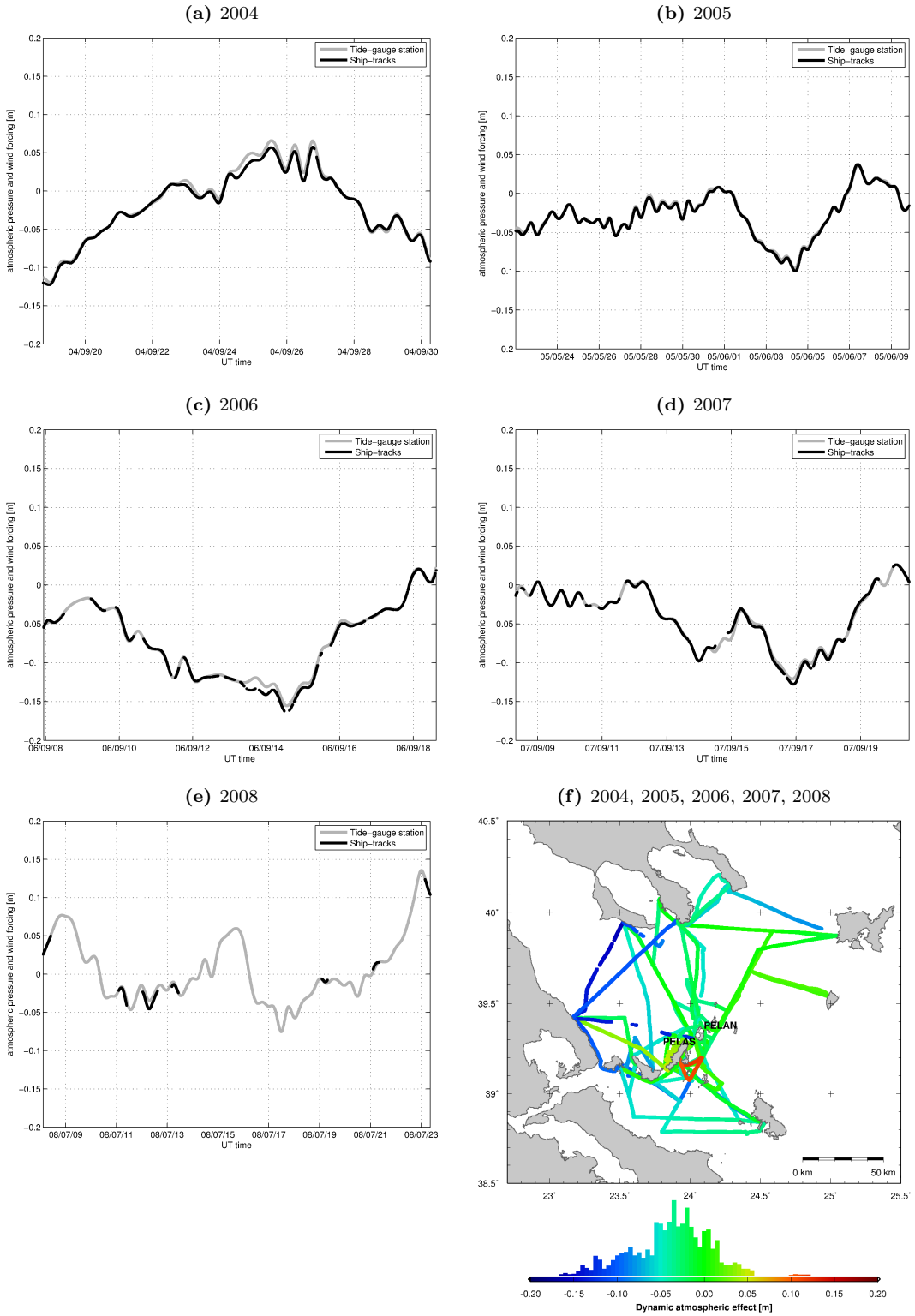

Figure 9.5: Effect of atmospheric pressure and wind forcing on sea surface height during shipborne surveys in 2004 **(a)**, 2005 **(b)**, 2006 **(c)**, 2007 **(d)** and 2008 **(e)**, based on MOG2D correction grids. Black line: time-series along ship tracks. Grey line: time-series at PELAN tide-gauge station. **(f)** Effect along ship tracks during all campaigns, corresponding to the time-series of (a) to (e).

Figure 9.6: Left: Pressure tide-gauge station PELAN, with GPS antenna for the determination of absolute height and position. Right: view of the pressure gauge inside the black tube.

9.3.4 Validation of Tidal and Atmospheric Models with Tide-Gauge Data

A validation of the FES2004 and POL tide models, as well as the MOG2D atmospheric forcing model, was carried out using local tide-gauge data. The considered tide observations are from the PELAN pressure tide-gauge station, installed in the framework of this project (Fig. 9.6). The tide-gauge is located at 39.3444°N, 24.0757°E (Fig. 9.1). It is operated with an observation interval of 3 minutes and is logging average values covering 15 minutes. Tide data covering 9 consecutive months were analyzed (Fig. 9.7). In a first step, the atmospheric effect from MOG2D correction grids were removed from the tide-gauge observations (Fig. 9.7). In a second step, a remaining low frequency trend (period >48 h) was removed from the observations. This trend, ranging between -18.5 and 14.3 cm over the considered 9 months, mainly represents the remaining local effect of atmospheric forcing, not resolved by the MOG2D model (Fig. 9.7).

Differences between the corrected tide-gauge observations (Fig. 9.7, bottom) and predictions from FES2004 show a large standard deviation of 8.6 cm and large maximum values of up to 25 cm (Fig. 9.8). The FES2004 predictions do not match the observed tidal signal: e.g. the spring and neap tides do not coincide in time (Fig. 9.8b). Predictions from the POL model show a good agreement with the observed tidal signal. Differences have a standard deviation of 2.5 cm and maximum values of 8 cm (Fig. 9.9). Hence, despite the fact that only 4 tidal constituents (M2, S2, K1, O1) are included in the POL model (against 14 constituents for FES2004), the POL predictions are in better agreement with the local tide-gauge observations than FES2004. The remaining residuals of the tide-gauge data with respect to the POL model are most likely due to local coastal effects, not resolved by the tidal and atmospheric forcing model. It can be assumed that the model would perform better offshore, in the absence of strong and hardly predictable coastal effects. At the PELAN tide-gauge site in the North Aegean Sea, differences between tidal predictions from FES2004 and POL have a large standard deviation of 9.2 cm and large maximum values of 25 cm. As for the comparison with the observed tidal signal, the spring and neap tides predicted by FES2004 do not coincide in time with the ones predicted by the POL model.

In order to further analyze the tidal signal observed in the survey area of the North Aegean Sea, amplitudes and phase lags of the 9 major tidal constituents (M2, S2, K2, N2, 2N2, K1, O1, P1 and Q1) were estimated by harmonic analysis (3.4) of the tide-gauge data at PELAN (Fig. 9.7, bottom). The amplitudes and phase lags obtained by harmonic analysis are in excellent agreement

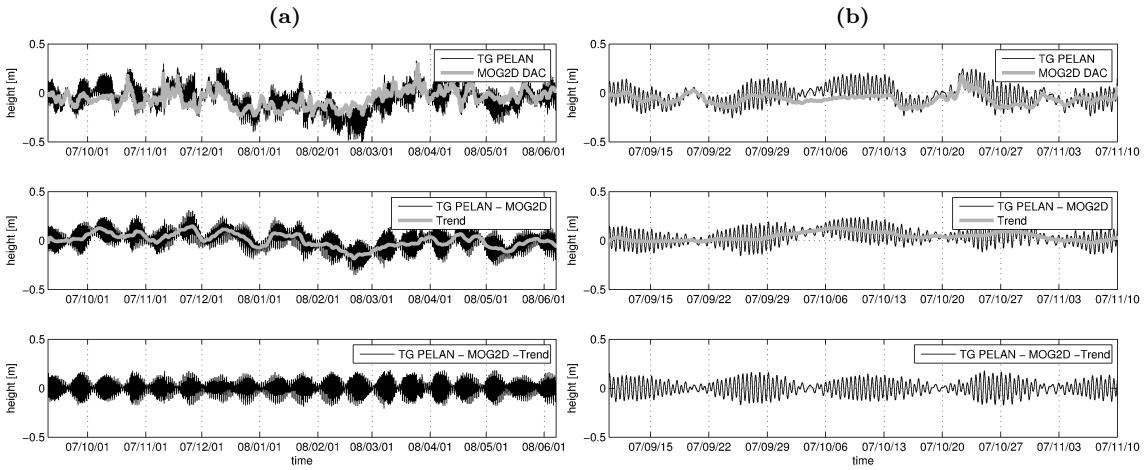

Figure 9.7: (a) Top: Sea level observations from PELAN tide-gauge station (black line) in the North Aegean Sea, from Sept. 2007 to June 2008 (9 months), and dynamic atmospheric correction (DAC) from MOG2D (grey line). Center: Tide-gauge data corrected with MOG2D DAC (black line) and remaining trend (grey line). Bottom: Tide-gauge data corrected with MOG2D DAC and with remaining trend removed. **(b)** Zoom into first 2 months of data of (a).

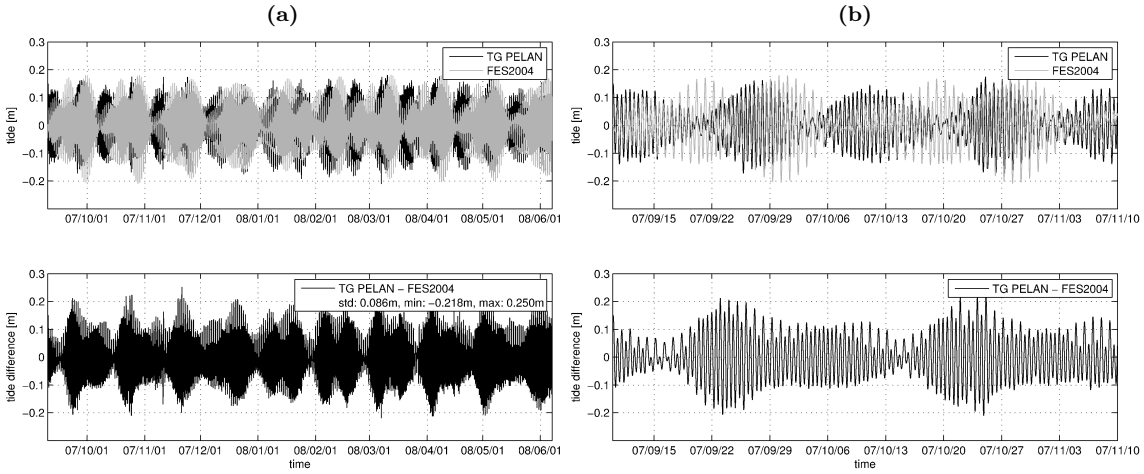

Figure 9.8: (a) Top: Tidal predictions from the FES2004 model (grey line) against observations from PELAN tide-gauge station (black line) in the North Aegean Sea, from Sept. 2007 to June 2008 (9 months), corrected with MOG2D DAC and with remaining trend removed (corresponding to Fig. 9.7, bottom). Bottom: Difference between tide-gauge data and FES2004 model. **(b)** Zoom into the first 2 months of (a).

with the ones of the POL model (Tab. 9.1). The amplitudes agree better than 0.4 cm and the phase lags better than 9°. On the other hand, the agreement with the amplitudes and phase lags of FES2004 is less good (Tab. 9.1). The maximum amplitude difference is 2.9 cm and the maximum phase lag difference is 107°. The bad phase lags of most of the tidal constituents are at the origin of the poor predictions of FES2004 in this area. These bad phase lags are probably a consequence of a lack of Aegean tide-gauge data in the assimilation of FES2004. This assumption was confirmed by computing differences between tidal predictions from FES2004 and POL at an arbitrary site in the Gulf of Lion in the Eastern Mediterranean, where local tide-gauge data are included in the assimilation of FES2004. In this area, the standard deviation of the differences between the predictions of the two models is only 2.0 cm, with maximum values of 6 cm.

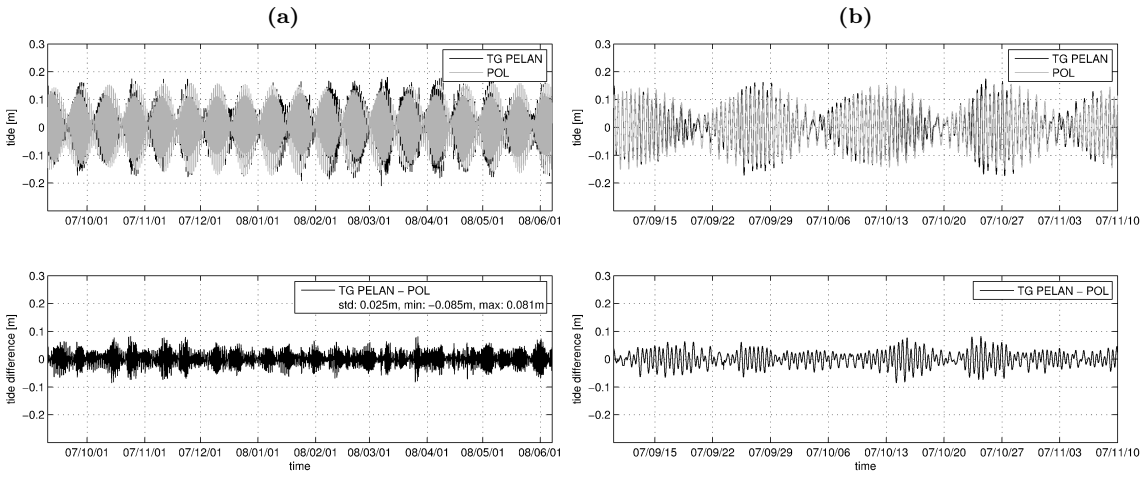

Figure 9.9: **(a)** Top: Tidal predictions from the POL model (grey line) against observations from PELAN tide-gauge station (black line) in the North Aegean Sea, from Sept. 2007 to June 2008 (9 months), corrected with MOG2D DAC and with remaining trend removed (corresponding to Fig. 9.7, bottom). Bottom: Difference between tide-gauge data and POL model. **(b)** Zoom into the first 2 months of (a).

Table 9.1: Amplitudes and phase lags of the major harmonic constituents of the astronomical ocean tide in the North Aegean Sea, estimated by harmonic analysis of local tide-gauge data (TG) and extracted from the FES2004 and POL grids.

	Period	Amplitude [m]			Phase lag [°]		
Wave	[days]	TG	FES2004	POL	TG	FES2004	POL
M2	0.51753	0.075	0.078	0.079	59	-25	68
S2	0.50000	0.052	0.035	0.054	80	103	82
K2	0.49863	0.020	0.014	-	52	88	-
N2	0.52743	0.015	0.044	-	55	-17	-
2N2	0.53772	0.002	0.006	-	85	74	-
K1	0.99727	0.029	0.017	0.029	-18	-69	-17
O1	1.07581	0.014	0.035	0.015	-47	-58	-40
P1	1.00275	0.009	0.007	-	-15	-70	-
Q1	1.11951	0.002	0.006	-	-71	36	-

Using the amplitudes and phase lags obtained by harmonic analysis of the tide-gauge observations (Tab. 9.1), local tides can be predicted (Fig. 9.10) using (3.4). Residuals between the corrected tide-gauge observation used in the harmonic analysis (Fig. 9.7, bottom) and the predictions based on the harmonic analysis have a small standard deviation of 1.3 cm and maximum values of 8 cm (Fig. 9.10). The small residuals show the good approximation of the observed tides by the harmonic model of the 9 major tidal constituents M2, S2, K2, N2, 2N2, K1, O1, P1 and Q1.

9.3.5 Sea Level Anomaly Correction

Sea level anomalies (SLA) were computed for the survey area in the North Aegean Sea during the five shipborne campaigns, based on the SSALTO/DUACS sea level anomalies (Section 2.4). During the five campaigns, the SLA took significant values between -6 and 13 cm (Fig. 9.11f). During the same campaign of 2 to 3 weeks, variations of the SLA by 5 to 10 cm were encountered (Fig. 9.11a to Fig. 9.11e). Systematic differences between the SLA during the various campaigns were observed. The campaigns of 2004, 2006 and 2007, all carried out in September, show positive

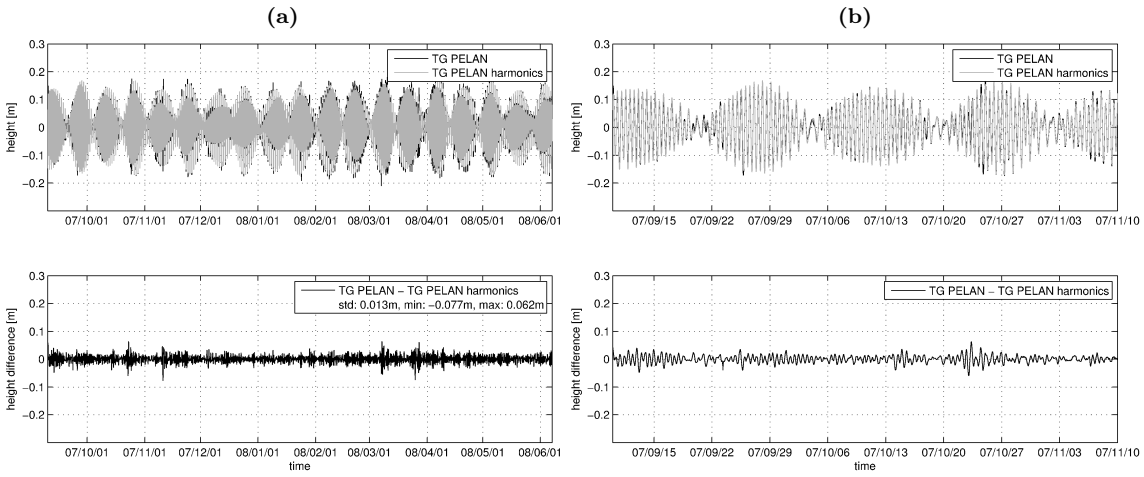

Figure 9.10: (a) Top: Sea level observations from PELAN tide-gauge station (black line) in the North Aegean Sea, from Sept. 2007 to June 2008 (9 months), corrected with MOG2D DAC and with remaining trend removed (corresponding to Fig. 9.7, bottom) against predictions based on the harmonic analysis of the corrected tide-gauge observations (grey line). Bottom: Difference between tide-gauge data and tidal predictions based on harmonic analysis. **(b)** Zoom into the first 2 months of (a).

SLA of 5 to 13 cm (Fig. 9.11a, Fig. 9.11c and Fig. 9.11d). On the other hand, the campaigns of 2005 and 2008, carried out in May/June and July, respectively, show negative SLA of -5 to 0 cm (Fig. 9.11b and Fig. 9.11e).

The SLA values show that the sea surface topography cannot be considered as constant from one campaign to the next, and even not during one individual campaign. The significant improvement of the height differences at crosspoints of the shipborne profiles after application of the SLA corrections is shown in Section 9.4.1. These corrections should therefore be applied when the resulting sea surface heights are meant to represent the mean sea surface MSS, as defined in (2.2) and (2.30). On the other hand, they must not be applied when the resulting sea surface heights are meant to represent corrected sea surface heights SSH_c, including the variable part of the dynamic topography, as defined in (2.1) and (2.29).

9.4 Repeatability Analysis

9.4.1 Crosspoint Analysis

The shipborne profiles yield a total of 1999 crosspoints, where the sea surface height was measured twice at the same geographic position (Fig.9.13a). Height differences at crosspoints are a good indicator for the repeatability and the accuracy of the shipborne altimetry system. An analysis of height differences at crosspoints using different combinations of tidal and atmospheric sea surface height corrections, as well as sea level anomaly (SLA) corrections, was carried out (Tab. 9.2 and Fig. 9.12). Significant differences were observed between the various combinations of corrections. The analysis showed that for the considered survey area, the tidal corrections of FES2004 has no significant improving impact on the height differences at crosspoints. On the other hand, the use of the POL (Proudman Oceanographic Laboratory) tidal corrections reduce the RMS on the height differences by 4.8 cm and the maximum absolute difference by 8.0 cm. Applying tidal corrections directly from tide-gauge data produced a slightly worse agreement with the shipborne data (not shown), due to the fact that tide-gauge data are affected by local coastal effects. The FES2004

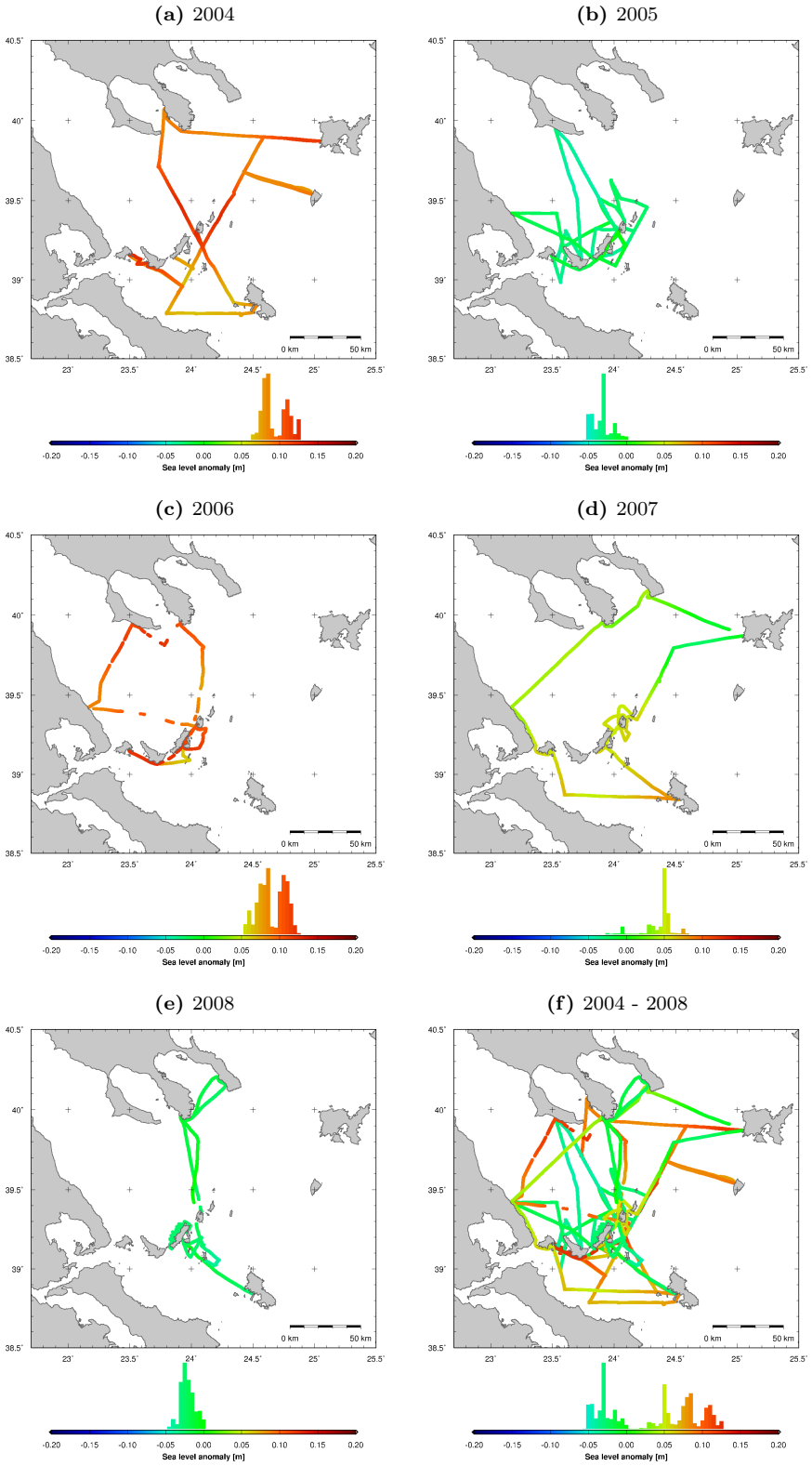

Figure 9.11: Sea level anomalies along ship-tracks, based on SSALTO/DUACS sea level anomalies, during shipborne surveys in 2004 **(a)**, 2005 **(b)**, 2006 **(c)**, 2007 **(d)**, 2008 **(e)** and from 2004 to 2008 **(f)**.

Table 9.2: RMS [m] of height differences at crosspoints for solutions with different combinations of tidal and atmospheric sea surface height corrections, without sea level anomaly (SLA) correction, with SLA correction and with combined SLA correction and LSQ adjustment.

	Tidal/Atmospheric sea surface height correction					
Tidal	-	FES2004	POL	-	FES2004	POL
Atmospheric	-	-	-	MOG2D	MOG2D	MOG2D
All 1999 crosspoints						
RMS [m]	0.162	0.164	0.126	0.152	0.159	0.117
RMS [m] (SLA)	0.143	0.138	0.099	0.127	0.127	0.079
RMS [m] (SLA+LSQ)	-	-	-	-	-	0.043
Inner-campaign 824 crosspoints						
RMS [m]	0.144	0.129	0.095	0.131	0.119	0.078
RMS [m] (SLA)	0.137	0.124	0.084	0.125	0.116	0.068
RMS [m] (SLA+LSQ)	-	-	-	-	-	0.038
Inter-campaign 1175 crosspoints						
RMS [m]	0.173	0.185	0.144	0.165	0.181	0.137
RMS [m] (SLA)	0.147	0.147	0.108	0.129	0.134	0.086
RMS [m] (SLA+LSQ)	-	-	-	-	-	0.047

tidal corrections had no improving effects on the height differences. The MOG2D atmospheric corrections reduce the RMS on the height differences by 2.0 cm and the maximum absolute difference by 7.7 cm. Finally, the SLA corrections reduce the RMS on the height differences by 3.8 cm and the maximum absolute difference by 8.6 cm.

The beneficial effect of the SLA corrections is further shown by analyzing height differences at crosspoints separately for every campaign. Offsets at crosspoints between the campaigns were estimated by LSQ adjustment (Tab. 9.3). Without SLA corrections, systematic offsets of up to 13.5 cm were observed when computing crosspoints between one campaign and the other four campaigns. These offsets were reduced to below 2 cm by applying SLA corrections.

The crosspoint analysis lead to the conclusion that the best results are obtained using POL tide corrections in combination with MOG2D atmospheric corrections and SSALTO/DUACS SLA corrections (Fig. 9.12). Using this set of corrections, the final RMS value of height differences at the 1999 crosspoints is 7.9 cm (Tab. 9.2 and Fig. 9.13b). The RMS at the 824 inner-campaign crosspoints is 6.8 cm, whereas the RMS at the remaining 1175 inter-campaign crosspoints is 8.6 cm. The height difference remains below 10 cm at 80% of the crosspoints, below 15 cm at 94% and below 20 cm at 99% of the crosspoints. The maximum observed height difference is 28.7 cm.

A final outlier rejection was only carried out during the surface generation and data gridding (Section 9.5). The outlier removal would further improve the height differences at crosspoints and eliminate most of the differences above 15 cm. At this stage, however, the objective of the crosspoint analysis was not to give the best possible results by eliminating all outliers, but to give a realistic impression of the accuracy and repeatability of the shipborne altimetry method, prior to a thorough outlier removal.

9.4.2 LSQ Adjustment based on Crosspoints

After the application of the best combination of corrections identified in Section 9.4.1, namely POL tide corrections in combination with the MOG2D atmospheric corrections and the SSALTO/DUACS SLA corrections, a relatively large amount (20%) of height differences at crosspoints remained above 10 cm. These misfits would cause severe problems during surface generation (Section 9.5). Hence, as a final correction, an LSQ adjustment of the profiles was carried out, estimating a linear correction for every ship-track that reduces the height differences at the crosspoints in a least-

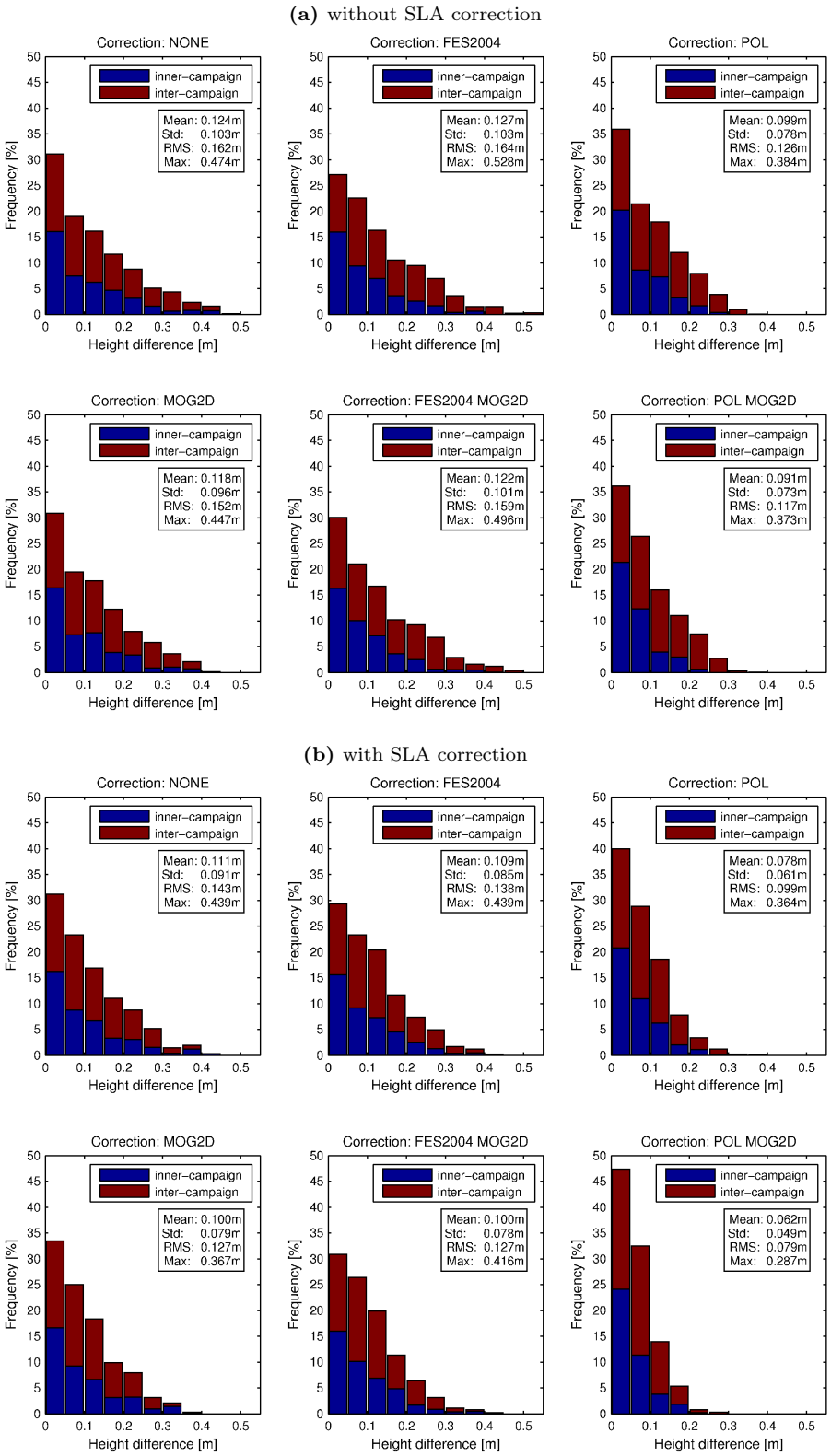

Figure 9.12: Distributions of height differences at crosspoints using different combinations of tidal and atmospheric corrections (corresponding to Tab. 9.2), without **(a)** and with **(b)** sea level anomaly (SLA) correction. Blue: inner-campaign crosspoints. Red: inter-campaign crosspoints.

Table 9.3: Offsets (dh) and their standard deviations (std) between height differences at crosspoints from different campaigns, obtained by LSQ adjustment. The offset of the 2004 campaign was set to 0.

	without SLA correction		with SLA correction	
Campaign	dh [m]	±std [m]	dh [m]	±std [m]
2004	0.000	±0.000	0.000	±0.000
2005	0.135	±0.005	0.002	±0.004
2006	0.027	±0.006	0.006	±0.005
2007	0.036	±0.006	-0.019	±0.006
2008	0.100	±0.007	-0.020	±0.007

squares sense. The irregular distribution of the ship-tracks yields an inhomogeneous distribution of crosspoints along the tracks, which makes the LSQ adjustment less efficient than in the case of the airborne data in Section 8.4.3. Corrections of up to 15.4 cm were obtained by the LSQ adjustment, providing a significant improvement of the height differences (Tab. 9.2 and Fig. 9.13). Using POL tidal corrections, MOG2D atmospheric corrections and SLA corrections in combination with the LSQ adjustment, the RMS of the height differences was reduced to 4.3 cm, corresponding to an improvement of 46%. After the LSQ adjustment, height differences remain below 5 cm at 77% of the 1999 crosspoints and below 10 cm at 97% of the crosspoints. The maximum observed height difference was reduced from 28.7 to 19.1 cm. The beneficial impact of the LSQ adjustment for the surface generation procedure is shown in Section 9.5.

9.5 Time-Independent Sea Surface Topography

By subtracting the time-dependent corrections (Section 9.3) from the low-pass filtered instantaneous sea surface heights (Section 9.2, Fig. 9.2 and Fig. 9.3), time-independent sea surface height profiles are obtained (Fig. 9.14). The sea surface heights are heights above the WGS84 ellipsoid. Based on the analysis of sea surface height corrections in Section 9.4.1, the observed sea surface heights were corrected using POL tidal corrections, MOG2D atmospheric corrections and SLA corrections from SSALTO/DUACS. Furthermore, the sea surface heights were corrected using an LSQ adjustment of the profiles in order to reduce the height differences at crosspoints (Section 9.4.2).

The resulting punctual time-independent sea surface heights were interpolated onto a regular grid using a bicubic spline interpolation with continuous curvature and adjustable tension. In a second step, the obtained gridded sea surface heights were low-pass filtered using a 2D FFT filter with a cut-off wavelength of 10 km. The cut-off wavelength of the FFT filter was optimally chosen in order to keep the residuals small, without obtaining an unrealistically rough surface. The final gridded data are forming a surface representing the time-independent sea surface topography (Fig. 9.15).

A final indication for the accuracy of the sea surface heights is given by the residuals between the time-independent sea surface height profiles (Fig. 9.14) and the gridded sea surface topography (Fig. 9.15). Without the LSQ adjustment (Section 9.4.2), along-track the residuals have a standard deviation of 5.5 cm and large local values of up to 29.4 cm (Fig. 9.16a). After the LSQ adjustment, the residuals are significantly improved (Fig. 9.17a). The standard deviation was reduced to 4.7 cm, but large residuals of up to 29.0 cm remained locally. In order to avoid unrealistic strong gradients in the gridded sea surface topography, it is advisable to eliminate along-track data presenting large residuals prior to the surface generation. Using the LSQ adjustment, less observations had to be removed (Fig. 9.16b and Fig. 9.17b). After the removal of the outliers, the final residuals are all below 12 cm, with a standard deviation of 3.4 cm only (Fig. 9.17b).

The sea surface height results in the North Aegean Sea reveal a distinct depression of the sea surface in the western part of the survey area, associated with the bathymetric low of the south-western

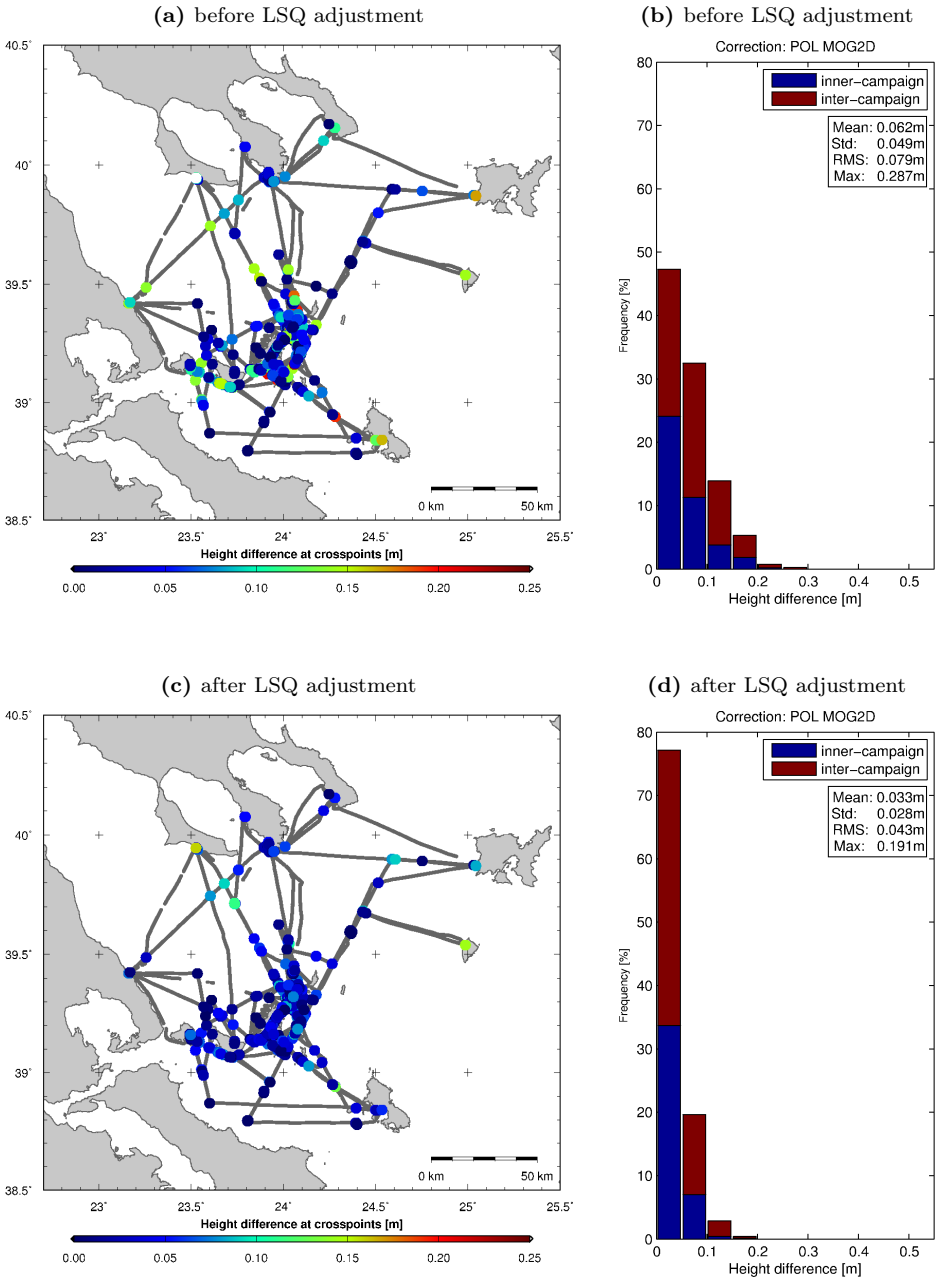

Figure 9.13: **(a)** Crosspoints of sea surface height profiles with color-coded height differences for the solution using POL tidal corrections, MOG2D atmospheric corrections and SSALTO/DUACS sea level anomaly (SLA) corrections. **(b)** Distribution of height differences. Blue: inner-campaign crosspoints. Red: inter-campaign crosspoints. **(c)** Same as (a), but with LSQ adjustment of ship-tracks based on crosspoints. **(d)** Same as (b), but with LSQ adjustment of ship-tracks.

end of North Aegean Trough (Fig. 9.15). The depression reaches a minimum of 37.9 m above the WGS84 ellipsoid, while the height in the surrounding area is more than 39.5 m and reaches even 40.5 m towards the north of the survey area. Further analysis and interpretation of the observed sea surface heights are treated in Chapter 12.

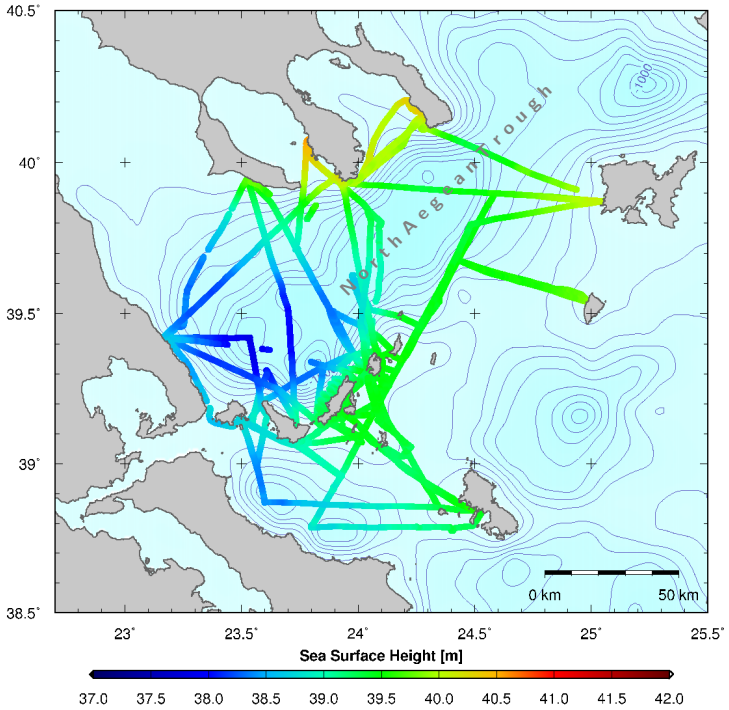

Figure 9.14: Time-independent sea surface height profiles (color-coded) from shipborne altimetry in the North Aegean Sea. The sea surface height profiles were low-pass filtered using a windowed median filter. Background: bathymetry in [m] (contour interval 100 m), with deep-water zone of the North Aegean Trough.

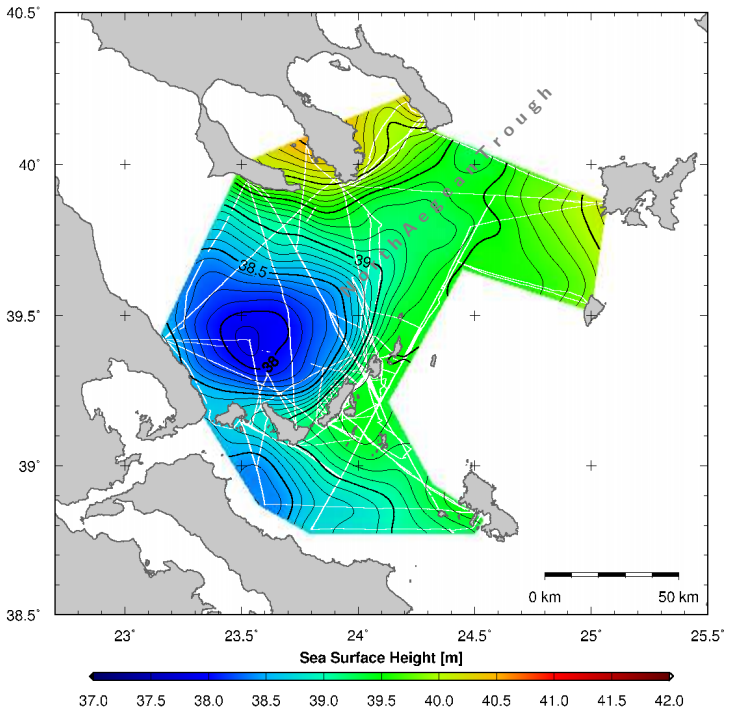

Figure 9.15: Sea surface topography obtained from shipborne altimetry profiles in the North Aegean Sea (Fig. 9.14) bicubic spline interpolation. The sea surface topography was low-pass filtered using 2D FFT filter with a cut-off wavelength of 10 km. White lines: ship-tracks. Contour interval: 0.1 m.

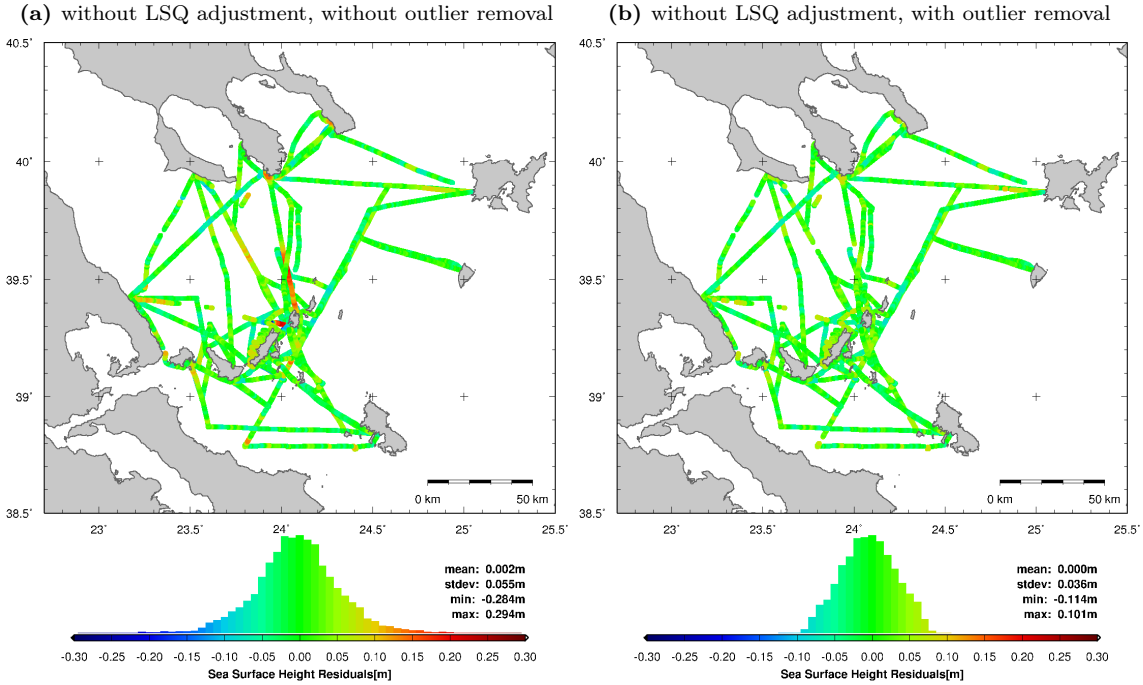

Figure 9.16: Residuals between along-track sea surface heights (Fig. 9.14) and gridded sea surface topography (Fig. 9.15), without correction from LSQ adjustment, before **(a)** and after **(b)** outlier-removal.

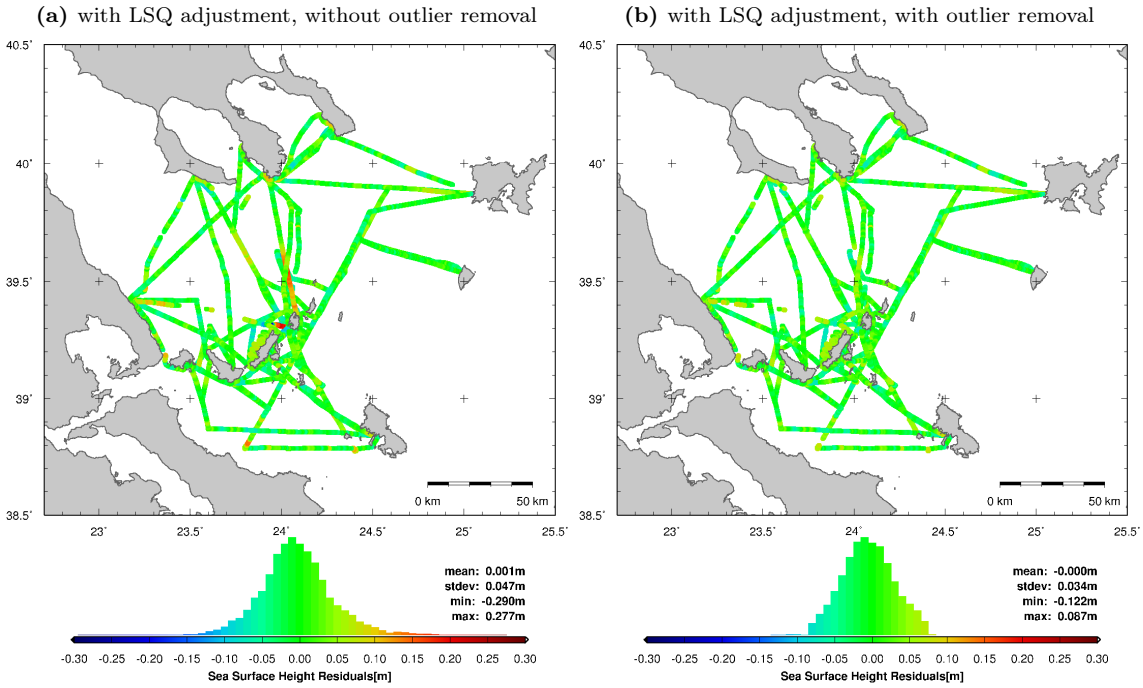

Figure 9.17: Residuals between along-track sea surface heights (Fig. 9.14) and gridded sea surface topography (Fig. 9.15), with correction from LSQ adjustment, before **(a)** and after **(b)** outlier-removal.

10 Validation of Spaceborne Radar Altimetry Data

10.1 Introduction

The basic means to monitor the sea surface on a global scale are satellite radar altimeters. Technological developments have transformed satellite radar altimetry from a technique by which major geoid features with order 10 m amplitude could be resolved to one where resolution of dynamic ocean signals as small as a few cm is possible (Chelton, 1988). Details on the technology of satellite radar altimetry can e.g. be found in (Chelton, 1988; Chelton et al., 2001; Picot et al., 2003; OSTM, 2008).

An important aspect when analyzing spaceborne radar altimetry data in region with steep geoid gradients is the slope-induced height error. Altimeters measure the two-way travel time to the nearest point on the Earth's surface within the antenna beamwidth (Chelton et al., 2001), representing a foot-print diameter of around 10 km for Jason-1 and TOPEX/Poseidon. Steep geoid topography can have minor effects on the observed sea surface heights, since the nearest point on the sea surface can differ from the geodetic sub-satellite point. For a planar surface of constant slope α, the vertical displacement ΔH with respect to nadir is given by (Zwally and Brenner, 2001) (Fig. 10.1):

$$\Delta H \;=\; H\;(1-\cos\alpha) \tag{10.1}$$

where H is the altitude of the spacecraft. The horizontal displacement δ with respect to nadir is given by (Zwally and Brenner, 2001):

$$\delta \;=\; H\;\cos\alpha\;\sin\alpha \tag{10.2}$$

Without prior detailed knowledge of the surface topography, the surface location from which the reflection originates cannot be determined. One difficulty in correcting for the slope-induced error is the variation of the slope within the beam-limited footprint, both along and across the satellite ground-track, which makes the selection of an appropriate slope α difficult (Zwally and Brenner, 2001). Due to these difficulties and the negligible impact of the slope-induced error in most cases, it is common practice not to correct satellite radar altimetry data for slope-induced errors.

In the survey area around Crete, extreme geoid gradients of up to 0.21 m/km (43 arcsec) were observed (Fig. 11.2a), corresponding to a slope α of 0.012°. With the equatorial reference altitude H of 1336 km for Jason-1, (10.1) yields a slope-induced height error ΔH of 2.9 cm. The associated horizontal displacement δ after (10.2) is 280 m. It can be concluded that under the extreme geoid gradients encountered in the survey area, the maximum slope-induced height error can reach noticeable values, but still remains within the expected accuracy level of airborne, shipborne and spaceborne altimetry.

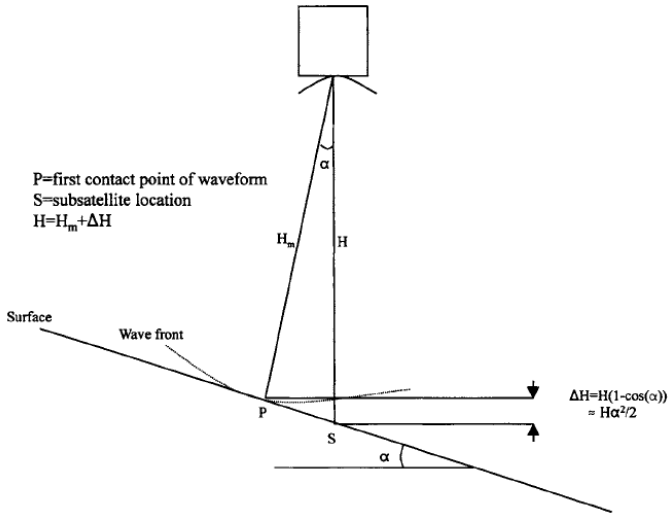

Figure 10.1: Slope-induced height error ΔH in spaceborne radar altimetry for an inclined planar surface, illustrating (10.1) and (10.2). From (Zwally and Brenner, 2001).

10.2 Validation of Instantaneous Jason-1 Data with Airborne Laser Altimetry

Two flights were conducted along the two Jason-1 ground-tracks traversing the survey area (ascending pass 109 and descending pass 18) (Fig. 8.1). The coinciding track of over 100 km of flight GRL05 on 2003/01/11 is of special interest, since airborne measurements were performed during a Jason-1 cross-over, providing quasi-simultaneous observations of the same sea surface (Fig. 10.2 left and Fig. 10.3a). Jason-1 passed over the isle of Gavdos at 10:09 UT and needed around 30 s to cross the area of interest, while the aircraft covered the same profile in 30 minutes, from 9:55 to 10:25 UT. Thus, the time offset between Jason-1 and airborne measurements is less than 15 minutes along the track. Variation of the sea surface height over this short time period can be neglected. Hence, in the comparison between the two datasets, there is no need to apply corrections for time-dependent sea surface height variations like tides, inverse barometer effect or currents. Hence, the airborne laser altimetry observations allow to make direct comparisons with the sea surface heights provided by Jason-1. However, since the sea surface heights from airborne laser altimetry are free of solid Earth tides due to differential GPS processing (Section 3.3.3), solid Earth tide corrections had to be applied to the Jason-1 data in the comparison. Prior to the comparisons, the sea surface heights from Jason-1 were transformed to the referenced to the WGS84 reference ellipsoid, yielding a mean vertical shift of -0.705 m at the considered latitude. In addition, cross-track gradient corrections have been applied to the airborne data in order to account for the horizontal offset between the radar altimeter ground-points and the airborne profile.

The observed differences between sea surface heights from Jason-1 and airborne laser altimetry reveal significant variations between -0.10 and 0.20 m along the dedicated profile of more than 100 km (Fig. 10.3b). These variations are too large to be explained by slope-induced errors described in (Section 10.1). However, the overall agreement is good, with a mean difference of only 0.04 m and a standard deviation of 0.08 m. The distinct negative difference reaching -0.65 m at the northern end of the airborne profile (Fig. 10.3a) is due to a lack of Jason-1 data approaching the coast, where sea surface heights from Jason-1 were interpolated from the next data points north of Crete. This underlines the need for satellite-independent methods like airborne laser altimetry to cover coastal regions. Additional comparisons were made between significant wave heights derived from airborne laser altimetry (Fig. 8.4) and from Jason-1 GDR data (Picot et al., 2003) along the

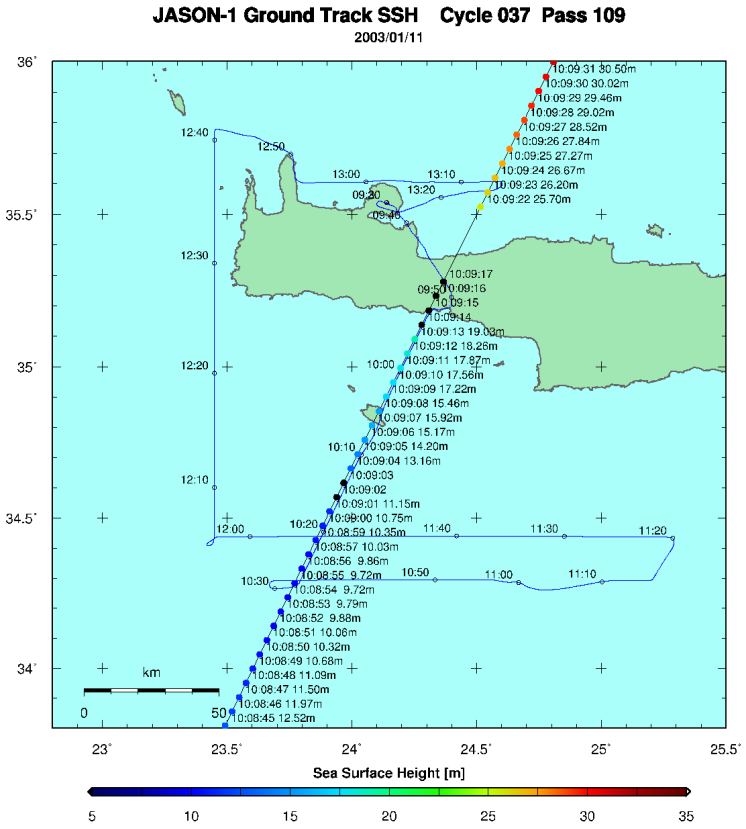

Figure 10.2: Ascending Jason-1 track 109 with 1 Hz sea surface height samples (color-coded dots, with time and height labels, black dots indicate erroneous data). Airborne laser altimetry flight (blue line with time labels) during the same day, covering Jason-1 track with direct cross-over.

dedicated profile (Fig. 10.3c). An excellent agreement of better than 20 cm was obtained using Jason-1 Ku-band data. Differences with the noisier C-band are larger.

10.3 Validation of Mean Sea Surface from Radar Altimetry around Crete

Comparison were made between the sea surface topography derived from airborne laser altimetry (Fig. 8.17) and mean sea surfaces (MSS) from multi-mission radar altimetry, namely CLS01 (Fig. 10.4a) and DNSC08 (Fig. 10.4b). Theoretically, the CLSO1 and DNSC08 resolve wavelengths down to 10-20 km. Further details on MSS, CLS01 and DNSC08 are given in Section 2.3. Both MSS were previously transformed to the WGS84 reference ellipsoid. Note that the sea surface topography from airborne laser altimetry includes SSALTO/DUACS sea level anomaly corrections (Sections 2.4 and 8.3.5).

The residuals between the sea surface topography from airborne laser altimetry and the MSS from CLS01 have a standard deviation of 8.6 cm (Fig. 10.5a and Tab. 10.1). A mean offset of 15.7 cm was previously removed. This implies that there is a bias of 5.7 cm in the survey area, additionally to the global bias of 10 cm between SSALTO/DUACS reference heights (mean profiles) and CLS01 (Section 2.4, Fig. 2.7). The overall agreement between the two datasets is very good. However, high residuals of up to 50 cm are observed in a belt of 20 km around the coast of Crete, where the strongest geoid gradients of the entire survey area occur, reaching impressive 0.21 m/km

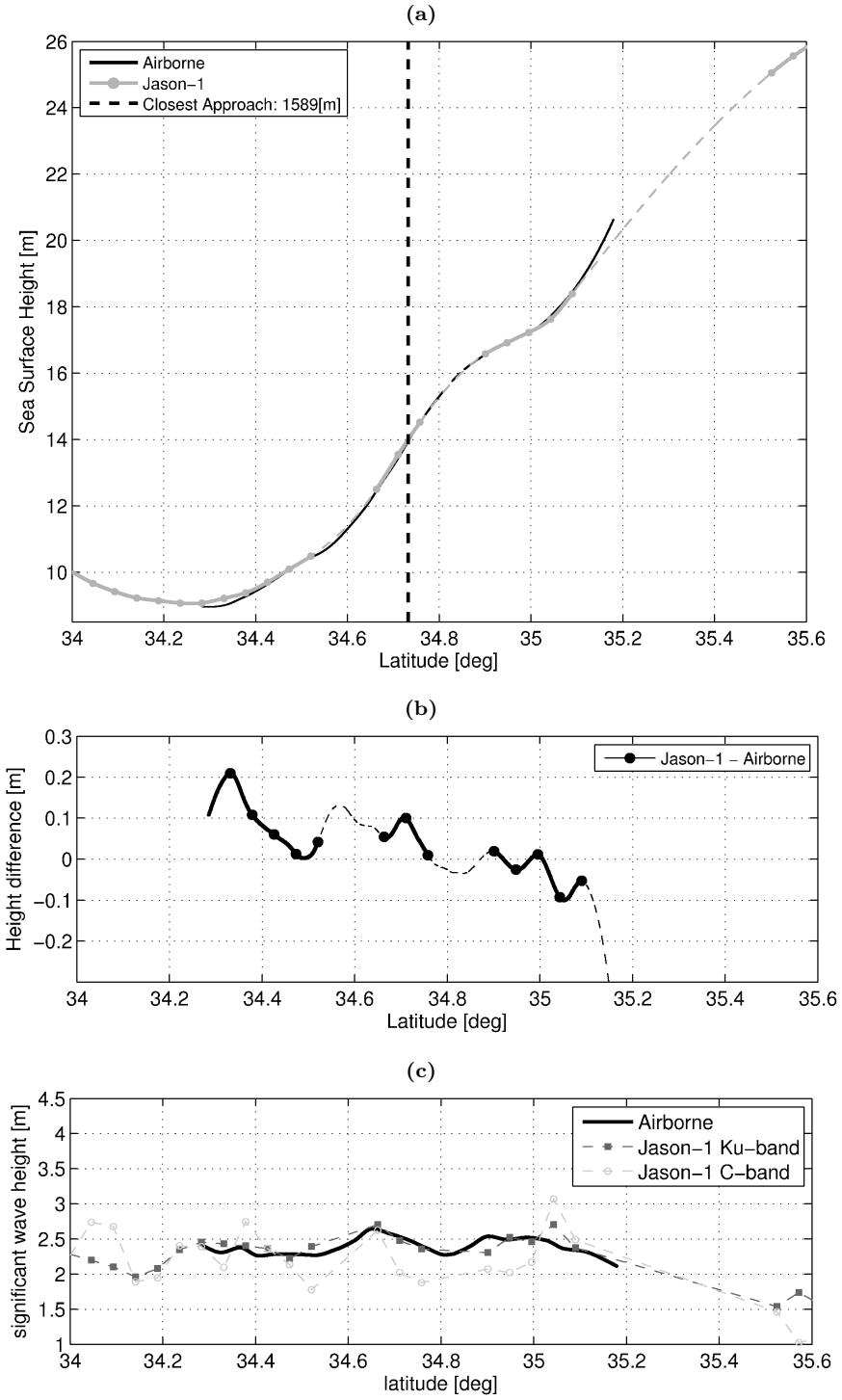

Figure 10.3: **(a)** Comparison between sea surface height profile from Jason-1 (grey line, with circles marking 1 Hz samples and dashed line marking lack of data) and airborne altimetry (black line), corresponding to Fig. 10.2. The encounter (closest approach) is marked by the dashed black line. **(b)** Height differences between Jason-1 and airborne altimetry data. The dashed line marks lacks of either Jason-1 or airborne data. **(c)** Significant wave heights from airborne altimetry (black line) and Jason-1 1 Hz GDR data (Ku-band and C-band).

Table 10.1: Mean offset and standard deviation (std) of residuals of local sea surface topographies (SST) from airborne laser altimetry around Crete and shipborne ultrasound altimetry in the North Aegean Sea with respect to mean sea surfaces CLS01 and DNSC08 from multi-mission radar altimetry.

		SST - CLS01	SST - DNSC08
Survey area	Method	Mean ± std [cm]	Mean ± std [cm]
Crete	Airborne	15.7 ± 8.6	17.7 ± 7.7
North Aegean	Shipborne	10.5 ± 6.9	10.7 ± 5.7

(Fig. 11.2a). In these coastal areas, CLS01 sea surface heights are interpolated due to a lack of satellite radar altimetry data. Since the coastline was not systematically covered by airborne laser altimetry, uncertainties also remain in the airborne sea surface topography regarding these areas. Similar residuals were observed between the airborne sea surface topography and the MSS from DNSC08 (Fig. 10.5b and Tab. 10.1). As compared to CLS01, the standard deviation improved to 7.7 cm. A similar offset of 17.7 cm was previously removed. As for CLS01, the highest absolute residuals of up to 50 cm are observed in a belt of 20 km around the coasts of the island of Crete. The good agreement with the MSS from CLSO1 and DNSC08 allowed to assess the good accuracy and resolution of the sea surface topography determined by airborne laser altimetry.

10.4 Validation of Mean Sea Surface from Radar Altimetry in the North Aegean Sea

Comparison were made between the sea surface topography derived from shipborne altimetry (Fig. 9.15) and mean sea surfaces (MSS) from multi-mission radar altimetry, namely CLS01 (Fig. 10.6a) and DNSC08 (Fig. 10.6b). Theoretically, the CLSO1 and DNSC08 resolve wavelengths down to 10-20 km. Further details on MSS, CLS01 and DNSC08 are given in Section 2.3. Both MSS were previously transformed to the WGS84 reference ellipsoid. Note that the sea surface topography from shipborne altimetry includes SSALTO/DUACS sea level anomaly corrections (Sections 2.4 and 9.3.5).

The residuals between the sea surface topography from shipborne altimetry and the MSS from CLS01 have a standard deviation of 6.9 cm (Fig. 10.7a and Tab. 10.1). A mean offset of 10.5 cm was previously removed. This bias corresponds exactly to the global bias of 10 cm between SSALTO/DUACS reference heights (mean profiles) and CLS01 (Section 2.4, Fig. 2.7), meaning that there is no additional bias between the two sea surface solutions in the survey area of the North Aegean Sea. The overall agreement between the two datasets is very good. They both nearly equally resolve the sea surface depression at the south-western end of the North Aegean Trough. An interesting feature is the positive difference of up to 20 cm near the island of Alonnisos. North of the island, extreme gradients of the sea surface of up to 10 cm/km were observed by dedicated shipborne surveys in this area (Fig. 12.2a). The mean sea surface from radar altimetry does not fully resolve this local steep gradient. However, the agreement of CLS01 with the shipborne data in the North Aegean Sea is slightly better than with the airborne data around Crete (Fig. 10.5a and Tab. 10.1). This is not necessarily a consequence of a better accuracy of the shipborne data, but rather related to the extreme sea surface height gradients encountered around Crete. Similar residuals were observed between the shipborne sea surface topography and the MSS from DNSC08 (Fig. 10.7b and Tab. 10.1). As compared to CLS01, the standard deviation improved to 5.7 cm. A similar offset of 10.7 cm was previously removed. The highest absolute residuals of up to 22 cm are observed in the north-eastern part of the survey area, probably linked to extrapolation of the shipborne data (Fig. 10.7b). The good agreement with the MSS from CLSO1 and DNSC08 allowed to assess the good accuracy and resolution of the sea surface topography determined by shipborne ultrasound altimetry.

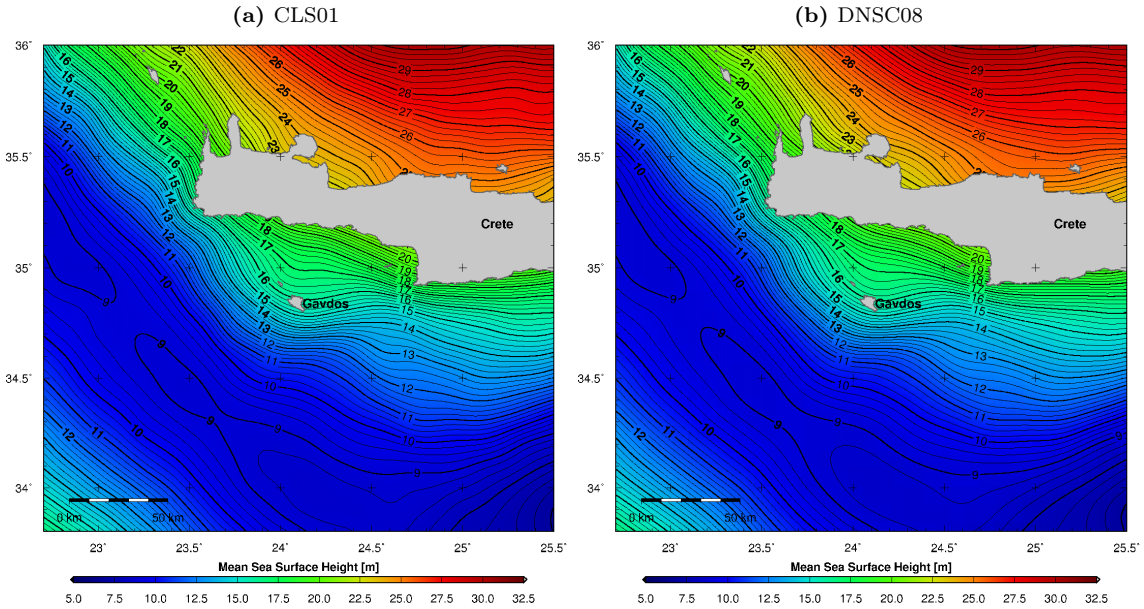

Figure 10.4: Mean sea surface heigths above the WGS84 reference ellipsoid from **(a)** CLS01 and **(b)** DNSC08. Contour intervals: 0.25 m.

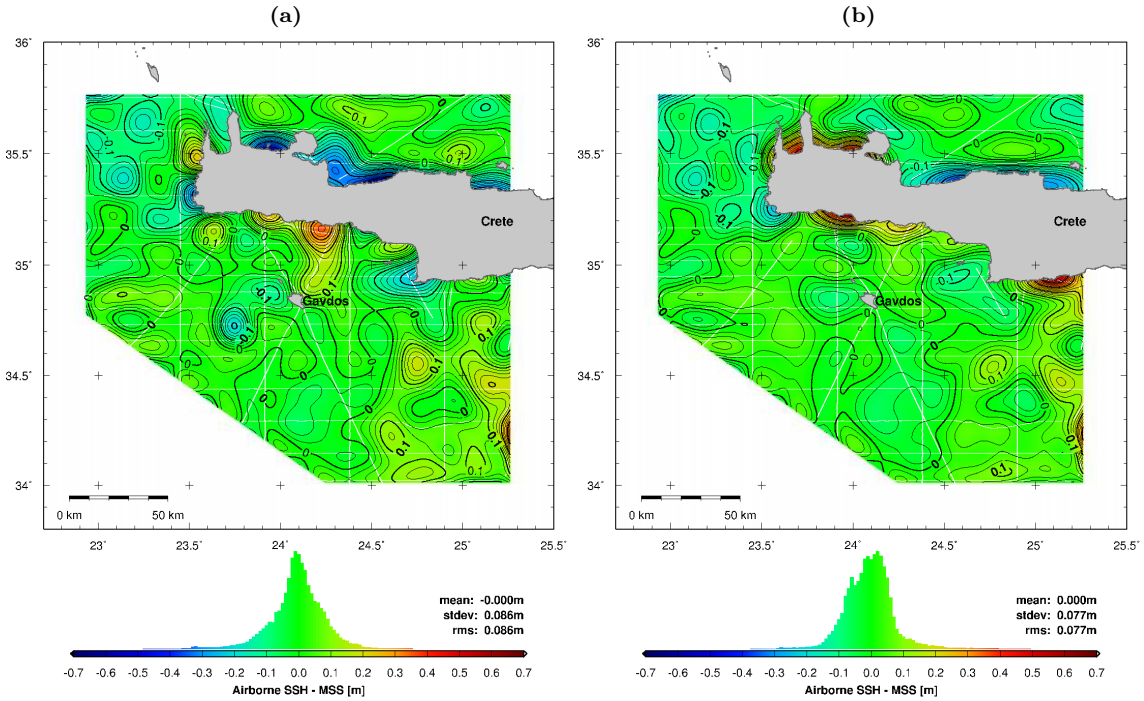

Figure 10.5: **(a)** Residuals between sea surface topography from airborne laser altimetry (Fig. 8.17) and mean sea surface (MSS) from CLS01 (Fig. 10.4a). A mean offset of 15.7 cm was previously removed. **(b)** Residuals between sea surface topography from airborne laser altimetry (Fig. 8.17) and MSS from DNSC08 (Fig. 10.4b). A mean offset of 17.7 cm was previously removed. White lines: airborne ground-tracks. Contour intervals: 0.025 m.

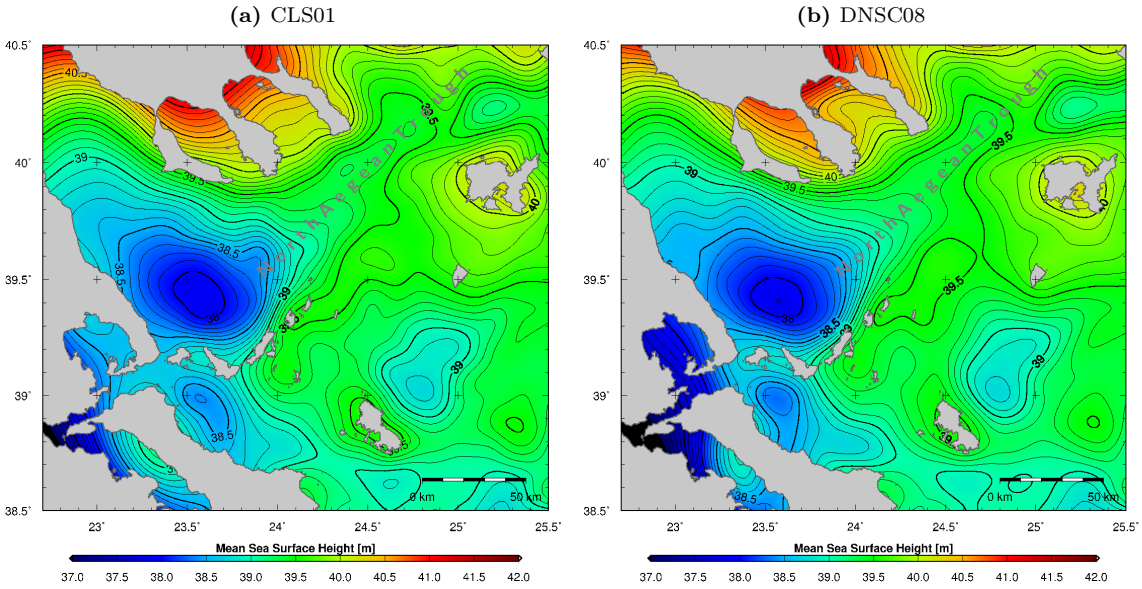

Figure 10.6: Mean sea surface heigths above the WGS84 reference ellipsoid from **(a)** CLS01 and **(b)** DNSC08. Contour intervals: 0.1 m.

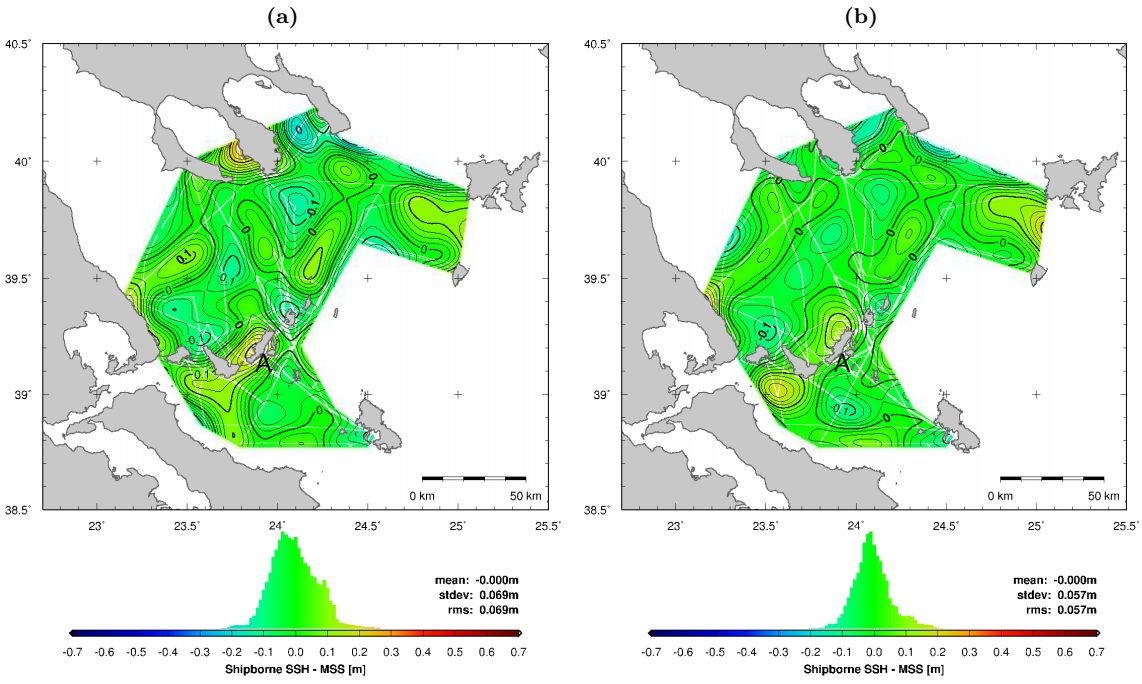

Figure 10.7: **(a)** Residuals between sea surface topography from shipborne altimetry (Fig. 9.15) and mean sea surface (MSS) from CLS01 (Fig. 10.6a). A mean offset of 10.5 cm was previously removed. **(b)** Residuals between sea surface topography from shipborne altimetry (Fig. 9.15) and MSS from DNSC08 (Fig. 10.6b). A mean offset of 10.7 m was previously removed. White lines: ship-tracks. A = Alonnisos. Contour intervals: 0.025 m.

11 Geoscientific Exploitation of Airborne Altimetry Data around western Crete

11.1 Marine Geoid, Gravity Anomalies and Deflections of the Vertical from Sea Surface Heights

Assuming the mean dynamic topography (MDT) as known, marine geoid heights can be derived from observed sea surface heights by subtraction of MDT based on (2.2). The MDT used in this study is the RioMed mean dynamic topography for the Mediterranean Sea (Section 2.5.3, Fig. 2.8a). The maximum effect of the MDT in the survey area reaches -15 cm south of Crete (Fig. 2.9a). By subtracting the RioMed MDT (Fig. 2.9a) from the sea surface heights obtained by airborne laser altimetry (Fig. 8.17), altimetric geoid heights above the WGS84 reference ellipsoid are obtained (Fig. 11.1a).

The altimetric geoid heights are characterized by an overall extremely strong gradient, with heights decreasing from 28 m in the north-eastern part of the survey area to 8 m beyond the Hellenic Trench in the southern part, along a distance of only 200 km. This strong gradient clearly indicates the strong gravity effects caused by the Hellenic Trench bathymetry and geodynamic system. An interesting feature is the weakened gradient around the isle of Gavdos, where the geoid height is increased by about 2 m as compared to the overall downward trend towards the Hellenic Trench. Further details on the geodynamic processes associated with the Hellenic Trench subduction zone are given in Section 1.2.

Gravity anomalies (Fig. 11.1b) were computed from the marine geoid heights (Fig. 11.1a), based on Laplace's equation (2.21) and the curvature of the geoid (Section 2.2.1). As compared to geoid heights, gravity anomalies have the advantage that they are not affected by the long-wavelength part of the gravitational potential and are therefore better suited for the analysis of local gravity anomalies. E.g. in Fig. 11.1b, the pronounced positive local gravity anomaly around the isle of Gavdos, reaching 120 mGal, is clearly depicted.

The extreme gradients of the geoid (Fig. 11.1a) were quantified by deriving horizontal gradients (Fig. 11.2a) and deflections of the vertical (Fig. 11.2b) from the geoid heights, using (2.20). The maximum gradients and deflections of the vertical are encountered along the southern and western coast of Crete, reaching impressive 0.22 m/km and 46 arcsec. Another local maximum of similar magnitude is observed south of the isle of Gavdos. The geoid gradients and deflections of the vertical become small towards the south-western border of the survey area, indicating a flat geoid structure.

A strong correlation is observed between the Hellenc Trench and the variations of the gravity anomalies and geoid gradients (Fig. 11.1b and Fig. 11.2a). An interpretation of the obtained geoid heights and gravity anomlies is carried out by the reduction of mass effects in Section 11.5.

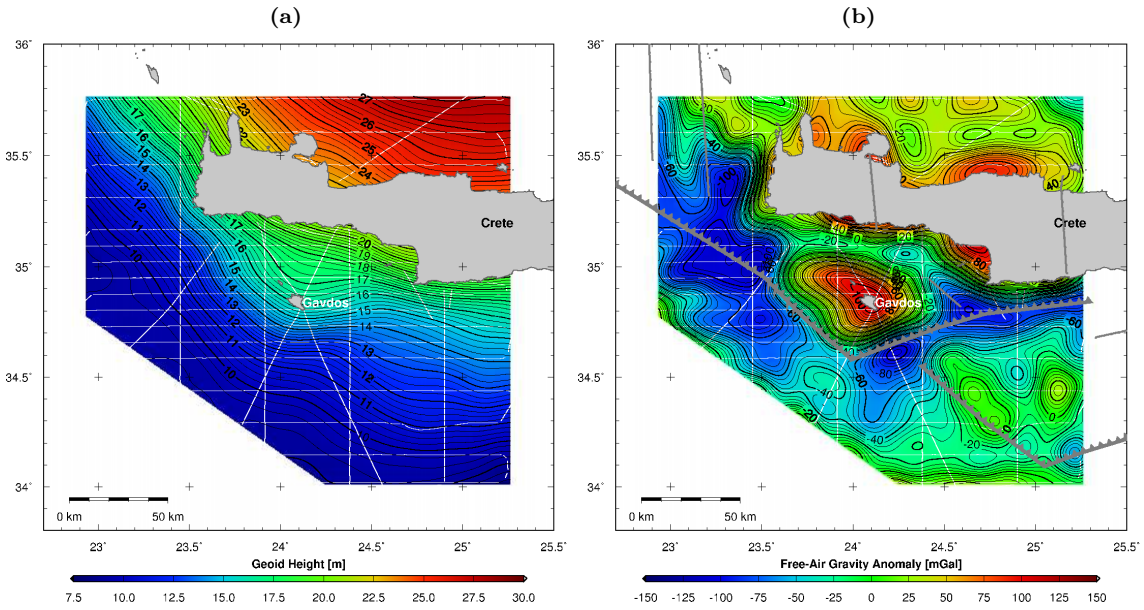

Figure 11.1: **(a)** Geoid heights computed from airborne laser altimetry, by subtracting the RioMed mean dynamic topography (Fig. 2.9a) from observed sea surface heights (Fig. 8.17). Contour interval: 0.25 m. **(b)** Gravity anomalies derived from geoid heights in (a). Contour interval: 5 mGal. Grey lines: fault system of the Hellenic Arc, including the Hellenic Trench. White lines: airborne laser ground-tracks.

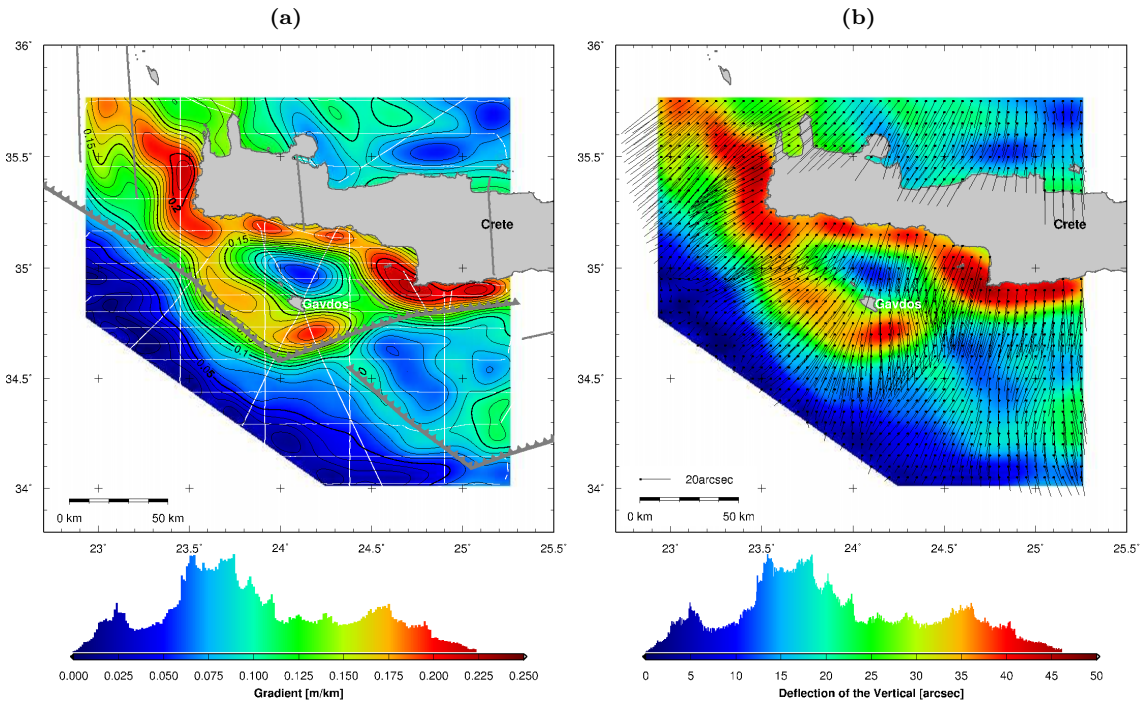

Figure 11.2: **(a)** Horizontal gradients of geoid heights in Fig. 11.1a. Contour interval: 0.01 m/km. White lines: airborne laser ground-tracks. Grey lines: fault system of the Hellenic Arc, including the Hellenic Trench. **(b)** Deflections of the vertical computed from geoid heights in Fig. 11.1a.

Table 11.1: Mean offsets and standard deviations (STD) between the altimetric geoid from airborne laser altimetry and geoid models.

Geoid Model	(degree,order)	mean offset [m]	STD [m]
EIGEN-5S	(150,150)	-0.23	0.81
EIGEN-5C	(360,360)	-0.18	0.40
EGM96	(360,360)	-0.20	0.40
EGM2008	(360,360)	-0.23	0.37
EGM2008	(2190,2159)	-0.14	0.11
AUTH2008	-	-0.24	0.15

11.2 Comparison of Local Altimetric Geoid with existing Models

In order to validate the marine geoid heights (Fig. 11.1a) computed from airborne laser altimetry (altimetric geoid) in Section 11.1, they were compared to geoid heights from several gravity models. The analyzed global gravity models are EGM96 to degree and order 360 (Fig. 11.3a), EGM2008 to degree 2190 and order 2159 (Fig. 11.3b), EIGEN-5S to degree and order 150 (Fig. 11.3c) and EIGEN-5C to degree and order 360 (Fig. 11.3d). All geoid heights were computed with respect to the WGS84 ellipsoid. A detailed description of the gravity models is given in Section 2.2.3. The increasing resolution of the different models from EIGEN-5S to EGM96 and EIGEN-5C, and finally to EGM2008 is clearly shown in Fig. 11.3, e.g. by their capability of resolving the anomaly around the isle of Gavdos.

The residuals between the altimetric geoid (Fig. 11.1a) and the geoid models (Fig. 11.3) are shown in Fig. 11.4. Mean offsets and standard deviations are summarized in Tab. 11.1. In the ideal case of error-free sea surface heights, dynamic topography and geoid models, these residuals should be zero according to (2.29). The residuals with respect to EIGEN-5S have large values of more than 1.5 m, large gradients and a high standard deviation of 0.81 m (Fig. 11.4c). The poor agreement is due to the low resolution (approx. 130 km) of the EIGEN-5S. The two combined geoid solutions EGM96 and EIGEN-5C have a theoretical resolution of 55 km. They produce very similar results in the survey area (Fig. 11.4a and Fig. 11.4d). The mean difference between the altimetric geoid and EGM96 and EIGEN-5C are -0.20 m and -0.18 m, respectively, both with a standard deviation of 0.40 m. As for EIGEN-5S, both models do not resolve the local positive anomaly around the isle of Gavdos, with residuals reaching 1 m. Similarly, the local negative anomaly north-east of Gavdos is not resolved by both models, with residuals reaching -1.2 m. The best agreement is obtained with EGM2008, with a mean difference of -0.14 m and a standard deviation of only 0.11 m (Fig. 11.4b). The good agreement is due to the high resolution of EGM2008. Its expansion to degree 2190 and order 2159 corresponds to a resolution of approx. 10 km.

The improved input data in terms of resolution and accuracy of the recent EIGEN-5C model, as compared to EGM96, does not lead to a significant improvement of the spatial resolution of the EIGEN-5C model (Fig. 11.4a and Fig. 11.4d). The limiting factor in terms of spatial resolution is the mathematical expansion of the spherical harmonics of the model. This was confirmed by computing an EGM2008 geoid solution with a spherical harmonics expansion limited to degree and order 360 (Fig. 11.5a). The residuals with respect to the altimetric geoid have a mean value of -0.23 m and a standard deviation of 0.37 m (Fig. 11.6a). These values are very similar to those of EGM96 (Fig. 11.4a) and EIGEN-5C (Fig. 11.4d). It can be concluded that the extension of the expansion of EGM2008, from degree and order 360 to degree 2190 and order 2159, leads to an improvement of 0.26 m of the standard deviation with respect to altimetric geoid, corresponding to an improvement of 69%.

Additional residuals were computed between the altimetric geoid and the local gravimetric geoid

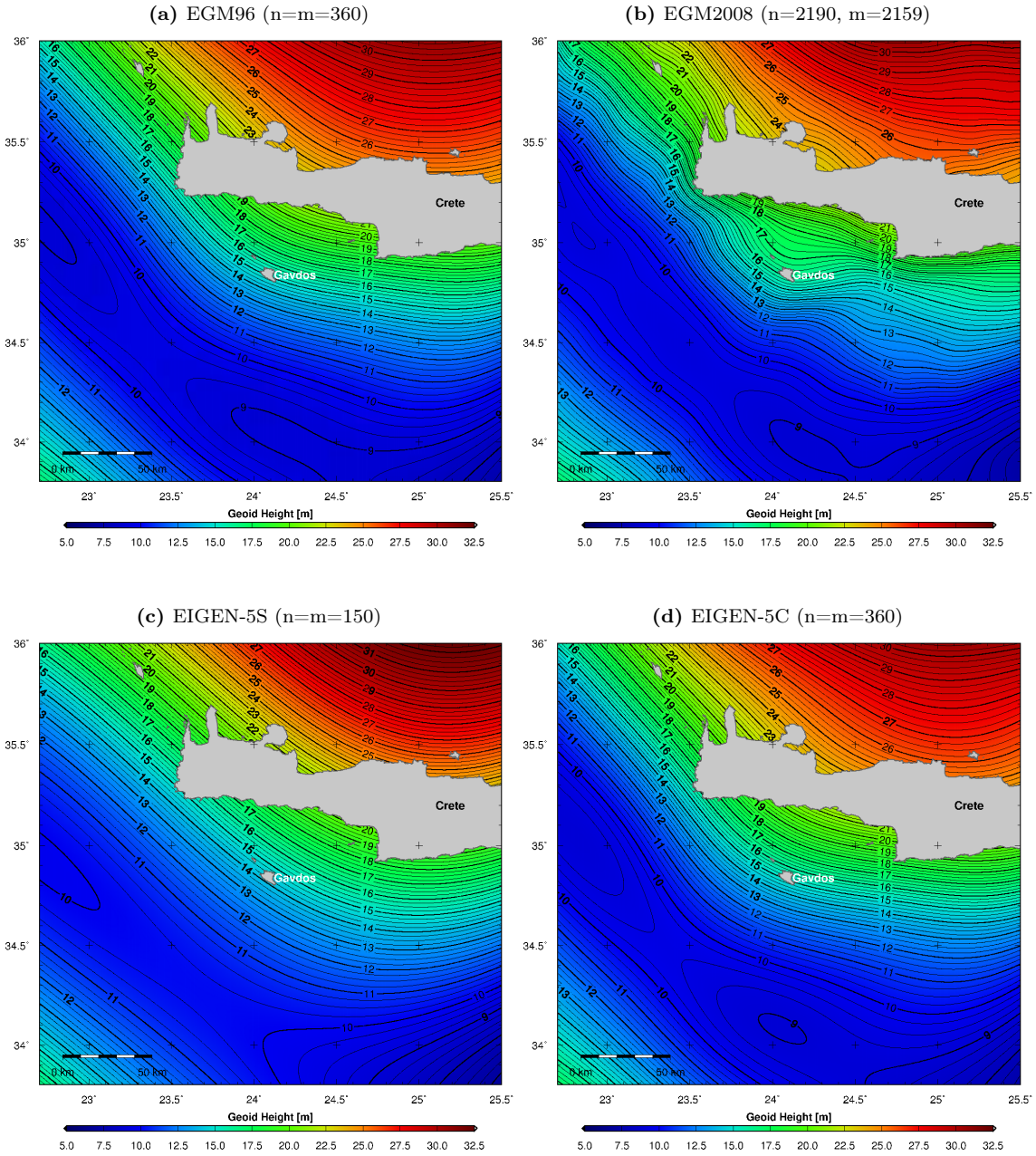

Figure 11.3: Geoid heights to degree n and order m with respect to WGS84 from **(a)** EGM96, **(b)** EGM2008, **(c)** EIGEN-5S and **(d)** EIGEN-5C. Contour intervals: 0.25 m.

model AUTH2008 (Fig. 11.5b). A description of AUTH2008 is given in Section 2.2.3. The obtained residuals are larger than those obtained with respect to EGM2008, with a mean difference of -0.24 m and a standard deviation of 0.15 m (Fig. 11.6b). However, the agreement is much better than with EGM96, EIGEN-5S and EIGEN-5C.

The mean offsets (Tab. 11.1) are different from the ones obtained with respect to the airborne altimetric geoid around Crete (Section 12.2, Tab. 12.1), indicating discrepancies in the long wavelength geoid undulations of the two models between the two areas under investigation. Since the absolute geoid height is not great importance, the offsets are not critical.

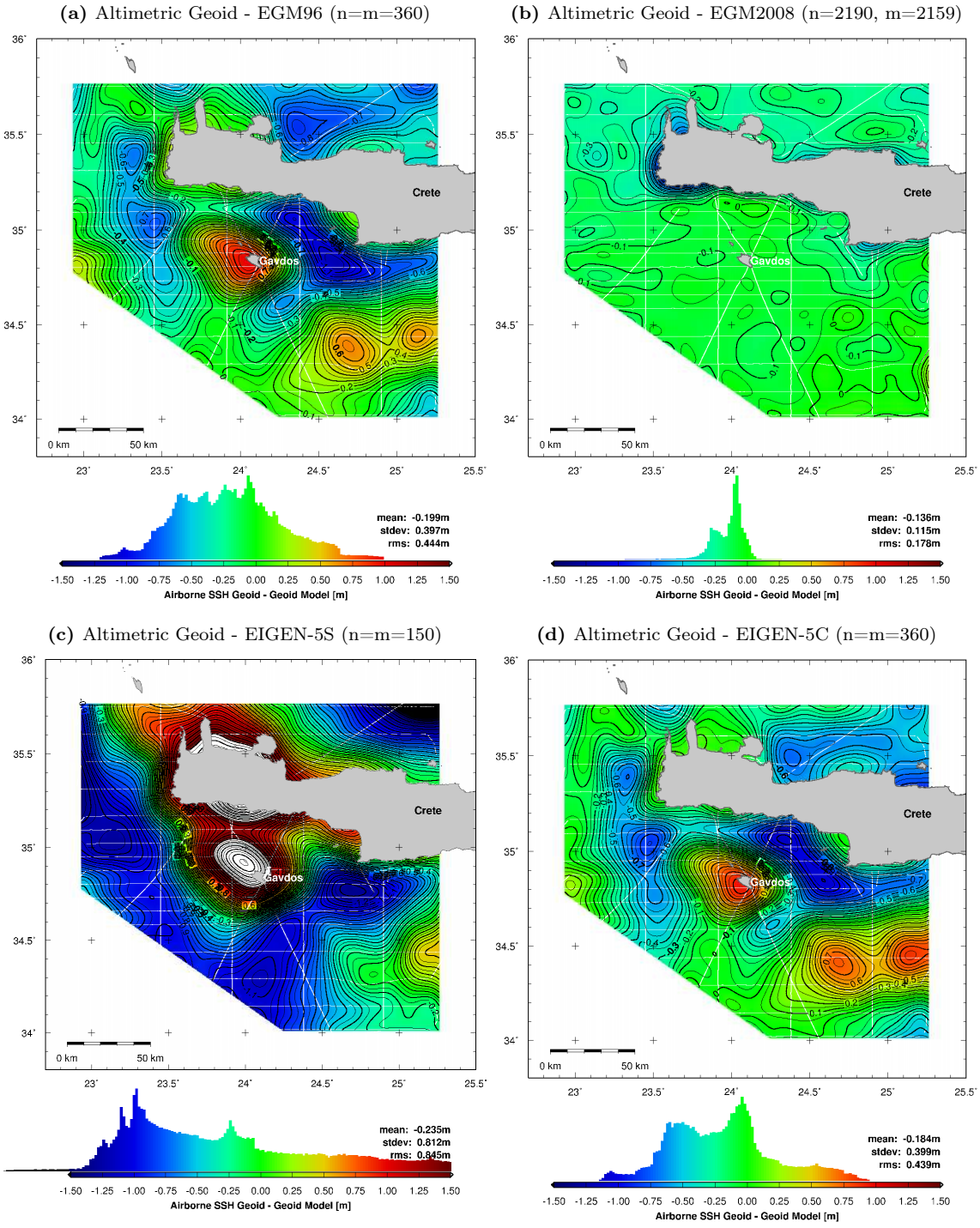

Figure 11.4: Difference between airborne altimetric geoid (Fig. 11.1a) and geoid heights to degree n and order m from **(a)** EGM96, **(b)** EGM2008, **(c)** EIGEN-5S and **(d)** EIGEN-5C. White lines: airborne laser ground-tracks. In **(c)**, black or white surface colors indicate differences below or above the range of -1.5 to 1.5 m. Contour intervals: 0.05 m.

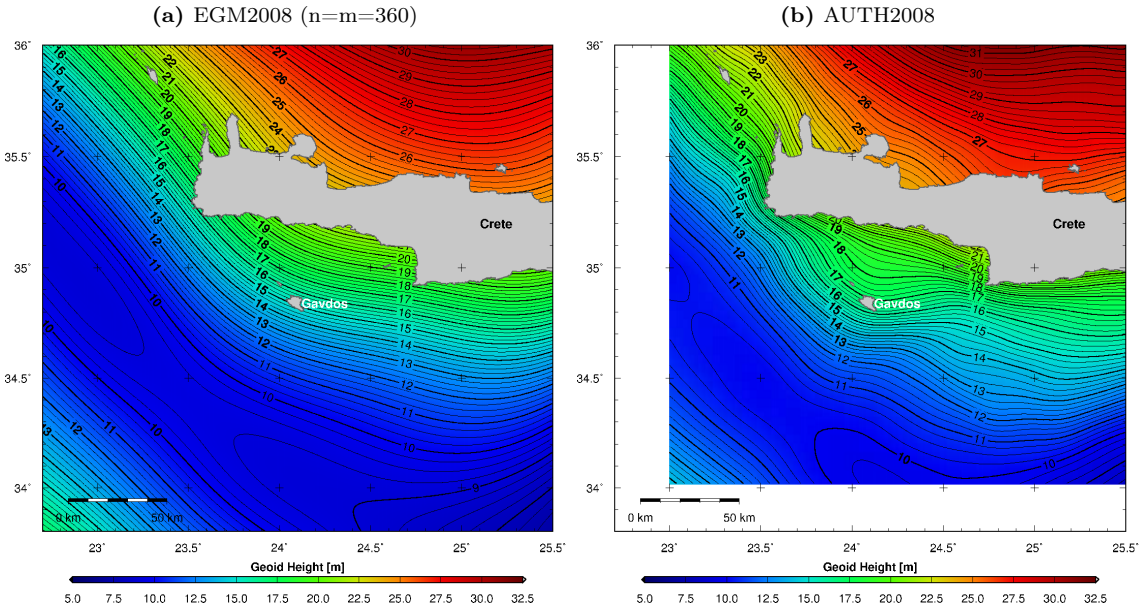

Figure 11.5: Geoid heights with respect to WGS84 from **(a)** EGM2008 with expansion limited to degree and order 360 and from **(b)** the gravimetric model AUTH2008. Contour intervals: 0.25 m.

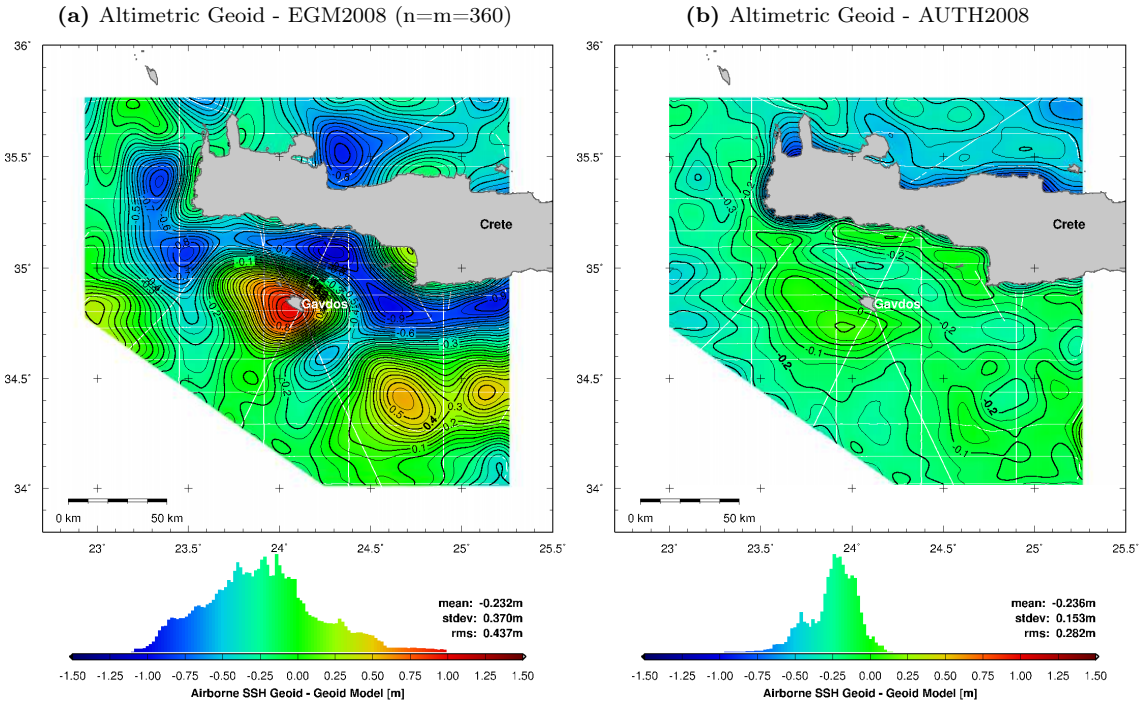

Figure 11.6: Difference between airborne altimetric geoid (Fig. 11.1a) and geoid heights from **(a)** EGM2008 to degree and order 360 and **(b)** AUTH2008. White lines: airborne laser ground-tracks. Contour intervals: 0.05 m.

11.3 Mean Dynamic Topography Estimation

Among the geoid models used in Section 11.2, the satellite-only solution EIGEN-5S and the local gravimetric geoid model AUTH2008 are the only geoid solution that are independent of altimetric sea surface height data. Hence, they would be the only appropriate models to determine the mean dynamic topography (MDT) using the direct method after (2.30) (Section 2.5). The pronounced residuals between the airborne data and EIGEN-5S (Fig. 11.4c) are obviously making the EIGEN-5S unusable for realistic MDT determination at wavelengths below 130 km. The same remark holds for EGM96 and EIGEN-5C (Fig. 11.4a and Fig. 11.4d). Even if these two models were assumed independent of altimetric data, they would not be appropriate to determine the MDT at wavelengths below 55 km.

Hypothetic MDT were computed from the residual fields of the sea surface heights from airborne laser altimetry (Fig. 8.17) with respect to EGM2008 (Fig. 11.7a) and AUTH2008 (Fig. 11.7b) geoid heights. Geostrophic circulation fields were derived from the hypothetic MDT based on (2.32). Compared to the RioMed mean geostrophic circulation (Fig. 2.9a), the obtained circulations are unrealistic and spoiled by noisy eddies. The main anti-clockwise circulation around Crete is not resolved. By increasing the filterwidths on both datasets, it was possible to eliminate the noisy eddies, but no significant circulation remained. Hence, it was not possible to derive a realistic circulation pattern based on the sea surface height observations and the used geoid models. The major reason lies in the fact that the presumed MDT, as e.g. by RioMed (Fig. 2.9a), only varies within a range of 10 cm over the entire survey area. Furthermore, the gradients of the MDT associated with the circulation are below 1 cm/10 km. Hence, the MDT signal in the survey area is close to the accuracy of the airborne sea surface heights and the used geoid models. It can be concluded that the sea surface height observations by airborne altimetry and the considered geoid models are not accurate enough to resolve such small dynamic effects. In addition, EGM2008 is not independent of altimetric sea surface height data.

11.4 Modeled Mass Effects on Geoid Heights and Gravity

11.4.1 Introduction

The effects of mass anomalies on geoid heights were computed for the survey area around western Crete, based on (2.24) and on cuboid masses (2.26). The area of influence considered in the modeling extends from 19°E to 29°E and from 31°N to 39°N (Fig. 11.8a). In addition to geoid heights, the effects of mass anomalies on gravity were computed, based on (2.25) and (2.27). As compared to geoid heights, gravity anomalies have the advantage that they are not affected by the long-wavelength part of the gravitational potential and are therefore better suited for the analysis of local gravity anomalies. On the other hand, geoid heights are comparable to low-pass filtered gravity anomalies, mainly affected by large-scale mass anomalies (Section 2.2.4). Hence, gravity anomalies were modeled in this section in order to obtain additional information on the local gravity field, although the major investigations were carried out on geoid heights. The gravity anomalies were computed at sea level, yielding e.g. exclusively negative effect of the topography on gravity anomalies. The mass effects computed in this section are used in the Section 11.5 to reduce the geoid heights and gravity anomalies derived from the sea surface heights obtained by airborne laser altimetry. The theoretical background of the computation of mass effects on geoid heights and gravity anomalies is given in Section 2.2.4.

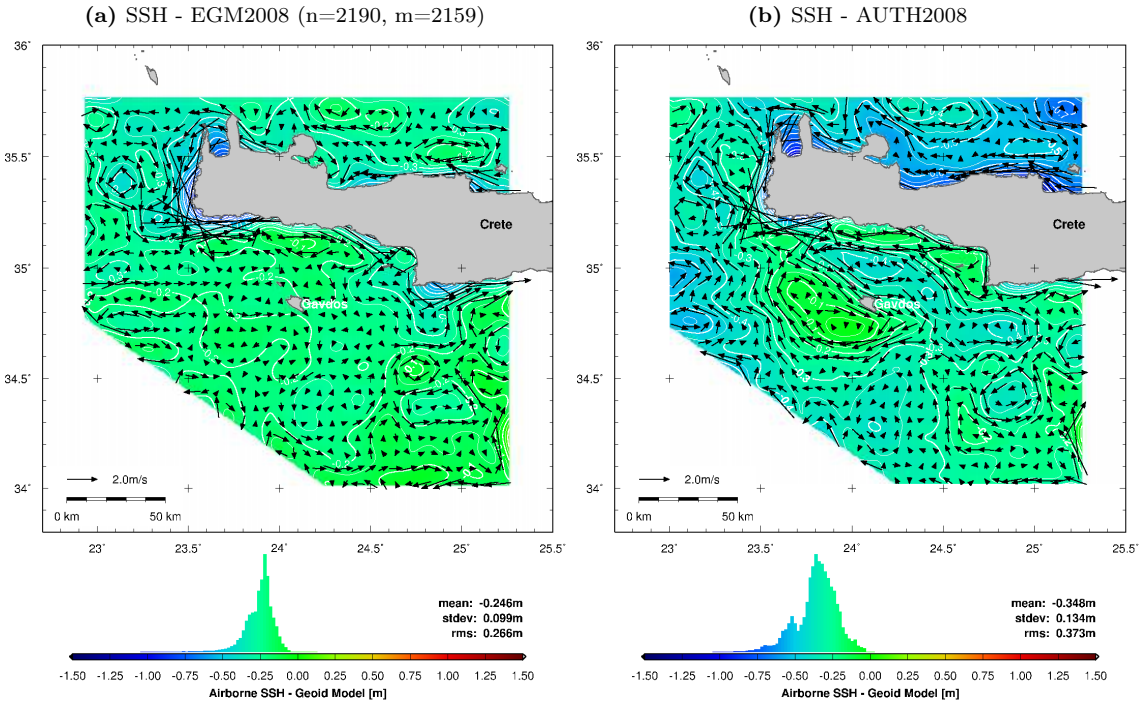

Figure 11.7: Hypothetic mean dynamic topography (background) and ocean circulation (arrows) from differences between sea surface heights from airborne laser altimetry (Fig. 8.17) and geoid heights from **(a)** EGM2008 and **(b)** AUTH2008.

11.4.2 Effect of Topography and Bathymetry

The topography and bathymetry of the area of influence is characterized by deep water zones of down to -4000 m (Fig. 11.8a). Hence, the topography and bathymetry (including water masses) are producing strong negative effects on geoid heights, range between -12 m north and -50 m west of Crete. Associated gravity anomalies are shown in Fig. 11.9b. Within the effect of topography and bathymetry, the water masses have strong positive effect on geoid heights, reaching 32 m west of Crete, related to the deep bathymetry in that area (Fig. 11.10a). Associated gravity anomalies are shown in Fig. 11.10b.

11.4.3 Effect of Sediments

The survey area is characterized by large layers of light sediments deposits along the Mediterranean Ridge, between Crete and the African coast (Fig. 11.8b). The sediments locally reach very large thicknesses of more than 10 km. The information on sediment thickness used in the modeling is based on (Makris and Yegorova, 2006). The mass deficiency associated with the sediments has a strong negative effect on geoid heights, between -6 m north and -25 m south of Crete (Fig. 11.11a). Associated gravity anomalies are shown in Fig. 11.11b.

11.4.4 Effect of ESC Moho depths

For the computation of the effect of crust/mantle boundary (Moho) anomalies, Moho depths from the digital Moho depth map published by the ESC (European Seismological Commission) Working Group (Grad et al., 2009) (Fig. 11.8c) were used. Further details on the ESC Moho depths are

given in Section 2.2.4. The Moho in the survey area is characterized by a strong uplift to up to -21 km south of Crete, along the Mediterranean Ridge. The mass excess caused by the uplift of the Moho south of Crete has a strong positive effect of up to 25 m on geoid heights, whereas the effect is only 0-5 m north of Crete (Fig. 11.12a). Associated gravity anomalies are shown in Fig. 11.12b.

11.4.5 Effect of Isostatic Moho depths

As an alternative to the ESC Moho, Moho depths were computed based on isostatic compensation of the masses topography, bathymetry, water and sediments (Section 2.2.4). A reference depth of -30 km was used. Since the model of isostatic compensation only reflects a theoretical correlation between the masses above the crust/mantle boundary (Moho) and the compensating depth of the boundary, it may sound more appropriate to use a Moho model predicted by real observations, like the ESC Moho. In the present study, however, better reduction results were obtained with the isostatic Moho (Section 11.5).

The isostatic compensation has a dominant uplifting effect on the Moho in the survey area, due to the large mass deficiency caused by the deep water and thick sediments along the Mediterranean Ridge (Fig. 11.8d). The isostatic Moho raises up to a depth of -16 km west of Crete, corresponding to an uplift of 14 km with respect to the reference depth of -30 km. Considering the fact that the water depth west of Crete is 3 km and the sediment thickness is 7 km, the crust thickness reaches values as low as 6 km in this area. The mass excess caused by the strong uplift of the isostatic Moho has a strong positive effect on geoid heights, ranging between 11 m north and 41 m west and south-east of Crete (Fig. 11.13a). Associated gravity anomalies are shown in Fig. 11.13b.

11.4.6 Combined Effects

By combining the effects of topography and bathymetry (Fig. 11.9a) with the effects of sediments (Fig. 11.11a), strong negative effects on geoid heights are obtained, ranging between -18 m north and -72 m west and south-east of Crete (Fig. 11.14a). Associated gravity anomalies are shown in Fig. 11.14b.

By combining the negative effects of topography, bathymetry and sediments (Fig. 11.14a) with the positive effects of the ESC Moho (Fig. 11.12a), an overall negative effect on geoid heights is obtained, ranging between -17 m north and -55 m west of Crete (Fig. 11.15a). The modeled geoid heights present very strong gradients in direction of the Mediterranean Ridge, along the southern coast of Crete and towards the North-West. Along the northern coast of Crete, the structure of the modeled geoid is rather flat. Associated gravity anomalies are shown in Fig. 11.15b.

By combining the negative effects of topography, bathymetry and sediments (Fig. 11.14a) with the positive effects of the isostatic Moho (Fig. 11.13a), an overall negative effect on geoid heights is obtained, ranging between -7 m north and -30 m west and south-east of Crete (Fig. 11.16a). The modeled geoid heights present very strong gradients in direction of the Mediterranean Ridge along the southern coast of Crete and towards the North-West. Along the northern coast of Crete, the structure of the modeled geoid is rather flat. Associated gravity anomalies are shown in Fig. 11.16b.

By visually comparing the sum of all modeled effects (Fig. 11.15a and Fig. 11.16a) to the observed geoid (Fig. 11.1a) and e.g. the EGM2008 geoid (Fig. 11.3b), an overall good agreement is observed, except for the flat structure of the modeled geoid north of Crete, not present in the observed and EGM2008 geoid.

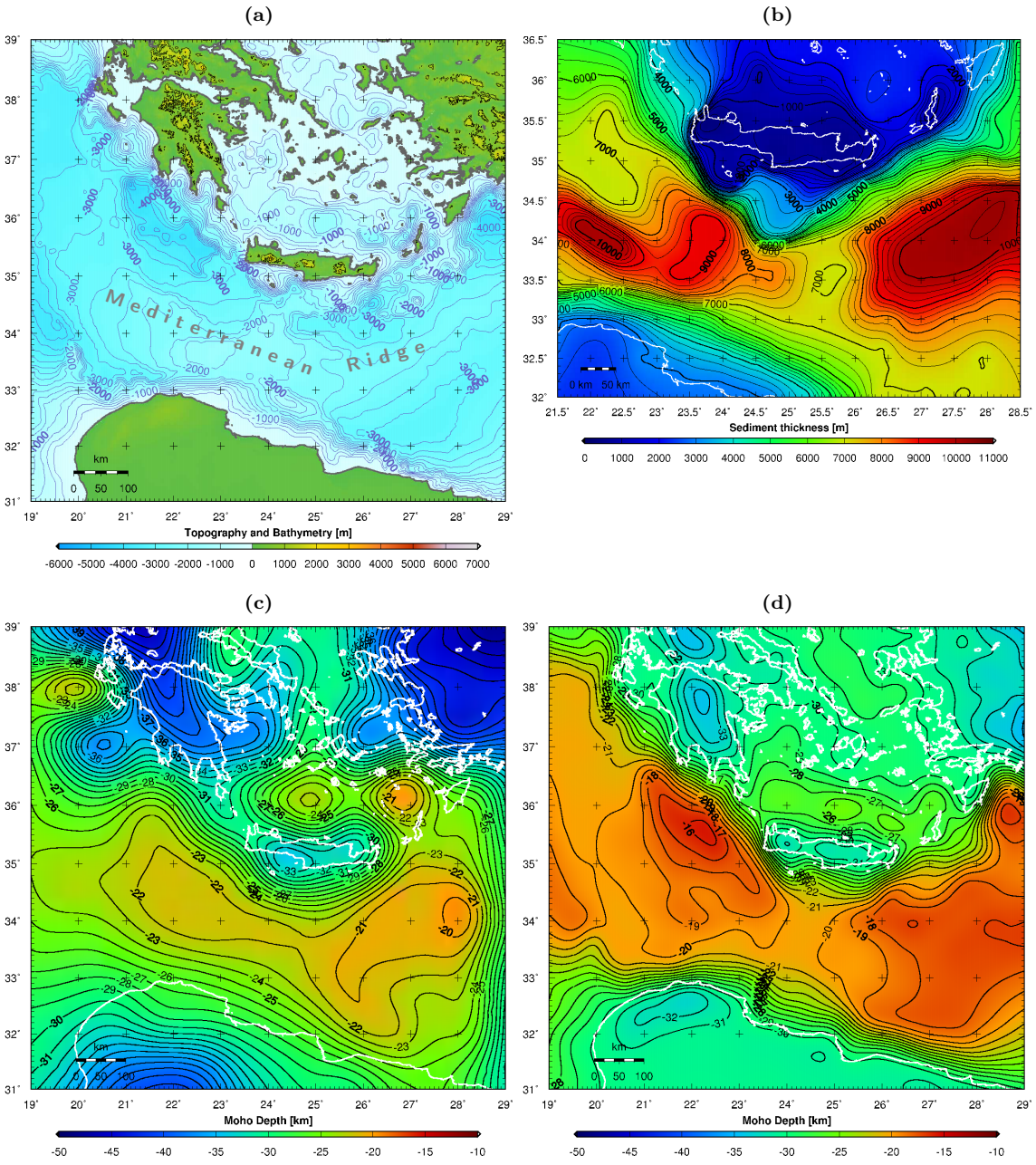

Figure 11.8: **(a)** Topography and bathymetry of the area of influence considered in the modeling of mass effects (contour interval bathymetry: 250 m, topography: 1000 m). **(b)** Light sediments thickness after (Makris and Yegorova, 2006) (contour interval: 250 m). **(c)** Moho depth in the area of influence from the digital Moho depth map published by the ESC (European Seismological Commission) Working Group (Grad et al., 2009) (contour interval: 1 km). **(d)** Moho depth in the area of influence from isostatic compensation (reference depth: -30 km, contour interval: 1 km).

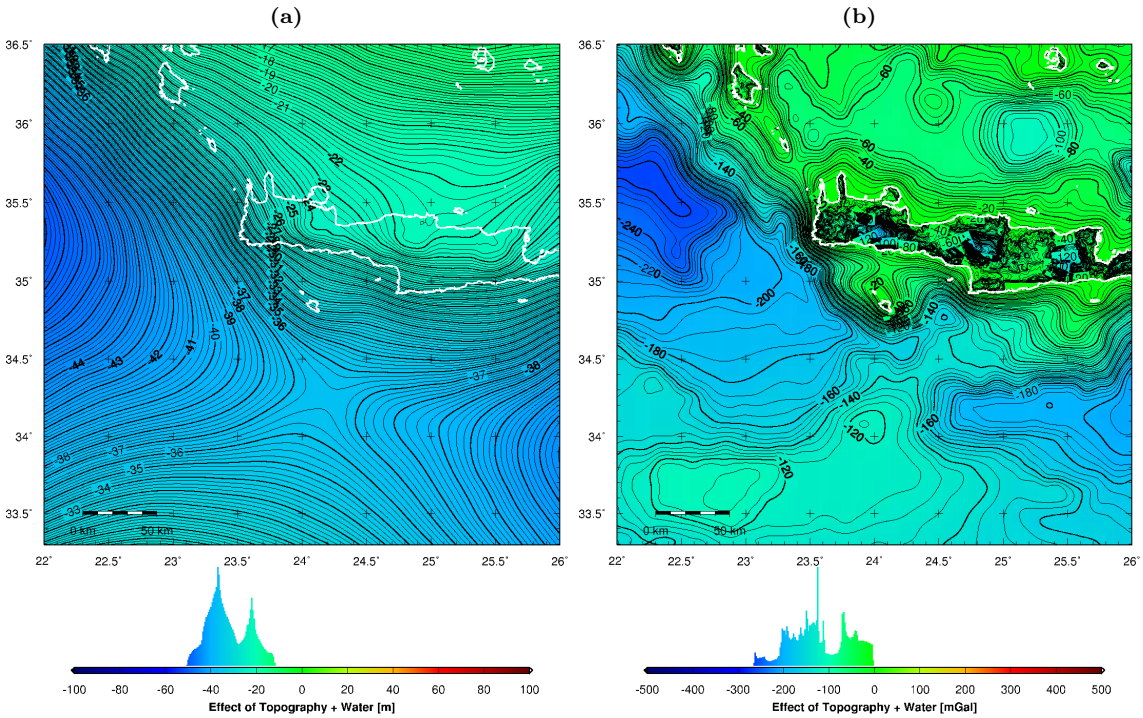

Figure 11.9: Effects of topography and bathymetry (including water masses) on **(a)** geoid heights (contour interval: 0.25 m) and **(b)** gravity (contour interval: 5 mGal).

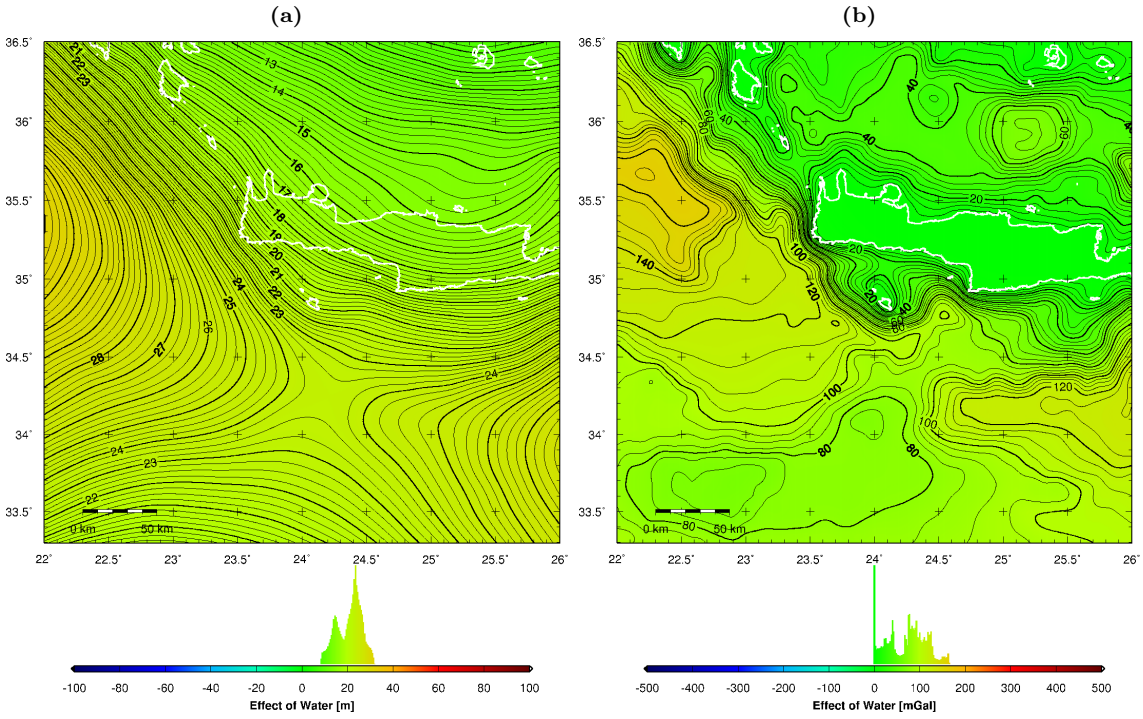

Figure 11.10: Effect of water masses on **(a)** geoid heights (contour interval: 0.25 m) and **(b)** gravity (contour interval: 5 mGal).

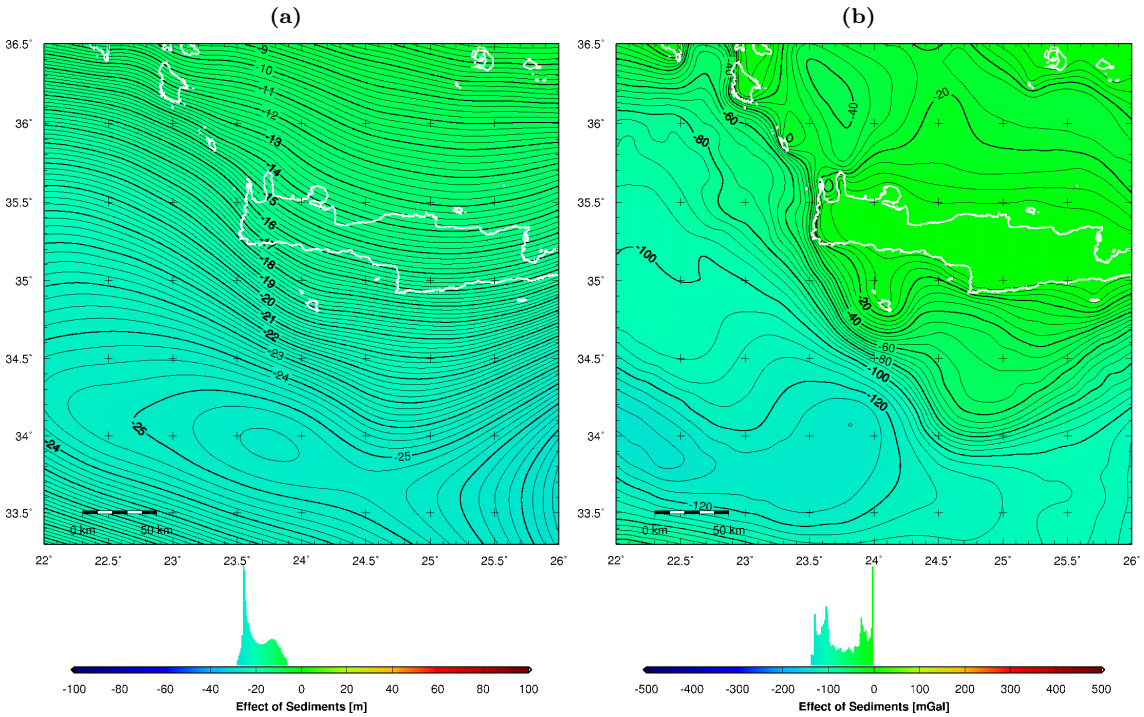

Figure 11.11: Effect of mass deficiency caused by sediments on **(a)** geoid heights (contour interval: 0.25 m) and **(b)** gravity (contour interval: 5 mGal).

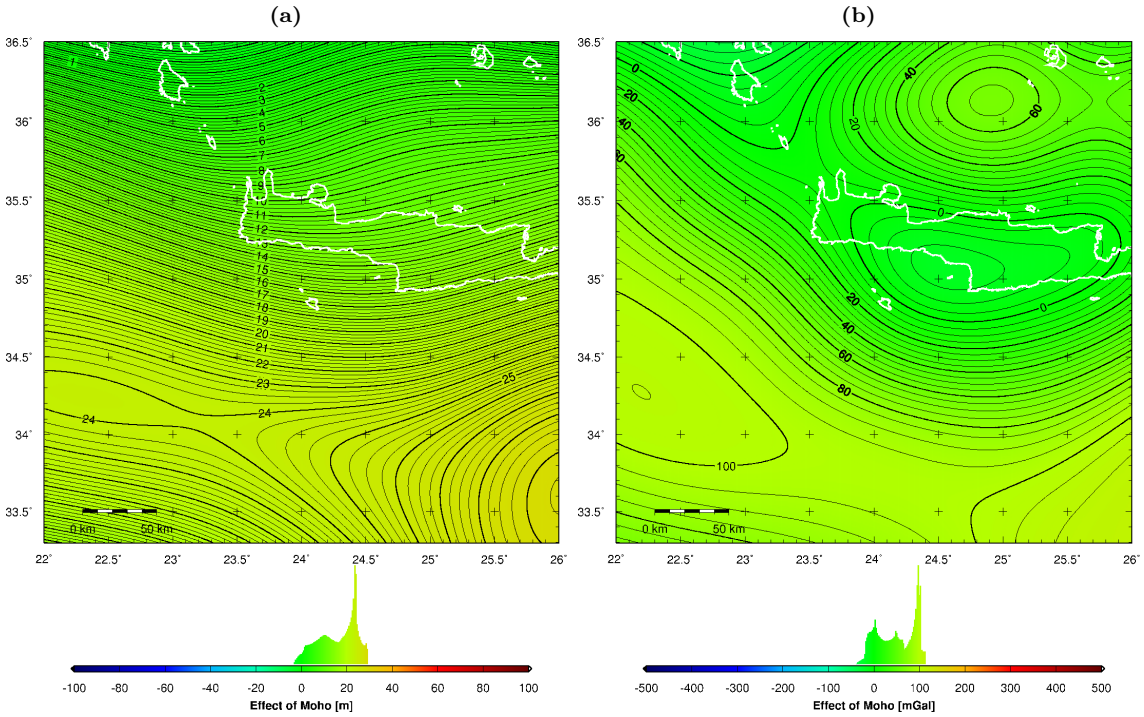

Figure 11.12: Effect of mass anomalies due to Moho depths from ESC map (Fig. 11.8c) on **(a)** geoid heights (contour interval: 0.25 m) and **(b)** gravity (contour interval: 5 mGal).

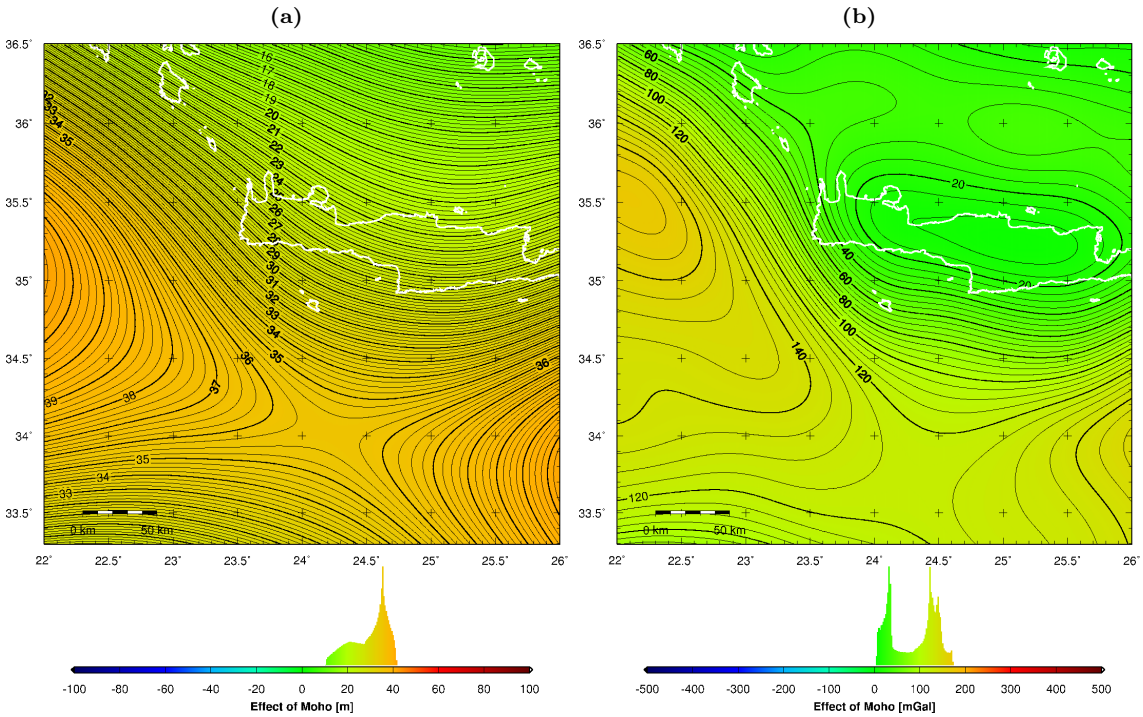

Figure 11.13: Effect of mass anomalies due to Moho depths from isostatic compensation (Fig. 11.8d) on **(a)** geoid heights (contour interval: 0.25 m) and **(b)** gravity (contour interval: 5 mGal).

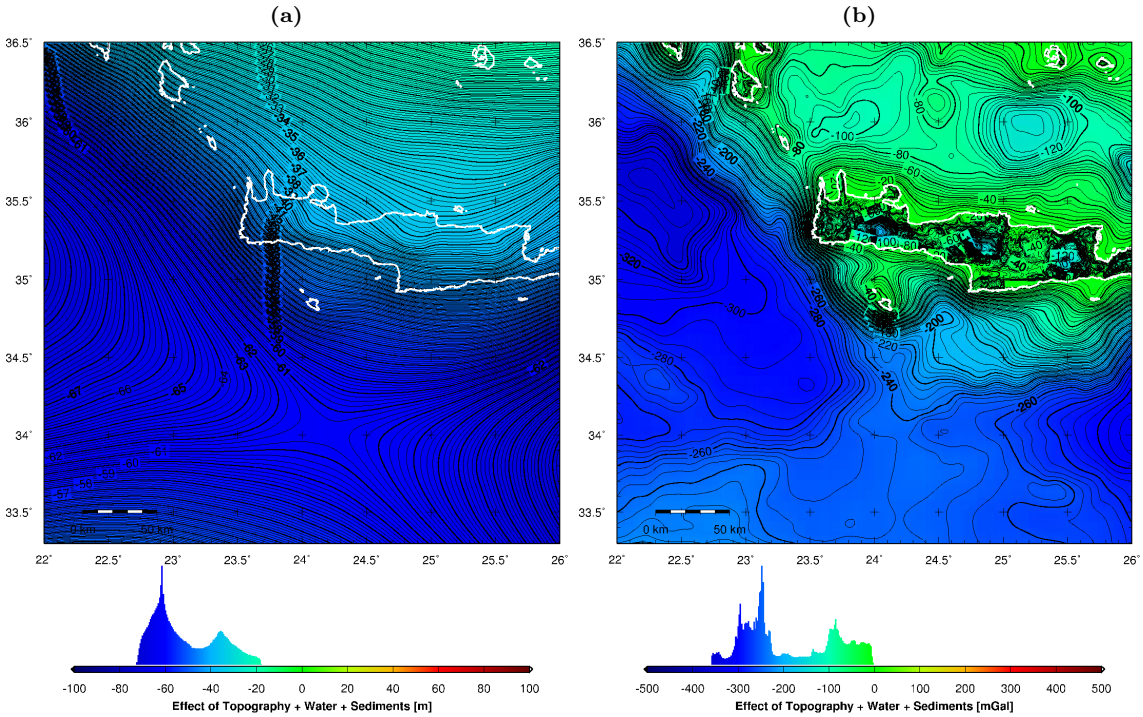

Figure 11.14: Sum of effects of topography, bathymetry (Fig. 11.9) and sediments (Fig. 11.11) on **(a)** geoid heights (contour interval: 0.25 m) and **(b)** gravity (contour interval: 5 mGal).

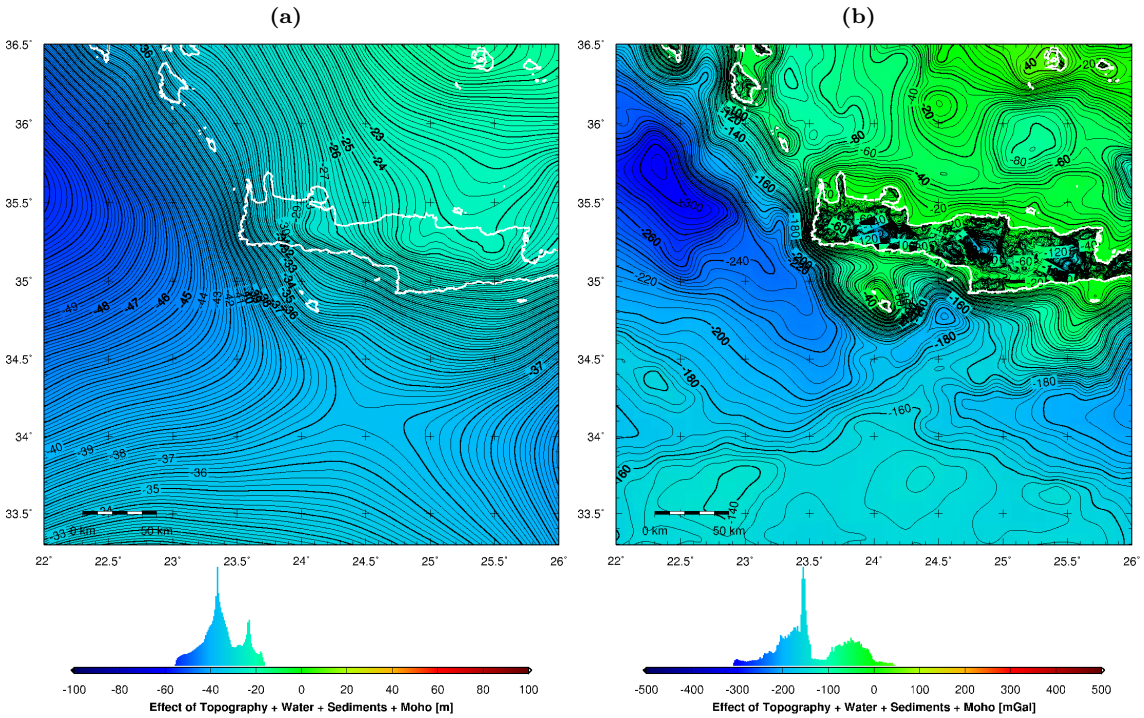

Figure 11.15: Sum of effects of topography, bathymetry, sediments (Fig. 11.14) and ESC Moho depths (Fig. 11.12) on **(a)** geoid heights (contour interval: 0.25 m) and **(b)** gravity (contour interval: 5 mGal).

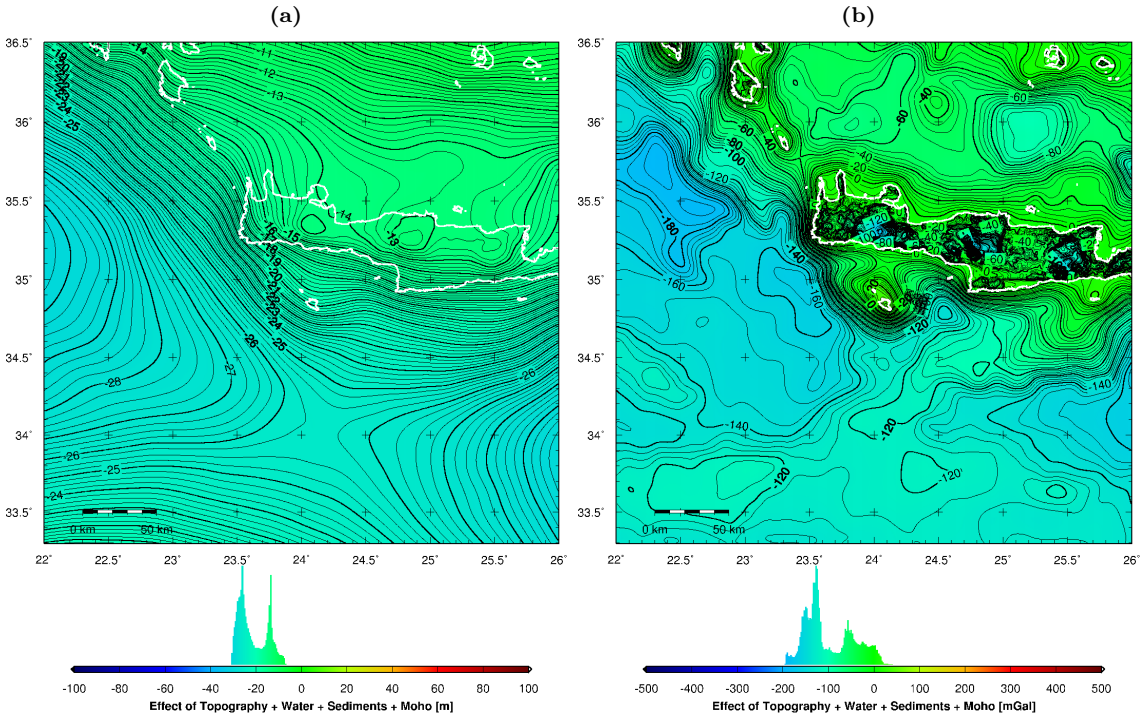

Figure 11.16: Sum of effects of topography, bathymetry, sediments (Fig. 11.14) and isostatic Moho depths (Fig. 11.13) on **(a)** geoid heights (contour interval: 0.25 m) and **(b)** gravity (contour interval: 5 mGal).

Table 11.2: Differences (mean offset, standard deviation (STD) and RMS) on geoid heights between mass effects computed by cuboid masses and point masses.

Effect	mean [cm]	STD [cm]	RMS [cm]
Topo/Bathy	-5.2	4.7	7.0
Sediments	-0.1	2.3	2.3
Moho	0.3	8.4	8.4
Topo/Bathy, Sediments	-5.3	7.0	8.8
Topo/Bathy, Sediments, Moho	-5.0	8.1	9.6

11.4.7 Cuboids vs. Point Mass Modeling

The mass effects shown in Fig. 11.9 to Fig. 11.16 were computed based on cuboid masses using (2.26) and (2.27). Since the computation of the effects of cuboid masses can be very CPU-intensive depending on the size and resolution of the grids, a simplified method to compute approximate mass effects on geoid heights and on gravity based on (2.24) and (2.25) consists in concentrating the mass of each cuboid at its center of mass. In order to assess the impact of this approximation, the effects computed by cuboid masses on geoid heights (Fig. 11.9a to Fig. 11.16a) were recomputed based on the center of mass (point mass) model. Differences on geoid heights are increased by the presence of elongated cuboids with large mass contrasts within a large distance range from the computation point. These elongated cuboids are typically produces by high mountains, deep sea, large sediment layers and large Moho depth variations.

The differences obtained between the two methods are summarized in Tab. 11.2. The smallest differences are obtained for the sediments. Larger differences are obtained for the effect of topography and bathymetry and the effect of the Moho. The differences of the effect of topography and bathymetry on the geoid are below 17 cm in the survey area (Fig. 11.17a). The differences of Moho effect on the geoid reach 25 cm in the survey area (Fig. 11.17b) and have a larger variation than the differences on the combined topography, bathymetry and water effect. The larger differences on the Moho effect are caused by the extremely elongated shape of the Moho cuboids that can reach heights of more than 10 km over large regions in the area of influence. The effect of the shape of the Moho cuboids predominates over the distance between the Moho cuboids inside the Earth and the computation point at sea level.

The differences on the final solution combining topography, bathymetry, sediments and Moho depths range between -25 cm and 10 cm with an RMS of 9.6 cm. Hence, if an accuracy better than 10 cm is sought, the application of the cuboid model is mandatory. In the present case, regarding the sizes of the residual geoid heights after the reduction of mass effects (Section 11.5, Fig. 11.18a to Fig. 11.21a), the approximation of the point mass model has no significant effect on the size and spatial structure of the residuals. In the present case, the uncertainties in the precise knowledge of topography, sediments and Moho, as well as of the exact mass distribution inside the different layers, induce larger errors than the point mass approximation. The same conclusions were drawn from a similar investigation in the survey area of the North Aegean Sea (Section 12.4.7).

11.5 Mass Reduction of Local Altimetric Geoid

11.5.1 Introduction

The mass effects computed in Section 11.4 were used to reduce the marine geoid heights obtained by airborne altimetry (Fig. 11.1a). In addition, marine gravity anomalies derived from airborne altimetry (Fig. 11.1b) were reduced. Gravity anomalies are well suited to describe the high-frequency part of the gravity field, mainly affected by local mass anomalies, while the geoid undulations are

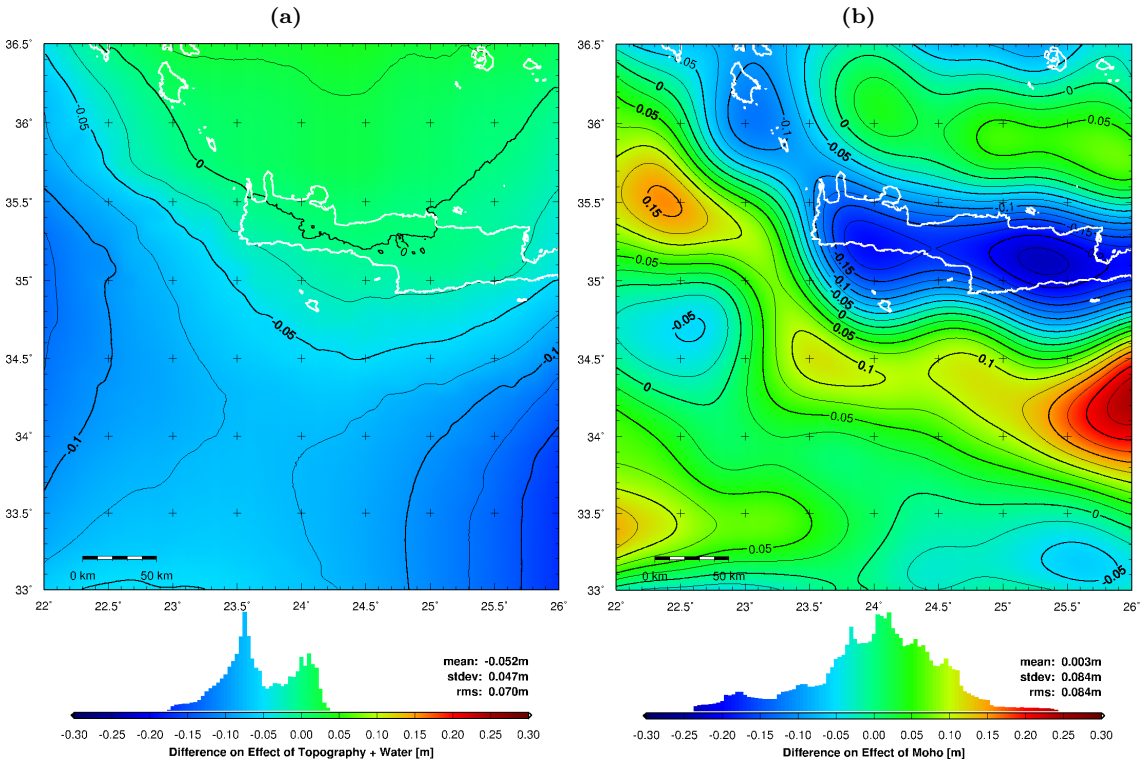

Figure 11.17: Differences on geoid heights between mass effects computed by cuboid masses and point masses from **(a)** topography/bathymetry and **(b)** Moho depths. Contour intervals: 0.025 m.

comparable to low-pass filtered gravity anomalies, mainly affected by large-scale mass anomalies. Hence, gravity anomalies were reduced in this section in order to obtain additional information on the local gravity field, although the major investigations were carried out on geoid heights.

11.5.2 Topography-Bathymetry Cogeoid

In a first step, marine geoid heights from airborne altimetry (Fig. 11.1a) were reduced for the effects of topography and bathymetry (including water) (Fig. 11.9a). The reduced geoid heights correspond to the topography-bathymetry cogeoid. After the removal of a constant offset, the reduced geoid heights range between -2.5 and 4.0 m (Fig. 11.18a). The local raise of the geoid around the isle of Gavdos (Fig. 11.1a) is no longer seen in the reduced geoid, meaning that this local anomaly is exclusively caused by the effects of the topographic masses of Gavdos and of its surrounding bathymetry. Strong residual gradients in different directions remain in the entire survey, indicating that the geoid heights are not caused exclusively by the effect of topography and bathymetry. However, the major part of the geoid slope of 20 m across the survey area (Fig. 11.1a) was reduced to 6.5 m by removing the effects of topography and bathymetry. Associated reduced gravity anomalies are shown in Fig. 11.18b.

11.5.3 Topography-Bathymetry-Sediments Cogeoid

In a second step, marine geoid heights from airborne altimetry (Fig. 11.1a) were reduced for the effects of topography, bathymetry and sediments (Fig. 11.14a). The reduced geoid heights correspond to the topography-bathymetry-sediments cogeoid. After the removal of a constant

offset, the reduced geoid heights range between -7 m in the north-east and 8 m in the south-west, with a strong positive gradient in south-west direction south of Crete (Fig. 11.19a). Associated reduced gravity anomalies are shown in Fig. 11.19b.

Assuming the ideal case that the entire effects of topography, bathymetry and sediments were removed by the reduction, and that no other mass anomalies except those from the Moho are present, the reduced geoid heights (Fig. 11.19a) and gravity anomalies (Fig. 11.19b) correspond to the effect produced by the real Moho. Under these assumptions, the strong residual gradients south of Crete are an indicator for a significant Moho uplift along the Mediterranean Ridge in the south of the survey area, caused by deep water and thick sediment layers. This conclusion is confirmed by the strong positive reduced gravity anomalies towards the south-west of the survey area, reaching up to 300 mGal (Fig. 11.19b). The residuals at the extreme border of the survey area need however to be considered carefully due to possible boundary effects. The predicted Moho uplift along the Mediterranean Ridge is in accordance with the uplift of the ESC Moho (Fig. 11.12a) and the isostic Moho (Fig. 11.8d). The nearly constant cogeoid north of Crete (Fig. 11.19a) indicates that the modeled geoid is nearly parallel to the observed geoid. This means that the remaining Moho effect on geoid heights has to be more or less constant in this area. This is, however, in complete disagreement with the modeled effects of the ESC Moho (Fig. 11.12a) and isostatic Moho (Fig. 11.13a).

11.5.4 Topography-Bathymetry-Sediments-Moho Cogeoid

In a third step, marine geoid heights from airborne altimetry (Fig. 11.1a) were reduced for the effects of topography, bathymetry, sediments and ESC Moho (Fig. 11.15a). The reduced geoid heights correspond to the topography-bathymetry-sediments-Moho cogeoid. After the removal of a constant offset, the reduced geoid heights range between -4.5 and 7.5 m, with a strong positive gradient in north-west direction across a large part of the survey area. (Fig. 11.20a). This strong gradient must be produced by a large positive mass anomaly, with respect to the modeled masses, beyond the western boundary of the survey area. The origin of this mass anomaly can be anomalously dense crust material, an overestimation of the thickness of the sediment layer or an anomalously high Moho discontinuity with respect to the ESC Moho. The last possibility would be confirmed by comparing the ESC Moho (Fig. 11.8c) with the isostatic Moho (Fig. 11.8d). The strong local uplift of the isostatic Moho west of Crete, produced by the deep water zone of 4000 m, is not present in the ESC Moho. Although the Moho anomaly associated with the subduction zone north of Crete is most likely better modeled by the ESC Moho than by the isostatic Moho, the overall strong gradient in north-west direction makes an interpretation of the topography-bathymetry-sediments-Moho cogeoid impossible in the area of the subduction zone north of Crete. Hence, another reduction was carried out below, using isostatic Moho depths.

11.5.5 Topography-Bathymetry-Sediments-Isostasy Cogeoid

In a final step, marine geoid heights from airborne laser altimetry (Fig. 11.1a) were reduced for the effects of topography, bathymetry, sediments and isostatic Moho (Fig. 11.16a). The reduced geoid heights correspond to the topography-bathymetry-sediments-isostasy cogeoid. After the removal of a constant offset, the reduced geoid heights range between -1.5 and 5 m (Fig. 11.21a). The positive gradient in south-west direction south of Crete, observed in the topography-bathymetry-sediments cogeoid (Fig. 11.19a), has almost disappeared, meaning that it was mainly caused by the effect of the isostatic Moho. South of Crete, the predominant negative geoid gradient towards the Mediterranean Ridge, reaching impressive 0.21 m/km and characterizing the entire region (Fig. 11.1a), was completely reduced by the modeled mass effects of topography, bathymetry, sediments and isostatic Moho. These effects are dominated by deep water (down to -4000 m) and extremely thick sediment deposits of up to 10 km. The spread of the residual geoid heights was

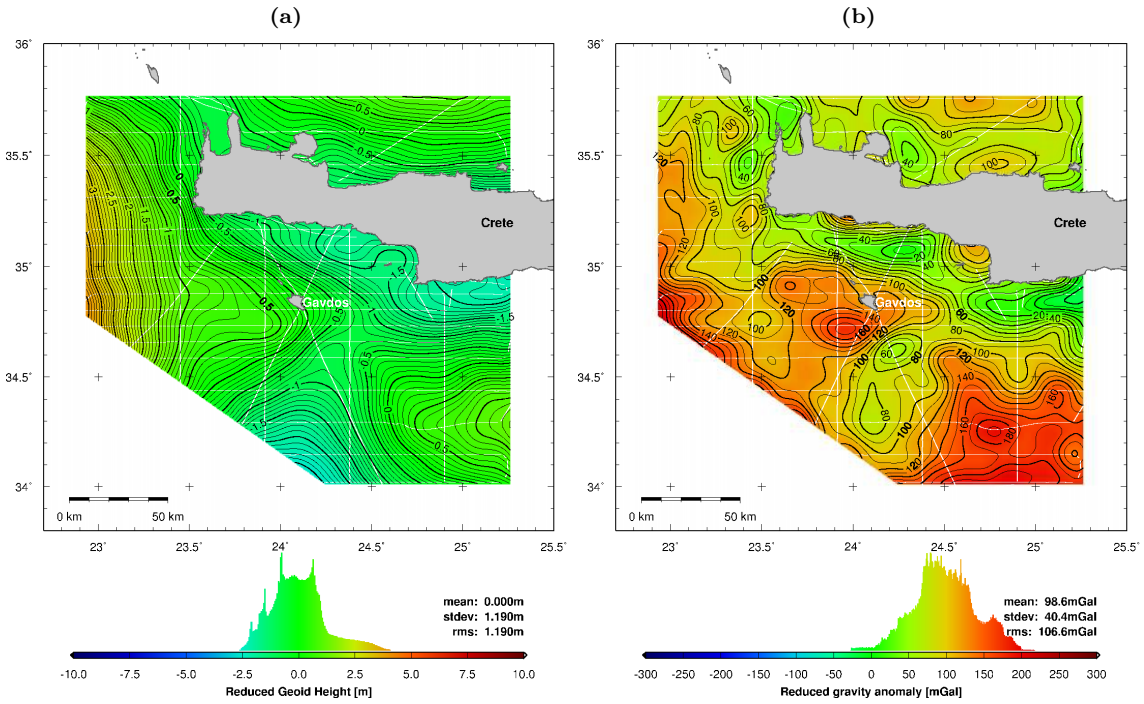

Figure 11.18: **(a)** Geoid heights from airborne altimetry (Fig. 11.1a) reduced for effects of topography and bathymetry (Fig. 11.9a), with mean offset removed. **(b)** Associated gravity anomalies from reduction of Fig. 11.1b with Fig. 11.9b. Contour intervals: 0.1 m and 10 mGal.

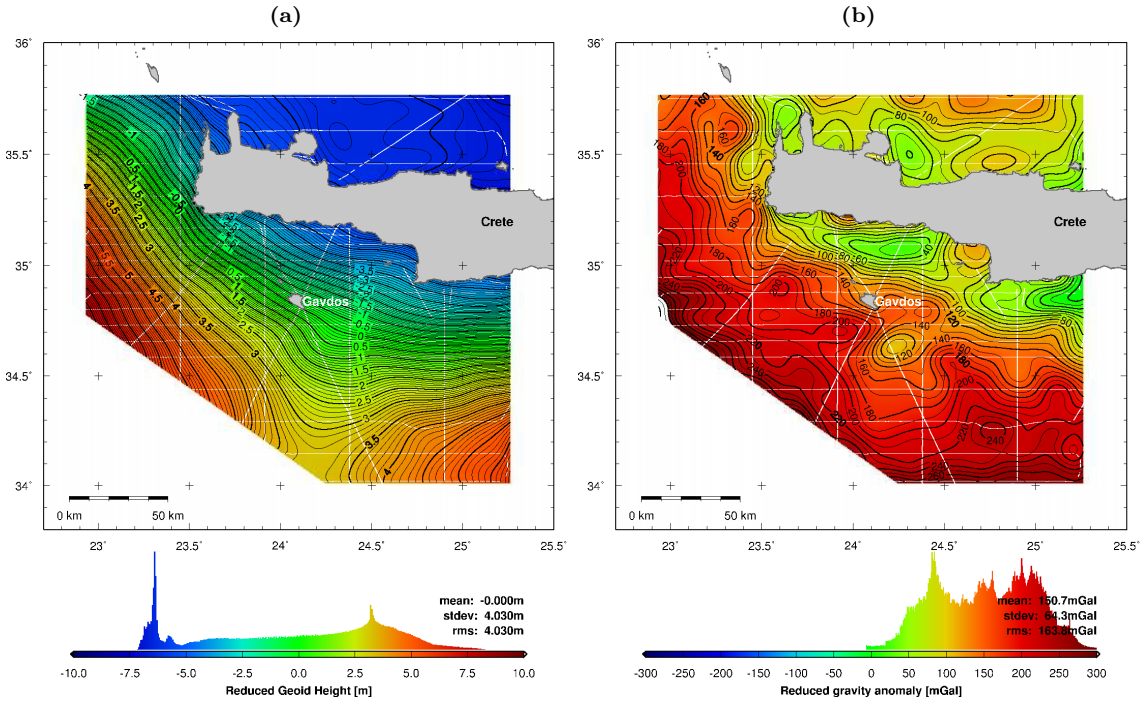

Figure 11.19: **(a)** Geoid heights from airborne altimetry (Fig. 11.1a) reduced for effects of topography, bathymetry and sediments (Fig. 11.14a), with mean offset removed. **(b)** Associated gravity anomalies from reduction of Fig. 11.1b with Fig. 11.14b. Contour intervals: 0.1 m and 10 mGal.

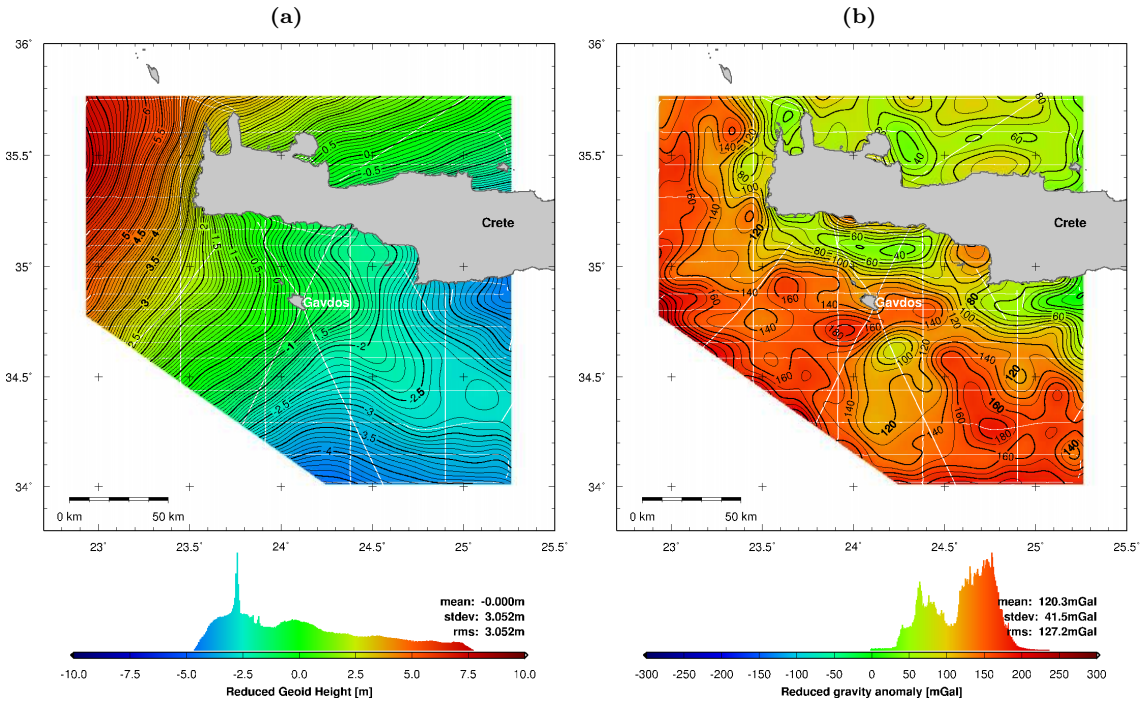

Figure 11.20: **(a)** Geoid heights from airborne altimetry (Fig. 11.1a) reduced for effects of topography, bathymetry, sediments and ESC Moho (Fig. 11.15a), with mean offset removed. **(b)** Associated gravity anomalies from reduction of Fig. 11.1b with Fig. 11.15b. Contour intervals: 0.1 m and 10 mGal.

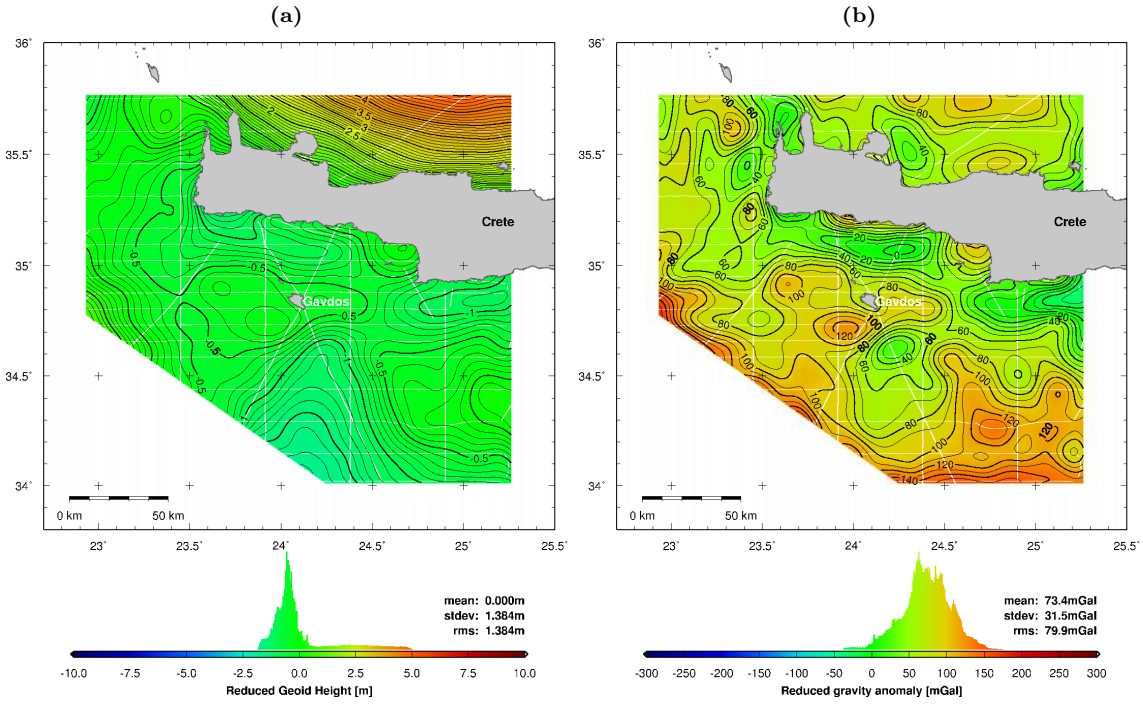

Figure 11.21: **(a)** Geoid heights from airborne altimetry (Fig. 11.1a) reduced for effects of topography, bathymetry, sediments and isostatic Moho (Fig. 11.16a), with mean offset removed. **(b)** Associated gravity anomalies from reduction of Fig. 11.1b with Fig. 11.16b. Contour intervals: 0.1 m and 10 mGal.

reduced to 1.7 m south of Crete, with weak gradients in several directions.

North of Crete, a strong positive geoid gradient of 0.1 m/km in north direction appears after the reduction (Fig. 11.21a), indicating a significant mass excess north of Crete. Since the gradient is not decreasing towards the northern border of the survey area, and since the reduced gravity anomalies (Fig. 11.21b) are not indicating a local mass excess inside the survey area, the positive mass anomaly must be situated beyond the survey area, towards the north. The origin of this mass anomaly can be anomalously dense crust material or an anomalously high Moho with respect to the isostatic Moho north of Crete. Both hypotheses are in accordance with density models based on seismic soundings in the area of the Hellenic subduction zone and the Hellenic Trench, characterized by the collision between the African and European lithospheric plates (Snopek et al., 2007; Makris and Yegorova, 2006; Casten and Snopek, 2006). These density models indicate an upwelling of the European mantle north of Crete, related to the subduction of the African oceanic lithosphere beneath the Eurasian (Aegean) continental lithosphere and causing a significant positive mass anomaly in this area. It is obvious that the complexity of the Moho discontinuity and mass anomalies associated with the subduction zone cannot be satisfactorily modeled by isostatic compensation.

12 Geoscientific Exploitation of Shipborne Altimetry Data in the North Aegean Sea

12.1 Marine Geoid, Gravity Anomalies and Deflections of the Vertical from Sea Surface Heights

Assuming the mean dynamic topography (MDT) as known, marine geoid heights can be derived from observed sea surface heights by subtraction of MDT based on (2.2). The MDT used in this study is the RioMed mean dynamic topography for the Mediterranean Sea (Section 2.5.3, Fig. 2.8a). The effects of the MDT in the survey area are small, with values between 0 and 5 cm only (Fig. 2.9b). By subtracting the RioMed MDT (Fig. 2.9b) from the sea surface heights obtained by shipborne altimetry (Fig. 9.15), altimetric geoid heights above the WGS84 reference ellipsoid are obtained (Fig. 12.1a).

The altimetric geoid heights reveal that the bathymetric low of the North Aegean Trough is associated with a distinct depression of the geoid at the south-western end of the North Aegean Trough. The depression reaches a minimum of 37.9 m, while the geoid height in the surrounding area is more than 39.5 m and reaches 40.5 m towards the north of the survey area. Further details on the geodynamic processes associated with the North Aegean Trough are given in Section 1.2.

Gravity anomalies (Fig. 12.1b) were computed from the marine geoid heights (Fig. 12.1a), based on Laplace's equation (2.21) and the curvature of the geoid (Section 2.2.1). As compared to geoid heights, gravity anomalies have the advantage that they are not affected by the long-wavelength part of the gravitational potential and are therefore better suited for the analysis of local gravity anomalies. Gravity anomalies in the survey area range from -60 mGal at the geoid depression at the south-western end of the North Aegean Trough to 60 mGal in the North (Fig. 12.1b).

The extreme gradients of the geoid (Fig. 12.1a) were quantified by deriving horizontal gradients (Fig. 12.2a) and deflections of the vertical (Fig. 12.2b) from the geoid heights, using (2.20). Maximum geoid gradients, reaching 0.1 m/km, were observed north of the island of Alonnisos, corresponding to a deflection of the vertical of 20 arcsec. For comparisons and validation purposes, deflections of the vertical from astrogeodetic observations are added in Fig. 12.2b. For details on the astrogeodetic observations, the reader is referred to (Somieski, 2008) and (Müller et al., 2006).

An interpretation of the obtained geoid heights and gravity anomalies is carried out by the reduction of mass effects in Section 12.5.

12.2 Comparison of Local Altimetric Geoid with existing Models

In order to validate the marine geoid heights (Fig. 12.1a) computed from shipborne altimetry (altimetric geoid) in Section 12.1, they were compared to geoid heights from several gravity models. The analyzed global gravity models are EGM96 to degree and order 360 (Fig. 12.3a), EGM2008

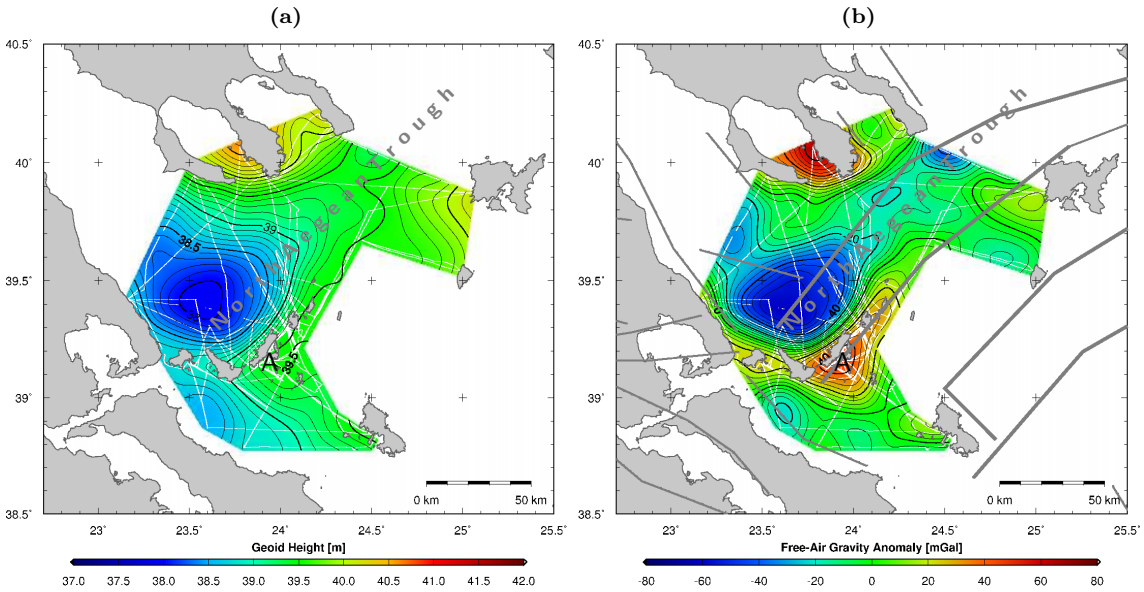

Figure 12.1: **(a)** Geoid heights computed from shipborne altimetry, by subtracting the RioMed mean dynamic topography (Fig. 2.9b) from the observed sea surface heights (Fig. 9.15). Contour interval: 0.25 m. **(b)** Gravity anomalies derived from geoid heights in (a). Contour interval: 5 mGal. Grey lines: North Aegean fault system. A = Alonnisos. White lines: boat-tracks.

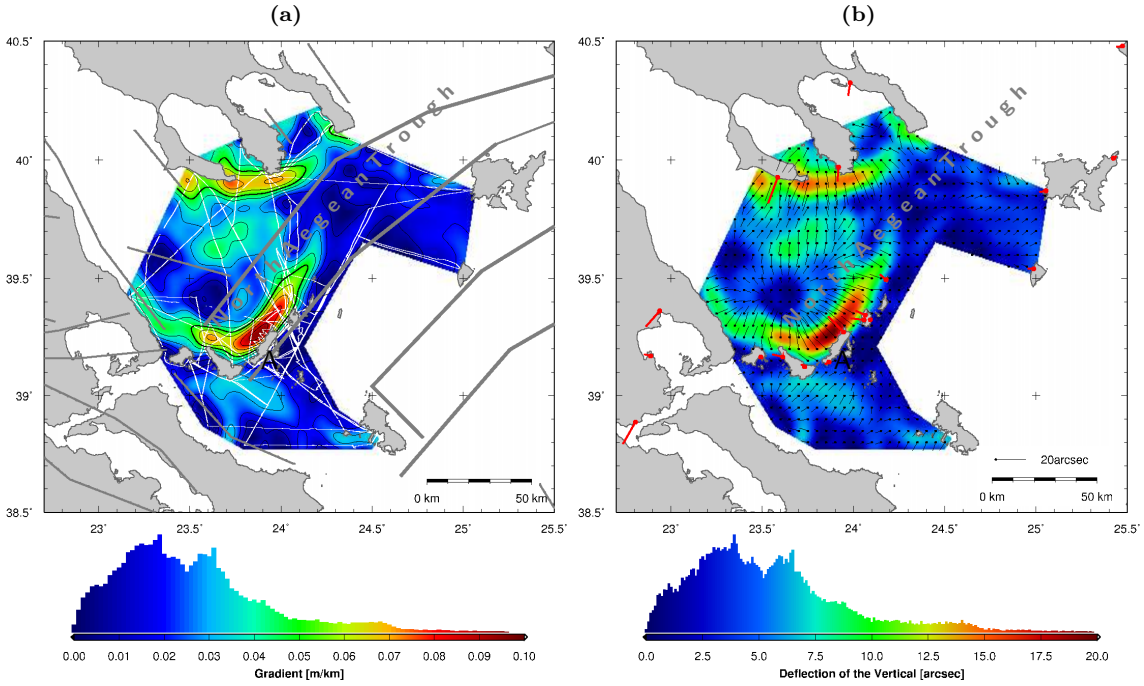

Figure 12.2: **(a)** Horizontal gradients of geoid heights in Fig. 12.1a. Contour interval: 0.01 m/km. Grey lines: North Aegean fault system. White lines: boat-tracks. **(b)** Deflections of the vertical computed from geoid heights in Fig. 12.1a. Red vectors: deflections of the vertical from astrogeodetic observations. A = Alonnisos.

Table 12.1: Mean offsets and standard deviations (STD) between the altimetric geoid from airborne laser altimetry and geoid models.

Geoid Model	(degree,order)	mean offset [m]	STD [m]
EIGEN-5S	(150,150)	-0.63	0.37
EIGEN-5C	(360,360)	-0.31	0.38
EGM96	(360,360)	-0.80	0.37
EGM2008	(360,360)	-0.42	0.25
EGM2008	(2190,2159)	-0.41	0.08
AUTH2008	-	-0.94	0.10

to degree 2190 and order 2159 (Fig. 12.3b), EIGEN-5S to degree and order 150 (Fig. 12.3c) and EIGEN-5C to degree and order 360 (Fig. 12.3d). All geoid heights were computed with respect to the WGS84 ellipsoid. A detailed description of the gravity models is given in Section 2.2.3. The increasing resolution of the different models from EIGEN-5S to EGM96 and EIGEN-5C, and finally to EGM2008 is clearly shown Fig. 12.3, e.g. by their capability of resolving the depression at the south-western end of the North Aegean Trough.

The residuals between the altimetric geoid (Fig. 12.1a) and the geoid models (Fig. 12.3) are shown in Fig. 12.4. Mean offsets and standard deviations are summarized in Tab. 12.1. In the ideal case of error-free sea surface heights, dynamic topography and geoid models, these residuals should be zero according to 2.29. The residuals with respect to EIGEN-5S have large values reaching 1.5 m, large gradients and a high standard deviation of 0.37 m (Fig. 12.4c). The poor agreement is due to the low resolution (approx. 130 km) of the EIGEN-5S. The two combined geoid solutions EGM96 and EIGEN-5C have a theoretical resolution of 55 km. The mean difference between the altimetric geoid and EGM96 (Fig. 12.4a) and EIGEN-5C (Fig. 12.4d) are -0.80 m and -0.31 m, respectively, with similar standard deviations of 0.37 m and 0.38 m. As for EIGEN-5S, both models do not resolve the local negative anomaly at the south-western end of the North Aegean Trough, with residuals reaching -1.55 m and -1.05 m, respectively. The best agreement is obtained with EGM2008, with a mean difference of -0.41 m[1] and a standard deviation of only 0.08 m (Fig. 12.4b). The good agreement is due to the high resolution of EGM2008. Its expansion to degree 2190 and order 2159 corresponds to a resolution of approx. 10 km.

The improved input data in terms of resolution and accuracy of the recent EIGEN-5C model, as compared to EGM96, does not lead to a significant improvement of the spatial resolution of the EIGEN-5C model. As already shown for the airborne data around Crete (Section 11.2), the limiting factor in terms of spatial resolution of the geoid models is the mathematical expansion of the spherical harmonics of the model. Again, this is confirmed by computing an EGM2008 geoid solution with a spherical harmonics expansion limited to degree and order 360 (Fig. 12.5a). The residuals with respect to the altimetric geoid have a mean difference of -0.42 m and a standard deviation of 0.25 m (Fig. 12.6a). These values are similar to those of EGM96 (Fig. 12.4a) and EIGEN-5C (Fig. 12.4d). It can be concluded that the extension of the expansion of EGM2008, from degree and order 360 to degree 2190 and order 2159, has lead to an improvement of 0.17 m of the standard deviation with respect to the altimetric geoid, corresponding to an improvement of 68%.

Additional residuals were computed between the altimetric geoid and the local gravimetric geoid model AUTH2008 (Fig. 12.5b). A description of AUTH2008 is given in Section 2.2.3. The obtained residuals are similar to those obtained with respect to EGM2008 in terms of standard deviation,

[1] It is a pure coincidence that the mean difference of -0.41 m between the altimetric geoid and EGM2008 corresponds to the value of 0.41 m subtracted from EGM2008 geoid heights to make them correspond to the mean sea surface. By using the same method to compute residuals in the area around Crete, a mean difference of -0.14 m was obtained (Fig. 11.4b. Furthermore, without subtracting 0.41 m from EGM2008, the mean difference would be 0.82 m and not 0.

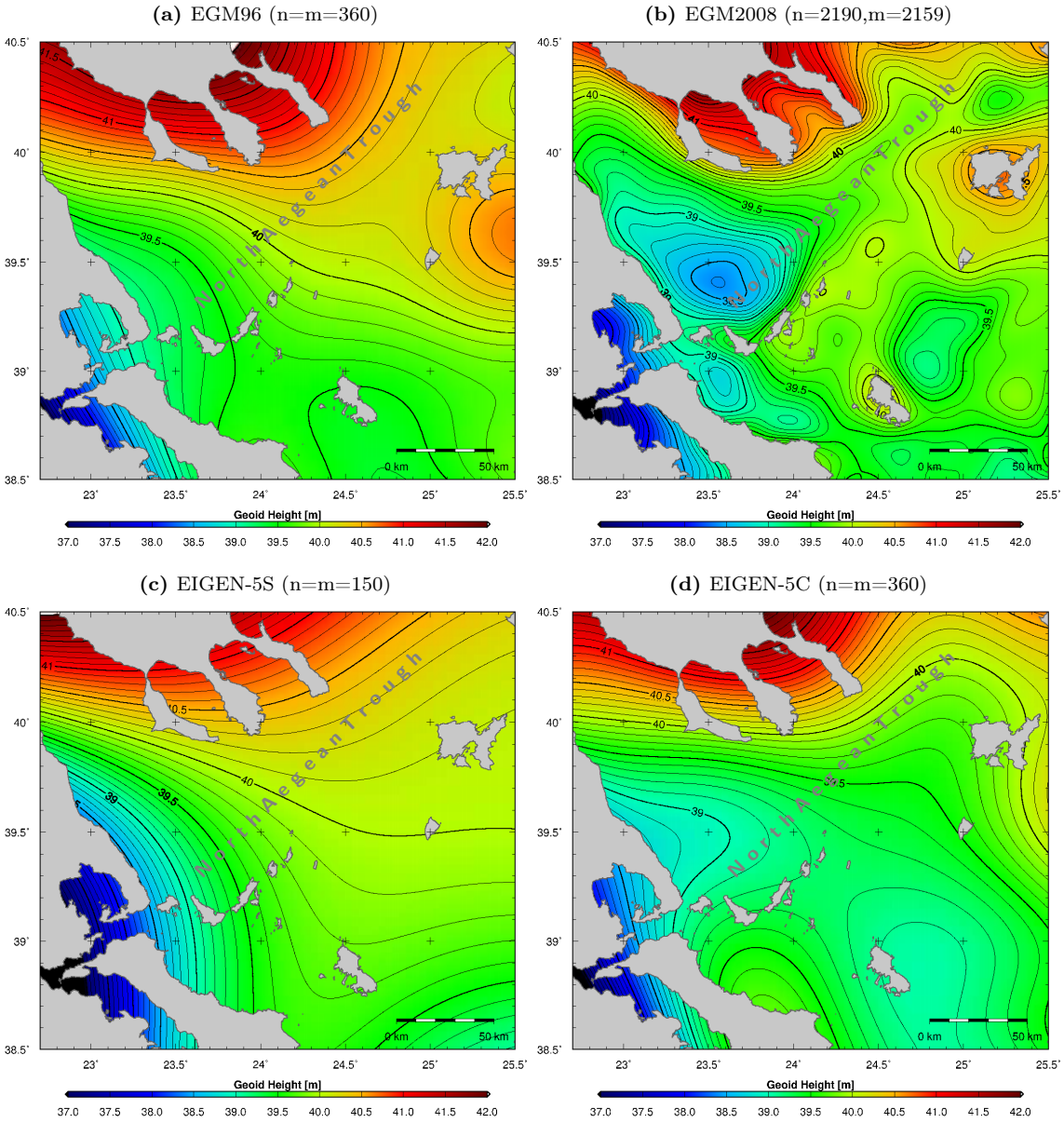

Figure 12.3: Geoid heights to degree n and order m with respect to WGS84 from **(a)** EGM96, **(b)** EGM2008, **(c)** EIGEN-5S and **(d)** EIGEN-5C. Contour intervals: 0.1 m.

with a value of 0.10 m (Fig. 12.6b). Hence, the spatial resolutions of both models are similar. However, a larger mean difference of -0.94 m between the altimetric geoid and AUTH2008 is observed in the survey area.

The mean offsets (Tab. 12.1) are different from the ones obtained with respect to the airborne altimetric geoid around Crete (Section 11.2, Tab. 11.1), indicating discrepancies in the long wavelength geoid undulations of the two models between the two areas under investigation. Since the absolute geoid height is not great importance, the offsets are not critical.

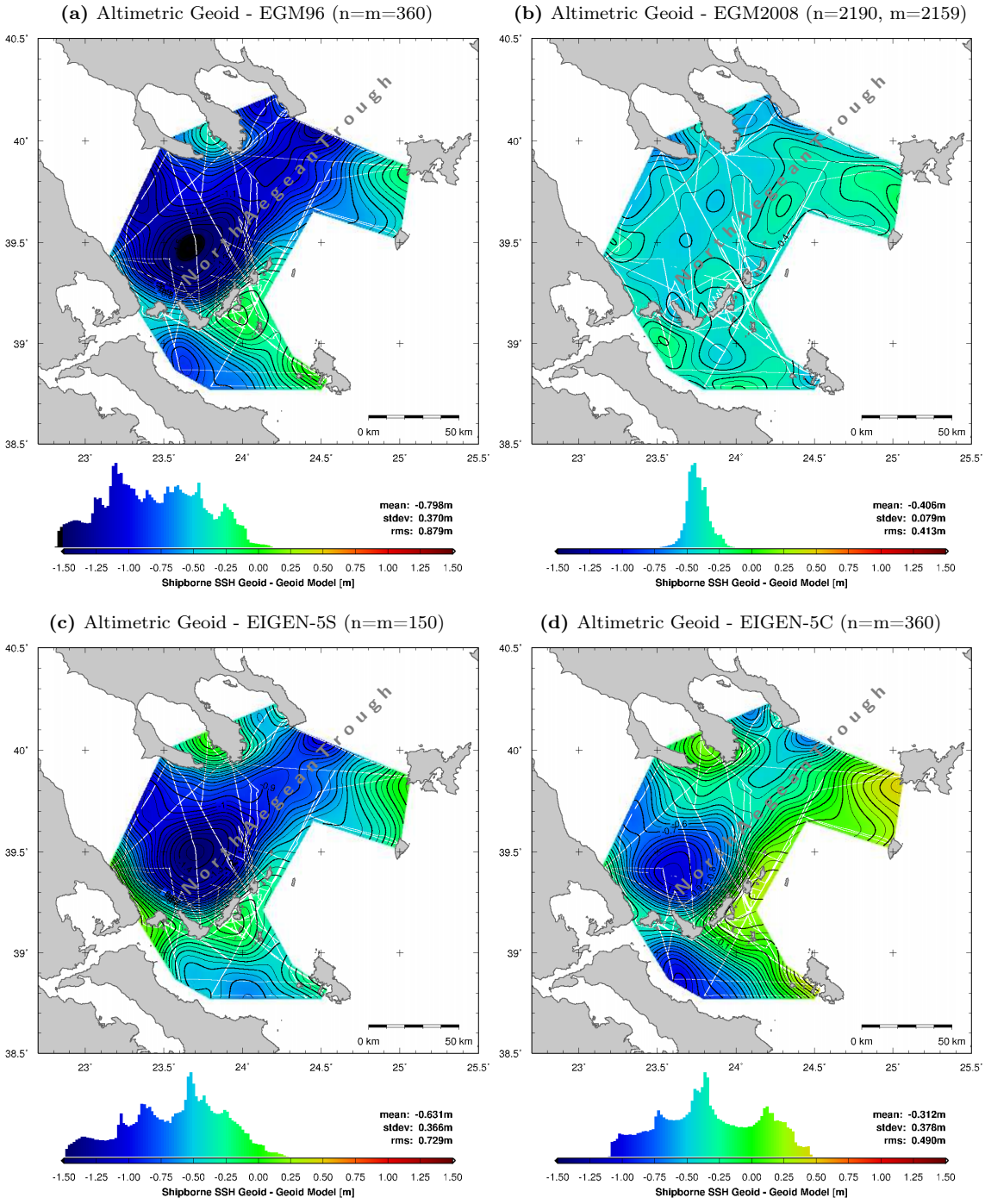

Figure 12.4: Difference between shipborne altimetric geoid (Fig. 12.1a) and geoid heights from **(a)** EGM96, **(b)** EGM2008, **(c)** EIGEN-5S and **(d)** EIGEN-5C. White lines: boat-tracks. Contour intervals: 0.05 m.

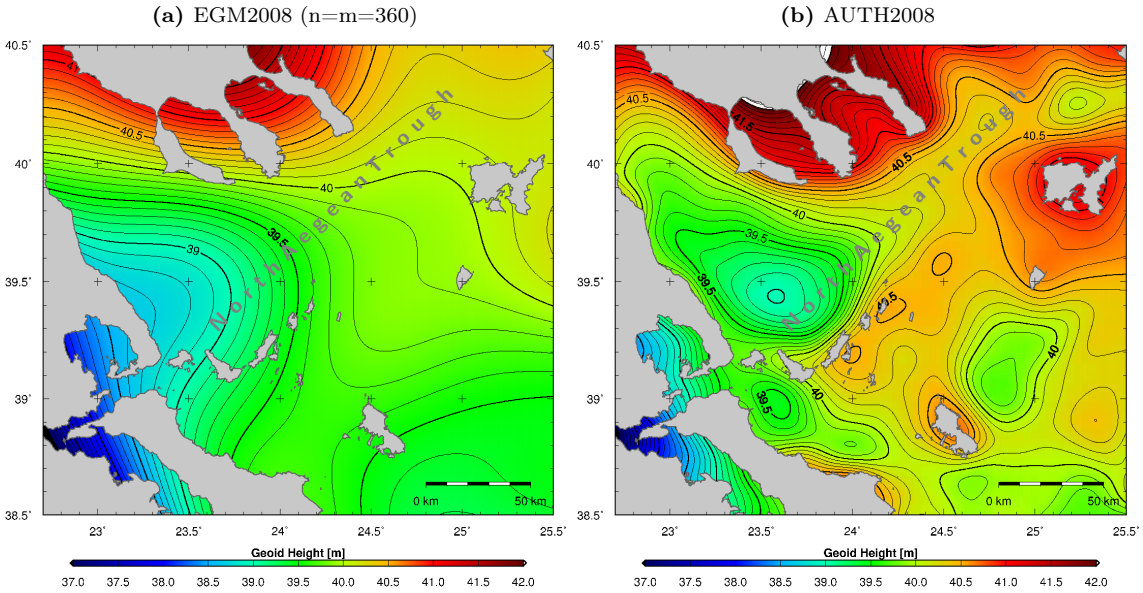

Figure 12.5: Geoid heights with respect to WGS84 from **(a)** EGM2008 with expansion limited to degree and order 360 and from **(b)** the gravimetric model AUTH2008 (b). Contour intervals: 0.1 m.

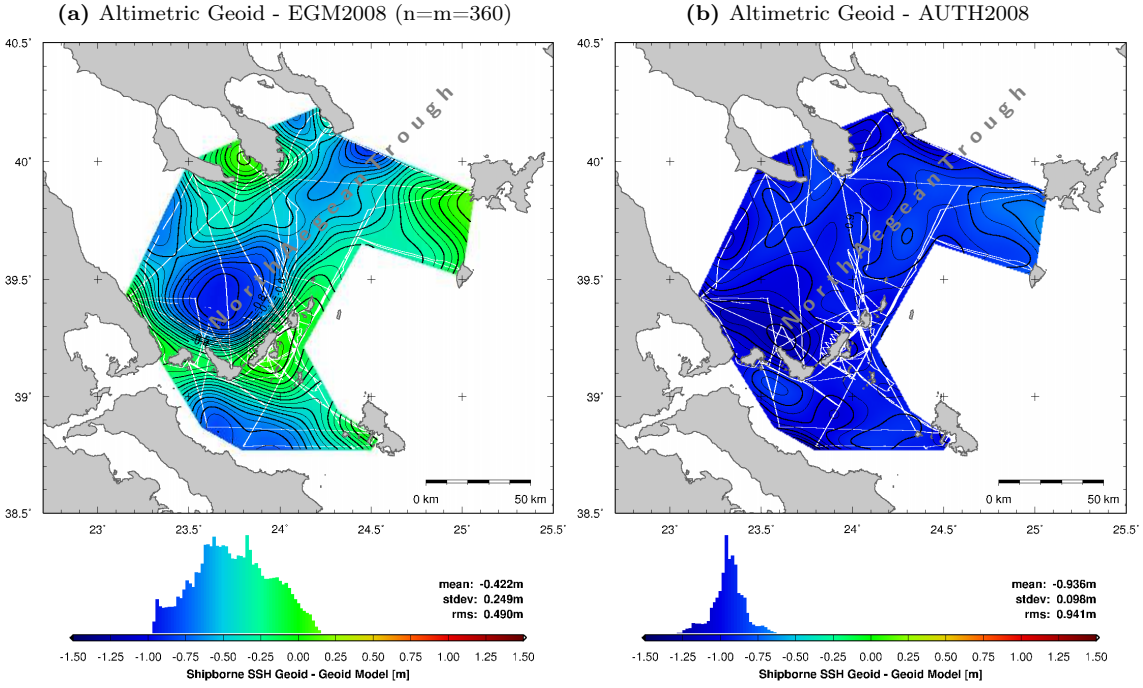

Figure 12.6: Difference between shipborne altimetric geoid (Fig. 12.1a) and geoid heights from **(a)** EGM2008 to degree and order 360 and **(b)** AUTH2008. White lines: boat-tracks. Contour intervals: 0.05 m.

12.3 Mean Dynamic Topography Estimation

Among the geoid models used in Section 12.2, the satellite-only solution EIGEN-5S and the local gravimetric geoid model AUTH2008 are the only geoid solution that are independent of altimetric sea surface height data. Hence, they would be the only appropriate models to determine the mean dynamic topography (MDT) using the direct method after (2.30) (Section 2.5). The pronounced residuals between the shipborne data and EIGEN-5S (Fig. 12.4c) are obviously making the EIGEN-5S unusable for realistic MDT determination at wavelengths below 130 km. The same remark holds for EGM96 and EIGEN-5C (Fig. 12.4a and Fig. 12.4d). Even if these two models were assumed independent of altimetric data, they would not be appropriate to determine the MDT at wavelengths below 55 km.

Hypothetic MDT were computed from the residual fields of the sea surface heights from shipborne altimetry (Fig. 9.15) with respect to EGM2008 (Fig. 12.7a) and AUTH2008 (Fig. 12.7b) geoid heights. Geostrophic circulation fields were derived from the hypothetic MDT based on (2.32). Compared to the RioMed mean geostrophic circulation (Fig. 2.9b), the obtained circulations are unrealistic and spoiled by noisy eddies. By increasing the filterwidths on both datasets, it was possible to eliminate the noisy eddies, but no significant circulation remained. Hence, it was not possible to derive a realistic circulation pattern based on the sea surface height observations and the used geoid models. The major reason lies in the fact that the presumed MDT, as e.g. by RioMed (Fig. 2.9b), only varies within a range of 4 cm over the entire survey area. Furthermore, the gradients of the MDT associated with the circulation are below 0.5 cm/10 km. Hence, the MDT signal in the survey area is smaller or in the same order of magnitude as the accuracy of the shipborne sea surface heights and the used geoid models. It can be concluded that the sea surface height observations by shipborne altimetry and the considered geoid models are not accurate enough to resolve such small dynamic effects. In addition, EGM2008 is not independent of altimetric sea surface height data.

12.4 Modeled Mass Effects on Geoid Heights and Gravity

12.4.1 Introduction

The effects of mass anomalies on geoid heights were computed for the survey area in the North Aegean Sea, based on (2.24) and on cuboid masses (2.26). The area of influence considered in the modeling of mass effects extends from 19°E to 29°E and from 36°N to 43°N (Fig. 12.8a). In addition to geoid heights, the effects of mass anomalies on gravity were computed, based on (2.25) and (2.27). As compared to geoid heights, gravity anomalies have the advantage that they are not affected by the long-wavelength part of the gravitational potential and are therefore better suited for the analysis of local gravity anomalies. On the other hand, geoid heights are comparable to low-pass filtered gravity anomalies, mainly affected by large-scale mass anomalies (Section 2.2.4). Hence, gravity anomalies were modeled in this section in order to obtain additional information on the local gravity field, although the major investigations were carried out on geoid heights. The gravity anomalies were computed at sea level, yielding e.g. exclusively negative effect of the topography on gravity anomalies. The mass effects computed in this section are used in the Section 12.5 to reduce the geoid heights and gravity anomalies derived from the sea surface heights obtained by shipborne altimetry. The theoretical background of the computation of mass effects on geoid heights and on gravity anomalies is given in Section 2.2.4.

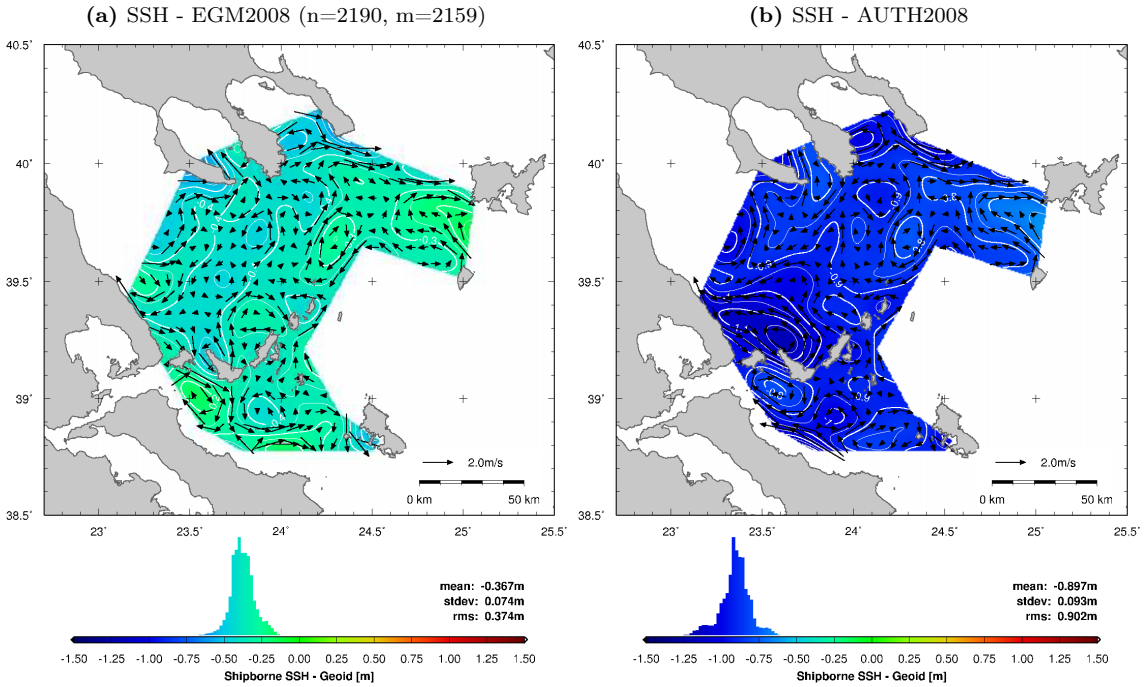

Figure 12.7: Hypothetic mean dynamic topography (background) and ocean circulation (arrows) from differences between sea surface heights from shipborne altimetry (Fig. 9.15) and geoid heights from **(a)** EGM2008 and **(b)** AUTH2008.

12.4.2 Effect of Topography and Bathymetry

The topography and bathymetry of the area of influence is characterized by the topographic masses surrounding the North Aegean Sea and locally by the bathymetry of the North Aegean Trough (Fig. 12.8a). The topography and bathymetry (including water masses) have mainly positive effects on geoid heights (Fig. 12.9a), since the positive effect of the topographic mass excess predominates over the negative effect of the mass deficiency due to the water. The effect ranges between 18 m in the north-west and -4 m in the south of the survey area. A relative depression at the North Aegean Trough, associated with the bathymetric low, can hardly be depicted, due to the strong overall geoid gradient in north-west direction caused by the topographic mass excess in the north-west of the area of influence. Associated gravity anomalies are shown in Fig. 12.9b. Within the effect of topography and bathymetry, the water masses have positive effects between 0.7 m on the northern mainland of the survey area and 2.7 m at the North Aegean Trough (Fig. 12.10a). In the south-western part, the effect reaches 9 m, caused by the influence of the deep water of the Ionian Sea in the south-western part of the area of influence. Associated gravity anomalies are shown in Fig. 12.10b.

12.4.3 Effect of Sediments

The survey area is mainly characterized by two marine sediment spots reaching thicknesses of 6 km (Fig. 12.8b). The information on sediment thickness used in the modeling is based on an unknown source. The mass deficiency associated with the sediments has a negative effect on geoid heights, with values down to -3 m above the thickest sediments (Fig. 12.11a). Associated gravity anomalies are shown in Fig. 12.11b.

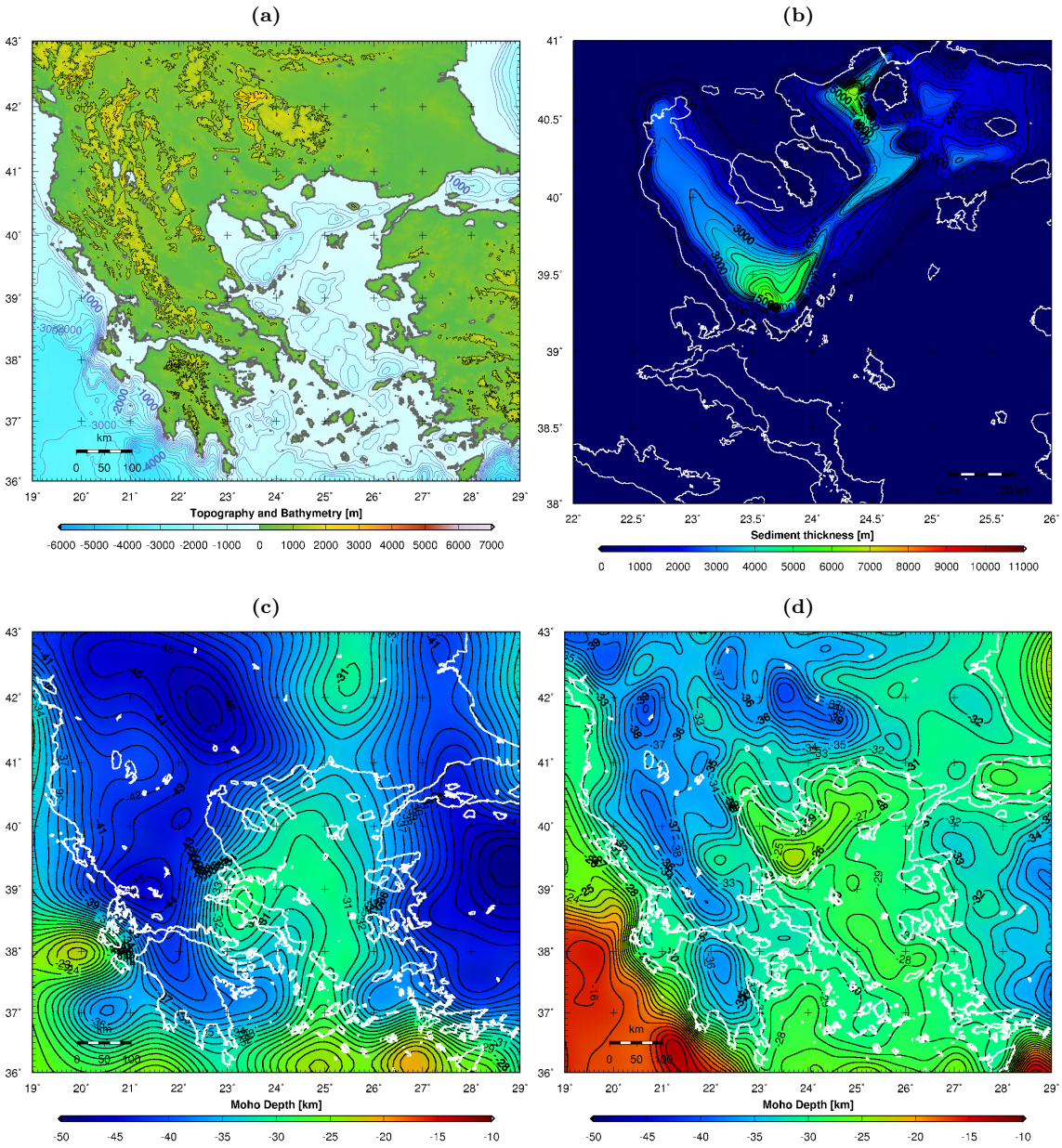

Figure 12.8: **(a)** Topography and bathymetry of the area of influence considered in the modeling of mass effects (contour interval bathymetry: 250 m, topography: 1000 m). **(b)** Light sediments thickness from unknown source (contour interval: 250 m). **(c)** Moho depth in the area of influence from the digital Moho depth map published by the ESC (European Seismological Commission) Working Group (Grad et al., 2009) (contour interval: 1 km). **(d)** Moho depth in the area of influence from isostatic compensation (reference depth: -30 km, contour interval: 1 km).

12.4.4 Effect of ESC Moho depths

For the computation of the effect of crust/mantle boundary (Moho) anomalies, Moho depths from the digital Moho depth map published by the ESC (European Seismological Commission) Working Group (Grad et al., 2009) (Fig. 12.8c) were used. Further details on the ESC Moho depths are given in Section 2.2.4. The Moho in the survey area is characterized by large-scale depressions over

the Greek and Turkish mainland, locally dropping down to -47 km. The mass deficiency caused by the depression of the Moho in the north-west of the area of influence causes strong negative effects of more than -20 m on geoid heights, whereas the effect in the south reaches more than 10 m (Fig. 12.12a). Associated gravity anomalies are shown in Fig. 12.12b.

12.4.5 Effect of Isostatic Moho depths

As an alternative to the ESC Moho, Moho depths were computed based on isostatic compensation of the masses of topography, bathymetry, water and sediments (Section 2.2.4). A reference depth of -30 km was used. Since the model of isostatic compensation only reflects a theoretical correlation between the masses above the crust/mantle boundary (Moho) and the compensating depth of the boundary, it may sound more appropriate to use a Moho model predicted by real observations, like the ESC Moho. In the present study, however, better reduction results were obtained with the isostatic Moho (Section 12.5).

The isostatic compensation has a weak uplifting effect on the Moho in the marine areas of the Aegean Sea (Fig. 12.8d), due to the mass deficiency caused by water and sediments. The isostatic Moho raises up to a depth of -25 km at the North Aegean Trough, corresponding to an uplift of 3 km with respect to the reference depth of -30 km. On the mainland, the Moho is characterized by large-scale depressions, locally dropping down to -39 km. In the north of the survey area, the drop of the Moho associated with a topographic mass excess, causes a mass deficiency. This mass deficiency has a negative effect on geoid heights, reaching -15.5 m in the north-west (Fig. 12.13a). In the south, a positive effect of the Moho on geoid heights is obtained, reaching 7.5 m in the south-west. Associated gravity anomalies are shown in Fig. 12.13b.

12.4.6 Combined Effects

By combining the effects of topography and bathymetry (Fig. 12.9a) with the effects of sediments (Fig. 12.11a), mostly positive effects on geoid heights are obtained (Fig. 12.14a). They range between 17.5 m in the North-West and -4 m in the South. The introduction of the effect of the sediments amplifies the relative depression at the North Aegean Trough by about 1 m, leading to a local minimum of 0 m. Associated gravity anomalies are shown in Fig. 12.14b.

By combining the effects of topography, bathymetry and sediments (Fig. 12.14a) with the effects of the ESC Moho (Fig. 12.12a), the resulting effects on geoid heights become small (Fig. 12.15a). They reach a maximum of 8 m in the South and a minimum of -6 m in the North-West. Associated gravity anomalies are shown in Fig. 12.15b. By visually comparing the sum of all modeled effects using ESC Moho depths (Fig. 12.15a) to the observed geoid (Fig. 12.1a) and e.g. the EGM2008 geoid (Fig. 12.3b), a poor agreement is observed. In the modeled geoid (Fig. 12.15a), no distinct depression is obtained at the North Aegean Trough, due to a strong remaining geoid gradient in north-west direction.

By combining the effects of topography, bathymetry and sediments (Fig. 12.14a) with the effects of the isostatic Moho (Fig. 12.8d), the resulting effects on geoid heights become small (Fig. 12.16a). They reach a maximum of 3 m in the West and North-West, associated with the major topographic mass excesses, and a local minimum of -2.2 m at the North Aegean Trough. Associated gravity anomalies are shown in Fig. 12.16b. The introduction of the effect of the isostatic Moho removes the major geoid gradient in north-west direction observed in Fig. 12.9a and Fig. 12.14a. As a consequence, the shape of the resulting geoid becomes much more realistic when compared for example to the geoid heights of EGM2008 (Fig. 12.3b).

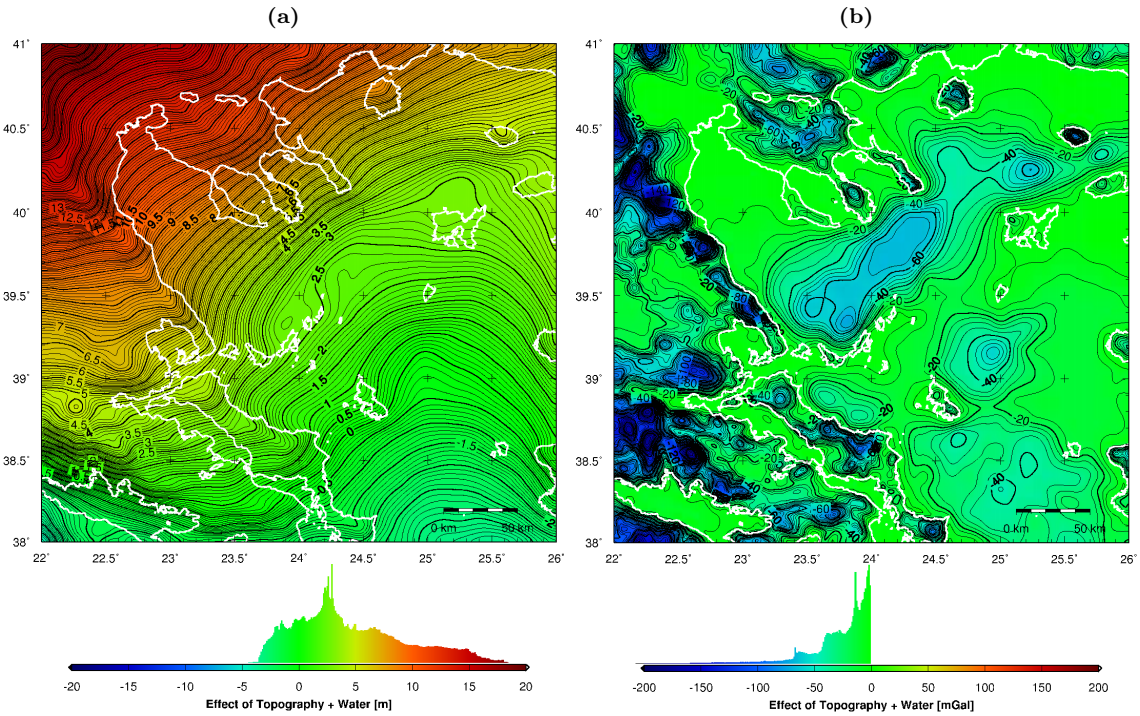

Figure 12.9: Effects of topography and bathymetry (including water masses) on **(a)** geoid heights (contour interval: 0.1 m) and **(b)** gravity (contour interval: 5 mGal).

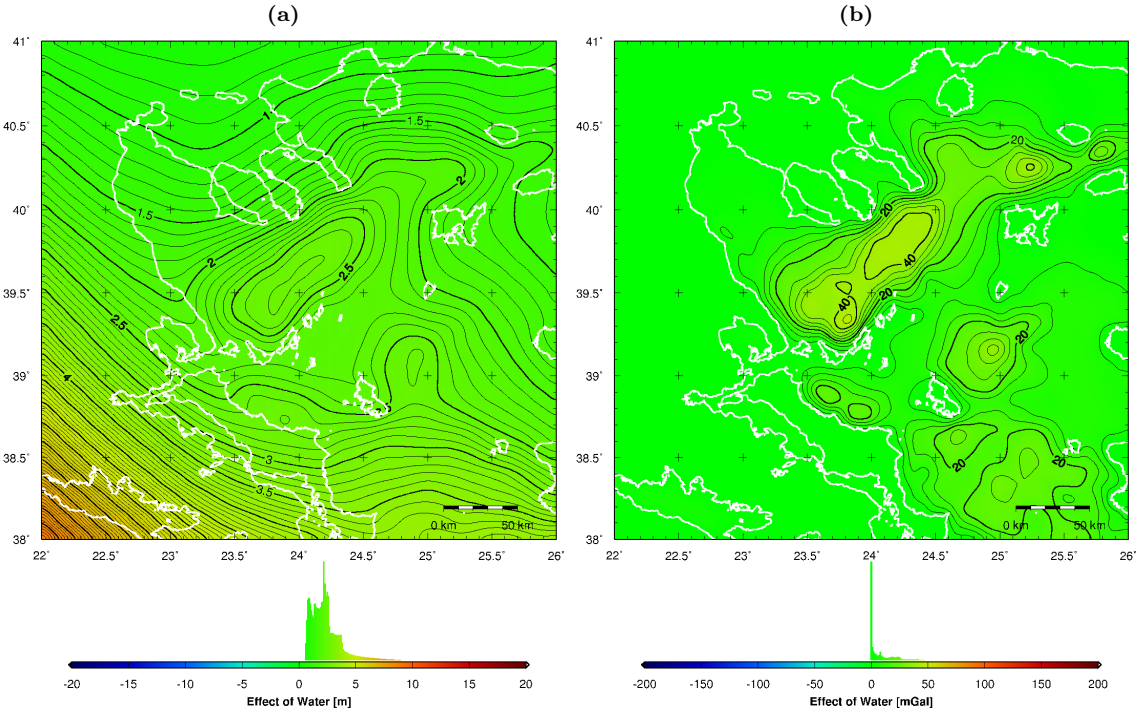

Figure 12.10: Effect of water masses on **(a)** geoid heights (contour interval: 0.1 m) and **(b)** gravity (contour interval: 5 mGal).

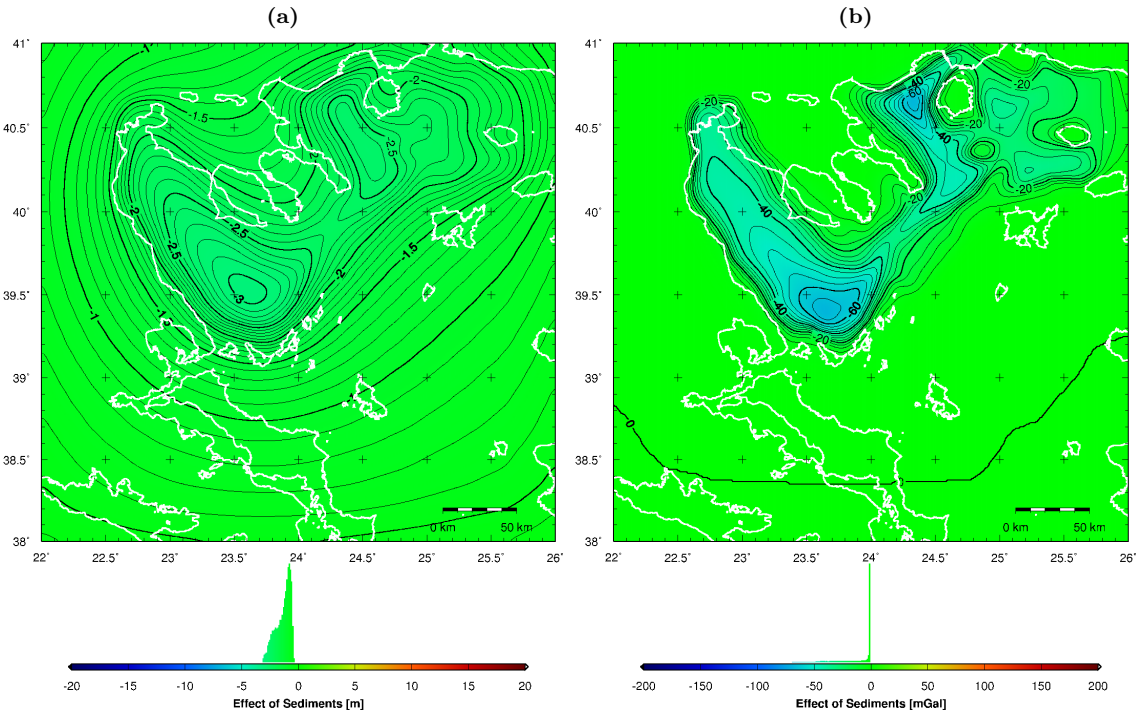

Figure 12.11: Effect of mass deficiency caused by sediments on **(a)** geoid heights (contour interval: 0.1 m) and **(b)** gravity (contour interval: 5 mGal).

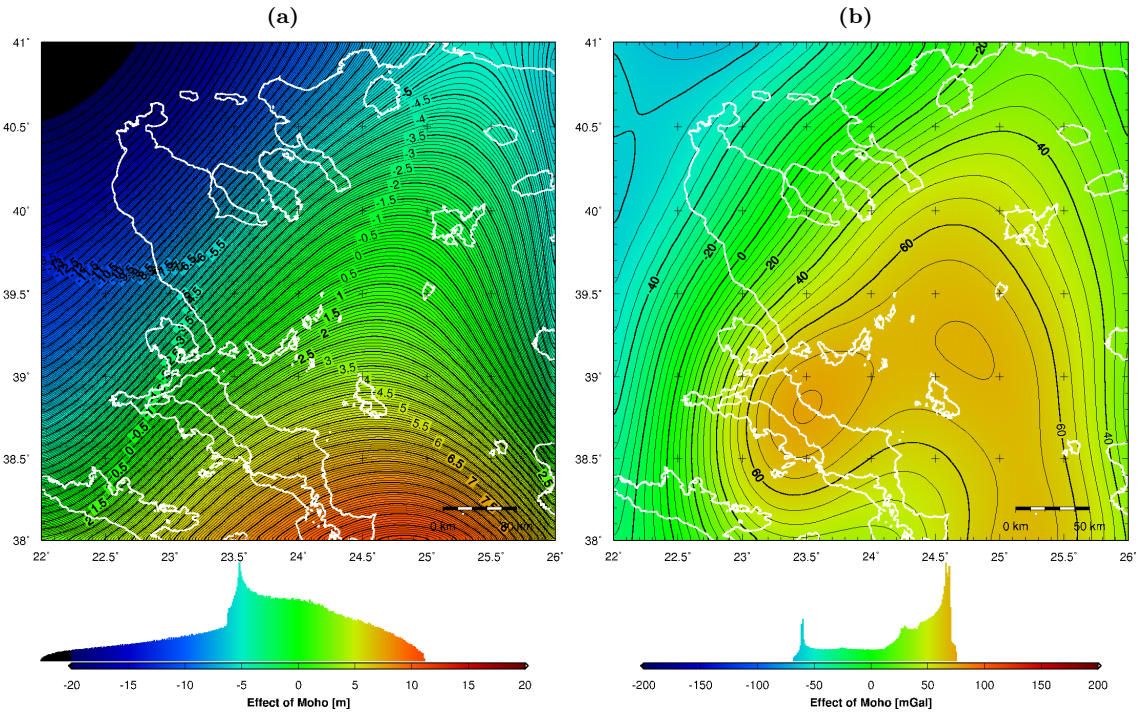

Figure 12.12: Effect of mass anomalies due to Moho depths from ESC map (Fig. 12.8c) on **(a)** geoid heights (contour interval: 0.1 m) and **(b)** gravity (contour interval: 5 mGal).

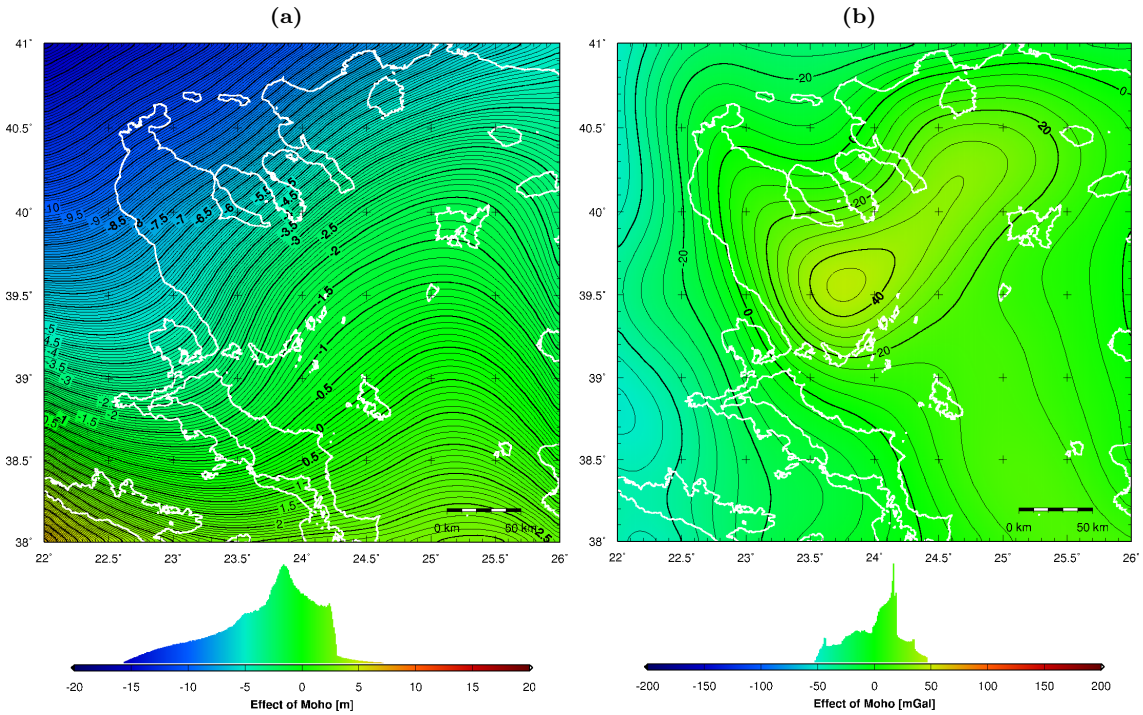

Figure 12.13: Effect of mass anomalies due to Moho depths from isostatic compensation (Fig. 12.8d) on **(a)** geoid heights (contour interval: 0.1 m) and **(b)** gravity (contour interval: 5 mGal).

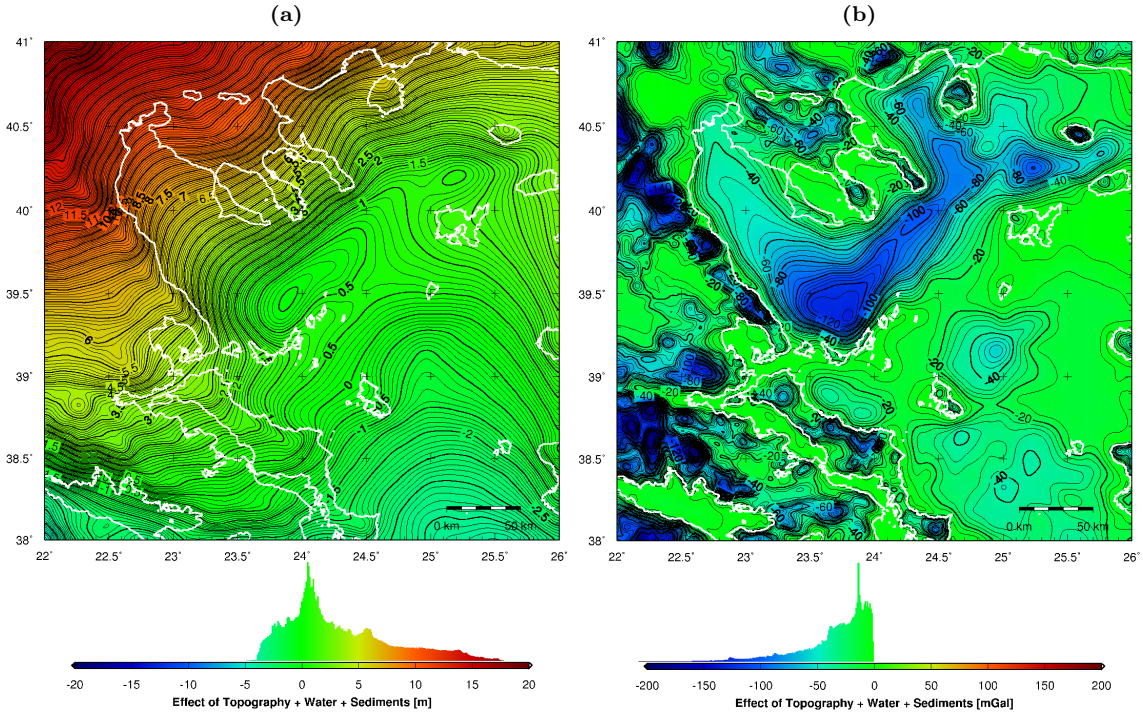

Figure 12.14: Sum of effects of topography, bathymetry (Fig. 12.9) and sediments (Fig. 12.11) on **(a)** geoid heights (contour interval: 0.1 m) and **(b)** gravity (contour interval: 5 mGal).

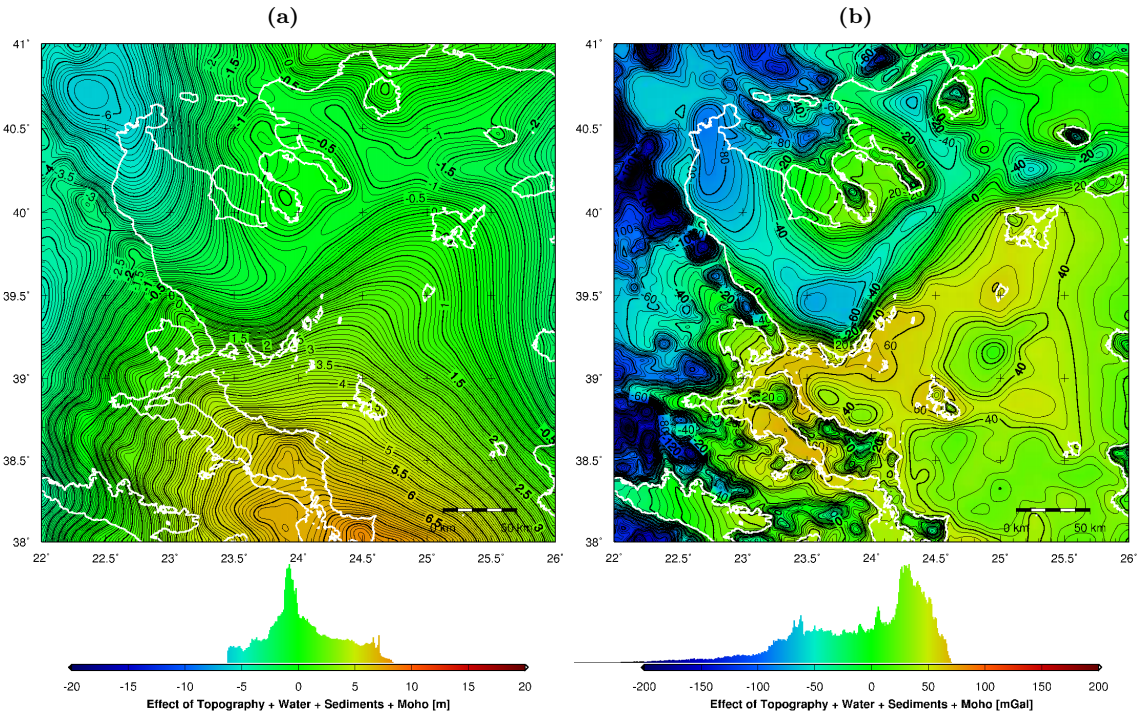

Figure 12.15: Sum of effects of topography, bathymetry, sediments (Fig. 12.14) and ESC Moho depths (Fig. 12.12) on **(a)** geoid heights (contour interval: 0.1 m) and **(b)** gravity (contour interval: 5 mGal).

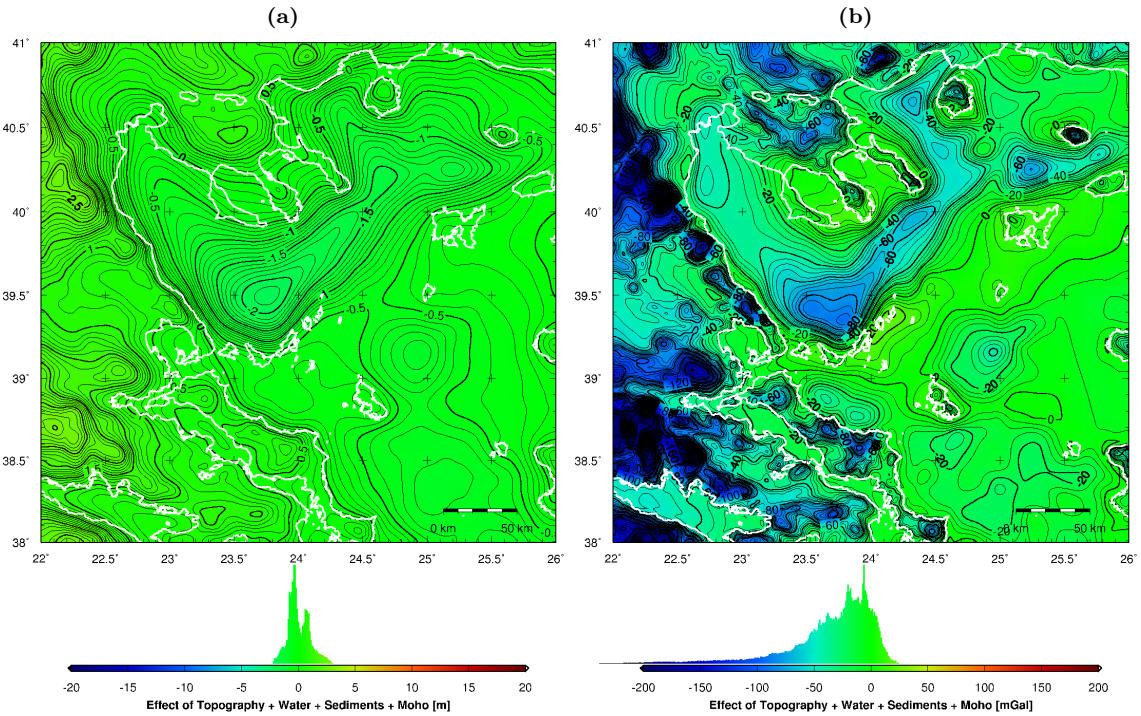

Figure 12.16: Sum of effects of topography, bathymetry, sediments (Fig. 12.14) and isostatic Moho depths (Fig. 12.13) on **(a)** geoid heights (contour interval: 0.1 m) and **(b)** gravity (contour interval: 5 mGal).

Table 12.2: Differences (mean offset, standard deviation (STD) and RMS) on geoid heights between mass effects computed by cuboid masses and point masses.

Effect	mean [cm]	STD [cm]	RMS [cm]
Topo/Bathy	2.0	2.4	3.1
Sediments	0.1	0.1	0.1
Moho	0.7	4.9	4.9
Topo/Bathy, Sediments	1.9	2.4	3.0
Topo/Bathy, Sediments, Moho	2.6	4.2	4.9

12.4.7 Cuboids vs. Point Mass Modeling

The mass effects shown in Fig. 12.9 to Fig. 12.16 were computed based on cuboids masses using (2.26) and (2.27). Since the computation of the effects of cuboid masses can be very CPU-intensive depending on the size and resolution of the grids, a simplified method to compute approximate mass effects on geoid heights and on gravity based on (2.24) and (2.25) consists in concentrating the mass of each cuboid at its center of mass. In order to assess the impact of this approximation, the effects computed by cuboid masses on geoid heights (Fig. 12.9a to Fig. 12.16a) were recomputed based on the center of mass (point mass) model. Differences on geoid heights are increased by the presence of elongated cuboids with large mass contrasts within a large distance range from the computation point. These elongated cuboids are typically produces by high mountains, deep sea, large sediment layers and large Moho depth variations.

The differences obtained between the two methods are summarized in Tab. 12.2. The smallest differences are obtained for the sediments. Larger differences are obtained for the effect of topography and bathymetry and the effect of the Moho. The differences of the effect of topography and bathymetry on the geoid are below 7 cm in the survey area (Fig. 12.17a). The differences of Moho effect on the geoid reach 15 cm in the survey area (Fig. 12.13a) and have a larger variation than the differences on the combined topography, bathymetry and water effect. The larger differences on the Moho effect are caused by the extremely elongated shape of the Moho cuboids that can reach heights of more than 10 km over large regions in the area of influence. The effect of the shape of the Moho cuboids predominates over the distance between the Moho cuboids inside the Earth and the computation point at sea level.

The differences on the final solution combining topography, bathymetry, sediments and Moho depths range between -5 cm and 15 cm with an RMS of 4.9 cm. Hence, if an accuracy better than 5-10 cm is sought, the application of the cuboid model is mandatory. In the present case, regarding the sizes of the residual geoid heights after the reduction of mass effects (Section 12.5, Fig. 12.18a to Fig. 12.21a), the approximation of the point mass model has no significant effect on the size and spatial structure of the residuals. In the present case, the uncertainties in the precise knowledge of topography, sediments and Moho, as well as of the exact mass distribution inside the different layers, induce larger errors than the point mass approximation. The same conclusions were drawn from a similar investigation in the survey area of western Crete (Section 11.4.7).

12.5 Mass Reduction of Local Altimetric Geoid

12.5.1 Introduction

The mass effects computed in Section 12.4 were used to reduce the marine geoid heights obtained by shipborne altimetry (Fig. 12.1a). In addition, marine gravity anomalies derived shipborne altimetry (Fig. 12.1b) were reduced. Gravity anomalies are well suited to describe the high-frequency part of the gravity field, mainly affected by local mass anomalies, while the geoid undulations are

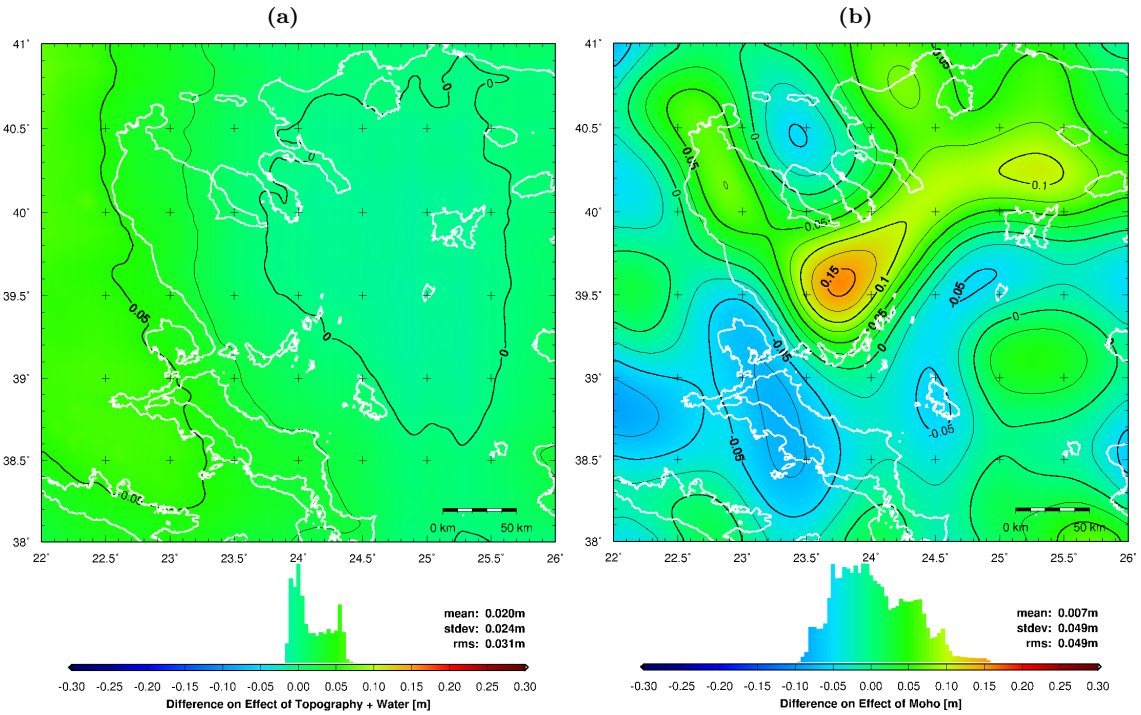

Figure 12.17: Differences on geoid heights between mass effects computed by cuboid masses and point masses from **(a)** topography/bathymetry and **(b)** Moho depths. Contour intervals: 0.025 m.

comparable to low-pass filtered gravity anomalies, mainly affected by large-scale mass anomalies. Hence, gravity anomalies were reduced in this section in order to obtain additional information on the local gravity field, although the major investigations were carried out on geoid heights.

12.5.2 Topography-Bathymetry Cogeoid

In a first step, marine geoid heights from shipborne altimetry (Fig. 12.1a) were reduced for the effects of topography and bathymetry (including water) (Fig. 12.9a). The reduced geoid heights correspond to the topography-bathymetry cogeoid. After the removal of a constant offset, the reduced geoid heights range between -3.9 and 3.2 m, with a strong negative gradient in north-west direction (Fig. 12.18a). Associated reduced gravity anomalies are shown in Fig. 12.18b.

12.5.3 Topography-Bathymetry-Sediments Cogeoid

In a second step, marine geoid heights from shipborne altimetry (Fig. 12.1a) were reduced for the effects of topography, bathymetry and sediments (Fig. 12.14a). The reduced geoid heights correspond to the topography-bathymetry-sediments cogeoid. After the removal of a constant offset, the reduced geoid heights range between -3.0 and 2.1 m (Fig. 12.19a). A strong negative gradient in north-west direction remains. The residual gradients north of the island of Alonnisos have mainly disappeared, indicating that the local geoid gradients in this area, as well as the predominant geoid depression at the western end of the North Aegean Trough, are mainly produced by the mass anomaly effects of the topography, bathymetry and sediments. Associated reduced gravity anomalies are shown in Fig. 12.19b.

Assuming the ideal case that the entire effects of topography, bathymetry and sediments were

removed by the reduction, and that no other mass anomalies except those from the Moho are present, the reduced geoid heights (Fig. 12.19a) and gravity anomalies (Fig. 12.19b)) correspond to the effect produced by the real Moho. Under these assumptions, the pronounced local maximum of 1.3 m of the geoid residuals above the North Aegean Trough predicts a mass excess associated with a Moho uplift in this area. Another strong indicator for a significant regional uplift of the Moho at the North Aegean Trough is given by the reduced gravity anomalies, showing positive values between 60 and 100 mGal expanding above the complete part of North Aegean Trough covered by the shipborne surveys (Fig. 12.19b).

12.5.4 Topography-Bathymetry-Sediments-Moho Cogeoid

In a third step, marine geoid heights from shipborne laser altimetry (Fig. 12.1a) were reduced for the effects of topography, bathymetry, sediments and ESC Moho (Fig. 12.15a). The reduced geoid heights correspond to the topography-bathymetry-sediments-Moho cogeoid. After the removal of a constant offset, the reduced geoid heights range between -4.0 and 2.5 m, with a strong positive gradient in north direction across the entire survey area. The strong gradient makes an interpretation of the topography-bathymetry-sediments-Moho cogeoid impossible. Hence, another reduction was carried out below, using isostatic Moho depths.

12.5.5 Topography-Bathymetry-Sediments-Isostasy Cogeoid

In a final step, marine geoid heights from shipborne altimetry (Fig. 12.1a) were reduced for the effects of topography, bathymetry, sediments and isostatic Moho (Fig. 12.16a). The reduced geoid heights correspond to the topography-bathymetry-sediments-isostasy cogeoid. After the removal of a constant offset, the reduced geoid heights range between -1.5 and 1.0 m (Fig. 12.21a). The strong negative gradient in north-west direction, observed in Fig. 12.19a has disappeared, indicating that it can be explained by the effect of the isostatic Moho. A negative gradient in south-west direction appears instead. The origin of this gradient can be the large mass deficiencies in the Ionian Sea, associated with the Mediterranean Ridge, which are only partly considered within the area of influence. A second hypothetic origin would be an anomalous Moho discontinuity in the survey area, with an inclination of the Moho in south-west direction with respect to the Moho modeled by isostatic compensation.

The reduced geoid heights (Fig. 12.21a) also show that the predominant geoid depression of about 1.5 m at the western end of the North Aegean Trough was completely elimiated by the reduction. Hence, the geoid depression can be completely explained by the effects of the considered masses. On the other hand, the reduced geoid heights show a local maximum of 1 m at the North Aegean Trough in the north-eastern part of the survey area (Fig. 12.21a). Thus, the actual geoid anomaly in the survey area is not the depression at the western end of the North Aegean Trough but the anomalously high geoid observed over the North Aegean Trough in the north-eastern part of the survey area (Fig. 12.1a). This maximum is associated with positive reduced gravity anomalies, between 40 and 60 mGal (Fig. 12.21b). The positive local anomaly is caused by a local mass excess not considered in the mass model. The reduced geoid heights and gravity anomalies do not allow to draw a conclusion whether the anomaly is caused by an anomalously dense crust, an overestimated sediment effect or an anomalously high Moho. For example, the positive reduced gravity anomalies in the order of 40 mGal would approximately correspond to a hypothetical local upwelling of the Moho by 4 km with respect to the isostatic Moho, yielding a theoretical local Moho depth of about 22 km in that area. The local anomaly is correlated with the position of the epicenters of two recent strike-slip earthquakes of magnitude 6.9 and 5.4, in 1982 and 1992, respectively (McNeill et al., 2004). Furthermore, the anomaly lies on the northern fault bounding the North Aegean Trough. The area is identified as a major strike-slip boundary, characterized by high seismicity, separating the Anatolia-Aegean plate from Eurasia (McNeill et al., 2004). It is accompanied with dextral

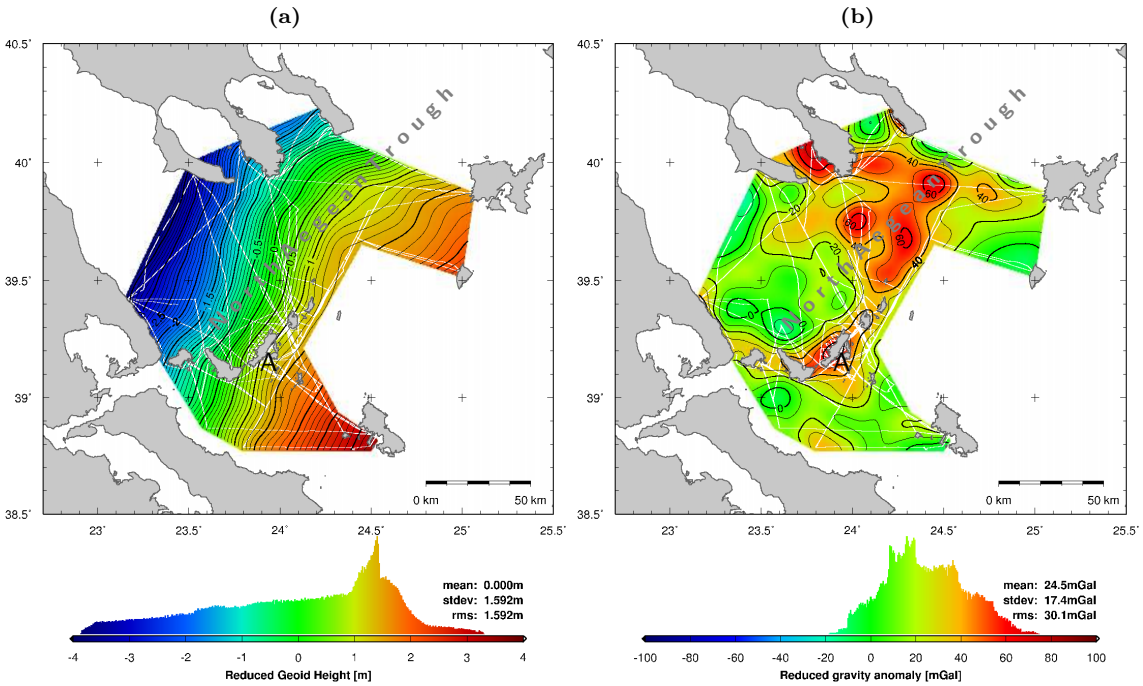

Figure 12.18: **(a)** Geoid heights from shipborne altimetry (Fig. 12.1a) reduced for effects of topography and bathymetry (Fig. 12.9a), with mean offset removed. **(b)** Associated gravity anomalies from reduction of Fig. 12.1b with Fig. 12.9b. Contour intervals: 0.1 m and 10 mGal. (A = Alonnisos).

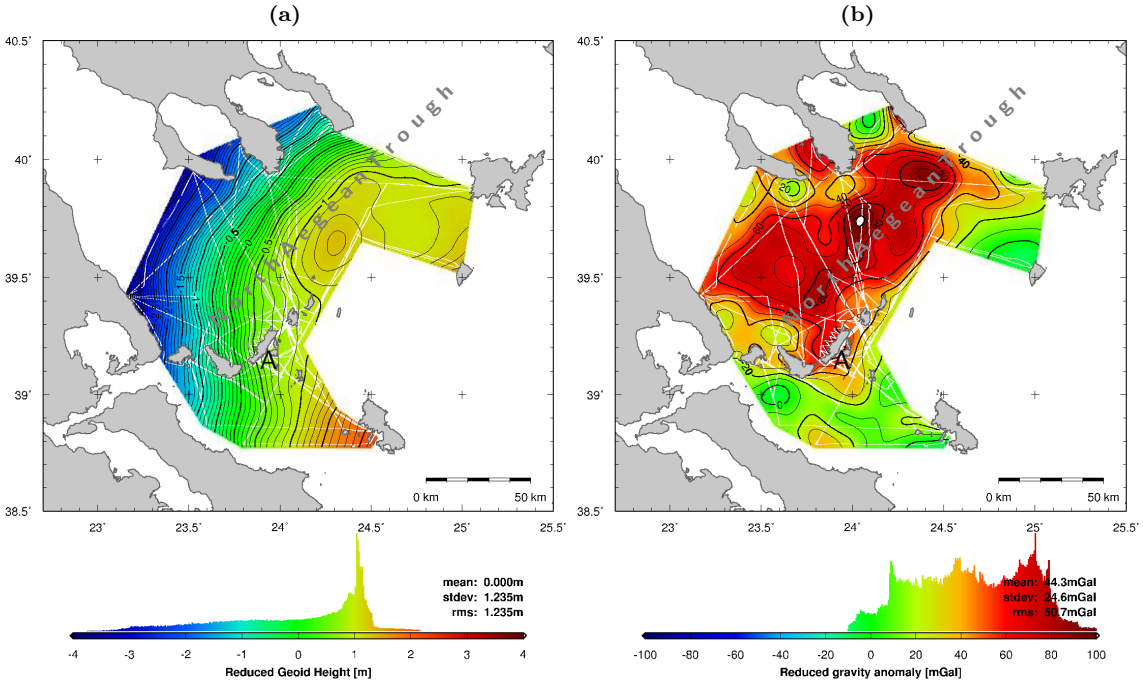

Figure 12.19: **(a)** Geoid heights from shipborne altimetry (Fig. 12.1a) reduced for effects of topography, bathymetry and sediments (Fig. 12.14a), with mean offset removed. **(b)** Associated gravity anomalies from reduction of Fig. 12.1b with Fig. 12.14b. Contour intervals: 0.1 m and 10 mGal. (A = Alonnisos).

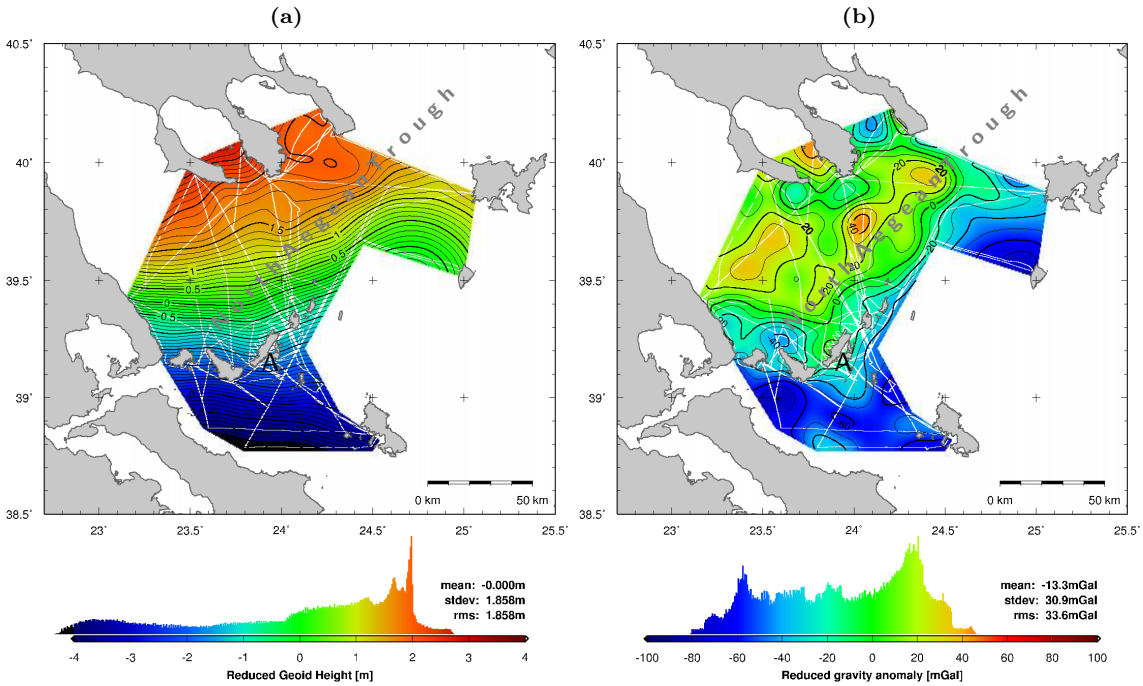

Figure 12.20: **(a)** Geoid heights from shipborne altimetry (Fig. 12.1a) reduced for effects of topography, bathymetry, sediments and ESC Moho (Fig. 12.15a), with mean offset removed. **(b)** Associated gravity anomalies from reduction of Fig. 12.1b with Fig. 12.15b. Contour intervals: 0.1 m and 10 mGal.

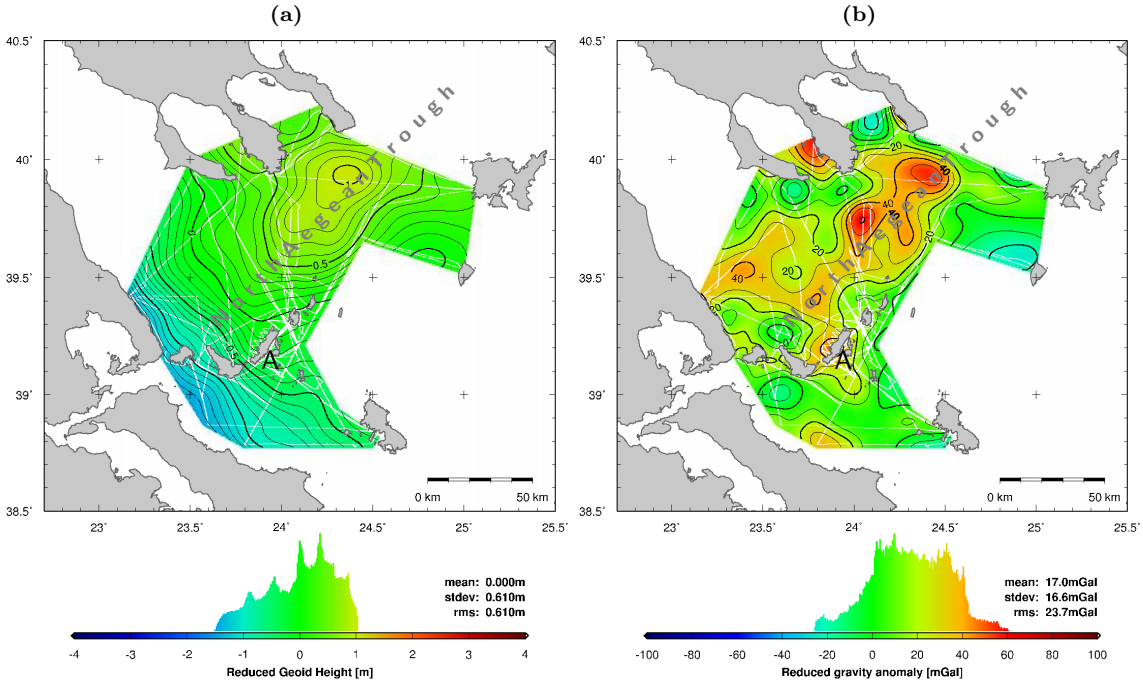

Figure 12.21: **(a)** Geoid heights from shipborne altimetry (Fig. 12.1a) reduced for effects of topography, bathymetry, sediments and isostatic Moho (Fig. 12.16a), with mean offset removed. **(b)** Associated gravity anomalies from reduction of Fig. 12.1b with Fig. 12.16b. Contour intervals: 0.1 m and 10 mGal.

shear strain rates, combined with normal extension and isolated normal compression (Fig. 1.6) (Hollenstein, 2006). These considerations indicate that the observed geoid and gravity anomalies are caused by an anomalous upwelling of dense material linked to the geodynamic system of the North Aegean Trough.

13 Summary and Conclusions

The method of airborne laser altimetry was successfully developed and deployed for precise high-resolution ellipsoidal sea surface height determination in the area of western Crete. Since airborne laser altimetry is very cost-intensive, a major aim of this thesis was the development of an alternative method for precise local-scale sea surface topography determination. A novel method of shipborne sea surface height measurements was developed in the framework of this project. The method relies on one or two low-cost industrial ultrasonic distance sensors mounted on a boat, providing continuous measurements of the distance to the sea surface, in combination with a multi-antenna GPS system and a low-cost inertial measurement unit for position and attitude determination. Due to its analogy to airborne laser altimetry, the method is called shipborne ultrasound altimetry. The successful implementation of the new technique during several survey campaigns proved that shipborne ultrasound altimetry is a powerful method for providing offshore sea surface height measurements, even under rough sea conditions. Hence, the method provides a low-cost alternative to airborne laser altimetry. In this work, the scientific potential of both airborne laser altimetry and shipborne ultrasound altimetry for precise sea surface height determination in local areas was demonstrated. The results were more than satisfying in terms of accuracy and repeatability, leading to high-resolution local sea surface topography solutions at sub-decimeter level, with some limitations stated below. In order to achieve best possible accuracies, a wide range of processing algorithms and corrections needs to be applied. On the instrumental level, they include precise kinematic GPS positioning, precise attitude retrieval and boresight misalignment. On the sea surface level, they include ocean waves, tides, atmospheric pressure forcing (inverse barometer) and high frequency response to wind forcing.

Differential kinematic GPS positions of the survey aircraft and boat were obtained at a vertical accuracy of better than 5 cm, even for baseline lengths of more than 100 km. However, it was seen in the airborne surveys that the vertical accuracy can be considerably degraded up to a level of 30 cm in case of extremely inhomogeneous atmospheric conditions. In this case, the inaccuracy of the corrections for tropospheric refraction and their impact on GPS height determination were found to be the limiting factor for the accuracy of the final sea surface topography by airborne laser altimetry. Based on these conclusions, investigations were made to assess the kinematic potential of Bernese GPS Software version 5 and its capabilities to estimate tropospheric path delays in kinematic mode. The existing source code had to be adapted to the estimation of path delays in kinematic mode. Results similar to the classic solution with path delays predicted from an a priori model were obtained under homogeneous atmospheric conditions. Under extreme tropospheric conditions, differences between the two solutions could easily reach 0.5 m. The analysis showed that under such conditions, the Bernese solution including the estimation of tropospheric path delays was extremely sensitive to tropospheric parameter settings. The instability of the solution led to the conclusion that the algorithms used to model the troposphere are not sophisticated enough to provide a realistic representation of extreme inhomogeneous atmospheric conditions (e.g. atmospheric inversion) in kinematic mode. In order to improve the accuracy of kinematic GPS positioning, and hence of the deduced sea surface heights, further research on modeling tropospheric influences under kinematic conditions is needed.

Attitude determination using a multi-antenna GPS array produced reliable data for both the survey-aircraft and sailing yacht. The excellent performance of the multi-antenna GPS attitude determination was demonstrated by comparing the solutions with the data of a high-precision INS platform coupled with GPS, operated simultaneously aboard the aircraft. Comparisons showed

a very good correlation between the attitude data provided by the two systems, with standard deviations in the order of 0.11° for the roll and pitch, and 0.06° for the yaw. The accuracy of attitudes derived from the multi-antenna GPS array was estimated to be in the order of 0.1° given the antenna configurations used. This value was found to meet the accuracy requirement established for the airborne and shipborne altimetry applications. The accuracy obtained would further enable the use of the multi-antenna GPS method for attitude determination in a wide range of airborne and shipborne applications, as well as in other applications where a high sampling rate is not required and where good GPS satellite visibility is warranted.

The boresight misalignment calibration method for airborne laser altimetry developed in this thesis is a truly self-calibrating technique, in the sense that the calibration exclusively relies on the sea surface height observations themselves. There is no need for overflying specially selected calibration surfaces. Additionally, the method relies directly on subsequent measurements within the same flight-line, with no need for overflying the same area more than once. Furthermore, the calibration algorithm is completely independent of any a priori information about the relief of the measured water surface, like e.g. geoid heights. It is applicable for both airborne laser scanners and profilers. The calibration method allowed to estimate boresight misalignment angles with an accuracy better than 0.1°, corresponding to the expected order of magnitude of boresight misalignment variations during flight operations, as well as to the estimated attitude accuracy. The boresight misalignment calibration allowed to mitigate systematic ground-point height errors of up to 10 cm, due to a systematic aerodynamic pitch of the aircraft. Due to the small ranges of less than 3 m in shipborne ultrasound altimetry, and the comparably large size of the footprint, there was no need for boresight misalignment calibration in shipborne ultrasound altimetry.

Various ocean tide models, including FES2004 and POL (Proudman Oceanographic Laboratory) (Tsimplis et al., 1995), as well as local tide-gauge data, were analyzed for the correction of ocean tides. A significant contradiction among the models was observed in the considered areas around western Crete and in the North Aegean Sea. Around Crete, differences of up to 3 cm were observed between the models, as well as with respect to local tide-gauge data. Since tidal amplitudes in the area are only in the order of 2.5 cm, the disagreement is significant. However, considering the small size of the encountered tidal amplitudes and of the differences between the models, the choice of the tide model is not crucial for the accuracy of the corrected sea surface heights. In the North Aegean Sea, tidal amplitudes are in the order of 15-20 cm, making the choice of the tidal model important. Significant differences of up to 20 cm were observed between the predictions of the global FES2004 model and the POL model. A validation with local tide-gauge data revealed large differences of up to 25 cm with respect to FES2004, while the differences with respect to the POL model were below 8 cm. The remaining residuals of the tide-gauge observations with respect to the POL model are most likely due to local coastal effects, not resolved by the tidal and atmospheric forcing model. It can be assumed that the model would perform better offshore, in the absence of strong and hardly predictable coastal effects. Despite the fact that only 4 short-period tidal constituents are included in the POL model (against 9 constituants for FES2004), the POL predictions are in better agreement with local tide-gauge observations than FES2004 predictions. Furthermore, the POL model showed a better agreement with the shipborne data, since it allowed to reduce the RMS on the height differences at crosspoints by 4.8 cm and the maximum absolute difference by 8.0 cm. Applying tidal corrections directly from tide-gauge data produced a slightly worse agreement with the shipborne data, due to the fact that tide-gauge data are affected by local coastal effects. The harmonic analysis of local tide-gauge observations allowed to show that the poor predictions of FES2004 in the North Aegean Sea are related to bad phase lag of most of the tidal constituents FES2004 in this area, probably linked to a lack of Aegean tide-gauge data in the assimilation.

Corrections of sea surface heights for atmospheric pressure and wind forcing were applied using MOG2D dynamic atmospheric corrections. Corrections between -16 and 12 cm were obtained by the model for the considered times and locations of the surveys. The MOG2D corrections allowed to reduce the RMS of height differences at crosspoints by 2.0 cm and the maximum absolute difference

by 7.7 cm. Furthermore, they produced a significant improvement of the observed sea surface heights, as compared to a classical inverse barometer correction computed using ECMWF pressure data. Sea level anomalies obtained from spaceborne radar altimetry were applied as additional correction to the airborne and shipborne observations. The beneficial effect of this correction, especially for the shipborne data collected over five years, was also demonstrated by the crosspoint analysis: the RMS on the height differences was reduced by 3.8 cm and the maximum absolute difference by 8.6 cm. This clearly reveals the good compatibility of the airborne and shipborne observations with spaceborne radar altimetry data.

The accuracy and repeatability of the airborne and shipborne altimetry methods were estimated by analyzing height differences at crosspoints using the best-available combination of sea surface height corrections described above. The height differences at 102 crosspoints of the airborne campaign showed an RMS of 8.6 cm, while the five shipborne campaigns yielded a total of 1999 crosspoints, with an RMS of 7.9 cm. After an LSQ adjustment of the height profiles based on the differences at crosspoints, the RMS values were further reduced to 4.5 and 4.3 cm, respectively. A standard deviation of only 3.1 cm was obtained for the residuals between the sea surface height profiles from airborne laser altimetry and the derived gridded and filtered sea surface topography. After an outlier removal based on the residuals, this standard deviation was reduced to 2.9 cm. The same procedure was applied to the shipborne data, yielding a standard deviation of 4.7 cm before and 3.4 cm after the outlier removal. The differences of less than 1 cm of the standard deviations and RMS values between the airborne and shipborne methods stated above have shown that the performance of both methods is very similar in terms of repeatability. Furthermore, the low standard deviation and RMS values obtained for the residuals and height differences at crosspoints underline the good inner accuracy and repeatability of the two methods. It has to be noted that the actual instrumental accuracy of the two methods is better than the RMS and standard deviation values stated above, since these values are not only affected by instrumental errors but also by residual errors in the geophysical sea surface correction models. In order to further asses the accuracy of the method, calibration measurements of the airborne laser altimetry system with GPS-buoy observations were performed in calm nearshore conditions, as well as in harsh offshore conditions with significant wave heights of 1 m. The calibration provided excellent results, with buoy and laser sea surface height measurements fitting better than 5 cm.

In order to validate sea surface height products from spaceborne radar altimetry missions, the local sea surface topographies obtained by airborne and shipborne altimetry were compared to the CLS01 and DNSC08 mean sea surfaces (MSS) CLS01 and DNSC08 derived from multi-mission radar altimetry. The residuals between the sea surface topography from airborne laser altimetry around Crete and both CLS01 and DNSC08 show an overall good agreement with standard deviations of around 8 cm. However, high residuals of up to 50 cm are observed in a belt of 20 km around the coast of Crete, where the strongest geoid gradients of the entire survey area occur, reaching impressive 0.21 m/km. In these coastal regions, CLS01 and DNSC08 sea surface heights are interpolated due to a lack of satellite radar altimetry data. Since the coastline was not systematically covered by airborne laser altimetry, uncertainties also remain in the airborne sea surface topography regarding these areas. The residuals between the sea surface topography from shipborne altimetry and both CLS01 and DNSC08 show an overall good agreement with standard deviations around 6 cm. The overall agreement of CLS01 and DNSC08 with the shipborne data in the North Aegean Sea is thus slightly better than with the airborne data around Crete. However, this is not necessarily a consequence of a better accuracy of the shipborne data, but rather related to the extreme sea surface height gradients encountered around Crete. Theoretically, the CLSO1 and DNSC08 resolve wavelengths down to 10-20 km. The good agreement with the MSS from CLSO1 and DNSC08 also allowed to assess the good accuracy and resolution of the sea surface topographies determined by airborne and shipborne altimetry.

Comparisons between airborne laser altimetry and nearly-simultaneous Jason-1 radar altimeter data along a dedicated profile of more than 100 km revealed variations of the height difference in the order of 0.1 m, in accordance with the accuracy of the airborne technique. Differences of up to

0.65 cm were observed near the coast, due to the lack of Jason-1 data. This underlines the need for satellite-independent methods like airborne laser altimetry to cover coastal regions. Additional comparisons were made between significant wave heights derived from airborne laser altimetry and from Jason-1 GDR data along the dedicated profile. An excellent agreement of better than 20 cm was obtained using Jason-1 Ku-band data.

Two local high resolution marine geoid solutions were derived from the sea surface heights observed by airborne and shipborne altimetry, by subtraction of the RioMed mean dynamic ocean topography. In addition, geoid gradients, deflections of the vertical and gravity anomalies were derived from the altimetric geoid heights.

The high accuracy of the two altimetric geoid solutions was demonstrated by comparison with solution from the global gravity models EGM96, EGM2008, EIGEN-5S and EIGEN-5C. The resolution of the two local altimetric geoid solutions was found to be significantly higher than the resolution of existing geoid models with a spherical harmonics expansion limited to degree and order 360 (EGM96, EIGEN-5C). The resolution of these models corresponds to approx. 55 km. Residuals between the two altimetric geoids and these models were found to have standard deviations of 0.37-0.40 m and maximum values of 1.5 m. It was shown that the resolution of these models is mainly limited by their mathematical expansion of spherical harmonics. Comparisons with the EIGEN-5S model, limited to degree and order 150, yielded even higher residuals, with standard deviations as high as 0.81 m and maximum values over 1.5 m.

Comparisons between the two local altimetric geoids and the recently released EGM2008 revealed very low residuals, with standard deviations of 0.08 and 0.11 m. Additional comparisons with the local gravimetric geoid model AUTH2008 (Tziavos and Andritsanos, 1999; Vergos et al., 2004; Grigoriadis, 2009) produced similar standard deviations of 0.15 and 0.10 m. Hence, all four geoid solutions have similar resolutions. The EGM2008 is expanded to degree 2190 and order 2159, corresponding to a spatial resolution of approximately 10 km. It is presumed that the geoid signal at wavelength below 10 km has amplitudes smaller than 0.1 m. The original sea surface height observations have a resolution between 0.1 m and a few meters along-track. However, the short-wavelength information contained in the observations is degraded by instrumental system noise and residual errors in geophysical corrections (tides, inverse barometer) of the same order of magnitude as the geoid signal at these wavelength. Hence, the high-frequency geoid signal cannot be separated from the noise. In order to eliminate the noise and avoid associated unrealistic high-frequency variations in the geoid heights, the sea surface height data has to be low-pass filtered with cut-off wavelengths around 10 km, similar to the resolution of EGM2008. In order to obtain reliable observations of higher-frequency geoid signals by airborne or shipborne altimetry, both system noise and geophysical corrections need to be improved.

From an oceanographic perspective, the primary purpose of sea surface height observations is the determination of the dynamic ocean topography induced by ocean currents. Attempts were carried out to determine the mean dynamic topography (MDT) by subtracting geoid heights from sea surface height observations (direct method). Among the geoid models used in this study, the satellite-only solution EIGEN-5S and the local gravimetric model AUTH2008 are the only geoid solution that are independent of altimetric sea surface height data. Hence, they would be the only appropriate models for MDT determination using the direct method. Due to the large residuals caused by its low resolution of approx. 130 km, satellite-only models like the EIGEN-5S are unusable for realistic MDT determination at wavelengths below 130 km. In closed seas with complex basin structures, like the Mediterranean, as well as in coastal areas, the resolution of scales shorter than 130 km is crucial for the determination of complex local-scale circulation. It can be expected that shorter scales of the Earth's marine gravity field, independent from sea surface heights, will be provided by the GOCE mission, scheduled in 2009. GOCE aims to provide geoid heights with cm precision at a resolution better than 100 km, constituting a major improvement of dynamic ocean topography determination and circulation studies. Hypothetic MDT were nevertheless computed from the residual fields of the sea surface heights from airborne and shipborne altimetry with re-

spect to EGM2008 and AUTH2008 geoid heights. Geostrophic circulation fields derived from the hypothetic MDT are unrealistic and spoiled by noisy eddies. Hence, it was not possible to derive a realistic circulation pattern based on the sea surface height observations and the used geoid models. The major reason lies in the fact that the presumed MDT only varies within a range below 10 cm in both survey areas. Furthermore, the gradients of the MDT associated with the circulation are below 1 cm/10 km. Hence, the MDT signal in these survey areas is in the same order of magnitude as the accuracy of the airborne and shipborne sea surface heights and the used geoid models. It can be concluded that the sea surface height observations by airborne and shipborne altimetry and the considered geoid models are not accurate enough to resolve such small dynamic effects. In addition, EGM2008 is not independent of altimetric sea surface height data.

For a final geophysical analysis and interpretation of the altimetric geoid solutions, mass effects on the gravity potential, geoid heights and gravity anomalies were modeled. Masses from topography, bathymetry, marine sedimentary deposits and crust/mantle boundary (Moho) depths, were considered in the modeling. It was shown that major geoid features can be explained to a large extent by the above-mentioned mass effects. On the other hand, the mass reduction allowed to identify distinct gravity anomalies related to mass anomalies with respect to the modeled masses.

South of Crete, the predominant negative geoid gradient towards the Mediterranean Ridge, reaching impressive 0.22 m/km and characterizing the entire region, was completely reduced by the modeled mass effects, dominated by deep water (down to -4000 m) and extremely thick sediment deposits of up to 10 km. On the other hand, a strong positive gradient of the mass-reduced geoid heights appears north of Crete, with 0.1 m/km in north direction. The geoid anomaly and related gravity anomaly indicate a significant mass excess north of Crete, beyond the survey area. The mass anomaly is most likely linked to the collision between the Eurasian and African lithospheric plates characterizing the region. Density models based on seismic soundings in the area of the Hellenic subduction zone and the Hellenic Trench are indicating an upwelling of the European mantle north of Crete, related to the subduction of the African oceanic lithosphere beneath the Eurasian continental lithosphere (Snopek et al., 2007; Makris and Yegorova, 2006; Casten and Snopek, 2006) and causing a significant positive mass anomaly.

Concerning the survey area of the North Aegean Sea, it was shown that the predominant geoid depression at the western end of the North Aegean Trough can be completely explained by mass effects caused by topography, bathymetry and sediment deposits. On the other hand, a widely-spread maximum of the mass-reduced geoid heights was observed south of Athos, reaching 1 m. This positive local anomaly indicates the presence of a local mass excess. The reduced geoid heights do not allow to draw a conclusion whether the anomaly is caused by an anomalously dense crust, an overestimated sediment effect or an anomalously high Moho. However, the local anomaly is correlated with the location of the epicenters of two recent strike-slip earthquakes of magnitude 6.9 and 5.4, in 1982 and 1992, respectively (McNeill et al., 2004). Furthermore, the anomaly lies on the northern fault bounding the North Aegean Trough. The area is identified as a major strike-slip boundary, characterized by high seismicity, separating the Anatolia-Aegean plate from Eurasia (McNeill et al., 2004). It is accompanied with dextral shear strain rates, combined with normal extension and isolated normal compression (Fig. 1.6) (Hollenstein, 2006). These considerations indicate that the observed geoid and gravity anomalies are caused by an anomalous upwelling of dense material linked to the geodynamic system of the North Aegean Trough.

Preliminary attempts to geophysically interpret the obtained gravity field information based on mass modeling and mass reduction showed very promising results and allowed to detect local mass anomalies. A future step in this direction would consist in a detailed and stringent geophysical interpretation of the obtained gravity field results, based on a thorough investigation of existing density models and the application of advanced inversion algorithms. With the inversion of the obtained local geoid heights, models of mass distribution could be further constrained, helping to better understand the dynamics of Hellenic subduction zone and the westward continuation of the North-Anatolian Fault Zone.

Bibliography

Andersen, O. B. and Knudsen, P. (2008). The DNSC08 global Mean Sea Surface. Presentation at EGU-2008, Vienna, Austria, April, 2008.

Andersen, O. B., Knudsen, P., Toohey, J., Kenyon, S., and Pavlis, N. (2007). A new mean sea surface DNSC07. Poster at OSTST 2007.

AVISO (1996). *AVISO User Handbook for Merged TOPEX/POSEIDON Products*. AVI-NT-02-101, Edition 3.0.

AVISO (2008). *SSALTO/DUACS User Handbook: (M)SLA and (M)ADT Near-Real Time and Delayed Time Products*. CLS-DOS-NT-06.034, SALP-MU-P-EA-21065-CLS.

Barrell, H. (1951). The dispersion of air between 2500a and 6500a. *JOSA*, 41:295–299.

Barrell, H. and Sears, J. E. (1939). The refraction and dispersion of air for the visible spectrum. *Philosophical Transactions of the Royal Society of London*, A 238:1–64.

Baumann, H. (2003). *Absolute Airborne Gravimetry*. PhD thesis, ETH Zurich.

Becker, M., Zerbini, S., Baker, T., Bürki, B., Galanis, J., Garate, J., Georgiev, I., Kahle, H.-G., Kotzev, V., Lobazov, V., Marson, I., Negusini, M., Richter, B., Veis, G., and Yuzefovich, P. (2002). Assessment of height variations by GPS at Mediterranean and Black Sea coast tide gauges from the SELF projects. *Global and Planetary Change*, 34(1-2):5–35.

Beutler, G., Bock, H., Dach, R., Fridez, P., Gnäde, A., Hugentobler, U., Jäggi, A., Meind, M., Mervart, L., L.Prange, Schaer, S., Springer, T., Urschl, C., and Walser, P. (2007). Bernese GPS Software Version 5.0, edited by R. Dach, U. Hugentobler, P. Fridez and M. Meindl. Astronomical Institute, University of Berne.

Birch, K. P. and Downs, M. J. (1993). An updated Edlén equation for the refractive index of air. *Metrologia*, 30:155–162.

Birch, K. P. and Downs, M. J. (1994). Correction to the updated Edlén equation for the refractive index of air. *Metrologia*, 31:315–316.

Bonnefond, P., Exertier, P., Laurain, O., Ménard, Y., Orsini, A., Jan, G., and Jeansou, E. (2003). Absolute Calibration of Jason-1 and TOPEX/Poseidon Altimeters in Corsica. *Marine Geodesy*, 26(3-4):261–284.

Bufton, J. L., Hoge, F. E., and Swift, R. N. (1983). Airborne measurements of laser backscatter from the ocean surface. *Applied Optics*, 22(17):2603–2618.

Carrère, L. and Lyard, F. (2003). Modeling the barotropic response of the global ocean to atmospheric wind and pressure forcing - comparisons with observations. *Geophys. Res. Let.*, 30(6):1275.

Casten, U. and Snopek, K. (2006). Gravity modelling of the Hellenic subduction zone - a regional study. *Tectonophysics*, 417:183–200.

Chelton, D. B. (1988). WOCE/NASA Altimeter Algorithm Workshop. Technical Report No. 2, U.S. Planning Office for WOCE (World Ocean Circulation Experiment), College Station, TX.

Chelton, D. B., Ries, J. C., Haines, B. J., Fu, L.-L., and Callahan, P. S. (2001). *Satellite Altimetry and Earth Sciences*, chapter Satellite Altimetry, pages 1–131. Academic Press.

Ciddor, P. E. (1996). Refractive index of air: New equations for the visible and near infrared. *Applied Optics*, 35:1566–1573.

Ciddor, P. E. and Hill, R. J. (1999). Refractive index of air. 2. group index. *Applied Optics*, 38:1663–1667.

Cocard, M. (1995). *High Precision GPS Processing in kinematic mode.*, volume 52 of *Geodätisch-geophysikalische Arbeiten in der Schweiz*. Schweizerische Geodätische Kommission (ed.). 139 p.

Cocard, M., Geiger, A., Kahle, H.-G., and Veis, G. (2002). Airborne laser altimetry in the Ionian Sea, Greece. *Global and Planetary Change*, 34(1-2):87–96.

Coulson, C. A. and Jeffrey, A. (1977). *Waves*. Longman Mathematical Texts.

Cox, C. and Munk, W. (1954). Measurement of the roughness of the sea surface from photographs of the sun's glitter. *Journal of the Optical Society of America*, 44(11):838–850.

Dobslaw, H. (2007). Modellierung der allgemeinen ozeanischen Dynamik zur Korrektur und Interpretation von Satellitendaten. Technical Report STR07/10, GeoForschungsZentrum Potsdam, Germany.

Dodson, A., Shardlow, P., Hubbard, L., Elgered, G., and Jarlemark, P. (1996). Wet tropospheric effects on precise relative GPS height determination. *Journal of Geodesy*, 70:188–202.

Dorandeu, J. and Le Traon, P. Y. (1999). Effects of Global Mean Atmospheric Pressure Variations on Mean Sea Level Changes from TOPEX/Poseidon. *Journal of Atmospheric and Oceanic Technology, American Meteorological Society*, 16(9):1279–1283.

Edlén, B. (1966). The refractive index of air. *Metrologia*, 2:71–80.

Ekman, M. (1989). Impacts of Geodynamic Phenomena on Systems for Height and Gravity. *Bulletin Geodesique*, 63(3):281–296.

Favey, E. (2001). *Investigation and Improvement of Airborne Laser Scanning Technique for Monitoring Surface Elevation Changes of Glaciers*. PhD thesis, ETH Zurich.

Favey, E. and Schlatter, A. (1998). Geoidbestimmung am Lac Léman. Technical Report 282, Institut of Geodesy and Photogrammetry, ETH Zurich. 130 p.

Favey, E., Wehr, A., Geiger, A., and Kahle, H. G. (2002). Some examples of european activities in airborne laser techniques and an application in glaciology. *Journal of Geodynamics*, 34(3-4):347 – 355.

Fenoglio-Marc, L., Kusche, J., and Becker, M. (2006). Mass variation in the Mediterranean Sea from GRACE and its validation by altimetry, steric and hydrologic fields. *Geophys. Res. Lett.*, 33(L19606).

Foerste, C., Flechtner, F., Schmidt, R., Stubenvoll, R., Rothacher, M., Kusche, J., Neumayer, K.-H., Biancale, R., Lemoine, J.-M., Barthelmes, F., Bruinsma, J., Koenig, R., and Meyer, U. (2008). EIGEN-GL05C - A new global combined high-resolution GRACE-based gravity field model of the GFZ-GRGS cooperation. *General Assembly European Geosciences Union (Vienna, Austria 2008), Geophysical Research Abstracts*, 10(EGU2008-A-06944).

Fu, L.-L. and Chelton, D. B. (2001). *Satellite Altimetry and Earth Sciences*, chapter Large Scale Ocean Circulation, pages 133–169. Academic Press.

Geiger, A. (1987). Einfluss richtungsabhängiger Fehler bei Satellitenmessungen. Technical Report 130, Institute of Geodesy and Photogrammetry, ETHZ, Zürich. 40 p.

Geiger, A., Cocard, M., Peter, Y., and Kahle, H.-G. (1994). Precise DGPS and self calibrating laser altimetry for airborne marine geoid determination and detection of glacial fluctuation. In *Proceedings of 7th International Technical Meeting of The Satellite Division of The Institute of Navigation (ION), Salt Lake City, Utah, September 20-23*, pages 471–476.

Giacomo, P. (1982). Equation for the determination of the density of moist air. *Metrologia*, 18:33–40.

Gordon, H. R. (1977). One parameter characterization of the ocean's inherent optical properties from remote sensing. *Applied Optics*, 16(10):2627.

Goto, T., Miyakura, J., Umeda, K., Kadowaki, S., and Yanagi, K. (2005). A Robust Spline Filter on the basis of L2-norm. *Precision Engineering*, 29(2):157 – 161.

Grad, M., Tiira, T., and Group, E. W. (2009). IThe Moho depth map of the European Plate. *Geophys. J. Int.*, 176:279–292.

Grigoriadis, V. N. (2009). *Geodetic and geophysical approximation of the Earth's gravity field and applications in the Hellenic area*. PhD thesis, Aristotle University of Thessaloniki (AUTH), Department of Geodesy and Surveying, Greece.

Haines, B. J., Dong, D., Born, G. H., and Gill, S. K. (2003). The Harvest Experiment: Monitoring Jason-1 and TOPEX/Poseidon from a California Offshore Platform. *Marine Geodesy*, 26(3-4):239–259.

Hamad, N., Millot, C., and Taupier-Letage, I. (2005). A new hypothesis about the surface circulation in the eastern basin of the Mediterranean Sea. *Progress In Oceanography*, 66(2-4):287 – 298. Mediterranean physical oceanography and biogeochemical cycles: Mediterranean general circulation and climate variability.

Heiskanen, W. A. and Moritz, H. (1967). *Physical Geodesy*. W. H. Freeman and Company, San Fransisco.

Hernandez, F. and Schaeffer, P. (2000). Altimetric Mean Sea Surfaces and Gravity Anomaly maps inter-comparisons. Technical Report AVI-NT-011-5242-CLS, CLS, Ramonville St Agne.

Hernandez, F. and Schaeffer, P. (2001). The CLS01 Mean Sea Surface: A validation with the GSFC00.1 surface.

Hernla, M. (2000). Anwendung von Filtern bei der Auswertung gemessener Oberflächenprofile. *tm Technisches Messen, München*, 67(3):128–135.

Hofmann-Wellenhof, B. and Moritz, H. (2006). *Physical Geodesy*. Springer, Wien, New York, 2nd edition.

Hollenstein, C. (2006). *GPS deformation field and geodynamic implications for the Hellenic plate boundary region*. PhD thesis, ETH Zurich.

Hooper, W. P. and Gerber, A. (1983). Monte Carlo simulations of laser-generated sea surface aureole. *Applied Optics*, 27(24):2603–2618.

Hopfield, H. S. (1979). Improvements in the tropospheric refraction correction for range measurements. *Philosophical Transactions of the Royal Society of London*, A 294:341–352.

IUGG (1999). Resolution 3 of the International Association of Geodesy. Comptes Rendus of the XXII General Assembly. International Union of Geodesy and Geophysics (IUGG), 19–30 July 1999, Birmingham, 110–111.

Kahle, H.-G., Cocard, M., Peter, Y., Geiger, A., Reilinger, R., Barka, A., and Veis, G. (2000). GPS-derived strain rate field within the boundary zones of the Eurasian, African, and Arabian plates. *J. Geophys. Res.*, 105(B10):23353–23370.

Kahle, H.-G., Cocard, M., Peter, Y., Geiger, A., Reilinger, R., McClusky, S., King, R., Barka, A., and Veis, G. (1999). The GPS strain rate field in the Aegean Sea and western Anatolia. *Geophys. Res. Let.*, 26(16):2513–2516.

Kahle, H.-G. and Mueller, S. (1998). Structure and dynamics of the Eurasian-African/Arabian plate boundary system: Objectives, tasks and resources of the WEGENER group. *Journal of Geodynamics*, 25(3-4):303 – 325. WEGENER: Scientific Objectives and Methodological Challenges for the Application of Space-Geodetic Techniques to Earth Sciences.

Kayton, M. and Fried, W. R. (1997). *Avionics Navigation Systems*. John Wiley & Sons, Inc., 2nd edition.

Kourafalou, V. and Tsiaras, K. (2007). A nested circulation model for the North Aegean Sea. *Ocean Science*, 3(1):1–16.

Le Provost, C. (2001). *Satellite Altimetry and Earth Sciences*, chapter Ocean Tides, pages 267–303. Academic Press.

Le Traon, P. Y. and Morrow, R. (2001). *Satellite Altimetry and Earth Sciences*, chapter Ocean Currents and Eddies, pages 171–215. Academic Press.

Lemoine, F. G., Kenyon, S. C., Factor, J. K., Trimmer, R., Pavlis, N. K., Chinn, D. S., Cox, C. M., Klosko, S. M., Luthcke, S. B., Torrence, M. H., Wang, Y. M., Williamson, R. G., Pavlis, E. C., Rapp, R. H., and Olson, T. R. (1998). The Development of the Joint NASA GSFC and NIMA Geopotential Model EGM96. Technical Report NASA-TP-1998-206861, NASA Goddard Space Flight Center, Greenbelt, Maryland, USA.

Letellier, T. (2004). *Etudes des ondes de marée sur les plateaux continentaux*. PhD thesis, Université Paul Sabatier (Toulouse III, France.

Lighthill, J. (1978). *Waves in Fluids*. Cambridge University Press.

Luthcke, S., Blair, B., and Ekholm, S. (2002). Special issue on laser altimetry. *Journal of Geodynamics*, 34(3-4):343–594.

Lyard, F., Lefèvre, F., Letellier, T., and Francis, O. (2006). Modeling the global ocean tides: a modern insight from FES2004. *Ocean Dynamics*, 56:394–415.

Lynch, D. R. and Gray, W. G. (1979). A wave equation model for finite element tidal computations. *Computers and Fluids*, 7:207–228.

Mader, K. (1951). *Das Newtonsche Raumpotential prismatischer Körper und seine Ableitungen bis zur dritten Ordnung*. Sonderheft 11 der Österreichischen Zeitschrift für Vermessungswesen, Österreichische Kommission für International Erdmessung, Wien 1951.

Makris, J. and Yegorova, T. (2006). A 3-D density-velocity model between the Cretan Sea and Libya. *Tectonophysics*, 417:201–220.

Marini, J. W. and Murray, C. W. (1973). Correction of laser range tracking data for atmospheric refraction at elevations above 10 degrees. Technical Report NASA-TM-X-70555, NASA Goddard Space Flight Center, Greenbelt, Maryland, USA.

McCarthy, D. D. and Petit, G., editors (2004). *IERS Conventions (2003). IERS Technical Note No. 32*. International Earth Rotation and Reference Systems Service (IERS). Verlag des Bundesamts für Kartographie und Geodäsie. Frankfurt am Main.

McClusky, S., Balassian, S., Barka, A., Demir, C., Georgiev, I., Hamburger, M., Hurst, K., Kahle, H.-G., Kastens, K., Kekelidze, G., King, R., Kotzev, V., Lenk, O., Mahmoud, S., Mishin, A., Nadariya, M., Ouzounis, A., Paradissis, D., Peter, Y., Prilepin, M., Reilinger, R., Sanli, I., Seeger, H., Tealeb, A., Tokzoz, M., and Veis, G. (2000). GPS constraints on plate kinematics and dynamics in the eastern Mediterranean and Caucasus. *J. Geophys. Res.*, 105(B3):5695–5719.

McNeill, L. C., Mille, A., Minshull, T. A., Bull, J. M., Kenyon, N. H., and Ivanov, M. (2004). Extension of the North Anatolian Fault into the North Aegean Trough: Evidence for transtension, strain partitioning and analogues for Sea of Marmara basin models. *Tectonics*, 23(TC2016).

Millot, C. (1999). Circulation in the Western Mediterranean Sea. *Journal of Marine Systems*, 20(1-4):423 – 442.

Morel, A. and Prieur, L. (1977). Analysis of variations in ocean color. *Limnology and Oceanography*, 22:709–722.

Moritz, H. (1980). *Advanced Physical Geodesy*. H. Wichmann Verlag, Karlsruhe.

Mourre, B. (2004). *Etudes de configuration d'une constellation de satellites altimétriques pour l'observation de la dynamique océanique côtière*. PhD thesis, Université Paul Sabatier (Toulouse III, France.

Müller, A., Bürki, B., Limpach, P., Kahle, H.-G., Grigoriadis, V. N., Vergos, G. S., and Tziavos, I. N. (2006). Validation of Marine Geoid Models in the North Aegean Sea using Satellite Altimetry, Marine GPS Data and Astrogeodetic Measurements. In *Proceedings of the 1st International Symposium of the International Gravity Field Service (IGFS). Gravity Field of the Earth. August 2006, Istanbul, Turkey*, pages 90–95.

NGA (2004). *Handbook of Magnetic Compass Adjustment*. National Geospatial-Intelligence Agency (NGA), Bethesda, MD. Formely Pub.No. 226, as originally published by the Defense Mapping Agency, Hydrographic/Topographic Center, Washington, D.C., 1980.

NIMA (2000). Department of Defense World Geodetic System 1984—Its Definition and Relationships with Local Geodetic Systems. Technical Report 8350.2, National Imagery and Mapping Agency, USA. Third Edition, 172 p.

Numada, M., Nomura, T., Yanagi, K., Kamiya, K., and Tashiro, H. (2007). High-order spline filter and ideal low-pass filter at the limit of its order. *Precision Engineering*, 31(3):234 – 242.

Optech (1989). *Model 501SA Rangefinder Operator Manual*. Optech Systems Corporation, Toronto, Canada.

OSTM (2008). *OSTM/Jason-2 Products Handbook*. CNES:SALP-MU-M-OP-15815-CN, EUMETSAT:EUM/OPS-JAS/MAN/08/0041, JPL:OSTM-29-1237, NOAA:.

Pavlis, E., Mertikas, S., and the GAVDOS Team (2004). The GAVDOS mean sea level and altimeter calibration facility: Results for Jason–1. *Marine Geodesy*, 27(3-4):631–655. ISSN: 0149-0419.

Pavlis, N. K., Holmes, S. A., Kenyon, S. C., and Factor, J. K. (2008). An Earth Gravitational Model to Degree 2160: EGM2008. Presented at the 2008 General Assembly of the European Geosciences Union, Vienna, Austria, April 13-18, 2008.

Pepperl+Fuchs (2006). *Ultrasonic Sensors Catalogue, Factory Automation*. Pepperl+Fuchs, Mannheim, Germany.

Peter, Y. (1994). Aero-Laser-Profilierung zur Aufnahme von Geländeprofilen. Master's thesis, ETH Zurich.

Picot, N., Case, K., Desai, S., and Vincent, P. (2003). *AVISO and PODAAC User Handbook. IGDR and GDR Jason Products.* SMM-MU-M5-OP-13184-CN (AVISO), JPL D-21352 (PODAAC).

Plag, H.-P., Ambrosius, B., Baker, T., Beutler, G., Bianco, G., Blewitt, G., Boucher, C., Davis, J., Degnan, J., Johansson, J., Kahle, H.-G., Müller, S., and Zerbini, S. (1998). Scientific objectives of current and future WEGENER activities. *Tectonophysics*, 294:177–223.

Rapp, R. H. (1989). The treatment of permanent tidal effects in the analysis of satellite altimeter data for sea surface topography. *manuscripta geodaetica*, 14(6):368–372.

Ray, R. D. (1999). A global ocean tide model from TOPEX/POSEIDON altimetry: GOT99.2. Technical Report NASA-TM-1999-209478, NASA Goddard Space Flight Center, Greenbelt, Maryland, USA.

Rio, M.-H. and Hernandez, F. (2004). A mean dynamic topography computed over the world ocean from altimetry, in situ measurements, and a geoid model. *J. Geophys. Res.*, 109(C12032).

Rio, M.-H., Poulain, P.-M., Pascal, A., Mauri, E., Larnicol, G., and Santoleri, R. (2007). A Mean Dynamic Topography of the Mediterranean Sea computed from altimetric data, in-situ measurements and a general circulation model. *Journal of Marine Systems*, 65:484–508.

Rio, M.-H., Schaeffer, P., Hernandez, F., and Lemoine, J.-M. (2006). From the Altimetric Sea Level Measurement to the Ocean Absolute Dynamic Topography: Mean Sea Surface, Geoid, Mean Dynamic Topography, a Three-Component Challenge. In *Proceedings of the Symposium on 15 Years of Progress in Radar Altimetry, 13-18 March 2006, Venice, Italy.* (ESA SP-614, July 2006).

Roblou, L. (2001). *Modélisation de la variation de la surface libre en mer Mediterranée, validation de MOG2D.* Université Toulouse III - Paul Sabatier.

Sandwell, D. T. and Smith, W. H. F. (1997). Marine gravity anomaly from Geosat and ERS 1 satellite altimetry. *Journal of Geophysical Research*, 102(B5):10039–10054.

Schöne, T. (2003). *GPS Water Level Measurements. Report of IAG Special Study Group 2.194.* IUGG General Assembly XXIII Sapporo, Japan, 30 June – 11 July 2003.

Snopek, K., Meier, T., Endrun, B., Bohnhoff, M., and Casten, U. (2007). Comparison of gravimetric and seismic constraints on the structure of the Aegean lithosphere in the forearc of the Hellenic subduction zone in the area of Crete. *Journal of Geodynamics*, 44(3-5):173–185.

Somieski, A. (2008). *Astrogeodetic Geoid and Isostatic Considerations in the North Aegean Sea, Greece.* PhD thesis, ETH Zurich.

Tradowsky, K. (1975). *Laser.* Vogel-Verlag, 2nd edition.

Tratt, D. M., Menzies, R. T., and Cutten, D. R. (1996). Wind-driven angular dependence of sea surface reflectance measured with an airborne Doppler lidar. Technical report, Jet Propulsion Lab (JPL).

Tsimplis, M. N., Proctor, R., and Flather, R. A. (1995). A two dimensional tidal model for the Mediterranean Sea. *J. Geophys. Res.*, 100(C8):16223–16239.

Tziavos, I. N. and Andritsanos, V. (1999). Recent Geoid Computations for the Hellenic Area. *Phys. Chem. Earth (A)*, 24(1):91–96.

Tziavos, I. N., Andritsanos, V. D., Forsberg, R., and Olesen, A. (2004). Numerical investigation of downward continuation methods for airborne gravity data. In *Gravity, Geoid and Space Missions, GGSM 2004 IAG International Symposium*, volume 129 of *International Association of Geodesy Symposia*, pages 119–124. Springer Berlin Heidelberg.

Törnig, W. and Spellucci, P. (2000). *Numerische Mathematik für Ingenieure und Physiker, Band 2: Numerische Methoden der Analysis*. Springer-Verlag.

Verdun, J., Klingelé, E., Bayer, R., Cocard, M., Geiger, A., and Kahle, H.-G. (2003). The alpine Swiss-French airborne gravity survey. *Geophysical Journal International*, 152(1).

Vergos, G. S., Tziavos, I. N., and Andritsanos, V. D. (2004). Gravity data base generation and geoid model estimation using heterogeneous data. In *Gravity, Geoid and Space Missions, GGSM 2004 IAG International Symposium*, volume 129 of *International Association of Geodesy Symposia*, pages 155–160. Springer Berlin Heidelberg.

Škaloud, J. and Lichti, D. (2006). Rigorous approach to bore-sight self-calibration in airborne laser scanning. *ISPRS Journal of Photogrammetry and Remote Sensing*, 61(2006):47–59.

Škaloud, J. and Schaer, P. (2003). Towards a more rigorous boresight calibration. In *Proceedings ISPRS International Workshop on Theory Technology and Realities of Inertial/GPS/Sensor Orientation, Castelldefels, Spain, 22-23 September 2003*.

Wehr, A. and Lohr, U. (1999). Airborne laser scanning - an introduction and overview. *ISPRS Journal of Photogrammy and Remote Sensing*, 54:68–82.

Welch, A. J., Torres, J. H., and Cheong, W.-F. (1989). Laser Physics and Laser-Tissue Interactions. *Texas Heart Institute Journal*, 16:141–149.

Wessel, P. and Smith, W. H. F. (1998). New, Improved Version of Generic Mapping Tools Released. *EOS Trans., AGU*, 79(47):579.

Wessel, P. and Smith, W. H. F. (2005). *The Generic Mapping Tools (GMT) version 4.1 Technical Reference and Cookbook*. SOEST/NOAA.

WMO (1998). *Guide to Wave Analysis and Forecasting*. World Meteorological Organization (WMO), Geneva, Switzerland, 2nd edition. WMO-No.702.

Wunsch, C. (1972). Bermuda sea level in relation to tides, weather and baroclinic fluctuations. *Rev. Geophys. Sace Phys.*, 10:1–49.

Wunsch, C. and Stammer, D. (1997). Atmospheric Loading and the Oceanic "Inverted Barometer" Effect. *Rev. Geophys.*, 35(1):79–107.

Zerbini, S., Plag, H.-P., Baker, T., Becker, M., Billiris, H., Bürki, B., Kahle, H.-G., Marson, I., Pezzoli, L., Richter, B., Romagnoli, C., Sztrobryn, M., Tomasi, P., Tsimplis, N., Veis, G., and Verrone, G. (1996). Sea level in the Mediterranean: a first step towards separating crustal movements and absolute sea-level variations. *Global and Planetary Change*, 14(1-2):1–48.

Zissis, G. J., editor (1993). *The Infrared and Electro-Optical Systems Handbook, Vol. 1: Sources of Radiation*. Infrared Information Analysis Center, Environmental Research Institute of Michigan / SPIE Optical Engineering Press.

Zwally, H. J. and Brenner, A. C. (2001). *Satellite Altimetry and Earth Sciences*, chapter Ice Sheet Dynamics and Mass Balance, pages 351–369. Academic Press.

A Models of Atmospheric Refraction of Light

A.1 Barrell and Sears Model (1939)

In 1939, H. Barrell and J.E. Sears published one of the first equations for the refractive index as a function of the atmospheric parameters temperature, air pressure and water vapor pressure, derived from measurements on dry and moist air. The refractivity N of moist air is given by (Barrell and Sears, 1939):

$$\begin{aligned} N &= (n-1)\cdot 10^6 \\ &= \left[0.378125 + \frac{0.0021414}{\lambda^2} + \frac{0.00001793}{\lambda^4}\right] \frac{p\left(1+(1.049-0.0157t)\,p\cdot 10^{-6}\right)}{1+0.003661t} \\ &\quad - \left[0.0624 - \frac{0.00068}{\lambda^2}\right] \frac{e}{1+0.003661t} \end{aligned} \tag{A.1}$$

where

n	refractive index for atmospheric conditions t, p, e and wavelength λ
p	atmospheric pressure [Torr], with 1 Torr $\approx$ 1.333 hPa, or 1013 hPa = 760 Torr
t	temperature [°C]
e	partial water vapor pressure [Torr]
λ	wavelength of light in the vacuum [μm]

According to (Barrell and Sears, 1939), (A.1) is applicable for the ranges t = 10 - 30°C and p = 720 - 800 Torr ($\approx$ 959.7 - 1066.3 hPa). Under standard atmospheric conditions (t = 15°C, p = 1013.25 hPa (760 Torr), e = 0), the standard refractivity N_s can be derived from (A.1):

$$N_s = (n_s - 1)\cdot 10^6 = 272.5837 + \frac{1.5437}{\lambda^2} + \frac{0.01293}{\lambda^4} \tag{A.2}$$

The refractivity N can be rewritten as a function of the refractivity N_s under standard conditions, by combining (A.1) and (A.2):

$$\begin{aligned} N &= (n-1)\cdot 10^6 \\ &= N_s\,\frac{p\left(1+(1.049-0.0157t)\,p\cdot 10^{-6}\right)}{720.88261\,(1+0.003661t)} - \left[0.0624 - \frac{0.00068}{\lambda^2}\right]\frac{e}{1+0.0003661t} \end{aligned} \tag{A.3}$$

In (A.3), the dependency on the wavelength λ is given by N_s, following (A.2).

A.2 Barrell Model (1951)

In 1951, H. Barrell published an update of the (Barrell and Sears, 1939) model, where the refractivity N of moist air is given by (Barrell, 1951):

$$\begin{aligned} N &= (n-1)\cdot 10^6 \\ &= N_s \, \frac{p\left(1+(1.049-0.0157t)\,p\cdot 10^{-6}\right)}{720.883\,(1+0.003661t)} - \left[0.0624 - \frac{0.00068}{\lambda^2}\right] \frac{e}{1+0.0003661t} \end{aligned} \tag{A.4}$$

with the refractivity under standard conditions

$$N_s = (n_s-1)\cdot 10^6 = 272.729 + \frac{1.4823}{\lambda^2} + \frac{0.02041}{\lambda^4} \tag{A.5}$$

and

n	refractive index for atmospheric conditions t, p, e and wavelength λ
n_s	refractive index under standard conditions ($t = 15$°C, $p = 760$ Torr, $e = 0$)
p	atmospheric pressure [Torr]
t	temperature [°C]
e	partial water vapor pressure [Torr]
λ	wavelength of light in the vacuum [μm]

A.3 Edlén Model (1966)

The equations nowadays commonly used in physics and geodetic surveying to derive the refractive index from temperature, pressure and humidity are those published by B. Edlén. According to (Edlén, 1966), the refractivity N of moist air is given by:

$$\begin{aligned} N &= (n-1)\cdot 10^6 \\ &= N_s \, \frac{p\left(1+(0.817-0.0133t)\,p\cdot 10^{-6}\right)}{720.775\,(1+0.003661t)} - \left[0.057224 - \frac{0.000457}{\lambda^2}\right] e \end{aligned} \tag{A.6}$$

with the refractivity under standard conditions

$$N_s = (n_s-1)\cdot 10^6 = 83.4213 + \frac{24060.30}{130-\lambda^{-2}} + \frac{159.97}{38.9-\lambda^{-2}} \tag{A.7}$$

and

n	refractive index for atmospheric conditions t, p, e and wavelength λ
n_s	refractive index under standard conditions ($t = 15$°C, $p = 760$ Torr, $e = 0$)
p	atmospheric pressure [Torr]
t	temperature [°C]
e	partial water vapor pressure [Torr]
λ	wavelength of light in the vacuum [μm]

A.4 Birch and Downs Model (1994)

Since the publication of (Edlén, 1966), several updates of the set of equations have been performed by several authors. One of the revised models is the one published by K.P. Birch and M.J. Downs (Birch and Downs, 1993, 1994). The major difference with respect to the citepEdlen-1966 equations are the conversion to the SI units system and the change in the temperature scale from the International Practical Temperature Scale of 1948 (ITPS-1948) to the International Temperature Scale of 1990 (ITS-90). According to (Birch and Downs, 1994), the refractivity N of moist air is given by:

$$\begin{aligned} N &= (n-1)\cdot 10^6 \\ &= N_s \, \frac{p\left(1+(0.601-0.00972t)\,p\cdot 10^{-8}\right)}{96095.43\,(1+0.003661t)} - \left[0.00037345 - \frac{0.00000401}{\lambda^2}\right] e \end{aligned} \tag{A.8}$$

with the refractivity under standard conditions

$$N_s = (n_s - 1)\cdot 10^6 = 83.4254 + \frac{24061.47}{130-\lambda^{-2}} + \frac{159.98}{38.9-\lambda^{-2}} \tag{A.9}$$

and

n	refractive index for atmospheric conditions t, p, e and wavelength λ
n_s	refractive index under standard conditions ($t = 15$°C, $p = 101325$ Pa, $e = 0$)
p	atmospheric pressure [Pa]
t	temperature [°C]
e	partial water vapor pressure [Pa]
λ	wavelength of light in the vacuum [μm]

B Standard Atmosphere Model

Values for temperature, atmospheric pressure and water vapor pressure at an altitude h can be derived from a standard atmosphere model, as a function of altitude h and using reference values for a reference altitude h_0:

$$\begin{aligned} T(h) &= T_0 - 0.0065\,(h - h_0) \\ p(h) &= p_0\ (1 - 0000226\,(h - h_0))^{5.225} \\ H(h) &= H_0\ \cdot e^{-0.0006396(h-h_0)} \end{aligned} \tag{B.1}$$

where T, p, H are the temperature [K], pressure [hPa] and relative humidity [%] at altitude h of the measurement site, and T_0, p_0, H_0 are the corresponding values at the reference altitude h_0. Commonly used reference values for a standard atmosphere at sea level ($h_0 = 0$) are:

$$\begin{aligned} T_0 &= 288.15 \text{ K } (15^\circ\text{C}) \text{ or } 291.15 \text{ K } (18^\circ\text{C}) \\ p_0 &= 1013.25 \text{ hPa} \\ H_0 &= 50\ \% \\ e_0 &= 17 \text{ hPa} \end{aligned}$$

The water vapor pressure can be calculated from the relative humidity H by (Giacomo, 1982):

$$e(h) = \frac{H}{100} \cdot e_s \cdot f_w \tag{B.2}$$

where

$$e_s(h) = 0.01 \cdot e^{\left(1.2378847 \cdot 10^{-5}\ T^2\ -\ 1.9121316 \cdot 10^{-2}\ T\ +\ 33.93711047\ -\ 6.3431645 \cdot 10^{3}\ T^{-1}\right)} \tag{B.3}$$

and

$$f_w(h) = 1.00062\ +\ 3.14 \cdot 10^{-6}\ p\ +\ 5.6 \cdot 10^{-7}\ (T - 273.10)^2 \tag{B.4}$$

with e_s is the saturation water vapor pressure and f_w the enhancement factor.

C Specifications of Ultrasonic Sensors

Ultrasonic sensor
UC4000-30GM-IUR2-V15

Features

- Parameterisation interface for the application-specific adjustment of the sensor setting via the service program ULTRA 2001
- Current and voltage output
- Synchronisation options
- Adjustable acoustic power and sensitivity
- Temperature compensation

Electrical connection

Standard symbol/Connection:
(version IU)

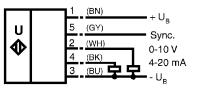

Core colours in accordance with EN 60947-5-2.

Connector V15

Dimensions

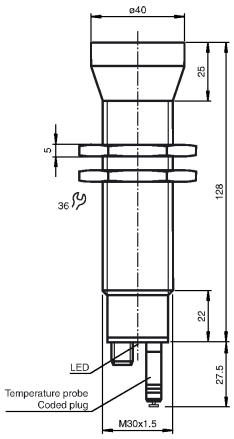

Technical data

CE

General specifications	
Sensing range	200 ... 4000 mm
Adjustment range	240 ... 4000 mm
Unusable area	0 ... 200 mm
Standard target plate	100 mm x 100 mm
Transducer frequency	approx. 85 kHz
Response delay	145 ms minimum 440 ms factory setting
Indicators/operating means	
LED green	permanent: Power-on flashing: Standby mode or TEACH-IN function object detected
LED yellow 1	permanent: object in evaluation range flashing: TEACH-IN function
LED yellow 2	permanent: object in detection range flashing: TEACH-IN function
LED red	permanent: temperature/TEACH-IN plug not connected flashing: fault or TEACH-IN function object not detected
Temperature/TEACH-IN connector	temperature compensation , TEACH-IN for evaluation range , output function setting
Electrical specifications	
Operating voltage	10 ... 30 V DC , ripple 10 $\%_{SS}$
Power consumption P_0	≤ 900 mW
Interface	
Interface type	RS 232, 9600 Bit/s , no parity, 8 data bits, 1 stop bit
Input/Output	
Synchronisation	bi-directional 0 level -U_B...+1 V 1 level: +4 V...+U_B input impedance: > 12 KOhm synchronisation pulse: ≥ 100 µs, synchronisation interpulse period: ≥ 2 ms
Synchronisation frequency	
Common mode operation	≤ 13 Hz
Multiplex operation	≤ 13/n Hz, n = number of sensors
Output	
Output type	1 current output 4 ... 20 mA 1 voltage output 0 ... 10 V
Resolution	evaluation range [mm]/4000, but ≥ 0,35 mm
Deviation of the characteristic curve	≤ 0,2 % of full-scale value
Repeat accuracy	≤ 0,1 % of full-scale value
Load impedance	current output: ≤ 500 Ohm Voltage output: ≥ 1000 Ohm
Temperature influence	≤ 2 % from full-scale value (with temperature compensation) ≤ 0.2 %/K (without temperature compensation)
Standard conformity	
Standards	EN 60947-5-2
Ambient conditions	
Ambient temperature	-25 ... 70 °C (248 ... 343 K)
Storage temperature	-40 ... 85 °C (233 ... 358 K)
Mechanical specifications	
Protection degree	IP65
Connection	connector V15 (M12 x 1), 5 pin
Material	
Housing	stainless steel 1.4303 plastic parts PBT
Transducer	epoxy resin/hollow glass sphere mixture; polyurethane foam
Mass	210 g

104094_ENG.xml

2004-11-05

Pepperl+Fuchs Group • Tel.: Germany +49 621 776-0 • USA +1 330 4253555 • Singapore +65 67799091 • Internet http://www.pepperl-fuchs.com

Ultrasonic sensor
UC6000-30GM-IUR2-V15

Features

- Parameterisation interface for the application-specific adjustment of the sensor setting via the service program ULTRA 2001
- Current and voltage output
- Synchronisation options
- Adjustable acoustic power and sensitivity
- Temperature compensation

Electrical connection

Standard symbol/Connection:
(version IU)

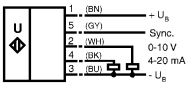

Core colours in accordance with EN 60947-5-2.

Connector V15

Dimensions

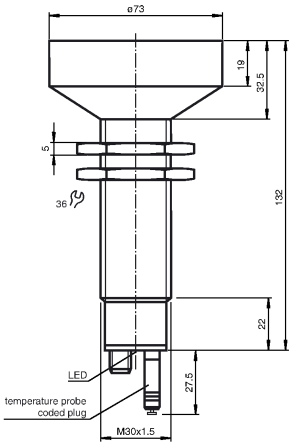

Technical data

CE

General specifications	
Sensing range	350 ... 6000 mm
Adjustment range	400 ... 6000 mm
Unusable area	0 ... 350 mm
Standard target plate	100 mm x 100 mm
Transducer frequency	approx. 65 kHz
Response delay	285 ms minimum 850 ms factory setting
Indicators/operating means	
LED green	permanent: Power-on flashing: Standby mode or TEACH-IN function object detected
LED yellow 1	permanent: object in evaluation range flashing: TEACH-IN function
LED yellow 2	permanent: object in detection range flashing: TEACH-IN function
LED red	permanent: temperature/TEACH-IN plug not connected flashing: fault or TEACH-IN function object not detected
Temperature/TEACH-IN connector	temperature compensation , TEACH-IN for evaluation range , output function setting
Electrical specifications	
Operating voltage	10 ... 30 V DC , ripple 10 $\%_{SS}$
Power consumption P_0	≤ 900 mW
Interface	
Interface type	RS 232, 9600 Bit/s , no parity, 8 data bits, 1 stop bit
Input/Output	
Synchronisation	bi-directional 0 level -U_B...+1 V 1 level: +4 V...+U_B input impedance: > 12 KOhm synchronisation pulse: ≥ 100 µs, synchronisation interpulse period: ≥ 2 ms
Synchronisation frequency	
Common mode operation	≤ 7 Hz
Multiplex operation	≤ 7/n Hz, n = number of sensors
Output	
Output type	1 current output 4 ... 20 mA 1 voltage output 0 ... 10 V
Resolution	evaluation range [mm]/4000, but ≥ 0,35 mm
Deviation of the characteristic curve	≤ 0,2 % of full-scale value
Repeat accuracy	≤ 0,1 % of full-scale value
Load impedance	current output: ≤ 500 Ohm Voltage output: ≥ 1000 Ohm
Temperature influence	≤ 2 % from full-scale value (with temperature compensation) ≤ 0.2 %/K (without temperature compensation)
Standard conformity	
Standards	EN 60947-5-2
Ambient conditions	
Ambient temperature	-25 ... 70 °C (248 ... 343 K)
Storage temperature	-40 ... 85 °C (233 ... 358 K)
Mechanical specifications	
Protection degree	IP65
Connection	connector V15 (M12 x 1), 5 pin
Material	
Housing	stainless steel 1.4303 plastic parts PBT
Transducer	epoxy resin/hollow glass sphere mixture; polyurethane foam
Mass	280 g

104095_ENG.xml

2004-11-05

Pepperl+Fuchs Group • Tel.: Germany +49 621 776-0 • USA +1 330 4253555 • Singapore +65 67799091 • Internet http://www.pepperl-fuchs.com

D Rotation Matrices

D.1 General Formulation

A rotation in a three dimensional coordinate system is performed by three consecutive rotations around the three coordinate axes:

$$\begin{bmatrix} \bar{x} \\ \bar{y} \\ \bar{z} \end{bmatrix} = \boldsymbol{R}_3(\alpha_3) \cdot \boldsymbol{R}_2(\alpha_2) \cdot \boldsymbol{R}_1(\alpha_1) \cdot \begin{bmatrix} x \\ y \\ z \end{bmatrix} = \boldsymbol{R} \cdot \begin{bmatrix} x \\ y \\ z \end{bmatrix} \tag{D.1}$$

with

$$\boldsymbol{R}_1 = \begin{bmatrix} 1 & 0 & 0 \\ 0 & \cos\alpha_1 & \sin\alpha_1 \\ 0 & -\sin\alpha_1 & \cos\alpha_1 \end{bmatrix} \quad \boldsymbol{R}_2 = \begin{bmatrix} \cos\alpha_2 & 0 & -\sin\alpha_2 \\ 0 & 1 & 0 \\ \sin\alpha_2 & 0 & \cos\alpha_1 \end{bmatrix} \quad \boldsymbol{R}_3 = \begin{bmatrix} \cos\alpha_3 & \sin\alpha_3 & 0 \\ -\sin\alpha_3 & \cos\alpha_3 & 0 \\ 0 & 0 & 1 \end{bmatrix}$$

and

$$\boldsymbol{R} = \boldsymbol{R}_3(\alpha_3) \cdot \boldsymbol{R}_2(\alpha_2) \cdot \boldsymbol{R}_1(\alpha_1) \tag{D.2}$$

$$\boldsymbol{R} = \begin{bmatrix} \cos\alpha_2\cos\alpha_3 & \cos\alpha_1\sin\alpha_3+\sin\alpha_1\sin\alpha_2\cos\alpha_3 & \sin\alpha_1\sin\alpha_3-\cos\alpha_1\sin\alpha_2\cos\alpha_3 \\ -\cos\alpha_2\sin\alpha_3 & \cos\alpha_1\cos\alpha_3-\sin\alpha_1\sin\alpha_2\sin\alpha_3 & \sin\alpha_1\cos\alpha_3+\cos\alpha_1\sin\alpha_2\sin\alpha_3 \\ \sin\alpha_2 & -\sin\alpha_1\cos\alpha_2 & \cos\alpha_1\cos\alpha_2 \end{bmatrix}$$

The rotation matrix $\boldsymbol{R}$ is orthogonal, and the transposed matrix is therefore equal to its inverse matrix. Additionally, the inverse of a rotation matrix is equal to three rotations in opposite order and around angles with opposite signs:

$$\boldsymbol{R}^{-1} = \boldsymbol{R}^T = \boldsymbol{R}_1(-\alpha_1) \cdot \boldsymbol{R}_2(-\alpha_2) \cdot \boldsymbol{R}_3(-\alpha_3) \tag{D.3}$$

$$\boldsymbol{R}^{-1} = \begin{bmatrix} \cos\alpha_2\cos\alpha_3 & -\cos\alpha_2\sin\alpha_3 & \sin\alpha_2 \\ \cos\alpha_1\sin\alpha_3+\sin\alpha_1\sin\alpha_2\cos\alpha_3 & \cos\alpha_1\cos\alpha_3-\sin\alpha_1\sin\alpha_2\sin\alpha_3 & -\sin\alpha_1\cos\alpha_2 \\ \sin\alpha_1\sin\alpha_3-\cos\alpha_1\sin\alpha_2\cos\alpha_3 & \sin\alpha_1\cos\alpha_3+\cos\alpha_1\sin\alpha_2\sin\alpha_3 & \cos\alpha_1\cos\alpha_2 \end{bmatrix}$$

In direct georeferencing, rotations are usually defined as:

$$\boldsymbol{R}_{\_} = \boldsymbol{R}_3(-\alpha_3) \cdot \boldsymbol{R}_2(-\alpha_2) \cdot \boldsymbol{R}_1(-\alpha_1) \tag{D.4}$$

$$\boldsymbol{R}_{\_} = \begin{bmatrix} \cos\alpha_2\cos\alpha_3 & -\cos\alpha_1\sin\alpha_3+\sin\alpha_1\sin\alpha_2\cos\alpha_3 & \sin\alpha_1\sin\alpha_3+\cos\alpha_1\sin\alpha_2\cos\alpha_3 \\ \cos\alpha_2\sin\alpha_3 & \cos\alpha_1\cos\alpha_3+\sin\alpha_1\sin\alpha_2\sin\alpha_3 & -\sin\alpha_1\cos\alpha_3+\cos\alpha_1\sin\alpha_2\sin\alpha_3 \\ -\sin\alpha_2 & \sin\alpha_1\cos\alpha_2 & \cos\alpha_1\cos\alpha_2 \end{bmatrix}$$

and the inverse matrix is:

$$\underset{\_}{\boldsymbol{R}}^{-1} = \underset{\_}{\boldsymbol{R}}^{T} = \boldsymbol{R}_1(\alpha_1) \cdot \boldsymbol{R}_2(\alpha_2) \cdot \boldsymbol{R}_3(\alpha_3) \tag{D.5}$$

$$\underset{\_}{\boldsymbol{R}}^{-1} = \begin{bmatrix} \cos\alpha_2 \cos\alpha_3 & \cos\alpha_2 \sin\alpha_3 & -\sin\alpha_2 \\ -\cos\alpha_1 \sin\alpha_3 + \sin\alpha_1 \sin\alpha_2 \cos\alpha_3 & \cos\alpha_1 \cos\alpha_3 + \sin\alpha_1 \sin\alpha_2 \sin\alpha_3 & \sin\alpha_1 \cos\alpha_2 \\ \sin\alpha_1 \sin\alpha_3 + \cos\alpha_1 \sin\alpha_2 \cos\alpha_3 & -\sin\alpha_1 \cos\alpha_3 + \cos\alpha_1 \sin\alpha_2 \sin\alpha_3 & \cos\alpha_1 \cos\alpha_2 \end{bmatrix}$$

For small angles $d\alpha_i \approx 0$, $\sin d\alpha_i \approx d\alpha_i$ and $\cos d\alpha_i \approx 1$, the rotation matrix $\boldsymbol{R}$ from (D.2) becomes:

$$\boldsymbol{R}(d\alpha) \approx \begin{bmatrix} 1 & d\alpha_3 & -d\alpha_2 \\ -d\alpha_3 & 1 & d\alpha_1 \\ d\alpha_2 & -d\alpha_1 & 1 \end{bmatrix} \tag{D.6}$$

D.2 Rotation from Local Level to Geocentric System

The transformation from geocentric to topocentric ENU (East, North, Up) coordinates is performed by a translation to the origin of the topocentric frame followed by two consecutive rotations:

$$\begin{bmatrix} E \\ N \\ H \end{bmatrix} = \boldsymbol{R}_1\left(\frac{\pi}{2} - \varphi\right) \cdot \boldsymbol{R}_3\left(\frac{\pi}{2} + \lambda\right) \cdot \left(\begin{bmatrix} X \\ Y \\ Z \end{bmatrix} - \begin{bmatrix} X_0 \\ Y_0 \\ Z_0 \end{bmatrix} \right) = \boldsymbol{R}_{ENH/G} \cdot \left(\begin{bmatrix} X \\ Y \\ Z \end{bmatrix} - \begin{bmatrix} X_0 \\ Y_0 \\ Z_0 \end{bmatrix} \right) \tag{D.7}$$

with

$$\boldsymbol{R}_{ENH/G} = \boldsymbol{R}_1\left(\frac{\pi}{2} - \varphi\right) \cdot \boldsymbol{R}_3\left(\frac{\pi}{2} + \lambda\right) = \begin{bmatrix} -\sin\lambda & \cos\lambda & 0 \\ -\sin\varphi\cos\lambda & -\sin\varphi\sin\lambda & \cos\varphi \\ \cos\varphi\cos\lambda & \cos\varphi\sin\lambda & \sin\varphi \end{bmatrix} \tag{D.8}$$

The transformation from geocentric to topocentric NED (North, East, Down) coordinates is performed by a translation to the origin of the topocentric frame followed by two consecutive rotations:

$$\begin{bmatrix} N \\ E \\ D \end{bmatrix} = \boldsymbol{R}_2\left(-\varphi - \frac{\pi}{2}\right) \cdot \boldsymbol{R}_3(\lambda) \cdot \left(\begin{bmatrix} X \\ Y \\ Z \end{bmatrix} - \begin{bmatrix} X_0 \\ Y_0 \\ Z_0 \end{bmatrix} \right) = \boldsymbol{R}_{NED/G} \cdot \left(\begin{bmatrix} X \\ Y \\ Z \end{bmatrix} - \begin{bmatrix} X_0 \\ Y_0 \\ Z_0 \end{bmatrix} \right) \tag{D.9}$$

with

$$\boldsymbol{R}_{NED/G} = \boldsymbol{R}_2\left(-\frac{\pi}{2} - \varphi\right) \cdot \boldsymbol{R}_3(\lambda) = \begin{bmatrix} -\sin\varphi\cos\lambda & -\sin\varphi\sin\lambda & \cos\varphi \\ -\sin\lambda & \cos\lambda & 0 \\ -\cos\varphi\cos\lambda & -\cos\varphi\sin\lambda & -\sin\varphi \end{bmatrix} \tag{D.10}$$

The rotation matrix $\boldsymbol{R}_{G/L}^{T}$ from the topocentric NED frame to the geocentric system can be derived from (D.10), using (D.3):

$$\boldsymbol{R}_{G/L} = \boldsymbol{R}_{NED/G}^{-1} = \boldsymbol{R}_3(-\lambda) \cdot \boldsymbol{R}_2\left(\varphi + \frac{\pi}{2}\right) = \begin{bmatrix} -\sin\varphi\cos\lambda & -\sin\lambda & -\cos\varphi\cos\lambda \\ -\sin\varphi\sin\lambda & \cos\lambda & -\cos\varphi\sin\lambda \\ \cos\varphi & 0 & -\sin\varphi \end{bmatrix} \tag{D.11}$$

E Differential Clock Bias in Moving Baseline GPS Processing

Like in conventional differential GPS processing, the vector $\boldsymbol{dx}(t_R)$ obtained by moving baseline GPS processing is given by the difference between the position $\boldsymbol{x}_m(t_{Rm})$ of the remote receiver at time of reception t_{Rm} and the position $\boldsymbol{x}_r(t_{Rr})$ of the reference receiver at time of reception t_{Rr}:

$$\boldsymbol{dx}(t_R) \;=\; \boldsymbol{x}_m(t_{Rm}) \;-\; \boldsymbol{x}_r(t_{Rr}) \tag{E.1}$$

Due to the receiver-specific clock biases τ_i, the two times of reception t_{Rm} and t_{Rr} are not identical. In order to compute the attitude of a platform, vectors are needed at nominal time t_N, that is the time at which the measurements should have been taken. The nominal time t_N, as well as the position of the reference receiver $\boldsymbol{x}_r(t_N)$ and the remote receiver $\boldsymbol{x}_m(t_N)$ at nominal time are given by (Favey, 2001):

$$t_N \;=\; t_{Ri} \;+\; \boldsymbol{\tau}_i \tag{E.2}$$
$$\boldsymbol{x}_r(t_N) \;=\; \boldsymbol{x}_r(t_{Rr}) \;+\; \boldsymbol{\tau}_r\; \boldsymbol{v}_r(t_{Rr}) \tag{E.3}$$
$$\boldsymbol{x}_m(t_N) \;=\; \boldsymbol{x}_m(t_{Rm}) \;+\; \boldsymbol{\tau}_m\; \boldsymbol{v}_m(t_{Rm}) \tag{E.4}$$

where $v_r(t_{Rr})$ is the velocity of the reference receiver at time of reception, $v_m(t_{Rm})$ is the velocity of the remote receiver at time of reception, $\boldsymbol{\tau}_r$ is the clock bias of the reference receiver and $\boldsymbol{\tau}_m$ is the clock bias of the remote receiver. Thus, the vector at nominal time t_N is obtained by subtracting (E.3) from (E.4), and using (E.1):

$$\begin{aligned} \boldsymbol{dx}(t_N) \;&=\; \boldsymbol{x}_m(t_N) \;-\; \boldsymbol{x}_r(t_N) \\ &=\; \boldsymbol{dx}(t_R) \;+\; \boldsymbol{\tau}_m\; \boldsymbol{v}_m(t_{Rm}) \;-\; \boldsymbol{\tau}_r\; \boldsymbol{v}_r(t_{Rr}) \end{aligned} \tag{E.5}$$

In the case of two static receivers, $v_m(t_{Rm}) = v_r(t_{Rr}) = 0$ and (E.5) becomes:

$$\boldsymbol{dx}(t_N) \;=\; \boldsymbol{dx}(t_R) \tag{E.6}$$

meaning that the difference between the two receiver clock biases has no effect. In the case of a static reference receiver and a moving remote receiver, $v_r(t_{Rr}) = 0$ and (E.5) becomes:

$$\boldsymbol{dx}(t_N) \;=\; \boldsymbol{dx}(t_R) \;+\; \boldsymbol{\tau}_m\; \boldsymbol{v}_m(t_{Rm}) \tag{E.7}$$

meaning that difference between the two receiver clock biases has no effect, considering (E.2). In the case of a moving baseline, with two moving receivers rigidly mounted on the same platform with small rotational velocities, $\boldsymbol{v}_m(t_{Rm}) \approx \boldsymbol{v}_r(t_{Rr})$ and (E.5) becomes:

$$\boldsymbol{dx}(t_N) \;=\; \boldsymbol{dx}(t_R) \;+\; (\tau_m - \tau_r)\; \boldsymbol{v} \tag{E.8}$$

where $\boldsymbol{v} \approx \boldsymbol{v}_m(t_{Rm}) \approx \boldsymbol{v}_r(t_{Rr})$ is the velocity of the platform, derived by differentiation of the known positions of the reference antenna. Thus, the vector deformation is given by the difference between the two receiver clock biases multiplied by the velocity of the platform. With a differential clock bias in the order of 1 ms and an aircraft velocity of 70 m/s, the vector distortion due to asynchronous receiver clocks would be 7 cm. For this reason, it is not advisable to introduce the known vector lengths in the GPS baseline processing as additional information in the case of highly-dynamic applications like airborne laser altimetry. The approach for differential clock bias correction described above is based on (Favey, 2001).

F ECMWF Atmospheric Pressure

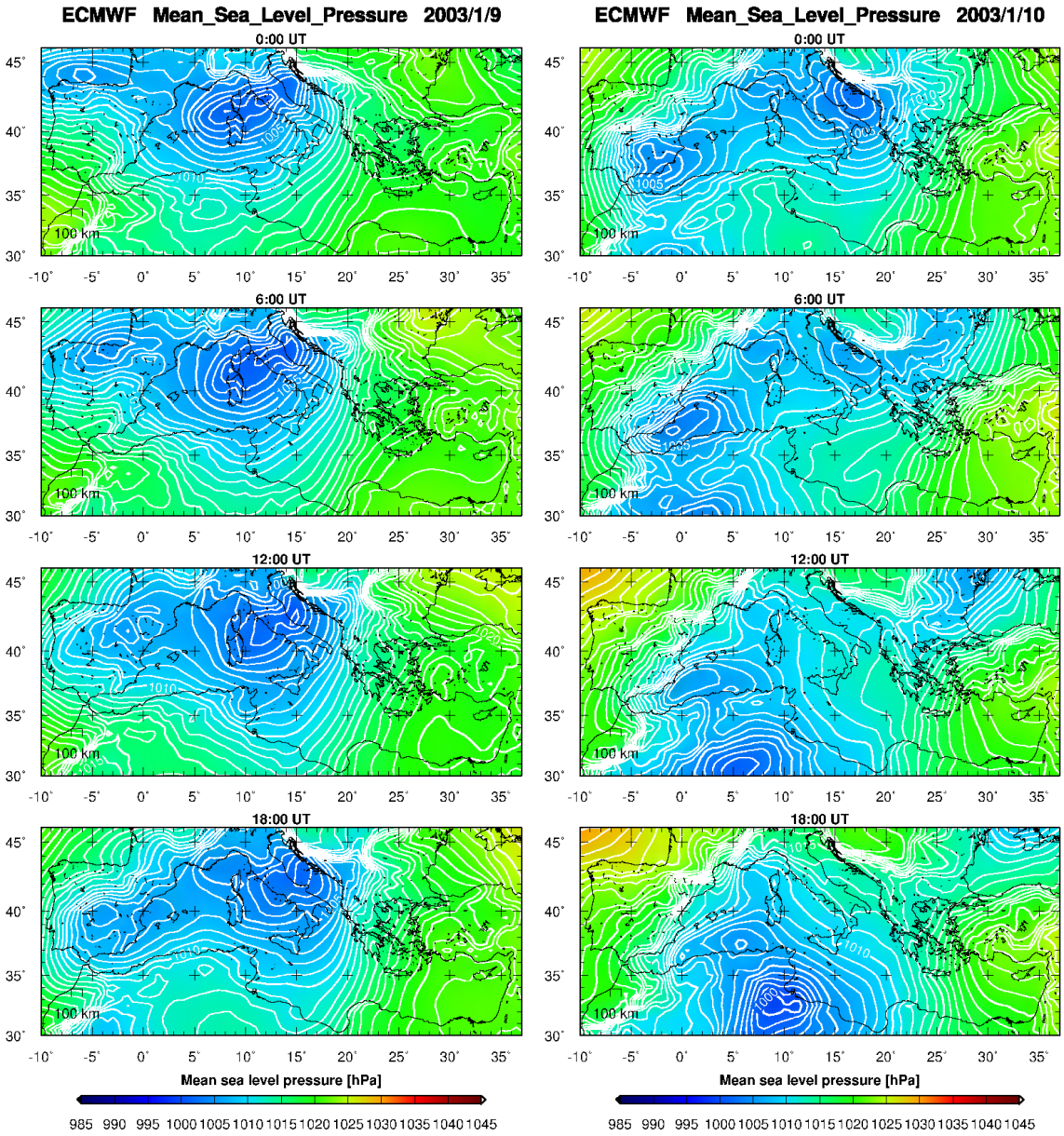

Figure F.1: ECMWF six hours atmospheric pressure at mean sea level over the Mediterranean Sea on 2003/01/09 and 2003/01/10. Contour interval: 1 hPa.

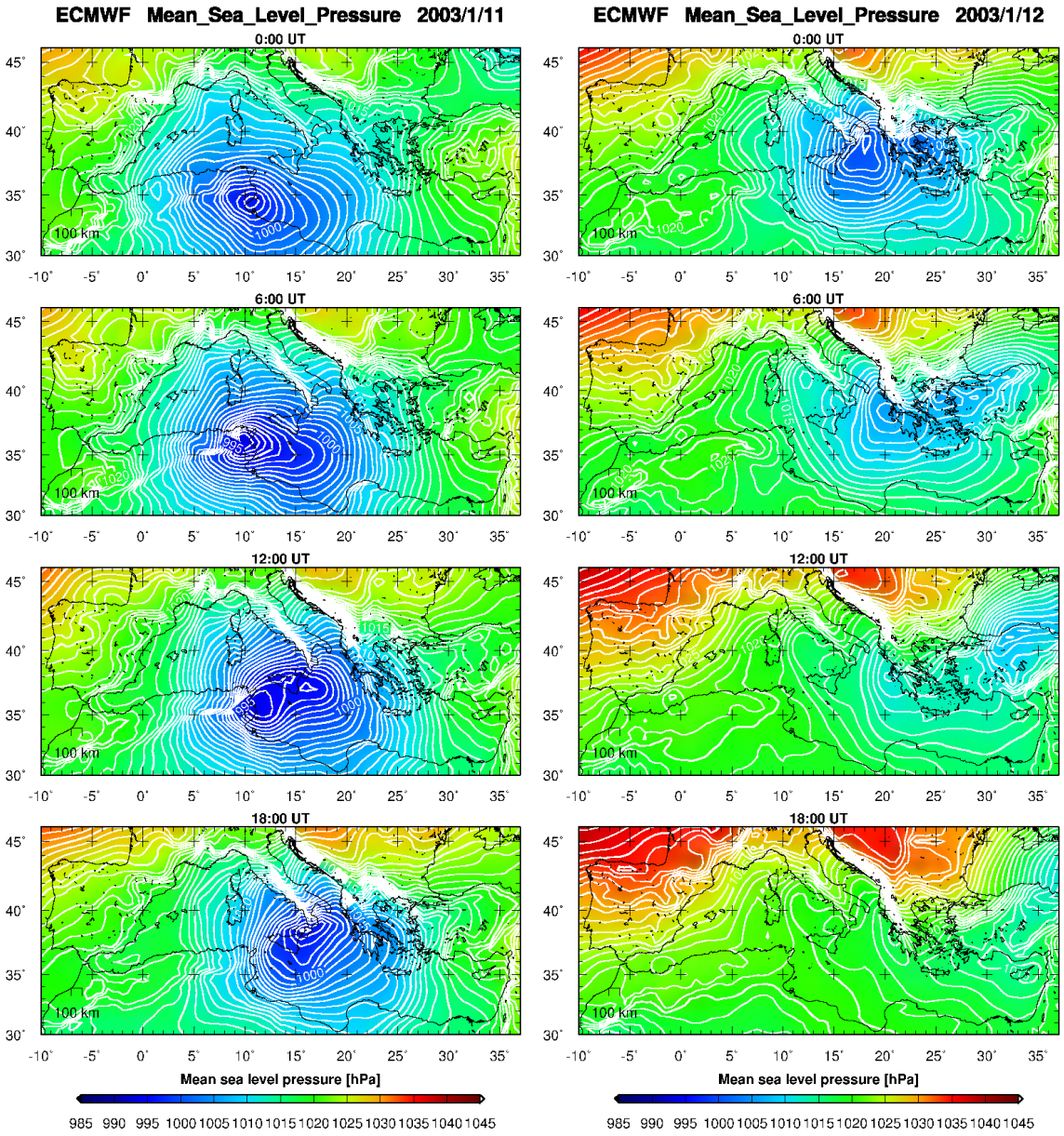

Figure F.2: ECMWF six hours atmospheric pressure at mean sea level over the Mediterranean Sea on 2003/01/11 and 2003/01/12. Contour interval: 1 hPa.

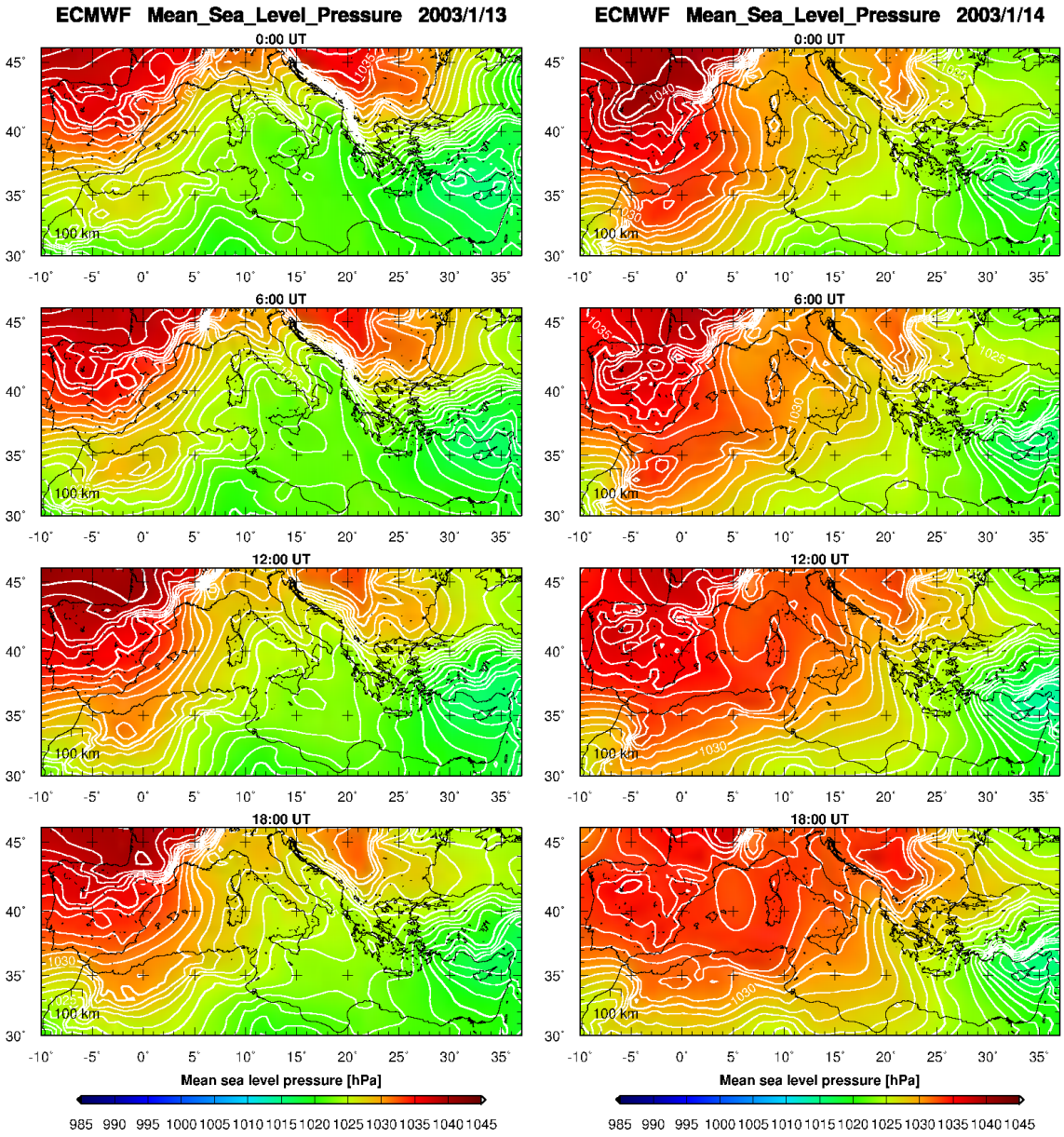

Figure F.3: ECMWF six hours atmospheric pressure at mean sea level over the Mediterranean Sea on 2003/01/13 and 2003/01/14. Contour interval: 1 hPa.

G MOG2D Dynamic Atmospheric Correction over the Mediterranean Sea

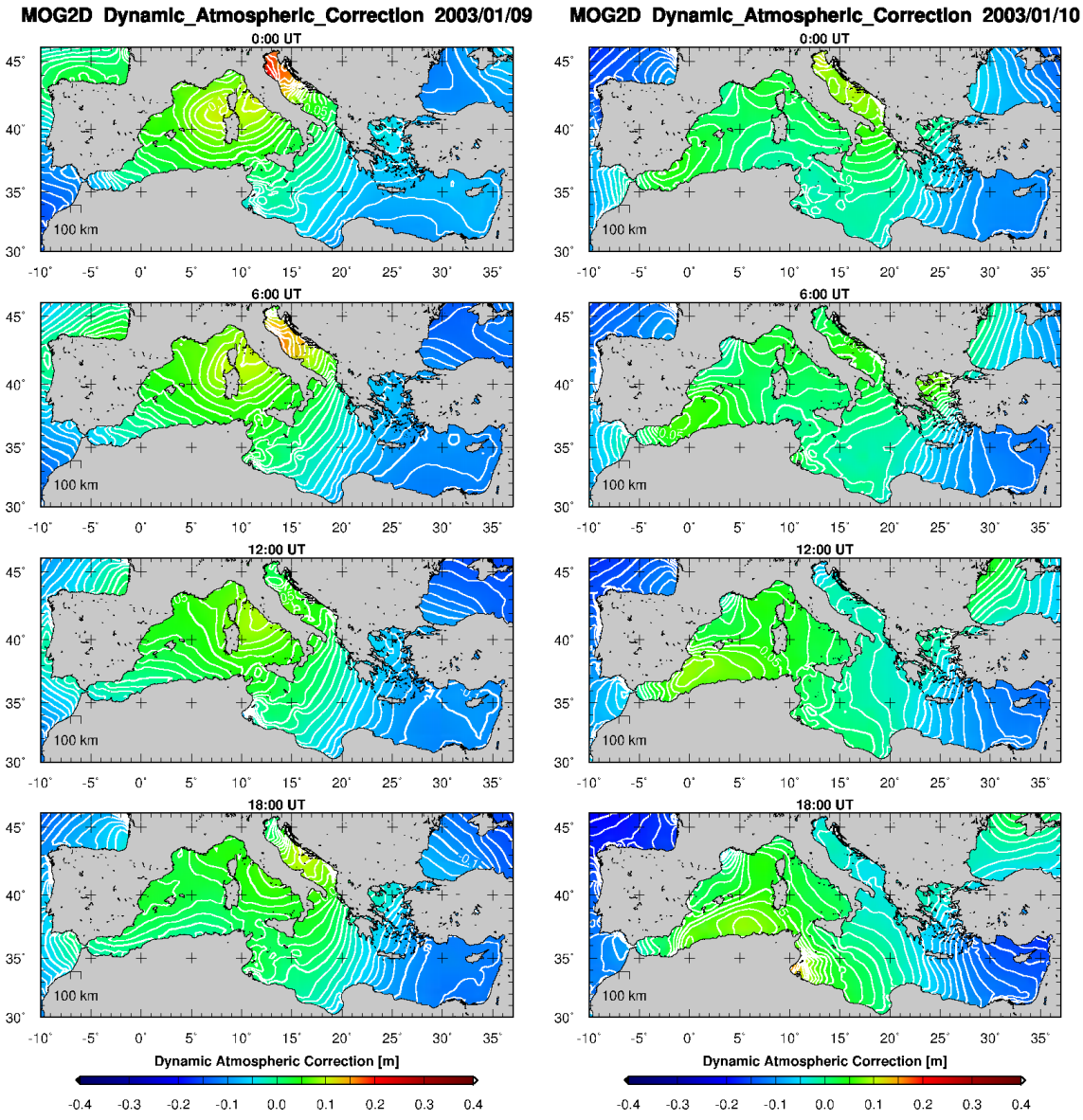

Figure G.1: MOG2D dynamic atmospheric correction grids over the Mediterranean Sea on 2003/01/09 and 2003/01/10, for the effect of pressure and wind forcing on sea surface height. Contour interval: 0.01 m. Corresponding ECMWF atmospheric pressure grids at sea level are shown in Appendix F, Fig. F.1.

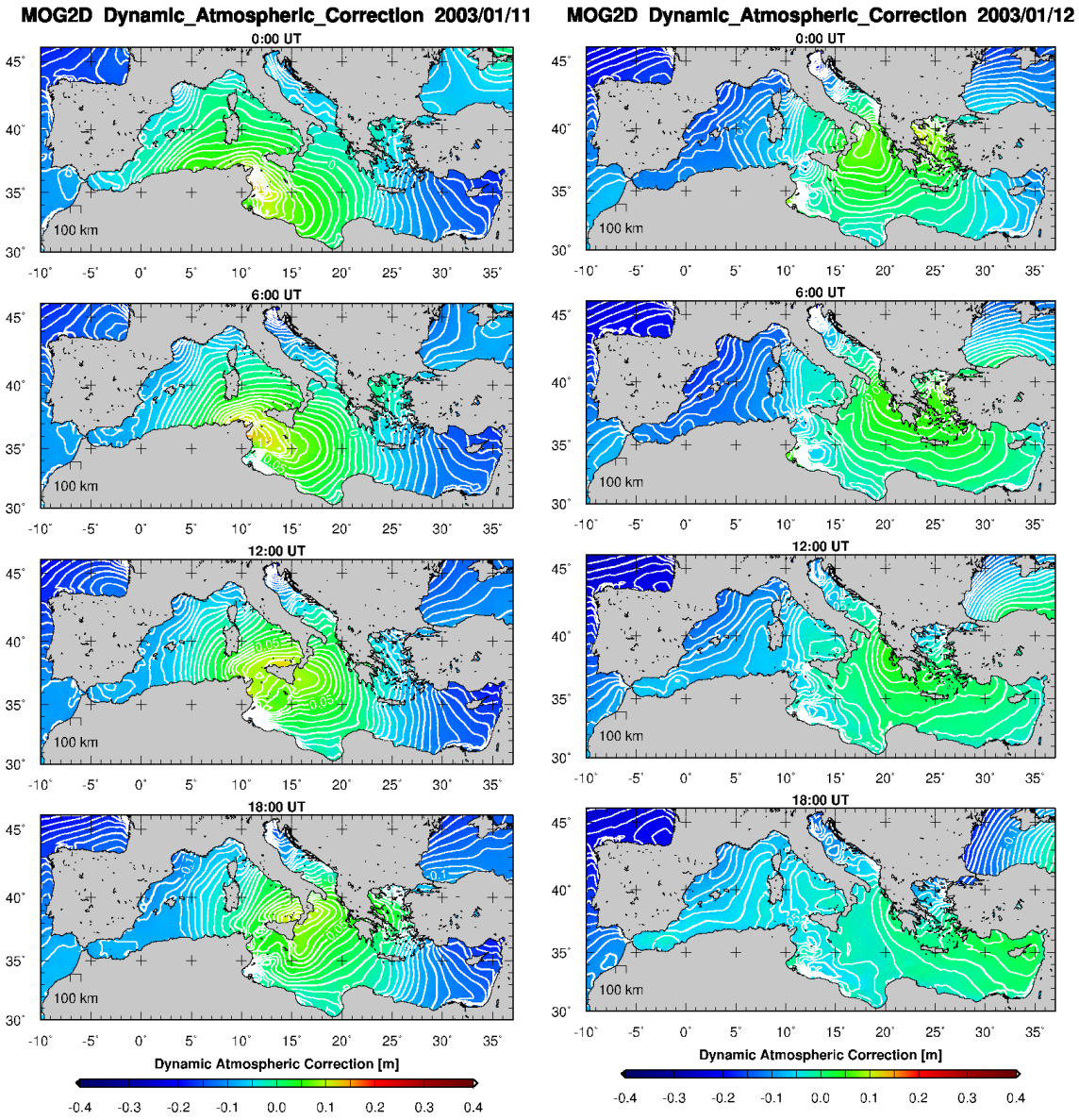

Figure G.2: MOG2D dynamic atmospheric correction grids over the Mediterranean Sea on 2003/01/11 and 2003/01/12, for the effect of pressure and wind forcing on sea surface height. Contour interval: 0.01 m. Corresponding ECMWF atmospheric pressure grids at sea level are shown in Appendix F, Fig. F.2.

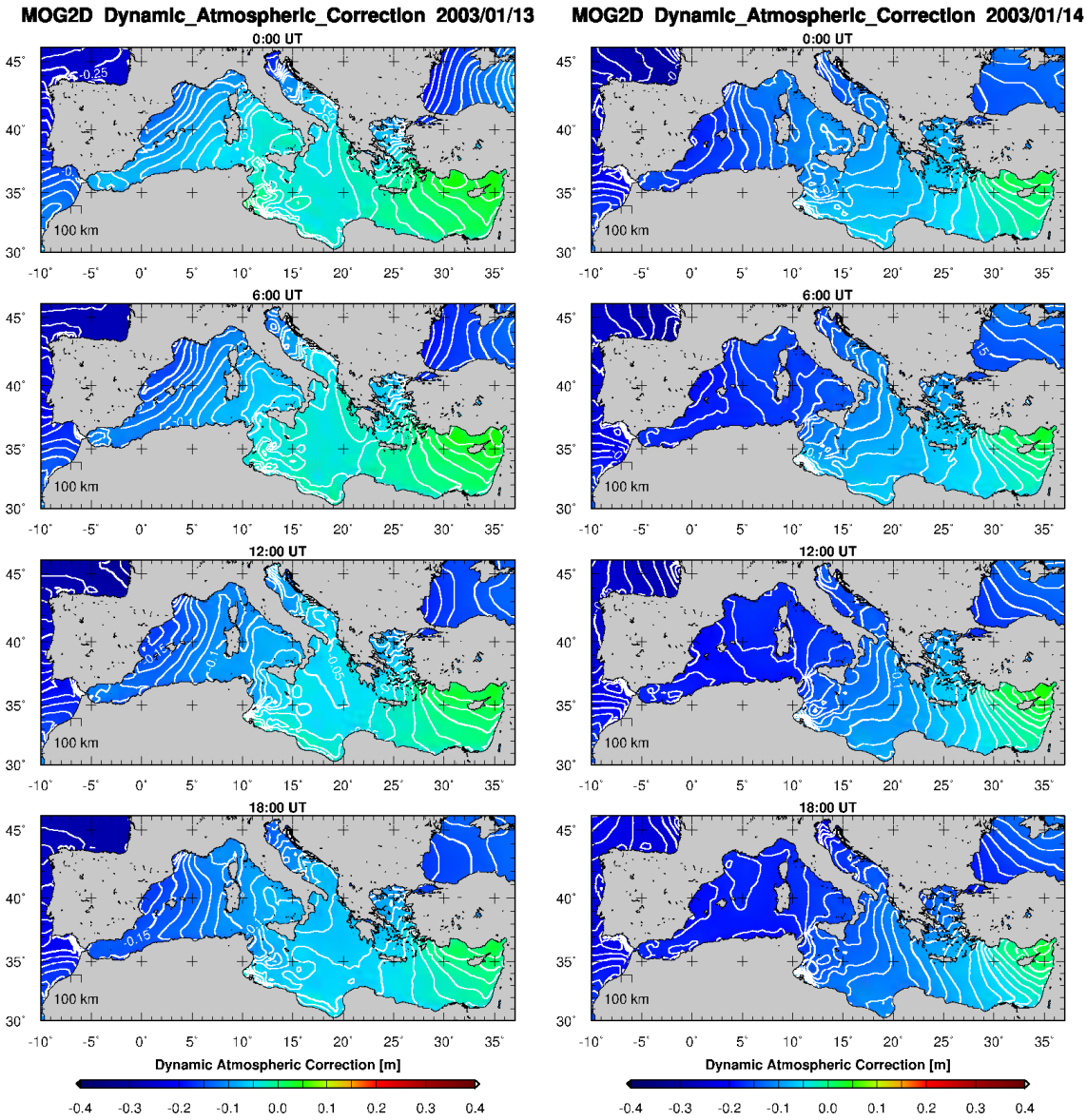

Figure G.3: MOG2D dynamic atmospheric correction grids over the Mediterranean Sea on 2003/01/13 and 2003/01/14, for the effect of pressure and wind forcing on sea surface height. Contour interval: 0.01 m. Corresponding ECMWF atmospheric pressure grids at sea level are shown in Appendix F, Fig. F.3.